UNIVERSIDADE DE SÃO PAULO

FACULDADE DE CIÊNCIAS FARMACÊUTICAS DE RIBEIRÃO PRETO

X-ray crystallographic fragment screening against the human prion protein

Varredura de fragmentos por cristalografia de raios-X contra a proteína priônica humana

VICTOR LOPES RANGEL

Ribeirão Preto
2021

UNIVERSIDADE DE SÃO PAULO

FACULDADE DE CIÊNCIAS FARMACÊUTICAS DE RIBEIRÃO PRETO

VICTOR LOPES RANGEL

X-ray crystallographic fragment screening against the human prion protein

Varredura de fragmentos por cristalografia de raios-X contra a proteína priônica humana

Direct Doctoral thesis presented to the Graduate Program of School of Pharmaceutical Sciences of Ribeirão Preto/USP for the degree of Doctor in Sciences.

Concentration Area: Chemistry and Biological Physics.

Supervisor: Flavio da Silva Emery.

Versão corrigida da Tese de Doutorado apresentada ao Programa de Pós-Graduação em Ciências Farmacêuticas em 20/08/2021. A versão original encontra-se disponível na Faculdade de Ciências Farmacêuticas de Ribeirão Preto/USP.

Ribeirão Preto
2021

Rangel, Victor Lopes

X-ray crystallographic fragment screening against the human prion protein. Ribeirão Preto, 2021.
218 p.; 30 cm.

Direct Doctoral thesis presented to the Graduate Program of School of Pharmaceutical Sciences of Ribeirão Preto/USP for the degree of Doctor in Sciences. Concentration Area: Chemistry and Biological Physics.

Supervisor: Emery, Flávio da Silva

1. Prion protein 2. Protein crystallography 3. Fragment screening
4. Prion disease 5. Fragment-based drug discovery

APPROVAL PAGE

Victor Lopes Rangel
X-ray crystallographic fragment screening against the human prion protein

Direct Doctoral thesis presented to the Graduate Program of School of Pharmaceutical Sciences of Ribeirão Preto/USP for the degree of Doctor in Sciences.

Concentration Area: Chemistry and Biological Physics.

Supervisor: Flavio da Silva Emery.

Approved on:

Examiners

Prof. Dr. _____

Institution: _____ Signature:_____

Prof. Dr. _____

Institution: _____ Signature:_____

Prof. Dr. _____

Institution: _____ Signature:_____

Prof. Dr. _____

Institution: _____ Signature:_____

This work is dedicated to the most important person in my life.
My best friend, partner, lover, and wife, Tainá.
For her unconditional support and for teaching me that
love makes everything possible.
I love you.

ACKNOWLEDGMENTS

The graduation course is a journey. You start with a map that looks perfectly linear, harmless, reasonable. But this map could not be more inaccurate. Graduation is about you attempting to amend your map. After each correct and incorrect decision, you grow, and as a matter of fact, it is amazing how science can prove you wrong in so many different ways. And as you reshape your map, you find wisdom, friendship, and love. And you learn that what is truly important is not where you arrived, but how. This journey had countless turnarounds and was only made possible because I had amazing people supporting me, and for that, I am grateful.

I thank my wife, Tainá, for her love, for always being there when I needed it, for believing in me, and for giving reason to this journey.

I thank my family and my parents, Elizete and Marcelo, for inspiring me with their love, hope, and kindness. For taking care of my daughter Bisous and being the best parents, I could possibly ask for. And my sister, Luíza, for many things, but especially for taking care of them while I was away.

To my friends, for all the support, countless beers, and happy moments.

To Prof. Maria Cristina Nonato, for her guidance, support, and for conceiving and getting final support for this project, and to the LCP group, for all the knowledge, discussions, and friendship.

To Prof. Flávio Emery, for walking the last miles with me.

To Frank von Delft, for supporting this project and receiving me in his lab.

To the XChem team and the SGC group, for their warm reception, discussions, and support.

To the Broad Institute, for discussions, support, providing compounds and protein used in this work.

To IFSC/CCP4 Macromolecular Crystallography School, where I learned so much about crystallography.

To the School of Pharmaceutical Sciences of Ribeirão Preto and the Pharmaceutical Sciences Graduate Program. Especial thanks to Eleni for her compassion.

To the XChem facility, the Research Complex at Harwell, and the SGC, where many experiments were performed.

To Synchrotron SOLEIL and Diamond Light Source, used for data collection.

To São Paulo Research Foundation (FAPESP, grant number 2016/22929-0 and 2017/26559-5) and National Council for Scientific and Technological Development (CNPq, grant number 141945/2018-4) for the financial support that enabled this project. This study was also financed in part by the Coordenação de Aperfeiçoamento de Pessoal de Nível Superior - Brasil (CAPES) – Finance Code 001.

RESUMO

RANGEL, Victor Lopes. **X-ray crystallographic fragment screening against the human prion protein**. 2021. 218f. Tese. Faculdade de Ciências Farmacêuticas de Ribeirão Preto – Universidade de São Paulo, Ribeirão Preto, 2021.

Doenças priônicas resultam do acúmulo de confôrmeros mal enovelados da proteína priônica celular (PrP^C), uma proteína de ancoragem glicosilfosfatidilinositol, expressa na superfície de membranas celulares. O evento crítico da doença priônica é a conversão da PrP^C em um confôrmero capaz de se automultiplicar, o príon *scrapie*, cuja propagação e acúmulo resulta em morte neuronal e amiloidogênese. O prognóstico da doença é devastador, com uma média de sobrevida de aproximadamente um ano após o início dos sintomas. Apesar dos tremendos esforços, a função e mecanismo de conversão da PrP ainda são desconhecidas. Esse trabalho teve como foco a utilização da técnica de varredura de fragmentos por cristalografia de raios-X para mapear o espaço químico da PrP para ajudar na busca de compostos de referência para o desenvolvimento de fármacos. A triagem da PrP, que atualmente carrega o estigma de proteína “não-drogável”, pode se beneficiar da estratégia de empregar fragmentos como fontes de novos *hits*. Essa abordagem se baseia na utilização de moléculas de baixo peso molecular para rastrear a superfície da proteína na busca de regiões de interação, aumentando as chances de encontrar ligantes que possam oferecer uma rota alternativa para o tratamento da doença. Fragmentos identificados como ligantes podem ser explorados no i) aumento da estabilidade da PrP^C, aumentando a barreira de energia para a conversão, ii) redução da estabilidade, induzindo a internalização e degradação da PrP^C, iii) bloquear sítios de interação proteína-proteína entre a PrP^C e a PrP^{Sc}, inibindo o processo de conversão. Nesse trabalho, foi estabelecido um protocolo reprodutível para produção e cristalização da PrP, para a qual mais de 1000 conjuntos de dados foram coletados e mais de 600 fragmentos foram testados. Os dados mostraram dois ligantes interagindo com a PrP, e revelaram o pirazol como motivo químico de interação em uma pequena cavidade gerada pela fechamento da cadeia lateral da Lys185 sobre o fragmento. A análise *in silico* dos dados coletados também revelaram uma rigidez inesperada para a região globular da PrP. Para superar a dificuldade em encontrar mais ligantes, foi realizada uma segunda varredura de fragmentos, que usou um cristal em condição mais favorável para esse tipo de experimentos. A busca por essa condição envolveu a varredura por uma nova forma cristalina, o uso de nano anticorpos específicos para PrP e condições com PEG. A segunda varredura de fragmentos testou mais de 100 fragmentos, sem positivos. Reunindo os dados gerados, o trabalho tem o potencial de ajudar na busca de fármacos baseado na estrutura da proteína priônica, além de providenciar uma análise profunda sobre varredura de fragmentos que pode auxiliar futuras campanhas.

Palavras-chave: Proteína priônica. Cristalografia de proteínas. Varredura de fragmentos. Doença priônica. Descoberta de fármacos baseada em estrutura.

ABSTRACT

RANGEL, Victor Lopes. **X-ray crystallographic fragment screening against the human prion protein**. 2021. 218f. Thesis. Faculdade de Ciências Farmacêuticas de Ribeirão Preto – Universidade de São Paulo, Ribeirão Preto, 2021.

Prion diseases result from the ordered accumulation of the misfolded conformer of cellular prion protein (PrP^{C}), a glycosyl-phosphatidylinositol (GPI)-anchored protein expressed on the cell surface. The critical event in prion diseases is the conversion of PrP^{C} into the self-propagating conformer scrapie prion protein, PrP^{Sc}, with resultant propagation and accumulation resulting in neuronal death and amyloidogenesis. Prognoses are devastating, with an average survival time of approximately one year after the onset of symptoms. Despite the tremendous efforts, PrP physiological function and its mechanism of conversion to PrP^{Sc} remain elusive. This research focuses on X-ray crystallographic fragment screening technique to map PrP chemical spaces in order to find lead compounds as part of the drug discovery process. Screening against human PrP, currently stigmatized as an “undruggable” target, can benefit from the fragment screening strategy. This approach relies on low molecular weight compounds to scan the protein surface in search of binding spots in the protein, enhancing the chances of finding ligands that could offer an alternative route to quest a treatment to prion disease. Any hits could be explored to be used for either i) increase PrP^{C} stabilization, increasing the energy barrier for the protein conversion, ii) destabilization, to induce PrP removal from the cell, thus reducing the quantity of PrP available for conversion, or iii) block protein-protein interaction sites between PrP^{C} and PrP^{Sc}, inhibiting the conversion process. We have established a reproducible crystal system for which we collected over 1000 X-ray datasets and screened over 600 fragments. Our data shows two ligands interacting with the prion protein and reveal a pyrazole chemical binding motif for an unprecedented small cavity created by a conformational change of the Lys185 sidechain. The *in silico* analysis of the collected datasets showed that the globular domain of the PrP is unexpectedly rigid. To overcome the difficulty of finding PrP binder molecules, we performed a second fragment screening assay. The second screening was enabled by achieving a more fragment screening-friendly crystal. This search involved screening for a new crystal system, the use of a PrP-specific nanobody, and PEG-based conditions. Our second screening tested over 100 fragments, with no hits. Together, we believe that our work has the potential to provide structural basis to aid the drug discovery regarding the prion protein while also providing an in-depth analysis that can support other X-ray fragment screening endeavors.

Keywords: Prion protein. Protein crystallography. Fragment screening. Prion disease. Fragment-based drug Discovery

FIGURES SUMMARY

TABLE SUMMARY

ABBREVIATION LIST

AMPA	A-amino-3-hydroxy-5-methyl-4-isoxazolepropionic acid
AU	Asymmetric unit
BB	Base buffer
BSE	Bovine spongiform encephalopathy
CC	Correlation coefficient
CCP4	Collaborative computational project number 4
CJD	Creutzfeldt-Jakob disease
COVID-19	Coronavirus disease 2019
CV	Column volume
CWD	Chronic wasting disease
DLS	Dynamic light scattering
DMSO	Dimethyl sulfoxide
DNA	Deoxyribonucleic acid
DSF	Differential fluorometry scanning
DSi	Diamond-SGC-inext
EG	Ethylene glycol
FBDD	Fragment-based drug discovery
fCJD	Familial CJD
FFI	Fatal familial insomnia
FSE	Feline spongiform encephalopathy
gCJD	Genetic CJD
GDA	Generic data acquisition
Gdn	Guanidin
GPI	Glycosyl-phosphatidylinositol
GSS	Gerstmann-sträussler-scheinker
HTS	High throughput screening
Hu	Human
iCJD	Iatrogenic CJD
IPTG	Isopropyl-β-D-1-thiogalactopyranoside
Mpro	Main protease
mRNAs	Messenger Ribonucleic acid
MS	Mass spectrometry

MST	Microscale thermophoresis
MX	Macromolecular crystallography
NMR	Nuclear magnetic resonance
Nsp3	Nonstructural protein 3
NTA	Nitrilotriacetic acid
ORF	Open reading frame
PanDDA	Pan-dataset density analysis
PDB	Protein data bank
PEG	Polyethylene glycol
PRNP	Prp gene
PrPC	Cellular prion protein
PrPSc	Scrapie prion protein
RMSD	Root mean square deviation
RSCC	Real-space correlation coefficient
SDS-PAGE	Polyacrylamide gel electrophoresis
siRNA	Small interfering RNA
SOLEIL	Synchrotron facility near Paris, France
SPR	Surface plasma resonance
TME	Transmissible mink encephalopathy
TROSY	Transverse relaxation optimized spectroscopy
vCJD	variant CJD
XCE	XChem Explorer

SUMMARY

1. INTRODUCTION

1.1 High-throughput screening in drug discovery

Drug discovery is a time-consuming, expensive, and complex learning process. Developing a drug from scratch can take 12-15 years and around $3 billion (DIMASI; GRABOWSKI; HANSEN, 2016; HUGHES et al., 2011). It commonly starts with early drug discovery studies, which involve target identification and validation, screening of compounds, hit and lead identification, and lead optimization. Preclinical studies and clinical trials then follow this stage. The early stage of this process can be roughly split into two steps: target selection and lead selection.

Target selection is defined as the decision to focus on finding an agent with a biological action anticipated to have therapeutic utility (GASHAW et al., 2012; KNOWLES; GROMO, 2003). It involves considering the disease pathologies and possible approaches to tackle them. Identifying a biological pathway and a target, such as an enzyme, a receptor, a modulator, or a gene using genomics, bioinformatics, biochemical assays, and previous knowledge about related diseases, consists of possible strategies to achieve it. This process ends with a validated and effective model linked to the pathology and can have a therapeutic effect on the disease.

The lead selection involves the path to discover a lead compound – or even a class of molecules(LAMOREE; HUBBARD, 2017). To do so, one will need to develop an assay to monitor binding – a biophysical technique, for example – and test candidates. The high throughput screening (HTS) is one of the many approaches available to select a lead compound. It has been increasingly gained attention in the past years and is particularly effective if no previous information is known about possible candidates to interact with the target. This approach involves the testing of a large scale (hundreds of thousands) of compounds against your chosen model. The success of this approach consists of the balance between time, quality, and costs. HTS assays are optimized to allow miniaturization to use small amount of reagents and sample, in a fast and automated way, generating thousands of data. On the downside, the development of a robust platform can be costly in terms of infrastructure and assay development, and intrinsic problems related to the screening such as technical variations and distinguish biologically active compounds from assay variability pose challenge to HTS(BLUCHER; MCWEENEY, 2014; SHUN et al., 2011). The quality of the results is related to the biophysical method chosen to perform the screening. Each

technique has its own advantages and disadvantages, which should be pondered on the situation; the selected method will not only define the throughput-ness of the results but also carry intrinsic features embedded with the technique, such as sensitivity and selectivity. The HTS can be used with a broad number of biophysical techniques that can be used solo or coupled. Some of the most employed biophysical techniques include surface plasma resonance (SPR)(HUBER et al., 2017), differential fluorometry scanning (DSF)(SORENSON; SCHAEFFER, 2020), microscale thermophoresis (MST)(RAINARD; PANDARAKALAM; MCELROY, 2018), mass spectrometry (MS)(ROHMAN; WINGFIELD, 2016), nuclear magnetic resonance (NMR)(WU et al., 2015), and X-ray crystallography(SCHIEBEL et al., 2016).

1.2 Fragment screening

The fragment-based drug discovery, or FBDD for short, is an approach that relies on the use of low molecular weight compounds to scan the target protein for binders(LI, 2020). These spots are often referred to as ‘warm’ or ‘hot’ spots (RATHI et al., 2017). The main goal of this approach is to identify chemical probes for drug targets: because of their small nature, each atom a fragment hit is often involved with binding interactions and exhibit thermodynamic-driven profiles(FERENCZY; KESERU, 2016), providing an efficient starting point for lead generation(FATTORI, 2004), and also helping to identify which region of the protein is more likely to bind a particular functional motif(MURRAY; REES, 2009). The identified hits can be optimized in a rational way by considering the mode of binding to the protein structure and nearby binding fragments, and common approaches include linking, growing and replacing(BAKER et al., 2020; LAMOREE; HUBBARD, 2017).

By definition, fragments are small molecules that follow the “rule of three” criteria, typically with molecular weight < 300 Da; clogP ≤ 3; number of hydrogen-bond donors ≤ 3; number of hydrogen-bond acceptors ≤ 3(OSBORNE et al., 2020). The fragment-based drug discovery is being increasingly more used because of its advantages over the common libraries HTS libraries. Some of them are a) the low complexity nature of fragment libraries, which makes them cheaper and easier to obtain; b) being small allows them to access chemical space of the target more efficiently; c) because of their efficiency, the fragment libraries can carry only a few hundred small molecules (O’REILLY et al., 2019; RESNICK et al., 2019; WOOD et al., 2019). On the downside, fragments usually make weak interactions with the proteins

because of their simple nature, with dissociation constant values ranging from 1 mM to 100 μM, posing a challenge to correctly identify and evaluate the hits (KONTEATIS, 2021; ROBSON-TULL, 2018). Fragment screening has become increasingly more used in the last 25 years, with four approved drugs and over 40 in the clinical trials (ERLANSON et al., 2016; LI, 2020).

1.3 X-ray crystallography fragment screening

HTS and FBDD results are the basis for the design of lead compounds that display both improved potency and physicochemical properties. The use of structural biology techniques is key for this purpose: the optimization ad efficient progression of hits usually rely on the identification of the correct binding mode of the ligand to the target so that follow-up molecules can be rationally selected and tested, and the absence of these information pose challenge to design iterations of chemistry(MURRAY; REES, 2009). In this scenario, the application of X-ray crystallography as the leading biophysical technique to drive the FBDD has been rising, mainly because X-ray crystallography is widely recognized as one of the most sensitive and least prone to false-positive technique (PATEL; BAUMAN; ARNOLD, 2014), while also providing extremely high-resolution information - these features have risen the popularity of this approach, leading many groups to employ this strategy in the process of drug discovery. Despite those advantages, crystallography was historically deprecated in screening approaches because it requires a crystallized sample and because of its low-throughput nature(LIN, 2018). However, robots in the crystallization procedure (LUFT; SNELL; DETITTA, 2011) improved reproducibility, increased the number of tested conditions, lowered the amount of sample used, and increasing the process throughput, thus significantly reducing costs and time. The improvement of synchrotron light sources also resulted in better data collection outcomes. The automated recharge of crystal pins and crystal centering (ABOLA et al., 2000), together with the fact that crystallographic fragment screening relies on using crystal ‘clones’ made room for a fully automated data collection pipeline, hastening one of the low throughput steps in X-ray crystallography. Further improvement in data processing software’s such as XDS and DIALS and its implementation in the beamline pipeline allowed the collected data to be fully and automated processed in situ.

The development of automated imaging and soaking experiments represented the final touch required to make X-ray crystallography fragment screening a high-

throughput technique (COLLINS et al., 2017). In particular, the XChem facility at Diamond Light Source, under the supervision of Prof Von Delft, gathered all the mentioned resources and display a streamlined process where one could go from the crystal drop to PDB deposition, being consolidated as the first high throughput X-ray crystallography fragment screening facility in the world. Many other platforms are now under development, such as FragMAX, hosted by Lund University in Sweden (LIMA et al., 2020).

1.4 The prion concept

The Scrapie Syndrome in sheep and goats was the first prion disease to be reported. It was identified in 1732 in imported Spanish merino sheep. The disease name was derived from one of the significant clinical signs of the condition in which the affected animal had the unusual habitude to scrape against rocks, trees, and fences (LEE et al., 2013). One of the first insights about the scrapie disease agent was introduced in 1950 by Greig. After the Animal Disease Research Association inadvertently attempted to build a vaccine against the agent, causing many sheep to be contaminated by the disease, he inferred that the agent was present in the brain, could remain infective in a concentration of 35% formalin, could be transmitted subcutaneously, and had a long incubation period. He also acknowledges Cuillé and Chelle (1938) for providing experimental evidence that the scrapie agent was an infective disease that could be transmitted by inoculation after being filtered by a porcelain filter, indicating it was potentially a filterable virus (GREIG, 1950).

In 1954, Björ Sigurdsson was working in Iceland on scrapie and visna of sheep provided microscopic information of infected sheep brain. In his lecture, Björ discusses Rida, the Icelandic name for the disease, which was prevalent in Iceland sheep. As Greig, Cuillé, and Chelle, he also noticed that the condition had a very long incubation period and could be transmitted artificially to healthy sheep through the intracerebral inoculation of extracts of diseased brains even after the extract was filtered through a bacterial filter, leading him to propose the agent should to a group of “slow virus” infections (SIGURDSSON, 1954).

On the opposite side of the globe, Gajdusek, who later was awarded the Nobel Prize, discovered Kuru (KLATZO; GAJDUSEK; ZIGAS, 1959) in Papua New Guinea, which in the Fore language means “to shiver”. Kuru is a neurodegenerative disorder and was an endemic disease among tribes of New Guinea aborigines, and was proven

transmissible (GAJDUSEK et al., 1967) and linked with the mortuary cannibalism culture of the Fore tribe, in which they ate the brains of dead people as part of a funeral ritual.

Two years later, a clairvoyant observation by William Hadlow noted epidemiological, clinical, and neuropathological similarities between Kuru and scrapie, leading him to suggest that Kuru could also be caused by a slow virus (HADLOW, 1959). In the same way, Igor Klatzo confirmed the similarities between Kuro and CJD, a human neurodegenerative disease, over the comparison of their microscopic pathology, revealing that kuru, scrapie, and CJD were distinct forms of the same neuropathy and transmissibility of Kuru, Scrapie, and CJD agents were experimentally demonstrated to various species (CHANDLER, 1961; GAJDUSEK et al., 1967).

The search involving the molecular architecture of the scrapie agent was majorly twisted when data pointed out that the agent's infectivity was resistant to procedures that alter nucleic acids. In 1966, Alper noticed the exceptionally small size of the scrapie agent and published many data reporting the ability to remain infective even after exposure to high doses of ultraviolet light (ALPER et al., 1967; ALPER; HAIG; CLARKE, 1966). He noted in 1966:

> the evidence that no inactivation results from exposure to a huge dose of ultraviolet light, of wavelength specifically absorbed by nucleic acids, suggests that the agent may be able to increase in quantity without itself containing nucleic acid. This possibility is supported by the data from electron irradiations, since these yield a target size which is implausibly small as a nucleic acid code. In any event, our data strongly support the conclusion of Pattison (1965) that this agent is likely to be of an unusual nature. (ALPER; HAIG; CLARKE, 1966, p. 283)

In 1982, Prusiner, who was awarded the Nobel prize for his research with prions in 1997, introduced the new term "prion" to denote this "a small proteinaceous infectious particle which is resistant to inactivation by most procedures that modify nucleic acids" (PRUSINER, 1982), that the protease-resistant PrP extracted from affected brains was of 27–30 kDa and became known as $PrP^{27–30}$, and confirmed that this protein was responsible for the disease came with the observation that no replication of prions in PrP-deficient was found (BÜELER et al., 1993).

1.5 The prion disease

The prion disease belongs to an invariably fatal group of neurodegenerative disorders that affect humans and other animals. In humans, include kuru, Creutzfeldt-Jakob disease (CJD), Gerstmann-Sträussler-Scheinker (GSS) syndrome, and fatal familial insomnia (FFI) (COLLINS; MCLEAN; MASTERS, 2001; LIBERSKI et al., 2012). The prion disease is also responsible for the chronic wasting disease (CWD) in cervids; bovine spongiform encephalopathy (BSE) in cattle, and its analogs in antelopes and wild felids; scrapie in sheep and goats; transmissible mink encephalopathy (TME) in ranch-reared mink; and feline spongiform encephalopathy (FSE) in domestic cats (AGUILAR-CALVO et al., 2015).

The scrapie prion protein, PrP^{Sc}, are originated by a misfolding of the cellular prion protein, PrP^{C}, into the self-propagating conformer PrP^{Sc} (PRUSINER, 1998). PrP^{Sc} is synthetized from its normal isoform PrP^{C} through a post-translational process whereby it acquires β-sheet content from its α-helical structure. This new conformer not only has the tendency to aggregate but also drives the formation of nascent PrP^{Sc} by binding to its homolog PrP^{C} (PRUSINER et al., 1990). After attaining some threshold, the accumulation of the abnormal protein isoform in neural tissue leads to the manifestation of the disease. It may manifest as sporadic (1), genetic (2), or infectious disorders (3) and can be hastened by exposure to exogenous prions or mutations(GAMBETTI et al., 2003). The worldwide incidence of prion disease is roughly 1 per 10^6 population per year for sporadic disease and 1 per 10^7 per year for familial disease(CHEN; DONG, 2016). Currently, Kuru is virtually extinct due to a ban on ritualistic cannibalism in the area of Papua New Guinea, where it was endemic. Active surveillance programs exist in Europe, the USA, Canada, Japan, China, Korea, Argentina, Australia, and Brazil (WATSON et al., 2021). They are demonstrated to be critical for disease mapping, control, and prevention. Approximately 85–90 % of CJD cases occur sporadically, familial/genetic CJD (fCJD/ gCJD) account for about 10 % of CJD cases worldwide, and acquired prion diseases include variant CJD (vCJD) and iatrogenic CJD (iCJD) and are observed in 2–5 % of CJD cases (CHEN; DONG, 2016; COLLINGE, 2001).

1.6 Prion gene and structure

The human *PRNP* gene is located on the short arm of chromosome 20 between the end of this arm and the position 12. The entire open reading frame (ORF) of all

known mammalian and avian PrP genes (*PRNP*) resides within a single exon, annulling the possibility of PrP^{C} and PrP^{Sc} isoforms to be the product of alternatively splice mRNAs (SCHÄTZL et al., 1995). PrP^{C} is ubiquitously expressed in mammals, and the alignment of the amino acid sequence of human against mouse, sheep, and chimpanzee sequences demonstrates that PrP^{c} is highly conserved across those species, revealing a high sequence identity of 89%, 89.7%, and 99.2% respectively (Figure 1).

Figure 1. PrP sequence alignment of human (Homo sapiens), chimpanzee (Pan troglodytes), rabbit (Oryctolagus cuniculus), sheep (Ovis aries), bank vole (Myodes glareolus), horse (Equus caballus), cattle (Bos taurus), dog (Canis lupus familiaris), mouse (Mus musculus) reveal a high sequence identity among prion protein of different species. Aligned in Multialin using ENDscript server(ROBERT; GOUET, 2014).

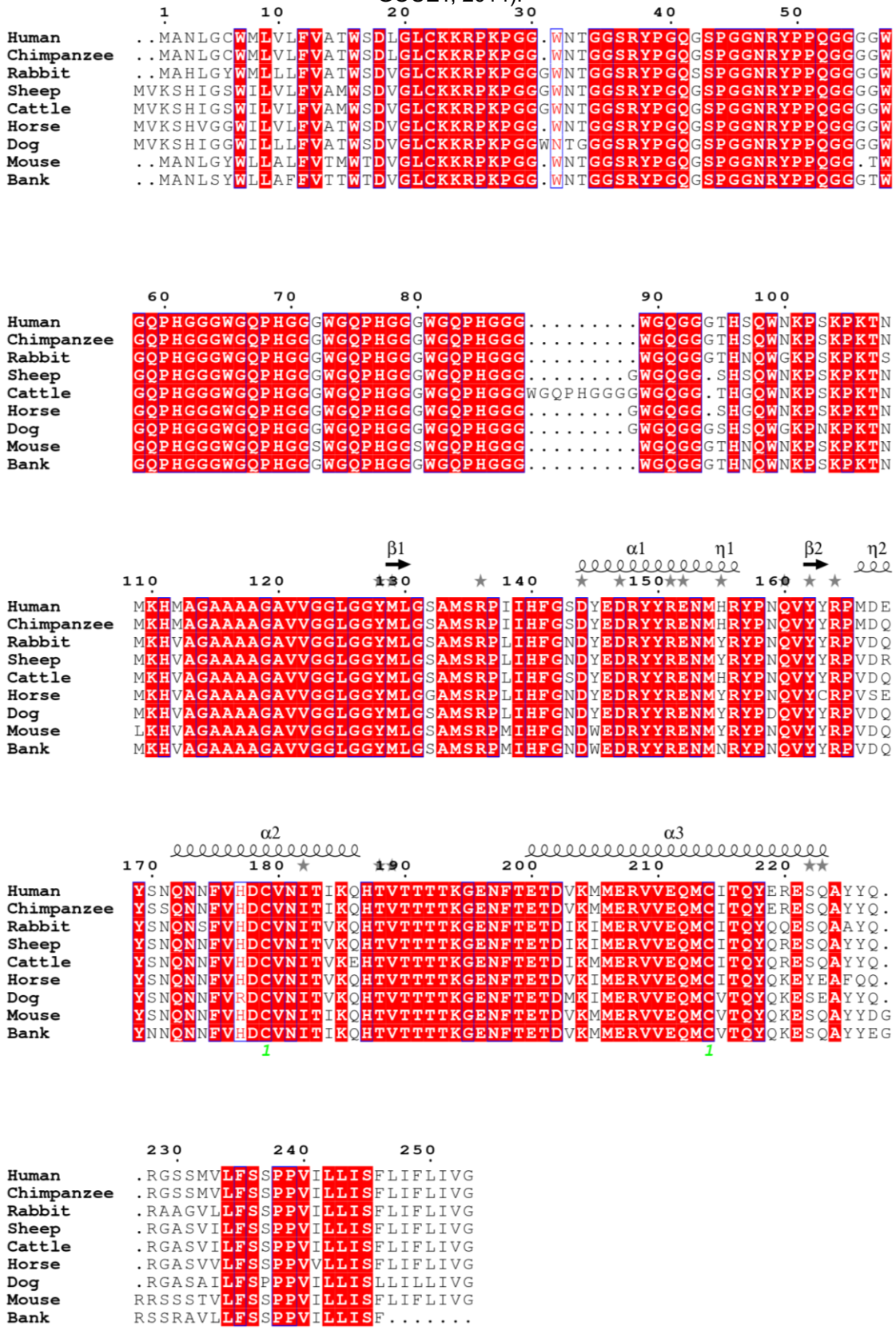

Source: own elaboration

Over 40 mutations in the *PRNP* gene have already been directly linked to the development of prion diseases and lead to different clinical phenotypes, including CJD, GSS, and FFI (MASTRIANNI, 2010). Mutations of the prion protein gene can be classified as point mutations, silent, or can cause the coding to prematurely terminate (stop or nonsense mutation) or insertions and deletions. These mutations affect the primary structure of PrP and may lead to changes in the secondary and tertiary structure that could result in the emergence of PrP^{Sc} conformers. Meanwhile, polymorphisms do not cause prion disease but may influence a person's risk of developing it. These mutations can lead to prion strains that differ in their clinical phenotype (CJD, FFI, GSS), incubation times, transmission properties, and neuropathological profiles. A penetrance quantification of prion diseases (MINIKEL et al., 2016) acknowledged strong pathogenicity for four missense variants: P102L, A117V, D178N, and E200K.

The human cellular prion protein is a glycosyl phosphatidyl inositol (GPI)-linked glycoprotein that undergoes facultative N-linked glycosylation at two sites (N181 and N197). It contains 253 amino acid residues in length and has a MW of 35-36 kDa depending on its glycosylation. It encodes a cleaved signal peptide (1–22) that addresses it to the outer membrane of cells, an octapeptide repeat-containing unfolded domain (51–91) with binding sites for Cu^{2+}, three α-helices (H1, H2, and H3), a disulfide bound (C179 - C214), one small antiparallel β-sheet (β1 and β2), and a GPI- anchoring signal at the C-terminus (Figure 2).

Figure 2. Scheme of the primary and secondary structure of the human prion protein PrP with the signal peptide, octapeptide repeats, hydrophobic region, and GPI anchor, N-glycosylation sites, and disulfide bond highlighted

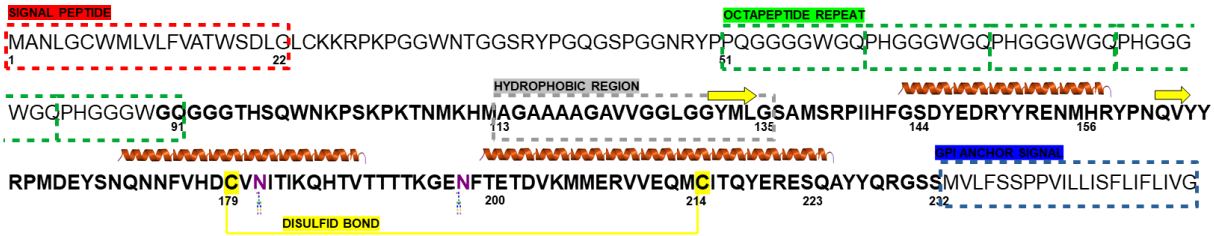

Source: own elaboration.

The first structure of PrP was solved via NMR at Kurt Wuthrich lab (PDB ID:1QM3), a pioneer on the use of NMR for biomolecules and who later was awarded the 2002 Nobel Prize in Chemistry "for the development of methods for identification and structure analyses of biological macromolecules". The first crystallographic structure was solved in 2001 (PDB: 1I4M) (KNAUS et al., 2001), and at the moment

there approximately 44 human PrP structures available at the Protein Data Bank (https://www.rcsb.org/) including native, fragments and mutant structures solved by NMR, X-ray crystallography and electron microscopy. Besides subtle differences related to the methodology and/or resolution, PrP was found in both monomeric and dimeric arrangements (Figure 3) (KNAUS et al., 2001). In the dimeric structure, the monomeric prion protein was shown to be able to undergo a dramatic conformational transition, described as a 3D domain-swapped dimer (KNAUS et al., 2001), where a rearrangement of α3 allows its packing against α2´ from the other monomer (Figure 3). At this point, it remains unclear whether these interactions can represent the functional dimer.

Figure 3. Cartoon representation for both monomeric (PDBID 6du9) and dimeric (PDBID 6DU9 and 3HAF) forms of PrP Dimerization is achieved by reducing an intramolecular disulfide bridge, torsion of the loop connecting helices 2 and 3, and forming an intermolecular bridge between α2 from one monomer to α3 from the neighbor monomer

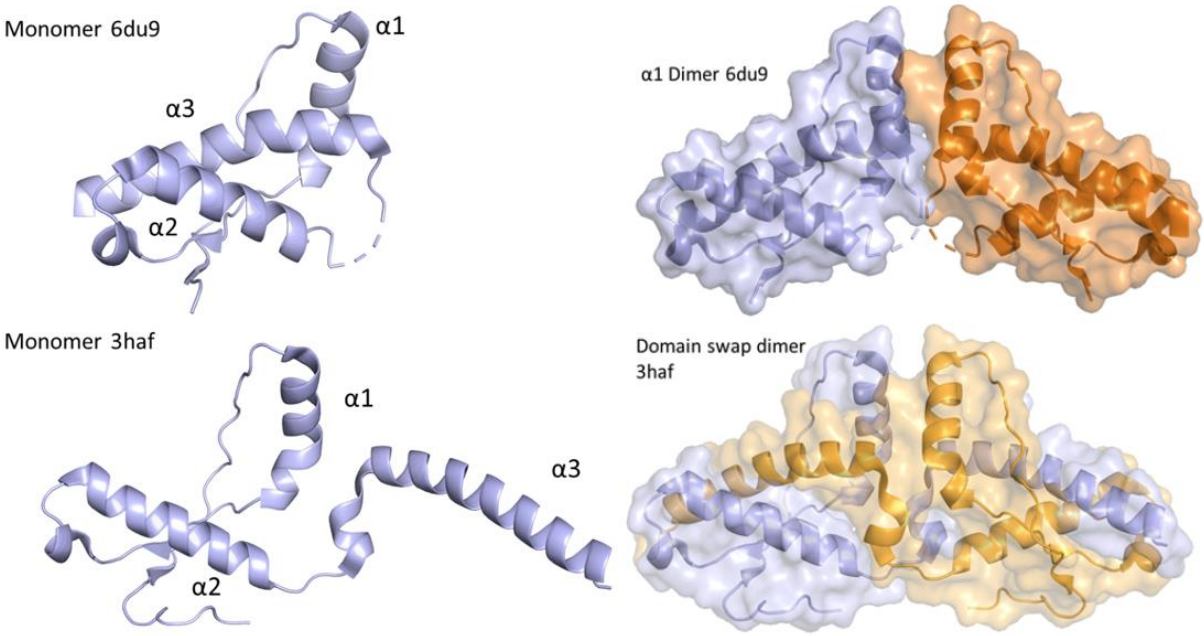

Source: own elaboration.

Recently, Prof Nonato, during her *work at Broad Institute of MIT and Harvard (March 2017 to Feb 2018, FAPESP 2016/22929-0,* Bolsa de Pesquisa – Exterior), crystallized PrP^C using a new and reproducible crystallization condition. In this new crystal form, human PrP^C was found in its monomeric form, providing an attractive model for X-ray fragment screening. Moreover, essential regions like the α2-α3 loop required for PrPc to undergo domain swapping are found solvent-exposed in this new

crystal packing contacts. We hypothesized that binders might stabilize the domain swapping by binding to the α2-α3 loop.

The conversion of PrP^{C} into PrP^{Sc} is thought to be the critical event in prion disease (PRUSINER, 1998). Profound changes in PrP physicochemical properties mark the structural transition. PrP^{C} presents as soluble, monomeric, protease-sensitive, while PrP^{Sc} has an insoluble profile, protease-resistant, presents an oligomeric form, and is more resistant to heat and sterilization (JUNG; PISTOLESI; PANÀ, 2003; MEYER et al., 1986; PRUSINER, 1982). Another intriguing aspect is that PrP^{Sc} does not evoke any immune response (ZABEL; AVERY, 2015). These differences appear to be based on their structural differences. Among the structural changes, data based on circular dichroism and infrared spectroscopy have shown that PrP^{C} is composed mainly of α-helices (42%) and has only a tiny fraction of β-sheet content (3%). In contrast, PrP^{Sc} contains predominantly β-sheets (>43%) (COHEN et al., 1993; SPAGNOLLI et al., 2019).

While conversion of α-helical into β-sheet features in the formation of PrP^{Sc} and thus seems to be the critical events underlying prion disease, the existence of scrapie strains remains perplexing (FRASER; DICKINSON, 1968). Different prion strains produce distinct patterns of PrP^{Sc} deposition in the brain and often have different incubation times.

Although the scrapie prion can transmit between the organism of the same species, a structural feature within the prion protein limits some interspecies transfer and is referred to as species barrier (RAYMOND et al., 2000); for example, human and mouse prion were found to be fully compatible, whereas hamsters and humans prions seems incompatible (VANIK; SUREWICZ; SUREWICZ, 2004). In the same study, amino acid positions 138 and 139 (isoleucine-isoleucine for humans, methionine-isoleucine for mouse and methionine-methionine for hamsters) were identified as responsible for the species barrier (VANIK; SUREWICZ; SUREWICZ, 2004). In another study, residues within the α-helix two and β-sheet two-loop were also determined to play a role in the prion disease and species barrier between humans and deer and elk (KURT; KONG; SIGURDSON, 2015), and the presence of individual substitutions Y169G, S170N or N174T are referred to increase the resistance to prion disease by introducing rigidity to the α-helix 2/β-sheet two loops (KURT et al., 2014). Another example of the importance of this region to the formation/resistance to scrapie prion formation is the observation of animals very resistant to the prion disease, such

as dogs, horses, and rabbits. Their naturally occurring amino acids D159 (dogs) and S167(horses) are known as ‘protective’ against the prion disease (FERNÁNDEZ-BORGES et al., 2017; SANCHEZ-GARCIA; FERNANDEZ-FUNEZ, 2018; VIDAL et al., 2020; ZHANG, 2011).

1.6.1 PrP physiological function

In humans, *PRNP* is mainly expressed as a GPI-anchored protein (Figure 4) outer membrane of neuronal cells in adult, uninfected brains (OESCH et al., 1985). Even though *PRNP* knockout mice exist since 1992, PrP^C physiological function remains elusive. A significant number of functions have been attributed to PrP^C. PrP^C is proposed to act in stress-protection, cellular differentiation, neuronal excitability, circadian rhythm, metal ion homeostasis in the immune system, mitochondrial homeostasis, among others (reviewed in Castle and Gill, 2017). One accepted role of PrP in the peripheral nervous system is myelin maintenance (BREMER et al., 2010) through FT-mediated Gpr126 agonism (KÜFFER et al., 2016) in Scwhann cells where it is highly expressed (FOLLET et al., 2002). On the opposite hand, this evidence does not explain the PrP^C role in the central nervous system, which is where the prion disease takes place.

Figure 4. Schematic diagram of PrPC structure. The carbohydrate moieties that are linked to Asn 181 (down) and Asn 197 (up) are shown in pink. The C-terminal GPI-anchor is shown in green and is extending into the cell membrane in blue and red. OR residues in the N-terminal domain are known to bind copper ions (shown in blue)

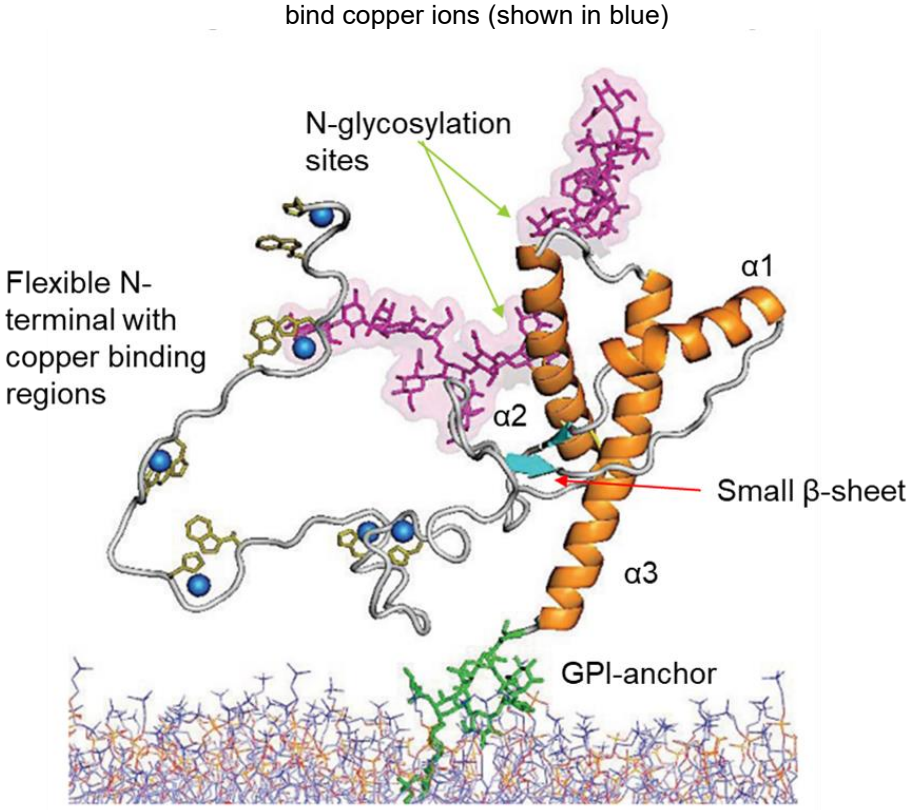

Source: adapted from Acevedo-Morantes and Wille (2014).

Because PrP^{C} has binding regions for Cu^{2+} in its N-terminal-octapeptide repeat region, it is hypothesized to participate in copper metabolism. Also, PrP^{C} is thought to be involved in zinc metabolism because of PrP^{C}'s ancestral relationship with ZIP proteins. Zinc is the most abundant trace metal in the brain and plays a significant role in axonal and synaptic transmission, and is necessary for nucleic acid metabolism and brain tubulin growth and phosphorylation (PFEIFFER; BRAVERMAN, 1982). Recent findings indicate that the PrP^{C} octapeptides and C-terminal domain's tertiary structure are driven upon Zn^{2+} binding. Interestingly, the C-terminal region that participates in this interaction happens to carry the majority of the point mutations that confer familial prion disease. The investigation of mutant PrP^{Sc} has found a relationship between the type of mutation and the apparent strength of this domain structure, suggesting it could be a mechanism by which physiologic metal ions control prion disease (SPEVACEK et al., 2013). This hypothesis corroborates with previous reports that both Cu^{2+} and Zn^{2+} inhibit *in vitro* amplification of prions (OREM et al., 2006). Another theory holds that the octapeptide repeats, along with the N-terminal region, mediates the influx of zinc into neuronal cells via α-amino-3-hydroxy-5-methyl-4-isoxazolepropionic acid

receptor (AMPA receptors). In this theory, the PrP^C role would be zinc sensing or scavenging, while AMPA receptor as zinc transporter (WATT; GRIFFITHS; HOOPER, 2013). Mutations associated with familial disease have shown to prevent inter-domain interaction between PrP^C and AMPA receptors, providing insights for the reduction of zinc in brains affected with prion disease (WATT; GRIFFITHS; HOOPER, 2013).

PrP was described to interact with other proteins, the excitatory amino acid transporter 3 , the multi-drug resistance protein 1, and γ-glutamyl transpeptidase, acting on the regulation of the astroglia and neuronal metabolism of the antioxidant glutathione and suggesting that these interactions play an essential role in the metabolic cross-talk between astrocytes and neurons and the protection of neurons by astrocytes from oxidative and glutamate-induced cytotoxicity (GUITART et al., 2015). And most recently studies are closing the gap and pointing PrP function to be centered in interacting with the Neuronal cell adhesion molecule 1 in the context of mesenchymal to epithelial transition(LINDEN et al., 2008; SCHMITT-ULMS et al., 2021).

1.7 Therapeutical strategies for prion disease, PrP as a drug target and anti-prion compounds

Despite the tremendous efforts, to date, no treatment is available to seize or delay the clinical disorder course of any prion disease. The prion disease holds a stigma of being undruggable because of the difficulty in finding micro molecules that interact with it. In addition to that, there is no structure of the scrapie form of PrP, and PrP^C has a ‘small’ globular domain, with shallow cavities, and a disordered N-terminal and. Also, little is known about the conversion of PrP into PrP^{Sc}, limiting a more rational approach to develop a drug based on the inhibition of PrP into PrP^{Sc} conversion.

A key achievement towards understanding the conversion was the development of the Protein Misfolding Cyclic Amplification (PMCA) (SABORIO; PERMANNE; SOTO, 2001). This technique resembles the polymerase chain reaction and is capable of detecting and reproduce the scrapie prion *in vitro* with minimal components (DELEAULT et al., 2007), enabling the test of conversion-inhibitor candidates and the identification of additional players in the conversion, such as polyanionic molecules, including RNA and DNA (GOMES; CORDEIRO; SILVA, 2008).

Despite the absence of treatment for prion disease, many therapeutic approaches to treat the disease have been proposed and many compounds with anti-

prion activities are known(ALTIERI et al., 2020; CONCEIÇÃO et al., 2019; IMBERDIS et al., 2016; MASHIMA et al., 2020). For instance, the reduction of PrP expression has an extremely strong proof of principle as a therapeutic strategy. Knockout mice are resistant to prion disease (BÜELER et al., 1993), and incubation time is inversely correlated with PrP expression level all the way from heterozygous knockouts to 10x overexpressors (BÜELER et al., 1994; FISCHER et al., 1996). Treatments aimed at the laminin receptor, an important accessory molecule in the conversion of PrP^{C} to PrP^{Sc} – neuroprotection, immunotherapy, siRNA, and antisense approaches, have provided some experimental promise (PANEGYRES; ARMARI, 2013). Cre-mediated conditional knockout of PrP around the time of first symptoms can reverse prion disease (MALLUCCI et al., 2003), and conditional downregulation to ~20% of wild-type levels using a Tet-off system can dramatically delay prion disease (SAFAR et al., 2005). Moreover, polyanionic compounds, like RNA aptamers, can prevent the conversion of PrP^{C} to PrP^{Sc} and might also sequester and down-regulate PrP^{Sc} (MASHIMA et al., 2020; PANEGYRES; ARMARI, 2013)

Anti-prion compounds also offer proof of principle that the proposed therapeutical approaches work, including chaperone-like compounds that increases PrP stability, such as the GN8(KUWATA et al., 2007; YAMAGUCHI et al., 2019), which binds to a small hydrophobic patch close to helix 3. Other compounds with anti-prion activity (some depicted in Table 1) in cell culture include Quinacrine, Hematein, Tacrolimus and Congo Red, with proposed mechanism of action ranging from removal of PrP from cellular membrane, promoting PrP degradation, stabilization of PrP, and blockage of PrP^{Sc} oligomer formation (BIGGI et al., 2020; SPEVACEK et al., 2013; WOOK HYEON et al., 2015). As so, one of the most popular and acceptable approaches to target the prion disease has been searching for compounds that (1) prevent PrP aggregation or (2) prevent the conversion of healthy PrP^{C} to misfolded PrP^{Sc}. Targeting PrP^{C} with ligands that may stabilize PrP^{C} native structure and preventing PrP^{Sc} replication constitutes a promising strategy to treat prion disease(PANEGYRES; ARMARI, 2013).

Table 1 – Examples of compounds with known anti-prion activity.

Compound	Proposed mechanism	Interacting region	Reference
Quinacrine	Improved clearance of PrP^{Sc}	Tyr225, Tyr226, and Gln227	(DOH-URA; IWAKI; CAUGHEY, 2000; M et al., 2003)
Chlorpromazine	Pharmacological chaperone	Helix 2 and the two β-sheets	(BARAL et al., 2014)
Methylene Blue	Inhibit oligomer formation	Asn146, Asn156, Tyr160, Lys188, Thr191, Val192, Thr194, Thr195, Gln215	(CAVALIERE et al., 2013)
Fe(III)-TMPyP	Pharmacological chaperones	C terminus of H3 / loop between residues 160 and 180	(CAUGHEY et al., 1998; PRIOLA; RAINES; CAUGHEY, 2000)
Congo red	Non-specific interaction	Non-specific interaction	(B; D; RE, 1993)
GN8	Pharmacological chaperones	Asn159 and Glu196	(KUWATA et al., 2007)

Source: own elaboration

1.8 Tackling prion disease with X-ray fragment screening

Within this context, the present work focuses on using the state-of-art methodology in drug discovery to search for compounds that could potentially bind and stabilize the native form of PrP^{C} and enlighten the path for treating prion's diseases. In this work, we employed X-ray crystallography fragment screening to shed light on the elusiveness surrounding the PrP^{C} structure and mechanism of action.

This work was conceived in the BROAD Institute of MIT and Harvard, in Prof Stuart Schreiber laboratory, and where Prof. Nonato began to work during her sabbatical year (FAPESP, grant number 2016/22929-0), taking advantage of X-ray crystallography and fragment screening to study this target. By using X-ray crystallography fragment screening associated with biophysical and biochemical tools, we expected to map ligand binding sites of PrP^{C}, elucidate ligand/PrP^{C} mechanism of interaction, and offer an alternative route to quest a cure/treatment to prion disease. This project continued to be developed in Brazil and received financial support from FAPESP (2017/26559-5) under the supervision of Prof Nonato. Here, we propose that the random fragment-screening profile of this approach may offer an advantage over standard libraries, which has been proven unsuccessful for screening compounds against protein-protein interaction(HUBBARD, 2016). Moreover, the high efficiency of fragment libraries may help overcome the 'undruggability' profile observed by the prion

protein. Because of the elusiveness surrounding this protein, hits identified within our X-ray crystallographic fragment screen can be explored in many ways, providing structural basis for hit optimization and information regarding exploitable sites in the prion protein. Fragments can serve as starting points to compounds that can be later used to: i) increase PrP^{C} stabilization, increasing the energy barrier for the protein conversion, ii) destabilization, to induce PrP removal from the cell, thus reducing the quantity of PrP available for conversion or iii) block protein-protein interaction sites between PrP^{C} and PrP^{Sc}, inhibiting the conversion process.

2. OBJECTIVES

This work aimed to use the fragment screening approach combined with X-ray crystallography technique. Our goal is to map PrP chemical spaces, identify regions capable of being explored in the prion structure, relevant function motifs for binding, and fragment hits that can provide starting point for optimization. Throughout the research, the high throughput pipeline for X-ray fragment screening XChem, was used and in-depth described to support future fragment screening endeavors. The identification of “hot spots” within the human PrP structure will provide basis that could further be used for the development stages of a lead compound. This project employed a broad range of techniques, including heterologous protein expression, purification, dynamic light scattering, X-ray crystallography, computational analysis, and other biophysical methods.

2.1 Specific objectives

Produce soluble, folded protein to support our follow-up experiments, which were enabled by the establishment of a protocol for protein heterologous expression and purification that fits our budget and yields enough soluble, stable, and correctly folded protein that will be confirmed with additional biophysical techniques.

Achieve a suitable crystal system to support X-ray fragment screening, followed by full characterization and in-depth structural studies to understand our target.

Identification of fragment hits that interact with the human prion protein through screening of fragments using X-ray crystallography technique.

Support future fragment screening endeavors by providing in-depth description of XChem’s streamlined process.

3. MATERIAL AND METHODS

3.1 Protein Production

The protocol developed for protein expression, purification, and refolding was adapted from the original protocol shared by our collaborators at the Broad Institute and available at http://www.cureffi.org/2014/07/30/recombinant-prion-protein-rocky-mountain-style and reported by us in a manuscript (BORTOT et al., 2020).

3.1.1 Heterologous Expression

The human prion protein (PrP) construct 90-231 (amino acid sequence MGQGGGTHSQWNKPSKPKTNMKHMAGAAAAGAVVGGLGGYMLGSAMSRPIIHFG SDYEDRYYRENMHRYPNQVYYRPMDEYSNQNNFVHDCVNITIKQHTVTTTTKGEN FTETDVKMMERVVEQMCITQYERESQAYYQRGSS) was previously cloned into the plasmid peT24. Our collaborator, Prof Stuart Schreiber, kindly donated the construct from the Broad Institute at MIT and Harvard.

Transformation and expression were carried out using chemically competent *Escherichia coli* ROSETTA BL21 (DE3) cells. Bacteria cultures stored at -80 °C as a glycerol stock were transformed by heat shock and plated in LB agar containing kanamycin (30 μg/mL) and chloramphenicol (34 μg/mL). Bacteria grew overnight at 37 °C. A single colony of cells harboring the construct was used to inoculate 10 ml LB media in the presence of the same antibiotics and incubated under agitation (180 rpm) overnight at 37 ºC. The starter culture was diluted 100-fold in LB media and grown at 37 ºC. When $O.D_{600\ nm}$ reached 0.5-0.6, isopropyl-β-D-1-thiogalactopyranoside (IPTG) (Sigma-Aldrich) was added to 1 mM final concentration, and PrP expression was carried out overnight at 37 ºC. The cells were harvested by centrifugation at 10,000 g for 6 minutes at 4 ºC and stored at -20 ºC until used.

3.1.2 Protein Purification and Refolding

Cells pellets corresponding to 250 mL of culture were resuspended in lysis buffer (100 mM Na_2HPO_4, 10 mM Tris pH 8.0, 1 mM PSMF, 10 μg/mL DNAse, 10 μg/mL RNAse, 1 μg/mL lysozyme), with a 10 mL of buffer for each 1 g of cell. The system was incubated for 20 minutes on a rocking shaker at 4 °C to allow membrane fragilization. Cells were lysed using 10 cycles of 30 s sonication with 30 s interval on ice, 10 W, and

centrifuged at 16,000 g for 30 minutes at 4 °C. Since the protein is expressed as inclusion bodies, the pellet was retained, and soluble fraction was discarded.

The “washing procedure” described above (resuspension, rocking shaker, centrifugation) was repeated 9 times. The pellet was washed three times with lysis buffer, three times with lysis buffer plus 0.5% Triton X-100, and three times with buffer A (100 mM Na_2HPO_4, 10 mM Tris pH 8.0) to remove the detergent. The protein was denatured in the two final washes with denaturing buffer (buffer A with 8 M guanidine) to solubilize the inclusion bodies. The supernatant was injected into a C1/10 column containing 5 mL Ni-NTA resin (QIAGEN©), previously equilibrated with buffer A supplemented with 6 M guanidine. The protein was refolded by dialysis using an ÄKTA-Purifier system (GE Life Sciences). An isocratic chromatographic run was carried out to fully and slowly remove the guanidine: 5 column volumes (CV) from 6 M to 0 M guanidine (buffer A) at 0.1 mL/min, followed by 2 CV of 100% buffer A for equilibration. The refolded PrP was eluted using a linear gradient of 2 CV from buffer A to elution buffer (100 mM Na_2HPO_4, 10 mM Tris pH 5.8, 500 mM imidazole) at 0.1 ml/min. The PrP was readily dialyzed against 5 L of 10 mM $NaC_2H_3O_2$ pH 5 using a 3.5 kDa cutoff dialysis membrane (Fisherbrand) and finally concentrated in a 10 kDa cutoff (Amicon®) centrifugal filter unit. Concentration was estimated using its theoretical extinct coefficient of $\varepsilon^{280nm/cm}$ = 1.36/(mg/mL) calculated by ProtParam (https://web.expasy.org/protparam/). Protein was stored at 4 °C until further used. All steps were monitored by SDS page.

3.2 Biophysical studies

3.2.1 Dynamic Light Scattering

After purification and refolding protocols to access protein quality as a function of its homogeneity and polydispersity, the DLS technique was employed to evaluate protein integrity after storage and prior to crystallization assays. DLS was performed in Nano Zetasizer S90 (Malvern©) using quartz cuvette ZEN2112 (Hellma®). The assay was performed at 4.5 mg/mL PrP in triplicates at 18 °C. Data were interpreted using Zetasizer software.

3.2.2 Protein Mass Spectrometry

For acquisition and analysis of native intact mass spectrum, we used electrospray mass spectrometry (ESI-TOF). A size exclusion chromatography was performed in-line prior to mass spectrometry using an Agilent 1100 HPLC system (Agilent Technologies inc. – Palo Alto, CA, USA). 20 µl of protein at a concentration of 1 mg/mL was injected onto a 2.1 mm x 12.5 mm AdvancedBio SEC 120 Å 1.9 µm housed in a column oven set at room temperature. The isocratic solvent system used consisted of 50 mM ammonium acetate (Sigma®) in Optima® LC/MS water (Fisher Chemical) with a final pH of 6.8. Chromatography was performed at a constant flow rate of 0.2 mL/min for 15 min. Protein native intact mass was determined using an MSD-ToF electrospray ionization orthogonal time-of-flight mass spectrometer (Agilent Technologies inc. – Palo Alto, CA, USA). The instrument was configured with the standard ESI source and operated in positive ion mode. The ion source was conducted with the capillary voltage at 3500 V, nebulizer pressure at 30 psig, drying gas at 325 °C, and drying gas flow rate at 10 L/min. The instrument ion optic voltages were as follows: fragmentor 425 V, skimmer 65 V, and octopole RF 300 V.

The data were interpreted using MassHunter Qualitative Analysis B.07.00 SP1, Agilent Technologies, Inc (with MassHunter BioConfirm B.07.00, Agilent Technologies, Inc). They consisted of extracting the m/z spectrum, deconvolution of the m/z spectrum to obtain the neutral mass and interpreting the m/z spectrum's different charge states by inputting the neutral mass in a charge table.

3.3 X-ray crystallography

3.3.1 Crystallization

Crystallization assays were performed using vapor diffusion methods in sitting or hanging drops. Crystallization experiments were optimized by screening variables such as protein concentration, protein to reservoir ratio in drop, pH, precipitant concentration, additives, and temperature based on conditions previously described (KNAUS et al., 2001; LEE et al.,) and optimized during Prof Nonato sabbatical developed at the Broad Institute: 100 mM Tris pH 7.6, 2.0-3.5 M NaCl, 15 mM $CdCl_2$ and glycerol 0-10%. Also, a broad range of protein volume/reservoir solution rates with final droplet volume varying from 2 to 4 µL was tested. The drops were equilibrated

against 500 µL of the reservoir at 21 ºC, with protein concentration set to 4.5 mg/mL in a 24-well 1-drop plate.

3.3.2 Quest for a different crystal form

Several crystallization commercial kits (such as Hampton Crystal Screen, MDL JCSG +, MDL BCS, MDL MIDAS +, MDL MORPHEUS) were used to establish a new crystal form for the human prion protein. These assays were performed using a Mosquito ® crystallization robot and 96- well 3-drop Swissci plates utilizing a range of protein to reservoir ratio (1:1, 2:1, and 1:2), different protein concentrations (from 4 to 10 mg/mL), and temperatures (4 ºC and 20 ºC) in the ROCK IMAGER 1000 by Formulatrix. Because of the nature of fragment screening, PEG-based conditions were prioritized. Promising conditions were optimized by varying pH, PEG percentage, and different salts as additives. Optimizations included conditions with additives such as zinc acetate, magnesium chloride, ammonium formate, rubidium chloride, cobalt chloride combined with different PEGs and pHs.

Attempts to reproduce our crystallization condition with cadmium while exchanging the NaCl to PEG were also made and included the screening of different pHs, buffers, cadmium concentrations, and PEG Smears low, broad, medium, and high, also at different concentrations. As the project progressed, attempts to reproduce crystal forms reported for in PDB 3hak, 1i4m, and 4n9o were also made.

3.3.3 Nanobody production

The Nb484 was expressed in an attempt to produce a crystal complex for our fragment screening. The pNIC-CTH0 vector containing the Nb484 sequence was purchased from Twist Bioscience. The sequence encodes the nanobody fused with a non-cleavable 6x His C-terminal tail and a cleavable N-terminal signal peptide PelB for periplasm expression. *E. coli* BL21 (DE3) competent cells were transformed by heat shock and plated in LB agar containing kanamycin (30 µg/mL). A single colony was used to inoculate 10 ml LB media in the presence of the same antibiotic and incubated under agitation (180 rpm) overnight at 37 °C. The starter culture was diluted 100-fold in autoinduction media for bacterial growth and protein expression. The system was incubated under agitation (180 rpm) for 48 hours, the first 5 hours at 37 °C and remaining at 18 °C. Cells were harvested by centrifugation, and 250 mL of pellet was

resuspended in 25 mL of base buffer (BB - 20 mM HEPES pH 7.5, 500 mM NaCl, 5% glycerol) supplemented with 1% Triton X-100 and 0.1 mg/mL lysozyme and stored at -80 ºC for later use.

The frozen pellet was thawed centrifuged, and the pellet was discarded. The supernatant was injected into a 1 mL IMAC column pre-equilibrated with BB and 20 mM imidazole for affinity purification. The column was subjected to multiple washes: 40x CV with BB supplemented with 20 mM imidazole, and 40 CV with BB supplemented with 40 mM imidazole. The Nb484 was eluted from IMAC with 2.5 CV BB with 500 mM imidazole directly into a PD10 column (GE Healthcare), pre-equilibrated with BB. Nb484 was eluted from PD10 with 3.5 mL of BB. All steps were monitored by SDS-PAGE.

3.3.4 PrP-Nb484 complex

Purified PrP and Nb484 were mixed in equal ratios for complex formation. The mixture was incubated for one hour at 4 °C, centrifuged at 16,000 g for 10 minutes, and submitted to a size exclusion chromatography in an SRT-10 SEC-300 (SEPAX) using 100 mM Tris pH 7.5, 150 mM NaCl as mobile phase at a flowrate of 3 mL/min. Pools containing the co-elution of PrP and Nb484 were subjected to analysis in MS for native spectrum acquisition for complex confirmation. The confirmed, purified PrP-Nb484 complex was concentrated using a 10 kDa cut-off membrane and submitted to crystallization procedures.

3.3.5 In-house fragment screening

Fragments identified by our collaborator in the Broad Institute, Dr. Andrew Reidenbach, as possible PrP binders were tested in our in-house fragment screening, in which soaking experiments were done manually. Around 50 fragments were tested. Drops containing fully grown crystals were unsealed, followed by gentle dispense of highly concentrated (100-500 mM) fragment stock solution on the drop, and resealed again. After the soaking period, crystals were harvested, and cryo-cooled All crystals were grown in the same condition: 100 mM Tris pH 7.6, 2.5 M NaCl, 15 mM $CdCl_2$, 10% glycerol. Only one fragment was tested per drop. In order to maximize resolution and crystal survival, total volume dispensed (which dictates the final ligand concentration) and soaking time were set as a function of crystal damage and

dissolution by the DMSO. The crystals were shipped to Synchrotron Soleil for X-ray data collection.

3.3.6 Fragment libraries

We have used three different fragment-based libraries in our screenings. The main one, the DSi-poised (Enamine) contains a total of 860 fragments in d6-DMSO, and has been designed by Diamond, SGC and iNEXT to allow quick synthesis of analogues. Its components contain at least one functional group that can be synthesized with well-known reactions like amide coupling, reductive aminations, synthesis of sulfonamides and Suzuki-Mayaura coupling, among others. It is obtained from Enamine, and its entire content is available at: https://www.diamond.ac.uk/Instruments/dms/MX/FragmentsResources/DSI_poised_Enamine_fragment_library0/DSI_poised_Enamine_fragment_library.xlsx.

The FragLite (WOOD et al., 2019) is a small library of 31 fragments. It is defined as ‘as small (≤13 heavy atoms) compounds bearing a pharmacophore doublet and a heavy halogen atom’. This library is unique because it counters the central issue of X-ray crystallography fragment screening: the lack of affinity between the fragment and the protein can result in low occupancy and increased mobility of the binder, making it sometimes not shape-recognizable. The main feature involving this library is that the incorporation of a heavy halogen atom into these compounds that allows an unambiguous identification and orientation of the fragments by their anomalous signal.

The MiniFrag (O’REILLY et al., 2019) was specifically constructed to sample chemical space in the ultra-low-molecular-weight, with a heavy atom count of 5-7. It comprises a total of 81 chemically diverse compounds. The critical advantage, in this case, is that they are highly soluble ligands, employing high-concentration aqueous soaks (1 M) to identify ligand-binding hot and warm spots on proteins. The aqueous feature of this library helps to overcome eventual issues with DMSO soaking. It can also be used coupled with a known binding molecule, mapping close binding areas that could be explored in the rational drug design.

3.3.7 High-throughput fragment screening at XChem

At XChem, all steps from crystallization to data collection and structural analysis were designed to allow the use of high-throughput X-ray crystallography techniques in

fragment screening and drug discovery. In order to enable the testing of hundreds of compounds at once, standardization of experimental tools, the crosstalk between software, and automation in data collection and data processing are crucial steps.

The first step was to adapt the crystallization protocol to be performed in 96-well 3-drop Swissci plates. These steps took place at the Research Complex at Harwell, located next to the Diamond Light Source. The experiments were performed using the Mosquito ® crystallization robot (Figure 5_A), and plates were stored at 20 ºC in the ROCK IMAGER 1000 by Formulatrix (Figure 5_B). A barcode was generated for each tray, and images could be visualized either on a local computer using RockMaker software or online via rockmaker.diamond.ac.uk server. The plate hotel is set to take images of all drops following the Fibonacci sequence for the number of days.

From crystal images and beyond, all experimental steps were monitored and controlled by SoakDB. SoakDB is an excel-based sheet that records your experiment setup and generates inputs and outputs for all steps in the sample preparation pipeline.

In this pipeline, the TexRank software (NG et al., 2014) was then used for crystal selection. Ranking the images taken by the imager enables the selection of the best crystals for the follow-up experiments. The user can save the coordinates of the exact position for soaking experiments targeting a coordinate in the drop for acoustic dispensing of the selected fragments to areas that were less likely to inflict damage to the crystals. The selection of the best crystals also allows the user to know how many fragments will be tested. The coordinates are then loaded by the Echo 550 (Labcyte) (Figure 5_C) acoustic liquid handling technology (COLLINS et al., 2017), which is used to transfer fragments to each individual crystal drop at the chosen coordinates. The Echo can precisely dispense a fixed size of 2.5 nL droplets at a rate of 200 Hz. (COLLINS et al., 2017).

Figure 5. Equipments of XChem and Harwell Research Complex laboratories

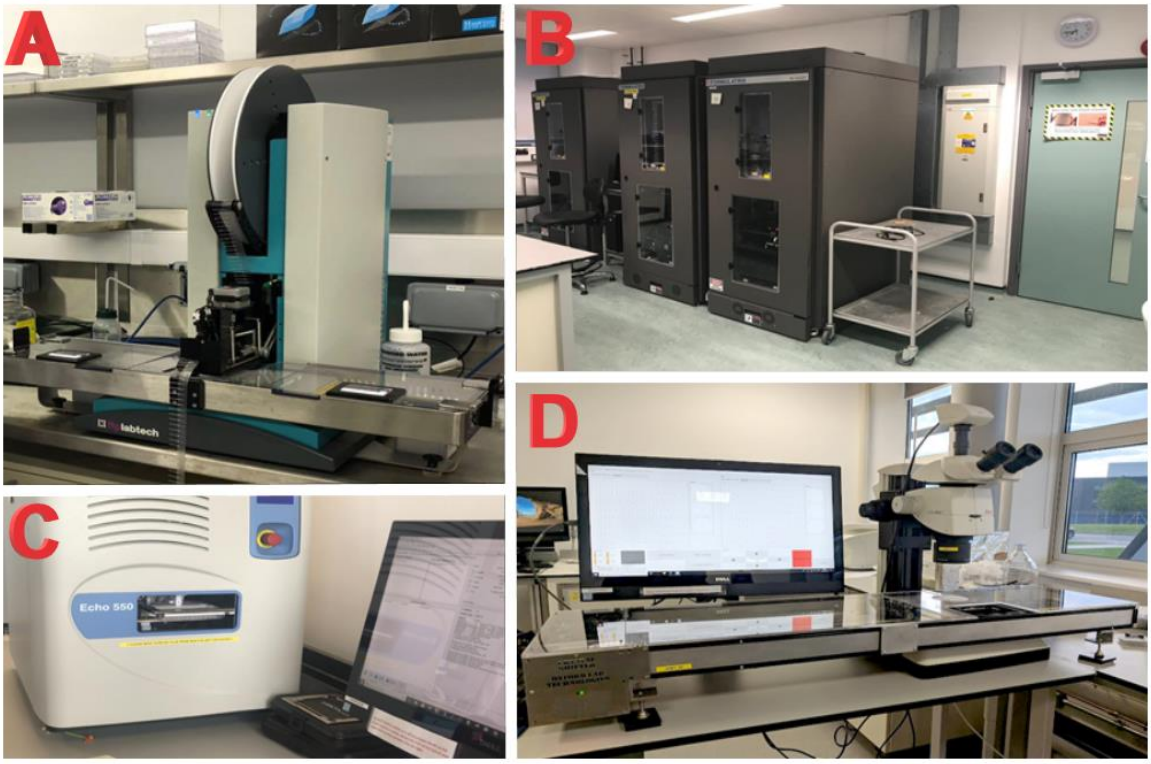

Figure caption
A: Mosquito ® crystallization robot.
B: ROCKIMAGER 1000 (Formulatrix).
C: Echo 550 (Labcyte).
D: Shifter Device (Oxford Lab Technologies). Photos were taken at Diamond Light Source and Research Complex at Harwell
Source: personal file.

After soaking, crystals were manually harvested and cryo-cooled with the aid of crystal Shifter Device (Oxford Lab Technologies) (Figure 5_D), which keeps a complete audit trail of the experiment, moves the plate to the desired drops chosen in the TeXRank software, assigns crystal IDs automatically and captures destination (puck and pin position) location. It is also possible to add information about the crystal environment –e.g., if the drop is clean or precipitate - and about the crystal itself – if it is normal, cracked, jelly, or melted. After cryo-cooled, the pucks and pins have their QR code scanned and are stored in a cryocooled dewar. The information is compiled by SoakDB and exported to the ISPYB server (Information System for Protein CrystallographY Beamlines), enabling the assessment of live data collection statistics and data processing outcomes.

The following steps are guided through the XChemExplorer (XCE) (KROJER et al., 2017). The molecular replacement and initial model refinement are generated with

DIMPLE (KEEGAN et al., 2015). Compound restrains generated with ACEDRG(LONG et al., 2017), Grade (http://grade.globalphasing.org/), or Phenix eLBOW (ADAMS et al., 2010). The density analysis can be made manually, using Coot (EMSLEY et al., 2010b) and PanDDA (PEARCE et al., 2017). PanDDA creates the pre and final ground state maps, and the models are refined using Coot and REFMAC5 (MURSHUDOV et al., 2011), calculate the event maps to allow an aided manual hit inspection. At the end of the pipeline, structures with ligands are refined with REFMAC5 or Buster (https://www.globalphasing.com/buster/), and a batch deposit system allows you to submit all the final models to PDB in a single move.

3.3.8 Data Collection

Crystals were manually loaded into a BART sample charger (Figure 6_B), with a sample capacity of 37 pucks (592 crystals). Collection and processing were controlled from the hutch control room (Figure 6_A and C) using the Generic Data Acquisition (GDA) software. Crystals were automatically loaded into the beam by the BART sample charger and aligned (Figure 6_D) using manual, X-ray, or optical centering depending on the crystal size.

Cryogenic X-ray diffraction data for the HuPrP fragment 90-231 was collected at the Diamond Light Source (beam line I04-1) using a single wavelength X-ray of 0.9159 Å. A broad range of data collection parameters was tested. Our deposited model was collected with the following strategy: 500 images with an oscillation angle (Ω) of 0.12º were collected using a beam of 0.04 s of exposure to a 1.6 e^{+11} ph/s flux with 30 µm aperture.

Figure 6 - Data collection features of I04-1 beam line

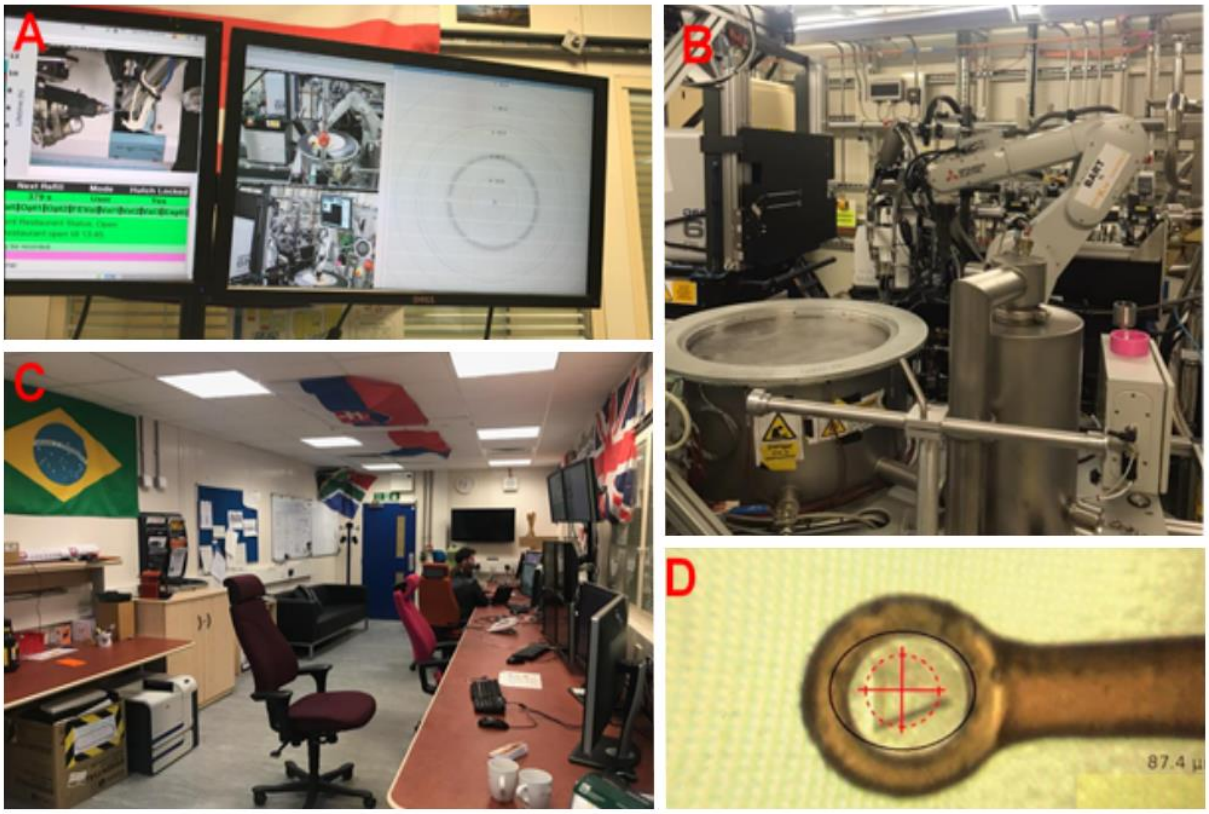

Figure caption
A: System control interface.
B: BART sample charger.
C: Control room.
D: PrP Crystal auto aimed and aligned. Photos were taken at Diamond Light Source and Research Complex at Harwell.
Source: own elaboration.

3.4 Data processing, structure determination and analysis

Images were indexed with either XDS(KABSCH, 2010) or DIALS (WINTER et al., 2018), and reduction was performed with Aimless (EVANS; MURSHUDOV, 2013) in the autoPROC (VONRHEIN et al., 2011) or CCP4i2 (POTTERTON et al., 2018) software package. The structure was determined to 2.3 Å resolution using the previously deposited model 3HAK (LEE et al.,) as a search model in Phaser (MCCOY et al., 2007), implemented in the PHENIX suite (ADAMS et al., 2010). Model building and refinement were performed with Coot (EMSLEY et al., 2010a) and REFMAC5 (MURSHUDOV et al., 2011) in the CCP4i2 suite (POTTERTON et al., 2018). Cd^{2+} and Cl^{-} sites were confirmed by Fourier anomalous difference map from data collected at 4.1, 3.1, and 2.7 keV (3.02, 3.99, and 4.59 Å) at the beamline i23). The wavelengths were chosen considering the theoretical absorption edge of cadmium and chloride ions (Figure 7). The data were also phased with Phaser Phenix, using the SHELXD

(SCHNEIDER; SHELDRICK, 2002). The quality of the final model was validated by MolProbity (CHEN et al., 2010). Figures were prepared with PyMOL. The structure was visualized with Coot and PyMol. Coordinates were deposited under the access code 6DU9.

Figure 7. X-ray absorption edges of Cl- and Cd2+

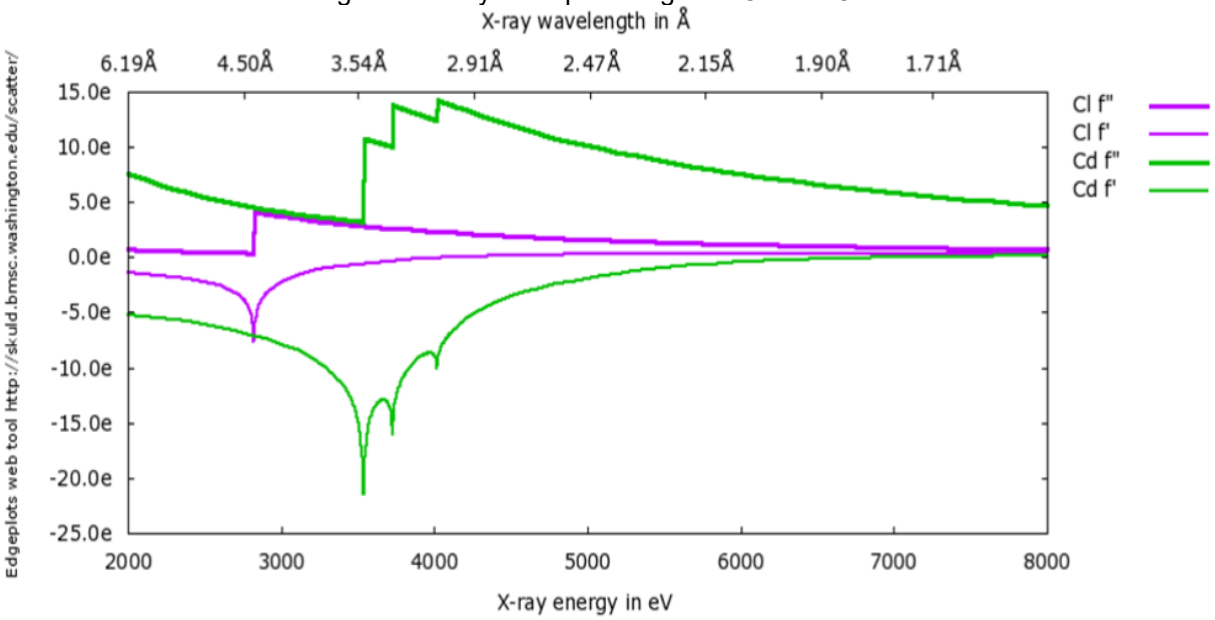

Source: own elaboration. Graphic generated using edgeplots tools avaiable at: http://skuld.bmsc.washington.edu/scatter/

All datasets derived from the in-house fragment screening were analyzed using our deposited structure 6DU9 as the model for ligand search using either the described method or utilizing the DIMPLE pipeline implemented in the CCP4i2 suite.

To evaluate and identify different conformations in the prion structures, the real-space correlation coefficient (RSCC) was calculated for every dataset collected at XChem. This was performed using fttmap (TEN EYCK, 1985) and edstats (TICKLE, 2012), available in the CCP4 suite(WINN et al., 2011). We used the DIMPLE output as an input model for our RSCC calculations. In order to increase the number of datasets in the analysis, a maximum resolution range was set to 2.5 Å. The mean RSCC was calculated for the main chain of every residue, and we establish an ‘outlier’ classification for residues in datasets with a deviation of –3*σ. All the datasets with outlier RSCC residues were manually (visually) investigated.

4. RESULTS AND DISCUSSION

4.1 Protein production

We successfully managed to establish an adapted protocol for protein expression, purification and refolding. HuPrP was expressed in *Escherichia coli* ROSETTA BL21 (DE3) cells as inclusion bodies. It is essential to highlight that a high temperature during the protein expression stage was key to make sure the protein was produced as inclusion bodies – a mild temperature would produce protein in the soluble form. The protein was initially purified by pellet-washing steps. Over the cycles of homogenization-and-centrifugation, the supernatant got progressively colorless, and the pellet changed from a brown appearance to an almost white color (Figure 8).

Figure 8. Coloration different of PrP-containing pellets. Pellets became progressively clear after multiple washes. Initial (left) and last pellet wash (right)

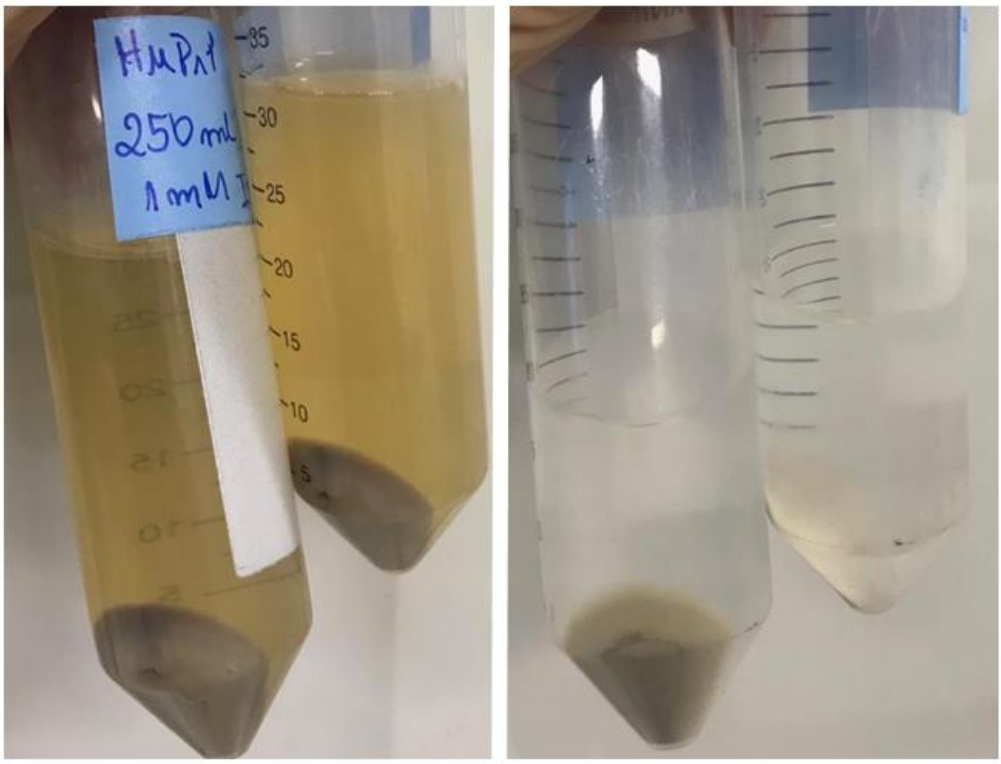

Source: personal file.

The inclusion bodies were solubilized by 8 M guanidine, which acts as a chaotropic agent, disrupting the inter and intramolecular network of hydrogen bonds, causing its denaturation. The protein sample was injected into a previously equilibrated Ni-NTA resin for refolding. After the slow removal of guanidine, the refolded PrP was successfully eluted from the column by a linear gradient of 500 mM imidazole (Figure 9). The protein eluted around 70% imidazole proportion, astonishingly high for a protein

without 6x His-tag. PrP was readily dialyzed to 10 mM $NaC_2H_3O_2$ pH 5, concentrated to 4.5 mg/mL, and stored at 4 °C until further used. Our protocol had a protein yield of approximately 8 mg of pure, soluble, and refolded PrP per liter of cell culture.

Figure 9. Chromatogram profile (280 nm) of refolding (top) and elution (bottom) with 500 mM Imidazole step

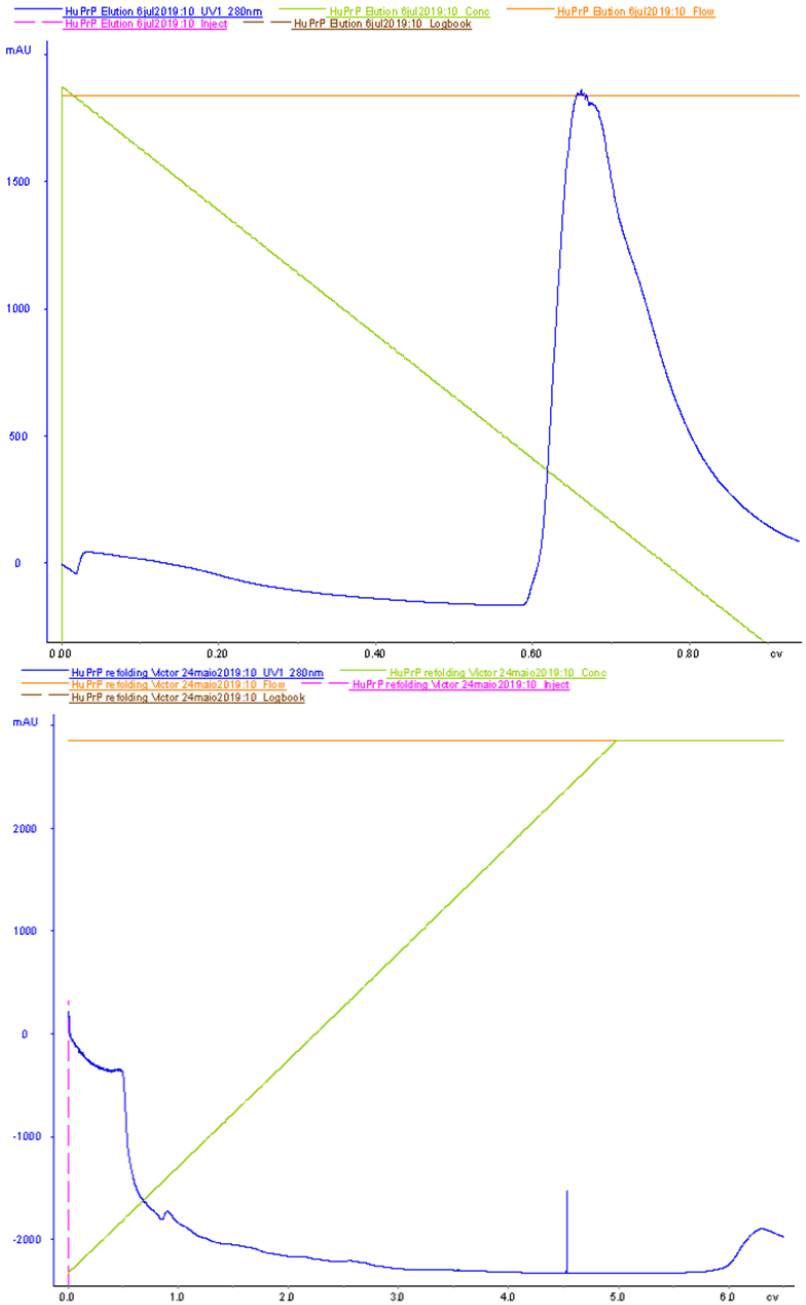

Source: personal file.

The main differences between our collaborator's protocol are at costly steps. These modifications were introduced to fit our budget. The modified steps are:

I. Use of autoinduction kits for protein expression.

II. 750 mL of cell pellet purified per purification.

III. This requires a column filled with 56 mL of Ni-NTA, which is discarded after each use.
IV. A third of a BugBuster bottle per purification.
V. 300 mL of 6 M guanidine per purification.

We successfully expressed PrP as inclusion bodies using IPTG as a protein expression inductor(I) to overcome those challenges. We managed to replace BugBuster® (Novagen) with lysis buffer(IV); in turn, we have increased the number of pellet-washing steps from 3 to 9. The first washes are essential to disrupt the bacterial membrane, release inclusion bodies, and get rid of soluble proteins. The subsequent washes contain 0.5% Triton x-100, removing membrane debris, lipids, and membrane proteins without solubilizing the inclusion bodies (PALMER; WINGFIELD, 2012). In the end, buffer A is used to remove the detergent. We also reduced the amount of resin to 5 mL, reused after cleansing with sodium hydroxide and guanidine(III), thus reducing the amount of guanidine used in the refolding step(V). This was possible by reducing the amount of purified pellet from 750 mL to 250 mL (II).

Our current protein yield of approximately 8 mg per liter of cell culture corresponds to 30% of our collaborator's yield. Despite being enough to perform our studies, we are aware that there is still room for improvement: we believe that a refinement of the refolding process can increase recovered protein. It is also important to further acknowledge our collaborators who have supplied us with protein, enabling many assays throughout this work.

4.2 Dynamic Light Scattering

Obtaining high-quality crystals is a major challenge in protein crystallography studies. It is a complex, multi-factorial technique, not yet fully comprehended. Multiple steps precede the crystallization experiments and directly impact the crystallization outcome, and the quality of the protein is a key one. Numerous studies point purity and homogeneity as crucial factors to obtain high-quality, reproducible crystal systems (GLUSKER, 2003; MCPHERSON; GAVIRA, 2014).

Since purification and refolding processes can yield a heterogenous mixture of folded and unfolded protein, we used the dynamic light scattering technique to assess the quality of our purified, refolded protein sample. DLS pointed the purified protein as homogeneous, with only one peak in the volume vs size distribution plot, pure, with 99.8% of the mass belonging to this peak, a low polydispersity index of only 9%. The sample was characterized by a hydrodynamic diameter of approximately 4 nm, compatible with the monomeric state of the PrP. We employed DLS assays as a quality control experiment, after the purification, and before the crystallization. The reported profile (Figure10) of size distribution by mass was identified as suitable for our crystallization assays, reproducibly yielding protein crystals. This assay also allowed us to save time and resources as proteins that did not follow this profile would not generate crystals.

Figure 10. Particle size and size distributions for human PrP after purification and refolding. Triplicate measurements were performed for each sample

Distribution Results

	Mode ± SD (nm)	%Pd	Est. MW (KDa) (Mode ± SD)*	% Intensity	% Mass	Peak Polydispersity
Peak 1:	4.062 ± 0.3716	9.0	17.7 ± 5.7	15.8	99.8	Monodisperse
Peak 2:	28.28 ± 4.622	15.4	1.66e+3 ± 450.4	9.0	0.2	Monodisperse
Peak 3:	81.85 ± 26.69	31.2	1.99e+4 ± 1.99e+3	58.2	0.1	Polydisperse

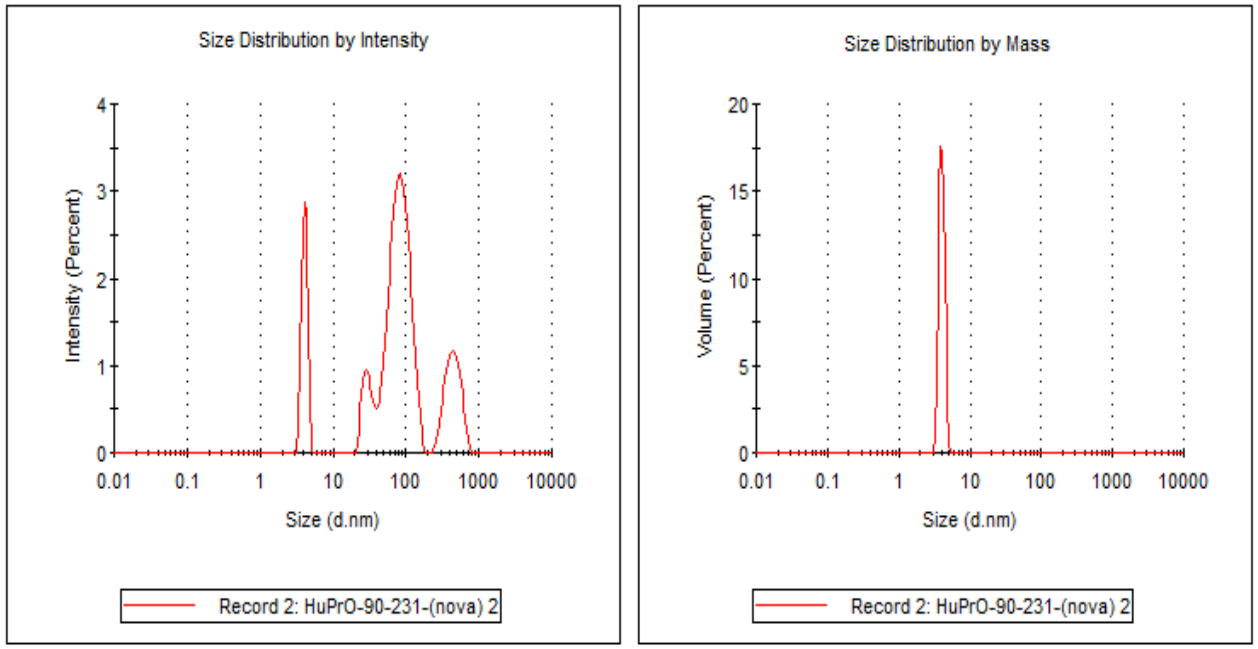

*The molecular weight reported here is only an estimate, calculated using an empirical mass vs. size calibration curve.

Source: personal file, generated in Malvern Zetasizer software.

4.2.1 Mass Spectrometry

We initially intended to do an orthogonal validation for the hits from our fragment screening assays. A possible binding assay is the utilization of native mass spectrometry as the biophysical technique to evaluate binding events. Mass spectrometry has excellent advantages for this purpose since it is exceptionally accurate, sensitive while also requiring very few amounts of samples. We expect that m/z shifts could identify binding events to the native state of the prion protein in accordance with the ligand mass. The first step for this was to evaluate if our protein system was suitable for this technique, and for that, an apo native mass spectrum was acquired. Our results (Figure 11) show that PrP appears as partially folded monomer, folded monomer, and possibly folded dimer, with a deconvoluted m/z peak of 16146.82 Da (Figure 12). This assay confirms the overall integrity of the protein in solution and the cleavage of the N-terminal methionine during protein expression in *E. coli*: our protein sequence has a calculated molecular weight of 16279.17 Da 16147.97 Da (Δ mass of 131 Da) for protein lacking the N-terminal methionine.

The presence of the folded protein in the spectrum is imperative for this type of binding assay since this is the form to which we expect a ligand to bind. The spectrum also confirms our system to be compatible with native MS.

Figure 11. Convoluted native mass spectrum of HPrP 90-231 shows PrP is in solution as partially folded, folded monomer and folded dimer.

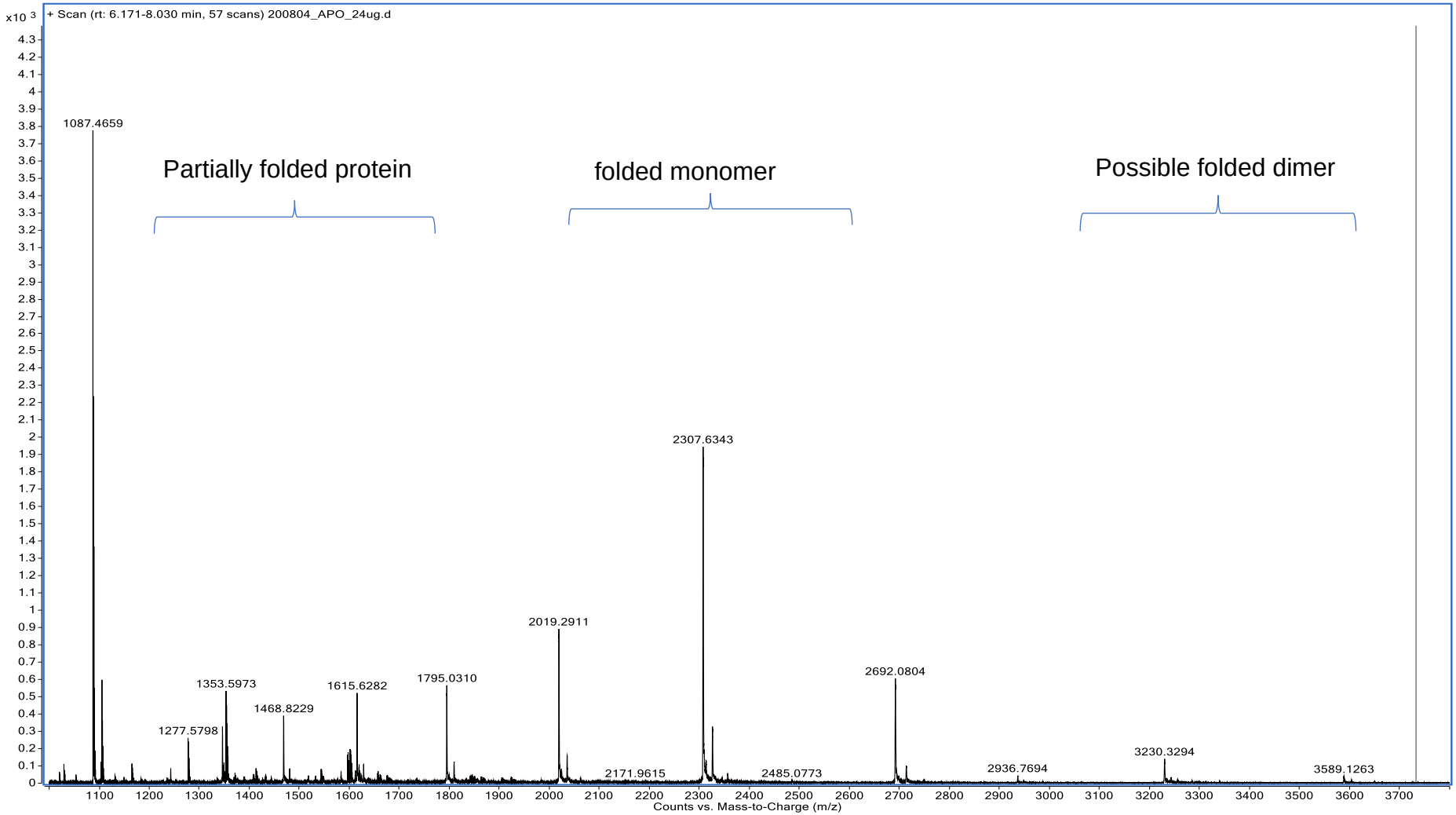

Source: personal file.

Figure 12. Deconvoluted native mass spectrum of our HuPrP 90-231 sample. Spectra contain the expected mass for the protein 16,278 Da, but the one main peak has ∆mass of 131 Da corresponding to the loss of methionine initiator

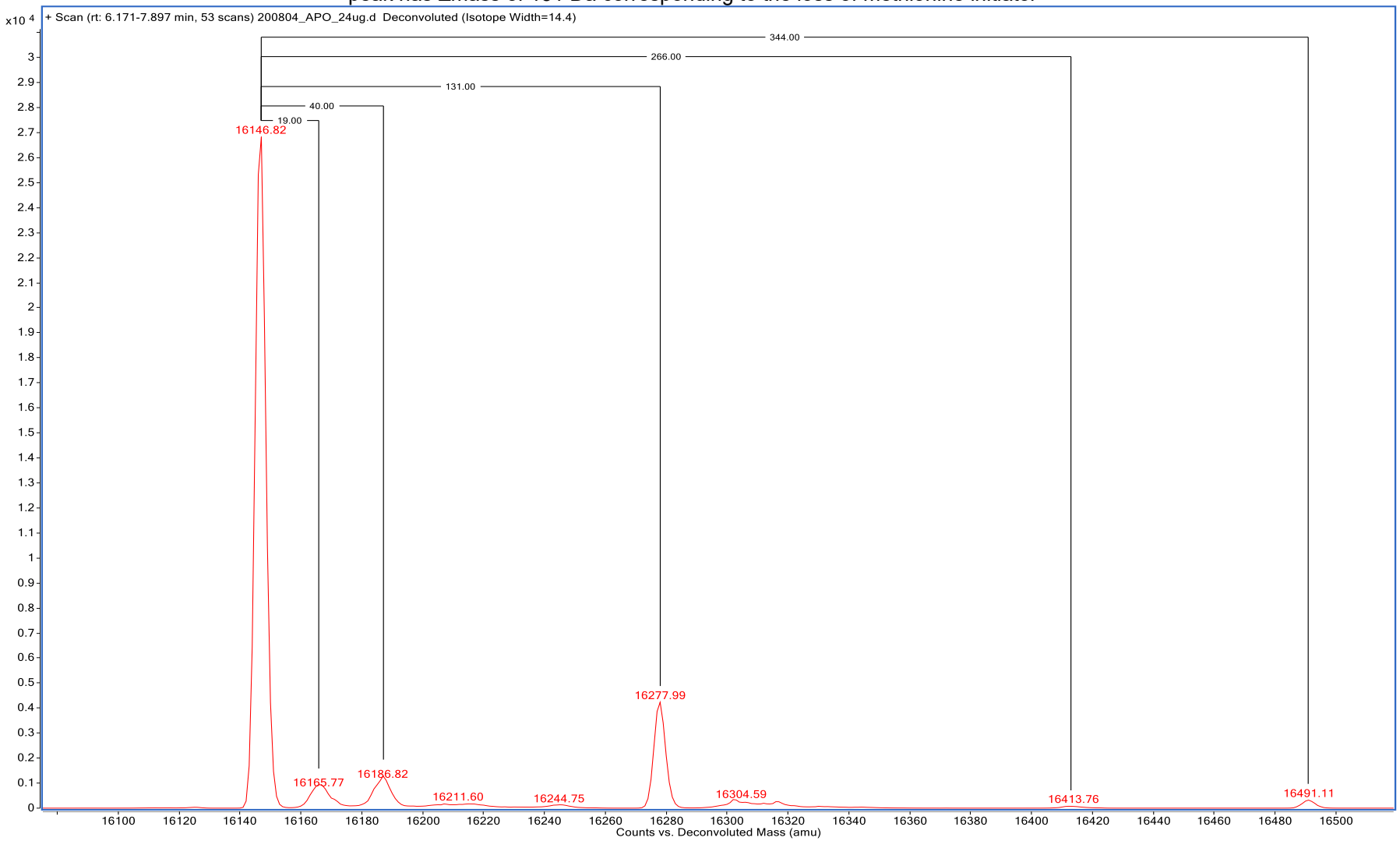

Source: personal file.

4.3 Structural studies

4.3.1 Structure determination

The bipyramidal-shaped crystals (Figure 13) of recombinant HuPrP 90-231 appeared within 3-4 days in the presence of 100 mM Tris pH 7.6, 2.5 M NaCl, 15 mM $CdCl_2$, 10% glycerol. Data processing showed the crystals belong to the tetragonal $I4_122$ space group. The prion structure was solved at 2.3 Å by molecular replacement method using a previous deposited structure (PDB ID 3HAK) (LEE et al.,) as the search model and contains sixteen protein chains in the unit cell.

Figure 13. HuPrP Crystals

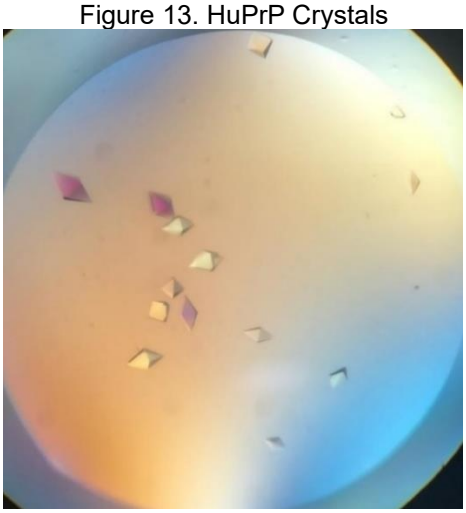

Source: personal file.

The final model contains 725 protein atoms, 1 Cl^-, 3 Cd^{2+}, and 18 water molecules. The final round of refinement reached R_{work} of 19.2% and R_{free} of 23.5%. The coordinates were deposited in the Protein Data Bank under accession code 6DU9 (Figure 14). More details of the data collection and refinement statistics are shown in Table 1.

Figure 14. Overall percentile scores for global validation metrics of our deposited model. Generated by wwPDB Validation

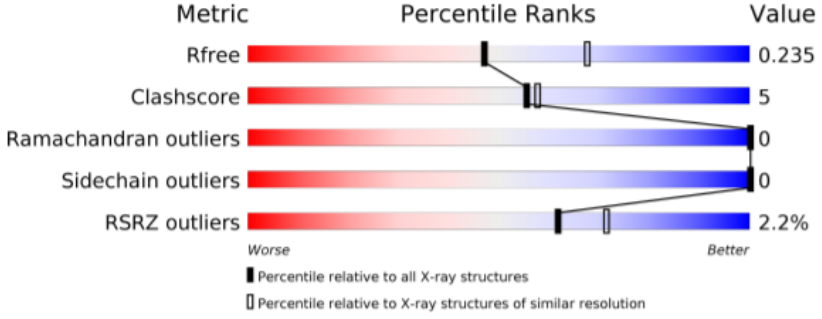

Source: personal file.

Table 2 – Data collection and refinement statistics. Statistics for the highest-resolution shell are shown in parentheses

Data processing	
Space group	*I 4_1 2 2*
Cell dimensions	
a, b, c (Å)	*72.17 72.17 158.55*
α, β, γ (°)	*90.00 90.00 90.00*
Wavelength (Å)	*0.91587*
Resolution (Å)	*65.71 - 2.31 (2.42 -2.31)*
Total reflections	*28629 (1373)*
Unique reflections	*6581 (329)*
Multiplicity	*4.4 (4.2)*
Completeness (ellipsoidal) (%)	*92 (71.5)*
<I/(σI)>	*9.7 (1.4)*
Wilson B-factor	*58.87*
R_{merge}	*0.092 (0.983)*
R_{meas}	*0.105 (1.122)*
R_{pim}	*0.049 (0.532)*
CC (½)	*0.997 (0.597)*
Refinement	
Reflections used in refinement	*5921(18)*
Reflections used for R_{free}	*660 (2)*
R_{work}	*0.1924 (0.3342)*
R_{free}	*0.2350 (0.3011)*
Number of non-hydrogen atoms	*747*
Macromolecules	*725*
Ligands	*4*
Solvent	*18*
Protein residues	*91*
RMS deviations	
Bonds (Å)	*0.012*
Angles (°)	*1.59*
Ramachandran plot	
Favored (%)	*98.85*
Allowed (%)	*1.15*
Outliers (%)	*0.00*
Rotamer outliers (%)	*0.00*
Clash score	*5.14*
Average B factor ($Å^2$)	*56.41*
Macromolecules	*56.81*
Ligands	*53.34*
Solvent	*41.11*

Source: own elaboration.

The cadmium sites were manually modeled in Coot, with several refinement rounds using REFMAC5. The modeling started with water placement into those sites, in which extra electron density was still spotted, as well as exceptionally low B-factors. To achieve the correct model, heavier atoms than water and that were present in the mother liquid were placed and refined. The positioning of cadmium ions suited well for these sites – Cd302 and Cd303 – required only further addition of coordinating waters to model the region correctly. However, the third site – Cd301 – showed still extra electron density after placement of the neighboring coordinating water. The solution came with its replacement by a chloride ion, which satisfied the electron density. Cd301 is positioned along a 2-fold symmetry axis; therefore, it was modeled with 0.5 occupancy. It intermediates the contact of two asymmetric units by coordinating with the imidazole sidechain of His177 and Cl304, with the interaction mimicked by the neighboring AU, so the Cd301 also coordinates with His177* and Cl304*. Cd302 connects the N-terminal loop with α1 by coordinating with the imidazole sidechain of His140 and the acidic side chain of Asp147. Additionally, three water molecules coordinate with it. The Cd303 is at the border of the asymmetric unit and intermediates the contact with the same protein chain of Cd301 through coordination with Glu207, Asp178*, and two additional water molecules.

Although satisfying the electron density, we decided to validate these atoms before moving on. To do so, we explored the anomalous signal for both Cd^{2+} and Cl^{-} ions. Our experiment was designed by Ramona Durma and Kamel El Omari in the beamline i23 at Diamond Light Source. Three wavelengths were chosen to maximize either Cd^{2+} or Cl^{-} signal. The wavelengths were chosen based on the theoretical absorption curves of these atoms (Figure 7). They were selected to be above Cd^{2+} absorption edge (4.1 keV) – maximizing Cd^{2+} signal – below Cd^{2+} edge and above Cl- edge (3.1 keV) – minimizing Cd^{2+} signal and maximizing Cl^{-} – and below both edges (2.7 keV). The data collected at 4.1 keV confirmed the position of all the three modeled Cd^{2+} ions (Figure 15). At this wavelength, the Cd^{2+} signal is so strong that it masks Cl^{-}'s. We noticed that the Cd^{2+} signal was still very strong, even below its edge for the following data. At 3.1 keV, the anomalous signal showed a triangular-shaped density (Figure 16_A), which confirmed the presence of both Cd^{2+} and Cl^{-} atoms. The 4.1 keV and 3.1 keV signals are superposed in Figure 17 for clarification. Importantly, this Cd^{2+} is situated in a symmetry axis, so it is coordinated with a second Cl^{-} molecule from the

symmetry mate. At 2.7 keV, both signals should have disappeared, but we still observed a signal for Cd^{2+} (Figure 16_B).

Figure 15. Anomalous signal resulted from SHELXD collected at 4.1 keV from Cd ions in our PrP structure, confirming the correct position of the modeled atoms

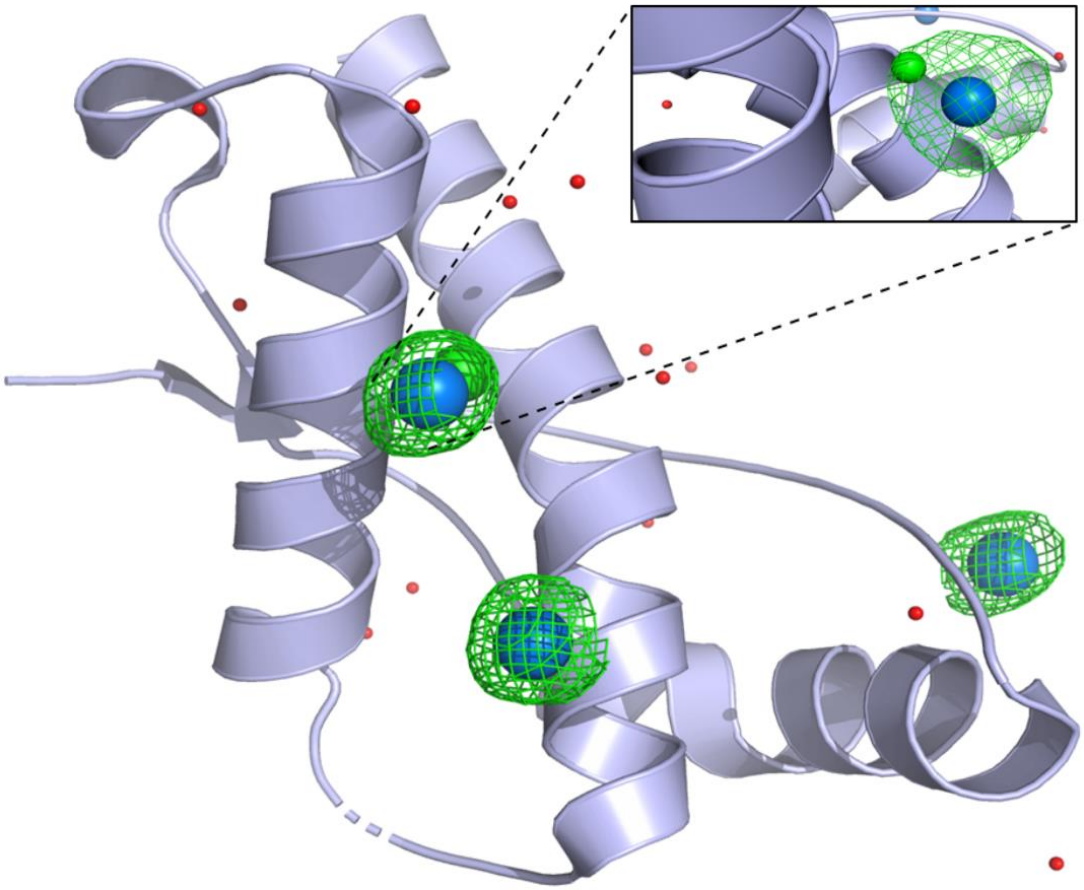

Source: own elaboration.

Figure 16. Anomalous signal for Cd301 site for data collected at 3.1 and 2.7 keV (A and B respectively). A show a triangular shaped density compatible with Cd-Cl coordination. CD atoms are shown in blue, Cl are shown in green

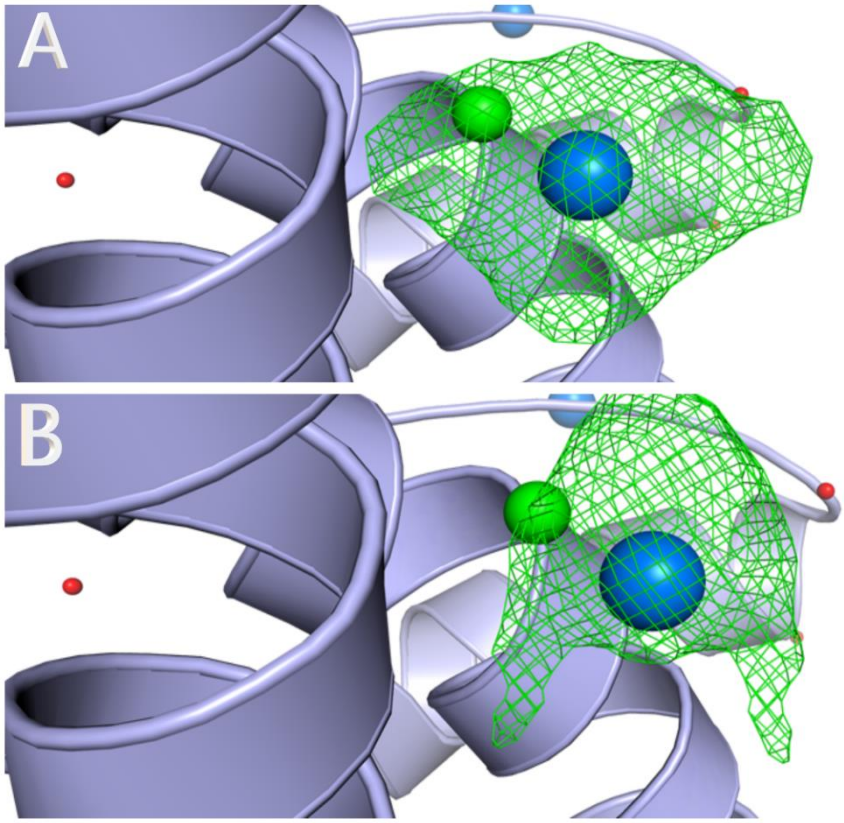

Source: own elaboration.

Figure 17. Superposition of 4.1 keV signal (blue) and 3.1 keV signal (green) clarifies the triangular shape of the signal

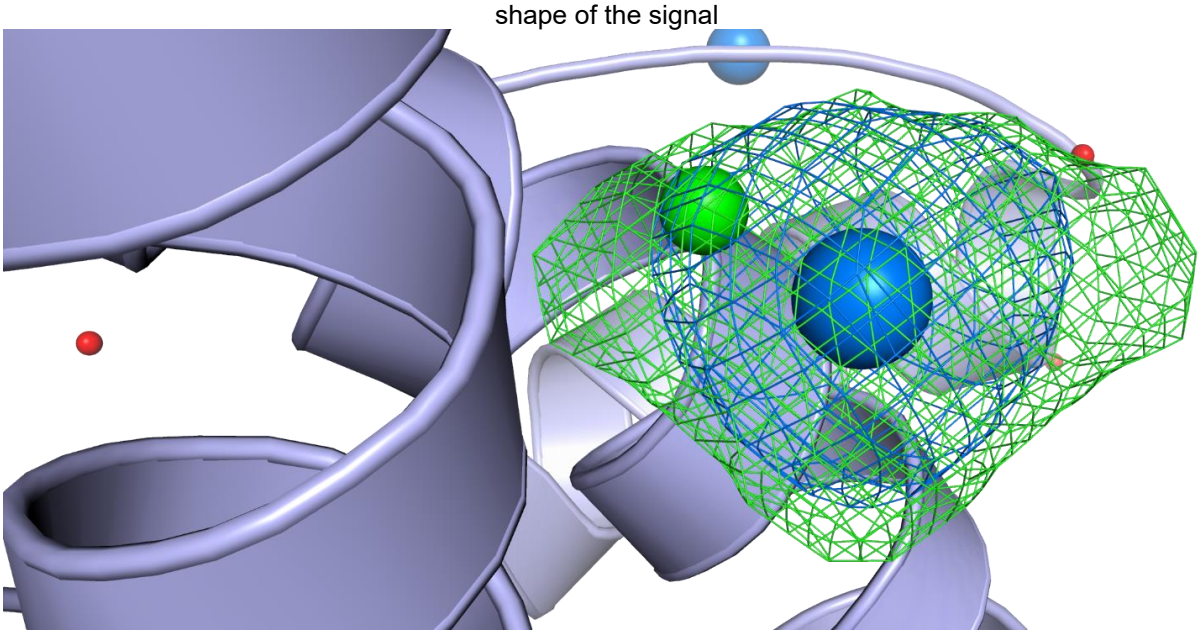

Source: own elaboration.

4.3.2 6DU9 Structure

The deposited structure has a monomer in the asymmetric unit with residues 127 to 224, which comprise the globular domain of PrP. The residues 90 to 126 are not modeled in our structure - the lack of electron density for the N-terminal portion was expected since this region is known to be intrinsically disordered (ZAHN et al., 2000). As expected for the globular domain of PrP, the deposited structure has a high α-helix content: the three conserved α-helices of the globular domain of PrP are present and span residues 143-157, 171-187, and 199-224, accounting for about 60% of helix content. Additionally, there is a small helix spanning residues 165-169. The structure contains an intramolecular disulfide bond between Cys179 and Cys214 that connects α2 and α3. Finally, the residues 190 to 196 were also not modeled. This loop connects helices 2 and 3 and is known to undergo conformation changes in the formation of a domain-swapped dimer (KNAUS et al., 2001) (Figure 18_C).

The monomer described by the asymmetric unit of the deposited structure is similar to other published structures of PrP. In particular, the most similar is PDB ID 2W9E (ANTONYUK et al., 2009) with an overall Cα Root Mean Square Deviation (RMSD) of 0.79 Å (Figure 18_A). Residue-wise RMSD analysis showed that the region in which the structures differ the most is around residues 140-145 (Figure 18_B), through which PrP is interacting with the ICSM 18 antibody in PDB ID 2W9E (ANTONYUK et al., 2009; BORTOT et al., 2020) (Figure 18_C). This novel packing reported here has the highest solvent fraction among all published crystallographic structures for PrP, namely 61.82% (Figure 18_D).

Figure 18. Comparison of our structure with all 94 structures of the globular domain of PrP that are currently available at the Protein Data Bank

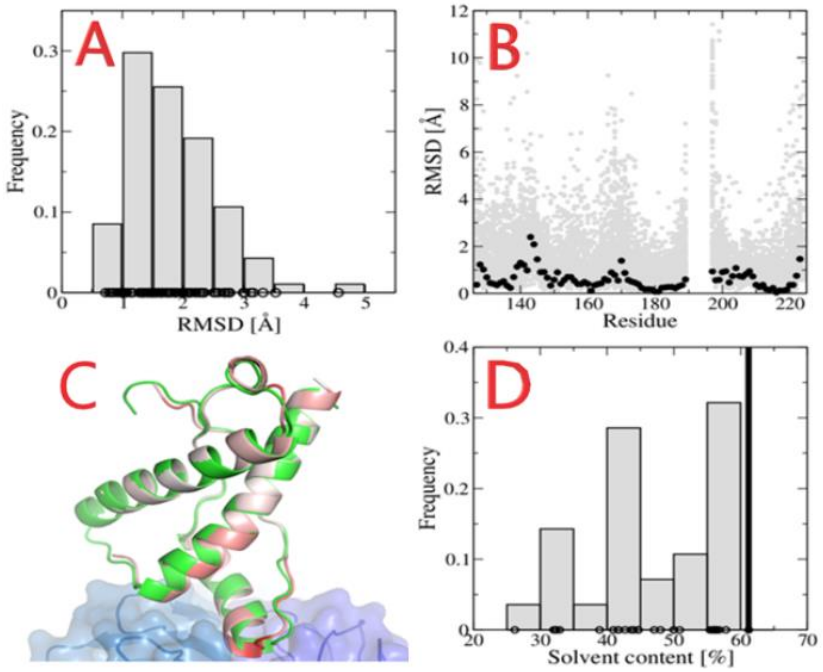

Figure caption
A: Overall Cα RMSD distribution.
B: Residue-wise Cα RMSD for all structures (gray) and for PDB ID 2W9E (ANTONYUK et al., 2009), which is the most similar to ours.
C: Structural alignment of PDB ID 2WCE showing PrP in green and the antibody in blue and our structure colored according to the residue-wise RMSD value (white = 0.0 Å, red ≥ 2.0 Å).
D: Distribution of the solvent fraction for all 28 crystallographic structures of the globular domain of PrP currently available at the Protein Data Bank (gray bars) and the value for our structure (black bar).
Source: adapted from Bortot et al. (2020). Special thanks to L. Bortot for his support and assistant with this analysis.

A series of oligomeric arrangements can be observed by applying different symmetry operations to the monomer at the asymmetric unit (Figure 19_A, Table 3). It is possible to observe the dimer, which is already described in the literature, by applying the (x,-y-1/2,-z+1/4) symmetry operation to the monomeric PrP present in the asymmetric unit (Figure 19_B). This dimer is stabilized by the interface formed between α1 and the loop that connects α2 and α3 and will be called “α1 dimer”. Specifically, the α1 dimer is mainly stabilized by the hydrogen bonds Arg148–Glu146, Glu152–Thr201, and Asn153–Tyr149 and stacking interactions involving Arg148 and Tyr145 from both chains.

Figure 19. Cartoon representation of oligomeric arrangements observed in the crystal packing

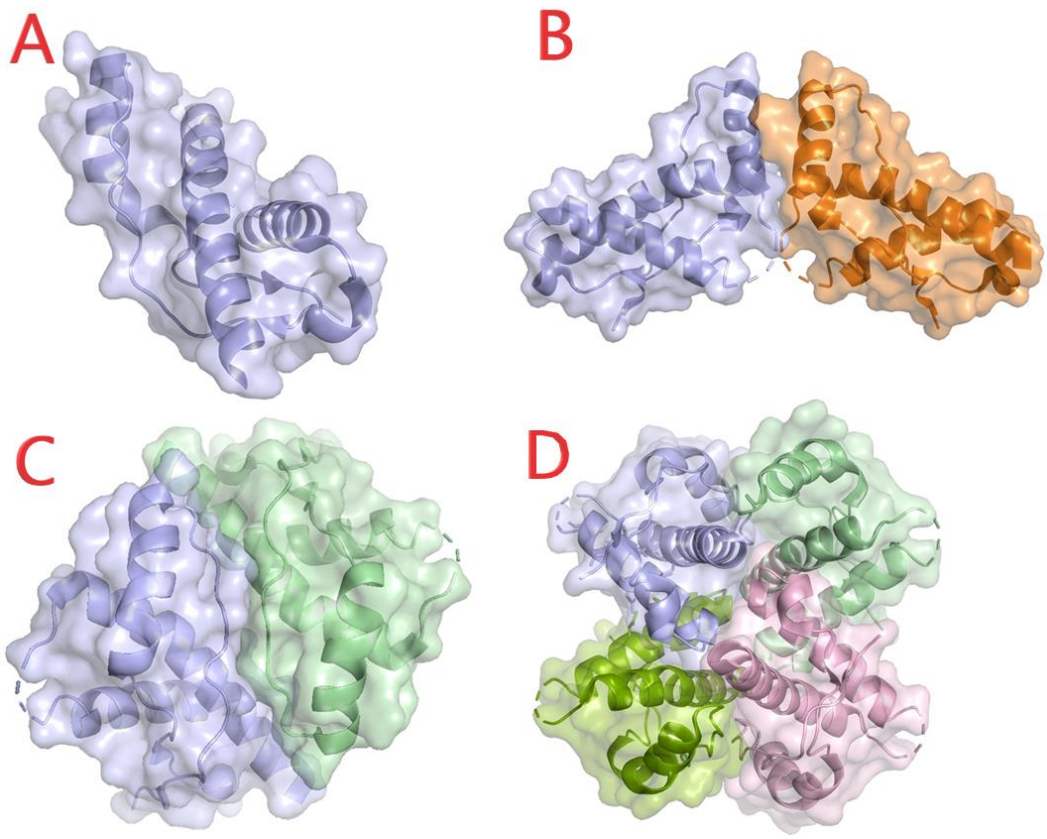

Figure caption
A: Monomer
B: α1 dimer
C: α3 dimer
D: Tetramer. Water molecules, cadmium, and chloride ions are represented as red, blue and green spheres, respectively.
Source: own elaboration adapted from Bortot et al. (2020).

Our structure also revealed a novel quaternary form for the human prion protein. This finding was deposited in the biorxiv repository in the form of a manuscript (BORTOT et al., 2020). We observe a new type of dimer formed by the packing of the N-terminal loop and the full extension of α3, and can be seen after applying the (-x+1,-y,z) symmetry operation to the monomeric asymmetric unit (Figure 19_C). Because of how the dimer is assembled, we referred to it as “α3 dimer”. This new dimeric form is stabilized by the hydrogen bonds between Arg208–Glu219, Arg208–Thr216, amine backbone of Gly142-Glu219, and a series of interaction mediated by the water 403 with Gln212 to Glu211, Gln212*, Arg208 (Figure 20, Bortot *et al.*, 2020). The flexible N-termini of each monomer stack against one another, and we observe His140–Arg136 hydrogen bonding and a possible secondary structure formation in which Ile138 of both chains interact by a hydrogen bond through their main chain, forming an interchain β-bridge, and by hydrophobic contacts via their side chains (Figure 20).

Figure 20. Interacting residues in the new dimer form. Interacting residues are shown as sticks. Cd and cl atoms are shown as blue and green spheres respectively. Image created in Pymol

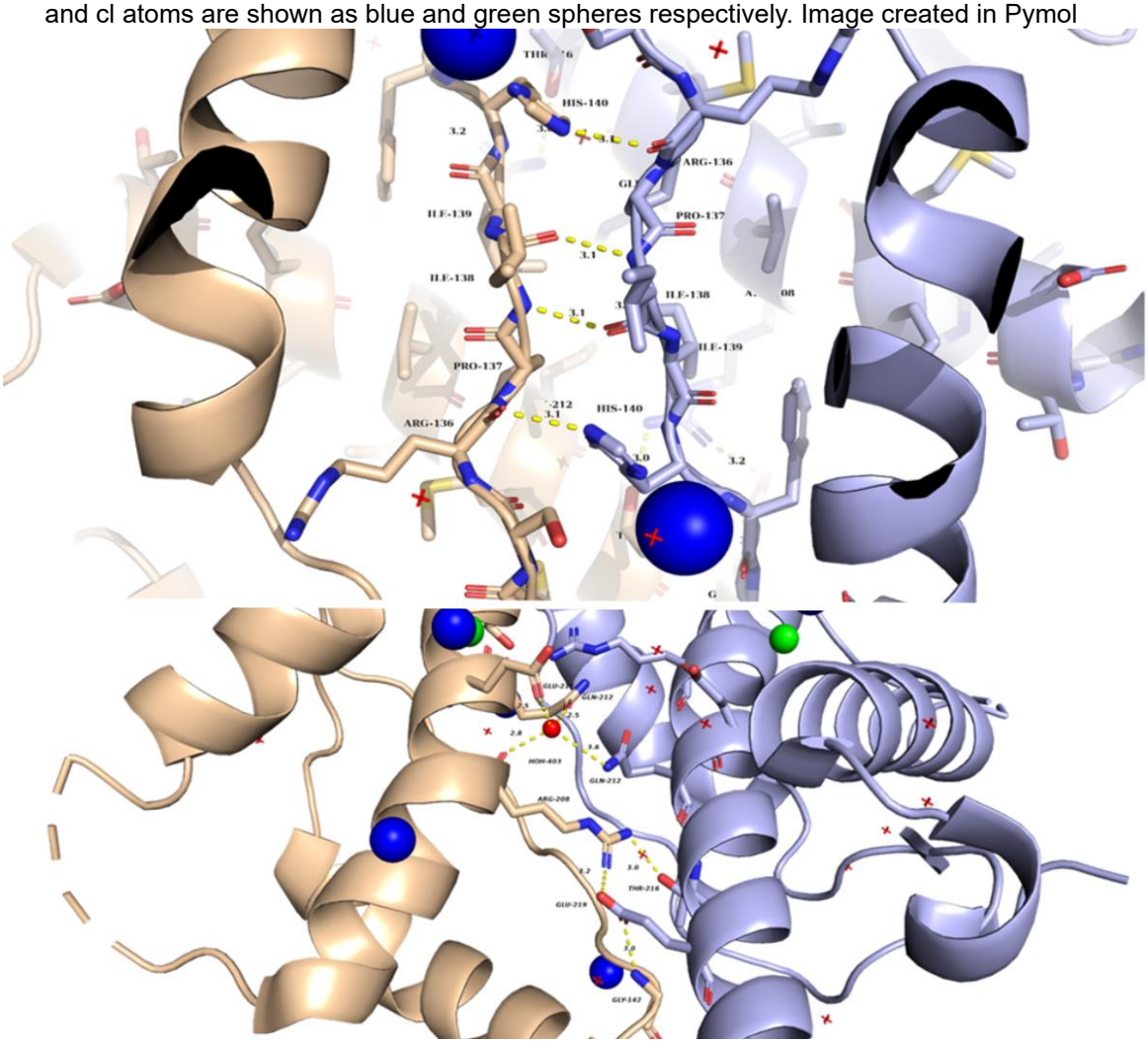

Source: own elaboration.

Although there is no reason to suggest that this novel dimeric arrangement is biologically relevant, this new oligomeric arrangement can possibly inspire new insights regarding the dimerization of the prion protein. Endogenous PrP^C dimers were observed in N2a cells, and the dimerization domain was mapped to an N-terminal region close to what we report here (amino acids 112 to 133) (RAMBOLD et al., 2008). Despite the presence of Cd^{2+} near the dimerization interface, the cation is not involved in interchain contacts.

The dimerization process of the prion protein was explored in a broad number of studies, many of which antagonize against one another, so it is fair to say that the dimer impact and relevance are still elusive. For instance, the dimerization was proposed as a physiologically relevant event for signal transduction role (ROUCOU, 2014) and having protection against the scrapie prion propagation (ENGELKE et al.,

2018), but also proposed as an intermediate and rate-limiting step in the prion conversion (HAFNER-BRATKOVIČ et al., 2011; LÜHRS; ZAHN; WÜTHRICH, 2006).

Pisa (KRISSINEL; HENRICK, 2007) also detected two additional interfaces with low $\Delta^{i}G$, which are mainly stabilized by cadmium coordination. By considering other symmetry mates, we observed a tetramer and a dimer that are stabilized by interchain Cd^{2+} complexation and are likely to be artifacts caused by the crystallization process. The tetramer is formed by two α3 dimers tighten together by Cd^{2+} ions and can be observed after applying symmetry operations to the asymmetric unit (Figure 19_D).

Our observations are backed up by results from the PDBePISA server (Table 3, Krissinel and Henrick, 2007), which detected the interface of the α3 dimer as the most stable in the unit cell, with an interface area of 647.4 $Å^2$ and solvation free energy of -3.7 kcal/mol, followed by the interface that corresponds to the α1 dimer with an area of 533.5 $Å^2$ and stability of -2.5 kcal/mol. Although we cannot imply about the relevance of this new dimer from the physiological or disease point of view, the dimerization of PrP has been studied as it is considered relevant. The presence of this new dimer will supply structural information for future insights.

Table 3 – Interface analysis in PDB 6DU9 crystal generated by PDBePISa

Assembly	Symmetry operation	Number of interacting residues	Interface Area ($Å^2$)	ΔiG (kcal/mol)
α3 dimer	-x+1,-y,z	19	647.4	-3.7
α1 dimer	x,-y-1/2,-z+1/4	14	533.5	-2.5
Cd coordinating dimer	-y+1/2,-x+1/2,-z+1/2	12	387.4	-0.3
Cd coordinating dimer	y+1/2,x-1/2,-z+1/2	15	363.9	2.1

Source: own elaboration.

4.3.3 Reducing cadmium usage

Since cadmium is an extremely toxic metal, a few attempts were made to remove the cadmium from the crystallization condition, mainly by trying to replace it with zinc. These attempts were unsuccessful, thus demonstrating this metal as essential for crystal formation. In previous studies, cadmium was noted to promote or improve protein crystallization (TRAKHANOV et al., 1998). We observe 3 Cd^{2+} per

asymmetric unit (AU), two of them are found at the interface of the asymmetric unit inter-mediating contact with the neighbor AU.

We designed an assay to reduce cadmium consumption in the crystallization plates, thus minimizing the environmental impact of cadmium-contaminated waste. We removed the cadmium from the reservoir solution but not from the crystal drop (Figure 21). This represents a slight change in the ionic strength that could negatively impact the vapor diffusion rate between the drop and reservoir. Our move successfully obtained crystals, hugely decreasing cadmium consumption from 500 µL to 2 µL - reducing by 99.6% the amount of cadmium used.

Figure 21. Schematic representation of a 24-well crystallization plate used in our experiments. The cadmium in the reservoir solution was successfully removed, reducing the amount of cadmium-contaminated waste

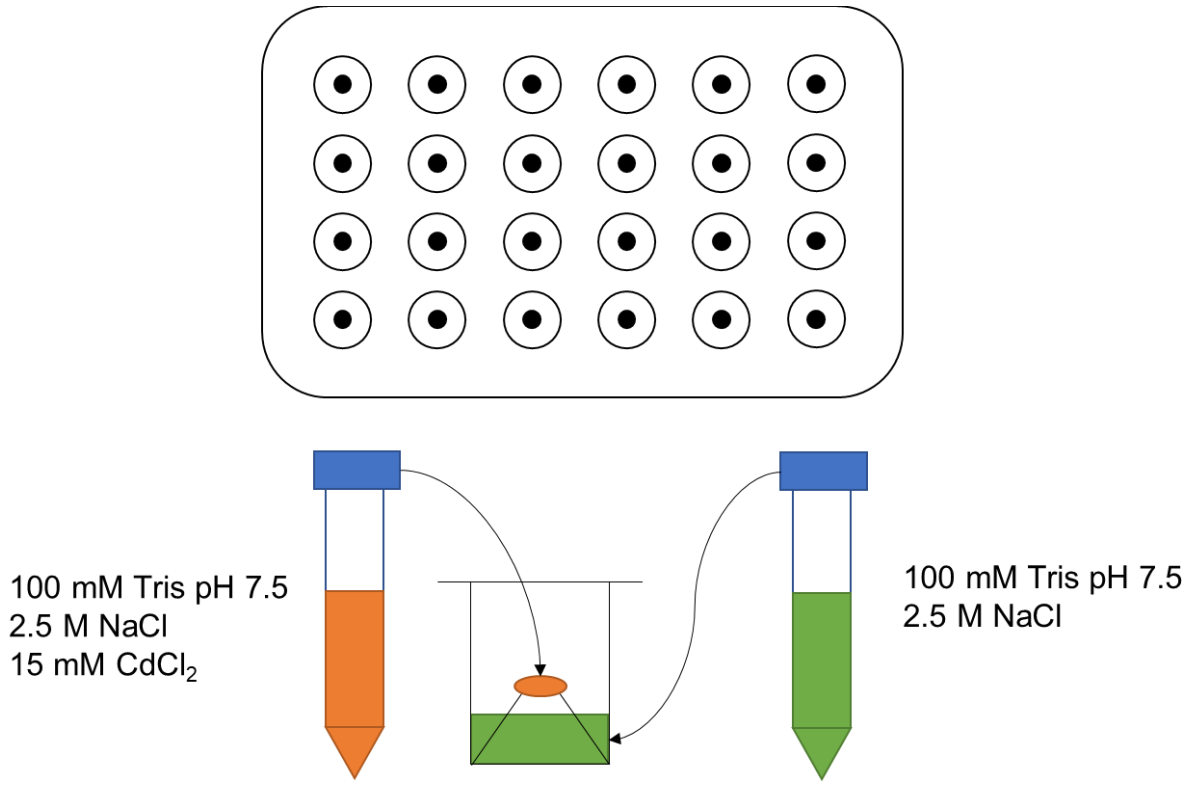

Source: own elaboration.

4.3.4 Handling cadmium-induced radiation damage

This event was not the only obstacle imposed by the presence of cadmium. In some of our data, we noticed warnings in parameters such as unit-cell expansion, inconsistent $R_{merge,}$ and loss of resolution during the course of the collection. Also, during the refinement step, we often observe some diffuse, noisy electron density in the surroundings of the cadmium sites, especially for the cadmium that coordinates

with His177. We attribute those effects to radiation damage induced by the cadmium atoms (Figure 22).

The radiation damage results from the absorbance of photons from the beam by the crystal. This can be derived from two physical effects: the photoelectric effect and Compton scattering. Those effects can result in ionization of an atom, which in turn generates the diffusion of hundreds other of low-energy electrons causing further ionization and excitation events. These events can increase unit cell volume, increase movement within the crystal, and cause structural changes to change the protein conformation during the measurements. As the damage progresses, radiation damage affects the crystalline order, and the diffracting spots fade away. Worth mentioning, data collection at cryogenic temperatures as a significant accomplishment in X-ray crystallography improved dose tolerance by lowering the diffusion rate of the radical species formed within the crystal structure.

In macromolecular crystallography (MX), radiation damage can be split into two types: the global and the specific. The global damage accounts for the loss of the measured intensities during the course of the collection and, in some cases, can be seen by eye by comparing initial and final diffraction patterns. Another way to identify this issue is during the data processing, as the radiation damage to the crystal can be detected through a series of data processing parameters, such as Wilson B-factors, that are routinely analyzed by processing pipelines. Some of these parameters usually include the time scale changes: in the unit-cell volume due to expansion, in the consistency between equivalent reflection measures (R_{meas}) (DIEDERICHS, 2006), in space group likelihood throughout the collection, and also elevated mosaicity and isotropic B factor (KMETKO et al., 2006). Since beamlines have data integrated processing software, this type of damage can be ‘easily identified’, allowing the scientist to address the problem through new data collection strategies.

Figure 22. Prion protein crystals before (left) and after (right) data collection. X-ray damage to the crystal (brownish color – right) is visible

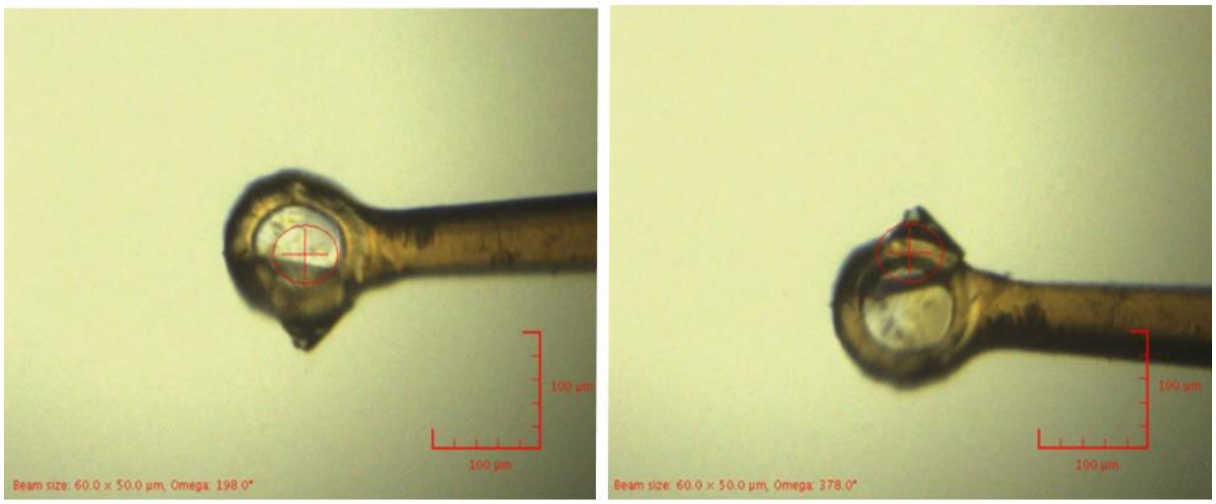

Source: own elaboration.

The specific damages are responsible for structural changes within the protein structure (HOLSTI, 1962). One of the significant difficulties related to specific effects of the radiation damage is that a refined structure is needed, making it a not trivial feature to monitor. Some of these changes can be seen in the electron density as blurry, diffuse, or absent densities, ultimately making it even uninterpretable or misleading. Some of the main symptoms felt in the structure are cleavage (AUGENSTEIN, 1958) of disulfide bridges, decarboxylation of glutamates and aspartates, removal of hydroxyl groups from tyrosine, and cleavage of carbon-sulfur in methionine. Heavy metals are also a concern because of their high absorption. This absorption results in the local heat of the crystal which facilitates the diffusion of radical molecules and inducing more damage. It is reasonable to say that the specific events have more impact from the structural point of view because they introduce structural changes that can mislead the apparent biological proprieties of the protein. Therefore, radiation damage must be managed to avoid compromising the biological information extracted from deduced structures.

We have optimized the data collection strategy to minimize the radiation damage. We could lower the dose by changing exposure time, oscillation angle, and reducing the number of images, taking advantage of the high symmetry order of our crystal. This enabled us to collect a lower number of images without compromising completeness (DAUTER, 2017). Initially, our strategy was set to collect 60°, and later on changed to 45°, just enough to achieve a full data set – all reflections within the AU

or symmetry equivalents have to be measured at least once – while also increasing the throughputness of data collection by making it faster.

Since data collection is done automatically, optimizing the data collection strategy was a must for our X-ray high-throughput fragment screening. After this accomplishment, we headed to our pre-screening and pre-fragment screening tests.

4.4 XChem

The complete characterization of our crystal system was a prerequisite to begin our fragment screening efforts. Our fragment screening campaign took place at the XChem facility in the Diamond Light Source and will be described in detail in the following sections. The screening workflow is sectioned into three main stages: solvent screening, pre-screening, and full screening.

4.4.1 Solvent Screening

The solvent screening was part of the initial training sections in XChem. Our goal was to establish a reproducible crystallization condition in a 96-well 3-drop plate and determine the best experimental setup for soaking experiments. The solvent screening is not only the first contact with the pipeline but also one of the most critical steps in the workflow and allowed us to evaluate cryo-protectant agents, determine what the optimal DMSO concentration (%) and incubation time that crystals can handle for fragment soaking, therefore minimizing losses in terms of diffraction power is. We also optimized the data collection strategy to avoid radiation damage induced by the cadmium ions in this step.

The *in-situ* crystallization of the prion protein was not straightforward as we expected. We have successfully miniaturized the crystallization experiments using the Mosquito ® crystallization robot to set the 96-well 3-drop Swissci crystallization plates after a deep optimization to suit the local conditions, such as temperature, drop, and reservoir volume was carried. The best condition was achieved by changing the protein:reservoir ratio to 125:25 nL while holding to the same crystallization condition. This was concluded after 50 crystallization trays, which represent more than 15840 crystal drops. The plates were set in a cold room to minimize the effects of drop evaporation. The drops were equilibrated against a 20 µL reservoir solution and stored at 20 ºC in the ROCK IMAGER 1000 (Formulatrix). The drops with the best crystals were chosen, and the coordinates for liquid dispensation by the ECHO were selected.

A total of 327 crystals were tested in the first two visits. Eighteen crystals were used to evaluate the need for cryo-protectant. Both glycerol (5, 20, and 40%) and ethylene glycol (5, 10, 20%) agents were tested as cryo-protectants with 1.5-hour soaking, from which we concluded that they were negatively impacting the diffraction power of our PrP crystals. None of the crystals soaked with ethylene glycol diffracted, while for glycerol, the mounting success rates were only 66, 33, and 0% for 5, 10, and 20% ethylene glycol. Since crystals without cryo-protectant had an almost 90% success rate, and our images were not affected by ice rings formation, we decided not to include this step.

The DMSO tolerance experiments were performed in two different ways, one with the simple addition of DMSO to the crystal drop and another with the addition of a few nano liters of reservoir solution to the crystal drop prior to soaking with DMSO. The goal of this experiment was to minimize the effects of the drop drying out, a constant issue that followed our assays throughout our journey. Increasing the drop volume by 33% by adding 50 nL of reservoir solution helps us harvest our crystals. However, it was not considered the ideal way out since it would add one step in the process, increasing time to perform the full screening, while also requiring a higher amount of fragment, thus increasing costs of the fragment screening.

We observed that our crystals were extremely sensitive to ethylene glycol and higher DMSO concentration and soaking times with this set of experiments. DMSO concentrations over 10% v/v solubilized the crystals, and soaking time over 2 hours negatively impacted the diffraction outcome. We concluded that a concentration of 5% DMSO for one hour without the addition of reservoir solution was the optimal condition for soaking our crystals. This system appeared to be more consistent, yielding a better average resolution and requiring one more minor step to execute the pipeline.

4.4.2 Pre-fragment Screening

After deciding 5% DMSO with 1-hour soaking was the best option, we headed to a pre-fragment screening test. In this test, our goal was to check our chosen parameters in a real situation: crystals were tested against a subset of 68 fragments of the DSi-Poised library (Enamine). The fragments used were selected randomly. The entire library contains 769 fragments, and one of the main features is that closely related compounds are commercially available, hastening future structure-activity relationship (SAR) studies.

The outcomes were assessed with maybe the most powerful software in the pipeline: the XCE (KROJER et al., 2017). Because the fragment screening generates an impressive amount of data, it is easy to lose track of the progress. The XCE is a software developed by the XChem group that combines the soaking information and integrates it to all steps that follow the data collection, helping the user to manage the high amount of data while also guiding you through all the steps until the structure deposition on PDB. These steps include assessing the diffraction results and auto processing pipelines while also allowing to reprocess with DIALS and XDS pipelines. A handy tool is the auto sorting of datasets with the highest score of resolution, completeness, and I/σI, which allows you to identify the best mtz files.

All the data collection and experimental settings are loaded in the 'Overview' sheet from your SoakDB SQL file. This enabled the rapid review of all experiment settings such as soaking time, compound ID, DMSO concentration, and diffraction outcome in terms of processing parameters such as resolution, CC(1/2), $R_{merge,}$ and completeness. Data processing statistics such as resolution, CC(1/2), Mn<I/sig(I)>, space group, and R_{meas}, and four crystals pictures are available in the next tab, 'Datasets'. This tab also allows to reprocess images manually. In this step, we have selected the best processing pipeline for our datasets and set the data collection outcome as 'success' or 'failed'. 'Failed' option contained additional comments such as 'low resolution', 'processing', 'no X-ray', 'unknown', 'no diffraction, 'centering failed', 'loop empty', 'loop broken'. These comments allow to run an experiment diagnostic and improve the following data collection.

Our pre-fragment screening used 68 crystal drops, each soaked with a different compound. Of them, 65 were successfully harvested and cryo-cooled. Data collection failed for eight samples, resulting in 56 fully collected data sets with an average resolution of 2.61 ± 0.32 Å (Figure 23). The datasets selected are analyzed with DIMPLE, which uses a reference model for molecular replacement, automated model refinement, and water addition. We have used our deposited model for PrP 6DU9 as input in this stage. A key feature in this step is that every dataset is linked to the compound ID and smiles code, so by selecting the datasets you want to move on with, you can generate CIF, PDB, and PNG files for all compounds. In the next step, we prepared to run PanDDA. We assessed DIMPLE results in terms of R_{work} and R_{free} and select/ignore any dataset.

When comparing the quality of the outcome of the solvent screening with the pre-fragment screening in terms of resolution, we were astonished by their difference. We had an average resolution of 2.87 Å (data not shown) for the first, and for the second, 2.61 Å (Figure 23). Since all the experiment setups were the same, we concluded that the difference relied on the crystals: although they belong to the same batch, the later had more time to grow and was visibly thicker. Due to limitations in terms of time, our crystals had a maximum of four days to grow for the first solvent screening assay, while for the pre-fragment screening, they had seven days. With so, we concluded that for the next visit – the full screening - larger crystals should be prioritized.

Before running PanDDA analysis, a PanDDA pre-run is necessary to calculate a mean map using all selected data sets. As noted in the PanDDA work (PEARCE et al., 2017), its usage relies on the fact that it might not be easy to pursue the structural changes that may occur upon ligand binding in macromolecular crystallography even the ligand itself, unless the signal is strong. Some of the critical difficulties in this process involve noisy data and weak signal – the last one resulting from either low occupancy or increased flexibility (or both). This problem is particularly accentuated in fragment screening, in which we expect the compounds to be low-affinity binders. PanDDA addresses this matter based on the assumption that the crystal structure is a superposition of all states. If not de-convoluted, a relevant part of the information is ‘lost’ or ‘ignored’. By subtracting a proportion of the ground-state map from your data set, PanDDA clarifies the electron density map for the changed state, thus extracting relevant signals from the background. This signal is called ‘residual partial difference map’, which is the same as ‘event map’. The software aligns multiple maps, divides them into grids, and calculates a Z-score for each. By comparing the Z-score of each grid against individual datasets, it can identify portions of that individual map that deviates from the ensemble of the datasets. Apart from highlighting these weak but significant density changes, PanDDA is particularly useful to eliminate ‘strong electron density blobs with no statistical significance’ from not modeled atoms.

For our PanDDA run, we selected a minimum resolution cut-off of 2.62 Å, from which we ended up with 36 datasets. Since PanDDA requires at least 40 datasets to correctly perform the statistical density analysis for building the mean map, we added ten datasets from our solvent screening. Our final set comprised 46 datasets with 2.46 ± 0.10 Å resolution range (Figure 23). This represented the last preparation step before

analyzing our pre-fragment screening with PanDDA. This selection is particularly important because PanDDA will work at the resolution shell in which there are at least 40 datasets. In our selection, 40 datasets are achieved at 2.57 Å; thus, the mean maps 'looked like' 2.57 Å map structures.

Figure 23. Left: Pre-fragment screening outcome: resolution distribution of the 56 collected datasets. Datasets in the red area (<2.6 Å) were excluded to avoid 'harming' our mean map; Right: PanDDA run of the pre-fragment screening datasets. The run was performed with 46 datasets 36 from the pre-screening plus 10 from the solvent screening

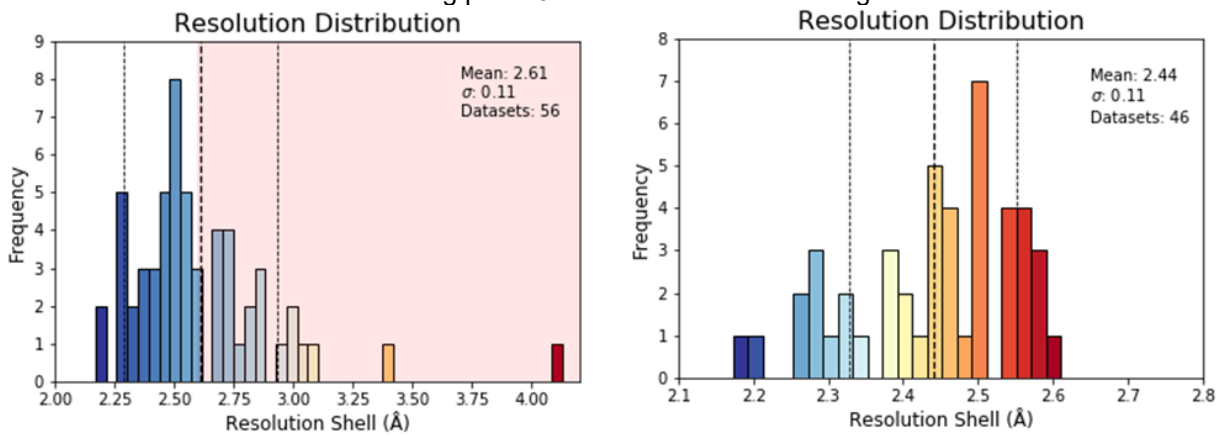

Source: own elaboration.

This map is imperative to build the ground-state model, which should be carefully modeled and refined. In this step, the main modification to the 6DU9 model was adding a few amino acid side chains. Our ground state model achieved a final R/R_{free} of 0.185/0.202 and used dataset number 237 with 2.26 Å resolution. The final ground-state model was then used for further DIMPLE run for model refinement against our selected data sets from the pre-fragment screening.

Our PanDDA analysis run returned 11 interesting events out of the 46 datasets. They are grouped into four sites: sites 1 and 2 contained 7 and 4 events, respectively, configuring a 'cluster'. Site 1 is located in a protein-protein interface, close to Cd303 binding site, while Site 2 is close to Asp167 and C-terminal. The event maps were manually reviewed in PanDDA inspect. The signal was compared against the ligand shape, and in some cases, DIMPLE maps were also loaded to aid ligand modeling. We carried on to the refinement stage with four possible hits.

After the refinement, all possible hits showed a week or absent density for the ligands. The weaker mode of binding and the flexibility and low occupancy poses are expected and a well-known issue in the fragment screening. Although they could be hits, the uncertainty of correct pose and the lack of electron density make them unreliable for the follow-up experiments.

4.4.3 The full fragment screening

For our full fragment screening, it was imperative to grow larger crystals. Our initial efforts were to modify our crystallization setup. Some options included lowering the precipitant concentration, changing protein concentration, or adding water diffusion modifying components to the crystallization solution. However, it was important to grow bigger crystals without modifying our crystallization to avoid generating possible conformational changes within the protein structure.

We were able to successfully optimize our crystallization protocol (Figure 24) to yield larger crystals. They were obtained reproducibly by increasing the drop volume from 150 nL to 400 nL and re-testing a broad range of protein to reservoir ratios and reservoir volume. The crystals achieved a desirable size using the same crystallization solution, but significantly increasing the proportion of protein to reservoir to 7:1 ratio, 15 μL of reservoir volume, and 4.5 mg/mL of protein at after 8 days. In some cases, crystals grew until the 13^{th} day of the experiment. The time-scale crystal growth is reported in Figure 25. Images were taken after 1, 2, 3, 5, 8, and 13 days.

Figure 24. HuPrP crystals optimization. The first two images represent the size of majority of the crystals in our initial visits. The third is optimized in our third visit

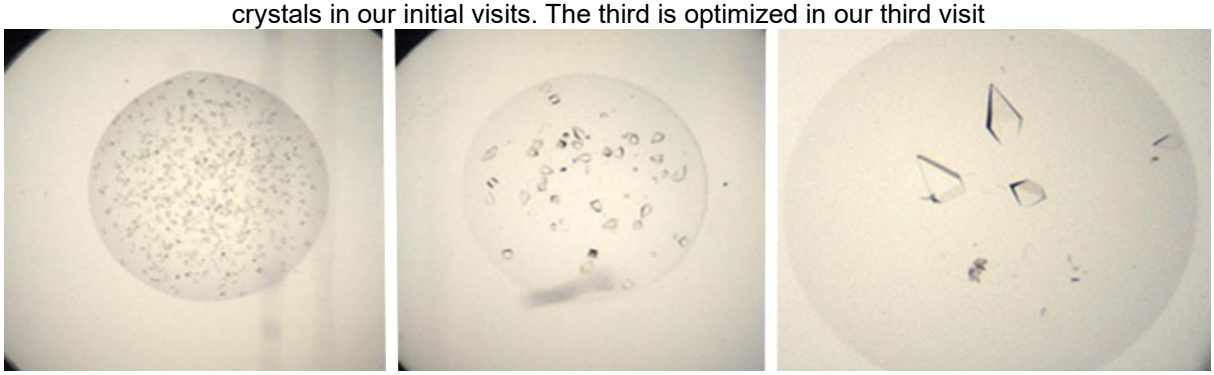

Source: own elaboration.

Figure 25. Time-scale crystal growth. From top left to bottom right, images were taken after 1, 2, 3, 5, 8 and 13 days

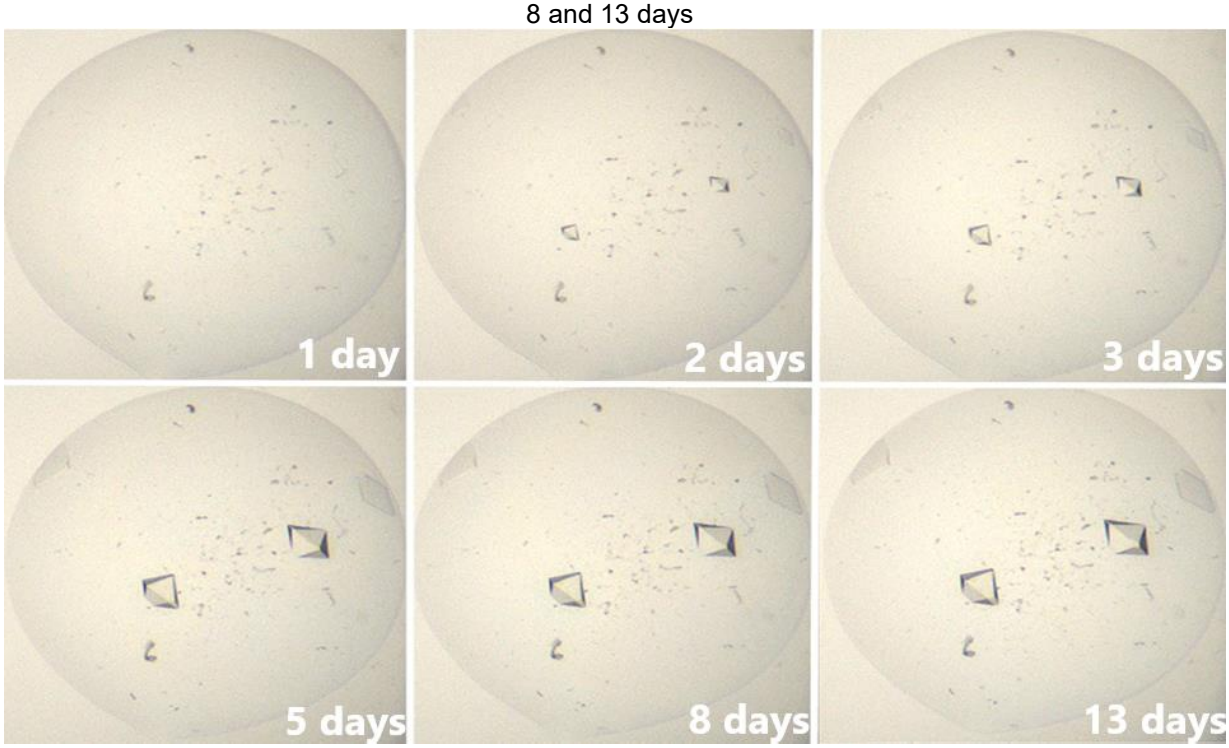

Source: own elaboration.

More than 25 crystallization trays were set, and about 800 crystals were used for the full screening. Because a new DSi-poised library with ethylene glycol (EG) as solvent became available, we decided to perform a new study to evaluate the stability of our crystals in the presence of EG. Thirty-two crystals were used for DMSO testing and 33 for EG. Again, our crystals showed to be extremely sensitive to EG, discarding this possibility. For the DMSO, we found that our larger crystals could withstand a greater concentration of DMSO, 10%, for 1 hour of soaking time and 2 hours for 5%. This larger time window for the 5% DMSO soaking was found very useful, enabling a longer exposure time of the crystals in the presence of the fragments and for facilitating our hands-on. Since our average mounting time was 13 minutes per puck, it enabled

us to soak and mount around 100 crystals in the same soaking batch, keeping the soaking time in the range of 50 minutes to 2 hours before starting the following one.

The fragment screening involved testing three libraries: the DSi-poised, the FragLite, and the MiniFrag. The libraries, number of fragments tested, and their final concentration in the drop are shown in Table 4.

Table 4 – Summary of the libraries used, number of fragments tested and final fragment concentration after soaking are shown

Library	Fragments Tested	Fragment Concentration
DSi-poised (5% DMSO)	417	25 mM
FragLite (10% DMSO	31	10 mM
FragLite (5% DMSO) (2x)	62	5 mM
MiniFrag (DipSoak)	78	1 M

Source: own elaboration.

Their main library, the DSi-poised, containing 500 mM stock fragments, was tested once for 417 fragments, totalizing 482 tested. The FragLite library, at 100 mM in DMSO, was tested three times: once with 10% DMSO and twice with 5% DMSO. The FragLite was screened more times because it is under development. The MiniFrag is another in-development library that was tested using quick dip-soaking for 1-5 s. In this case, the fragments were provided in powder and were manually weighted and solubilized in water at 2.5 M concentration. Each fragment was then mixed in a ratio of 4:6 with 4 M NaCl, 160 mM Tris pH 7.6 in a crystallization plate; therefore, we were able to achieve a 1 M final fragment concentration in our crystallization condition because of the high solubility of the fragments. 32 crystals were used to test if the dip-soaking method was harmful to our crystals, and no problems were observed. In the dip-soak procedure, you harvest the crystals and quick soak them into a new drop that contains the fragment into your crystallization solution. Out of the 81 fragments in the library, three were incompatible with our crystallization solution and were not used.

All the crystals were submitted to X-ray diffraction in the I04-1 beamline: a total of 513 datasets were successfully collected. The larger crystals and the student practice in handling all the steps in the pipeline yield a better outcome, with an average resolution of 2.58 ± 0.26 Å (Figure 26_B), and yielded the highest resolution for the prion protein in our work, 1.84 Å.

To generate a new, better mean map, we excluded the datasets with R_{free} above 0.26 and resolution lower than 3 Å for the PanDDA Analysis calculation. The mean map for density analysis was generated at 2.37 Å. The software chose the dataset

HuPrP-x0382 as the mean model (R_{free}= 0.257 and 2.12 Å resolution). No datasets were excluded by the analysis using the RMSD threshold of 1.5 Å: all 512 datasets analyzed with PanDDA aligned with the dataset HuPrP-x0382 with an average dispersion of RMSD of 0.16 ± 0.03 Å (Figure 26_C) and R_{free} distribution of 0.23 ± 0.03 (Figure 26_D). The default run ignored the datasets with R_{free} above 0.4, so two data sets were excluded. The program identified 206 events (Figure 26_A), spread to all the protein surfaces but grouped into 5 clusters. All the events were manually inspected, from which nine interesting fragments were exported to the refinement step (Table 5).

Figure 26. Fragment screening outcome

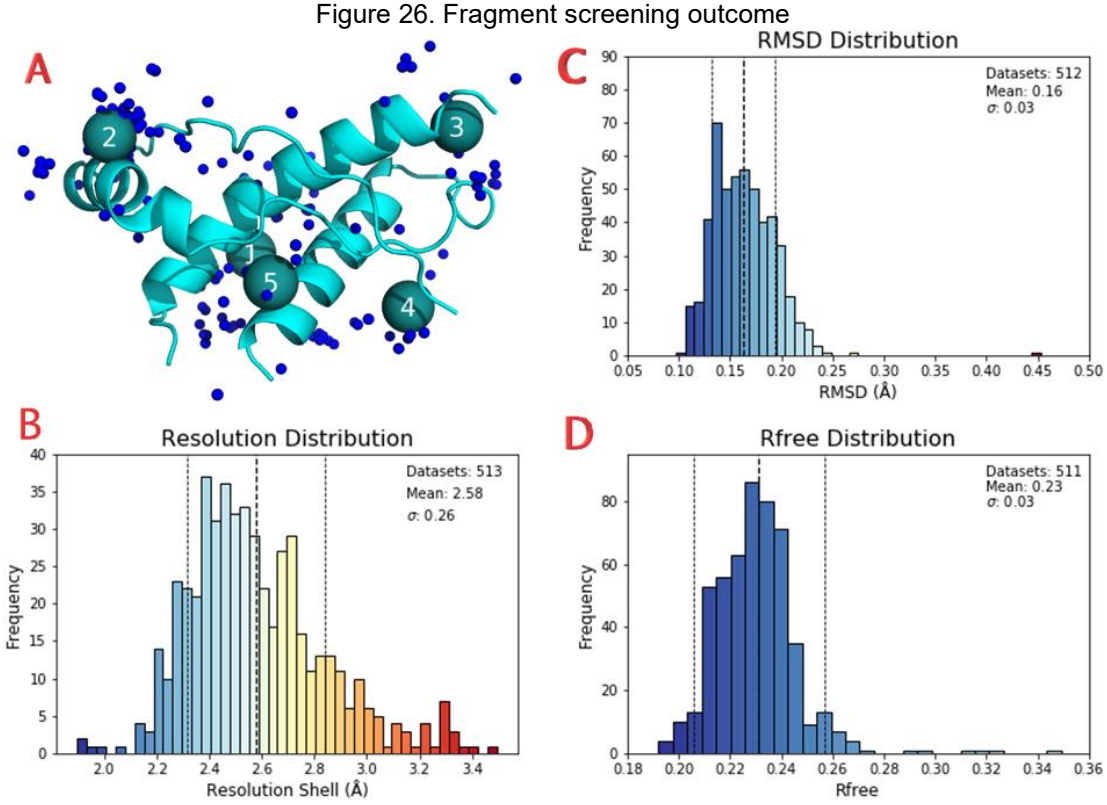

Graphic caption
A: Event distribution through the protein.
B: Resolution, RMSD and Rfree distribution of our processed datasets
C: Resolution, RMSD and Rfree distribution of our processed datasets
D: Resolution, RMSD and Rfree distribution of our processed datasets
Source: own elaboration.

Table 5 – List of datasets with promising events taken to the refinements step

Crystal ID	Compound	Library
HPrP-x0305 HPrP-x0335	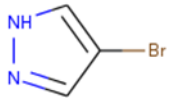	FragLite
HPrP-x0309 HPrP-x0369	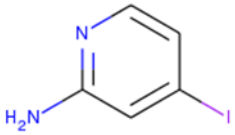	FragLite
HPrP-x0611	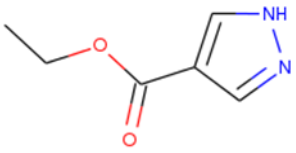	DSi-poised
HPrP-x0655	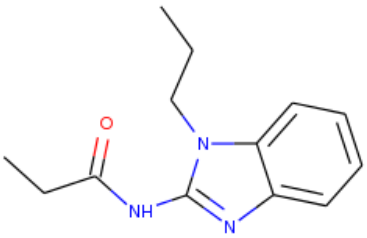	DSi-poised
HPrP-x0723	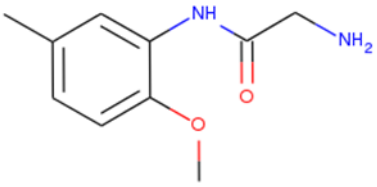	DSi-poised
HPrP-x0728	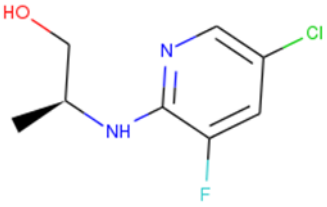	DSi-poised
HPrP-x0733	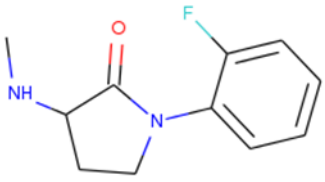	DSi-poised

Source: own elaboration.

The datasets were inspected multiple times to avoid losing any fragment hits. Their dimple maps were individually checked for difference peaks above three rmsd, and we also ran the pandda.analysis twice, one by generating another mean map with the same 100 best datasets and another one by reducing the grid spacing fin the PanDDA Analysis from 0.5 to 0.3 Å. No significant changes were observed, and no further hits were identified. Of all interesting fragments, only those from datasets HPrP-x0723, HPrP-x0611, and HPrP-x0305 responded well to refinement (Figure 27), but because fragment HPrP-x0723 bound in the interface of a dimer stabilized by Cd^{2+} coordination, we chose to discard it. After exporting to the refinement stage, fragments from datasets HPrP-x0728 and HPrP-x0733 misbehaved and were totally displaced after the refinement run, a clear indication of overfitting. Different refinement strategies were employed, like lowering its occupancy or fix its positions, but the resulting electron density was always incompatible. Even if we believe that such molecules could be potentially low-affinity binders, we had to make the decision to discard them to avoid follow-up experiments based on a bad chemical matter.

The fragment from dataset number HPrP-x0611, ethyl 4-pyrazolecarboxylate, showed very clear electron density, and its mode of interaction of PrPC could be precisely described (Figure 28). It explores a shallow hydrophobic region formed by Ile184 and Val203 and induced a conformational change in the Lys185 sidechain, which closes on top of the fragment and exposes an unprecedented cavity (Figure 29), and the pyrazole ring binds to the acidic side chain of Glu207. Although the fragment has a clear 2Fo-Fc signal, the conformational change observed for the Lys185 could only be spotted in the PanDDA event map.

Figure 27. Fragments fitted into their event map. Fragments from datasets number

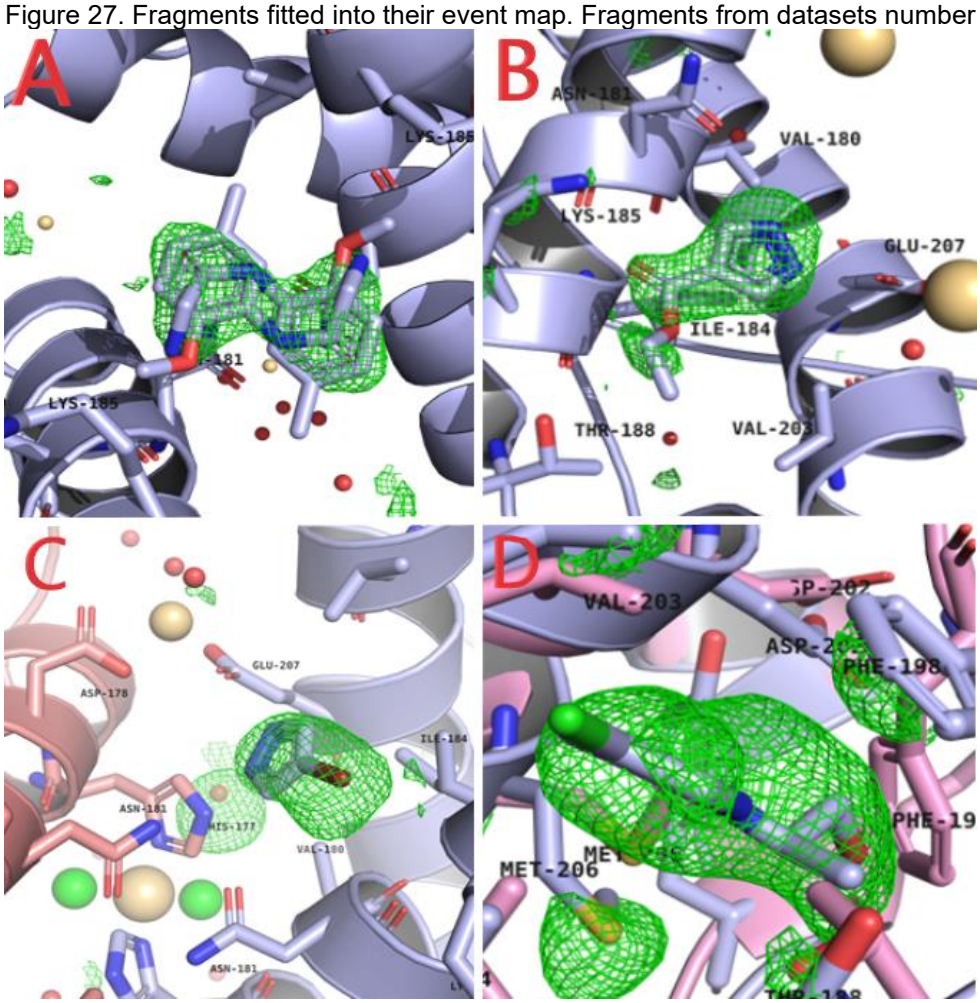

Figure caption
A: HPrP-x0723
B: HPrP-x0611
C: HPrP-x0305
D: HPrP-x0728
Source: own elaboration.

Figure 28. Binding mode of the fragment in dataset HPrP-x0611. Image adapted from LigPlot

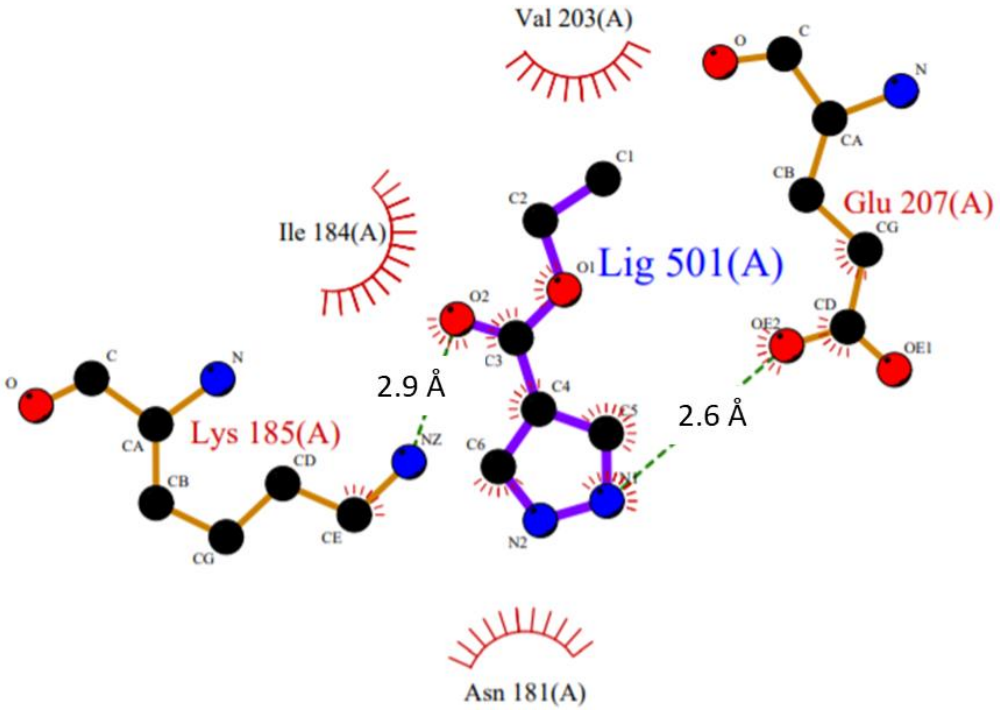

Source: own elaboration.

The design of larger ligands based on the identified fragment could explore even more the hydrophobic patch. This fragment connects the last residues of helix 2 with the beginning of helix 3 of the prion protein, and represents an attractive spot for drug design. This region has already been shown to have high intrinsic flexibility and play a role in disulfide reshuffling and domain swapping (TOMPA et al., 2002). In previous studies, domain swapping was shown to be of great importance in prion protein conversion(HAFNER-BRATKOVIČ et al., 2011). In addition, the loop connecting these two helices has diffused electron density in our structure (dashed line in the structure). We hypothesize a ligand exploring this region may induce structural stabilization of the protein, which could be explored as a lead compound for the design of anti-prion therapeutics.

We were very excited to see that both fragments identified as hits, in HPrP-x0611 and HPrP-x0305, share the same pyrazole ring motif and bind precisely in the same position in PrP structure (Figure 30). Indeed, fragments are usually low-affinity binders; therefore, further experiments are necessary to demonstrate pharmacological evidence, but we believe that these finding increases the relevance of the identified binding fragments and suggests this is a chemical binding motif for this region. To our knowledge, these are the first binder with reported mechanism of interaction with PrP

to be reported. Moreover, previous efforts to identify hot and warm spots in PrP structure identified a small hydrophobic close to where the fragment binds(KUWATA et al., 2007), on the other side of helix 3 (Figure 31), and to which anti-prion compounds, such as GN8, are known to interact(CONCEIÇÃO et al., 2019; YAMAGUCHI et al., 2019), thus suggesting that the fragment bind to an important region in the PrP structure. The GN8 anti-prion activity is attributed to a chaperone-like interaction, increasing the PrP stability and the proximity between GN8 and 4-pyrazolecarboxylate could be explored in merging approaches by linking through the loop 2.

Figure 29. Superposition) of 6DU9 (left) and dataset HPrP-x0864 (right). The red arrow highlights the structural chances induces by a simple movement of Lys185 and that “traps” the fragment in a shallow cavity

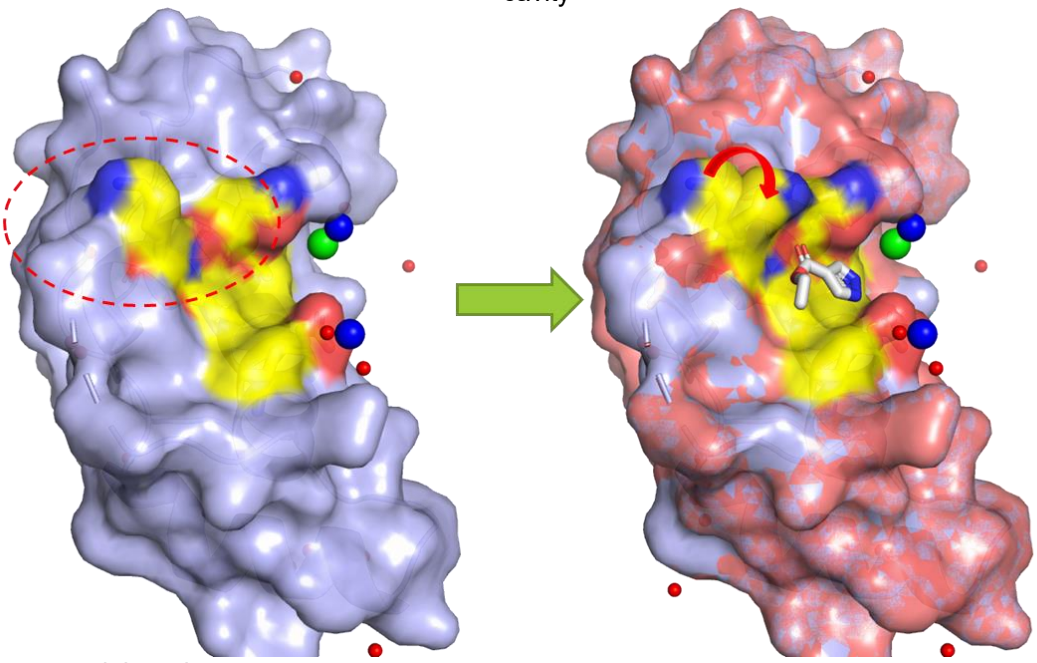

Source: own elaboration.

Figure 30. Cartoon representation of datasets HPrP-x0611 and HPrP-x0305. Structures are superposed and the pyrazole group of both fragments superposes perfectly

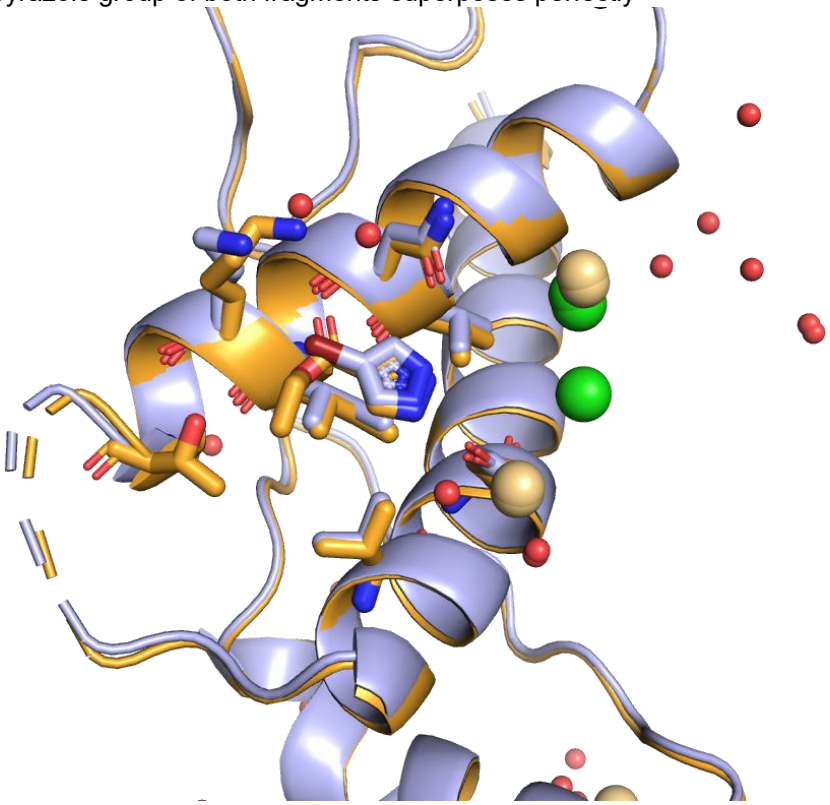

Source: own elaboration.

Figure 31. Proximity of the 4-pyrazolecarboxylate binding region to hydrophobic pocket where anti-prion compounds bind. Fragment site is depicted in blue and hydrophobic pocket in green.

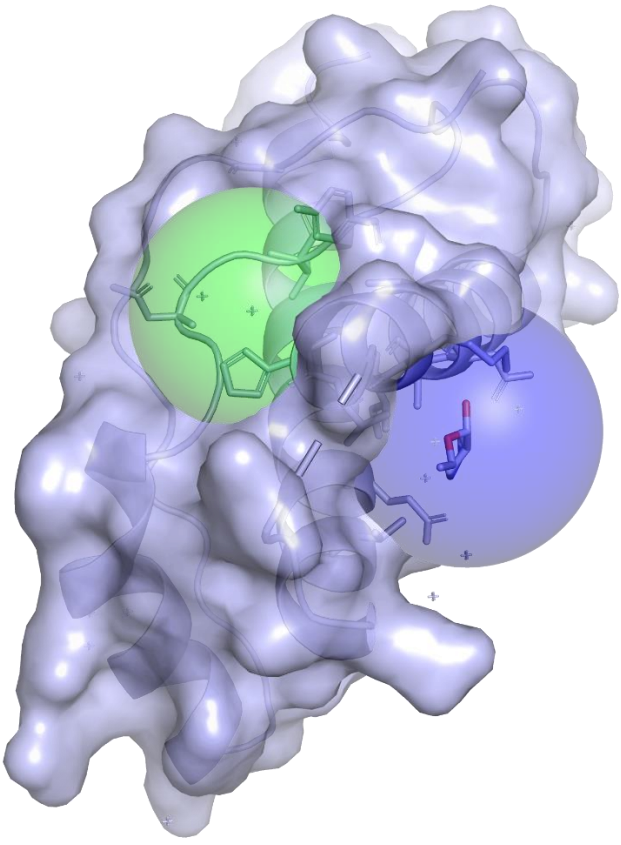

Source: own elaboration.

After analyzing our screening results, we decided to test all compounds flagged as interesting but were discarded in the refinement stage, including the fragment from dataset HPrP-x0611. These fragments were tested in triplicates at 5 and 10% of DMSO. Our new screening showed that none of the previously rejected fragments were confirmed as a hit. To our excitement, the ethyl 4-pyrazolecarboxylate bound again, in the same place and same pose. The dataset HPrP-x0864 diffracted to a lower resolution (2.22 vs 2.11 Å), however the electron density for the ligand looked sharper in the new dataset (Figure 32).

Figure 32. Surface representation of HPrP-x0864 structure. 2Fo-Fc signal for the fragment contoured at 1.0 σ. Cd2+and Cl- ions represented as wheat and green spheres

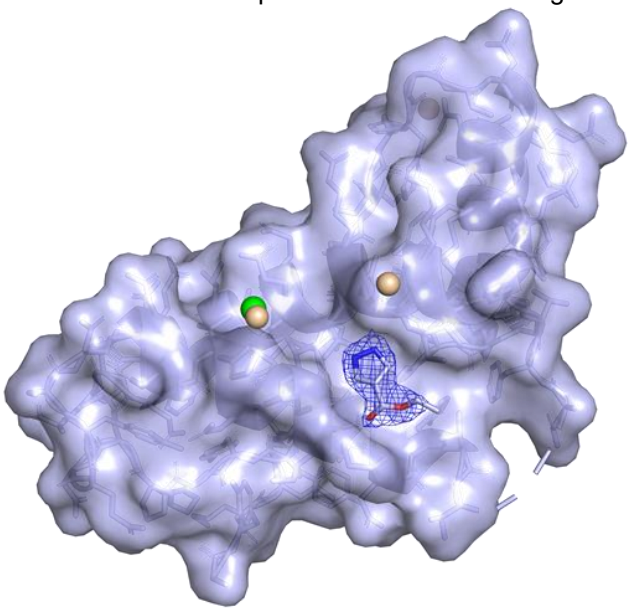

Source: own elaboration.

Despite having found the first ligand for the prion protein, we were somewhat disappointed with the outcome of our fragment screening. On average, XChem campaigns have around 4 to 8% of hit rate (not published), depending on how challenging the target is and intrinsic characteristics of the crystal system. Our campaign had a roughly 0.4% of hit rate with only two hits – way below the average – which highlights why the prion protein is considered a target not able to be modulated by small molecules.

We also believed that we could have had more hits with a different crystal system. First, the cadmium ions induce radiation damage to our sample, reducing the quality of our datasets, creating abnormal density around the region, which misleads the PanDDA analysis. In addition to that, the cadmium sites represent potential binding

sites that cannot be explored in our screenings. As we discovered, cadmium is essential to maintain the crystal packing, so removing it was not an option as it would disrupt the crystals. Second, our resolution was in the lower edge for fragment screening, making it more complicated and trickier to identify hits. Third, our crystal system was too sensitive to DMSO, resisting to 5-10% DMSO for approximately 1 hour. Finally, our crystallization condition contains a huge amount of salt, 2.5 M of sodium chloride, which precipitates some of the compounds, reducing the actual concentration of fragment being soaked while also competing for the binding sides. Some of these features are discussed in further detail in the following sections.

4.4.4 Structural analysis

Our fragment screening generated an unprecedented amount of crystallography data for the prion protein. We tried to get the maximum out of it by exploring conformational changes within the protein crystal. The prion protein is the key role player in the prion disease, and the conversion process to PrP^{Sc}, considered the critical event, is surrounded by elusiveness. Despite the actual structure of PrP^{Sc} being still unknown, the PrP^{C} certainly suffers a profound structural change, marked by changes in the prion physicochemical properties, such as protein solubility and stability. Therefore, we expect the PrP^{C} itself to have some plasticity. Plastic regions within the globular domain could be associated with features of the prion protein such as function, disease, or even drug development.

To identify potential plastic regions, we calculated the RSCC of the main chain residues of all the collected datasets in the XChem. Since the RSCC measures how the electron density map for the calculated model correlates with the electron density map for the model from the experimental data, we believed that residues with a significant deviation of RSCC value would indicate structural changes in the protein model. We also supposed that the automated refinement ran by REFMAC5 in the DIMPLE pipeline would not correct meaningful structural changes. However, since we did not know how sensitive this parameter was, we established a cutoff for defining ‘outlier’ residues as three times the standard deviation for that residue. We also set a low-resolution cutoff of 2.5 Å to avoid the inclusion of problematic datasets in the analysis while also excluding datasets for which the low resolution would not provide enough information to correctly position the atoms in case any structural change was identified. With that, 278 datasets were analyzed.

We identified 214 residues across 71 structures that contained main chain outlier residues (Figure 33). Most of the outliers were concentrated in regions N- and C-terminal, close to the flexible loop around residue 190 or close to cadmium sites. All the 214 outlier residues were visually investigated using Coot. To our surprise, none of the outlier residues could be correlated with meaningful electron density that could support structural changes within the protein. Thus, we concluded that the RSCC was not sensitive enough to identify structural changes in our datasets, or the globular domain of PrP is highly rigid, and it is legit that no significant structural changes are present in the datasets. It is important to add that the rigidity observed in our structures could also be driven by the crystal packing in our crystal system.

Figure 33. Distribution of the real-space correlation coefficient for the main chain residues in each dataset. Error bars correspond to three times the standard deviation for that particular residue

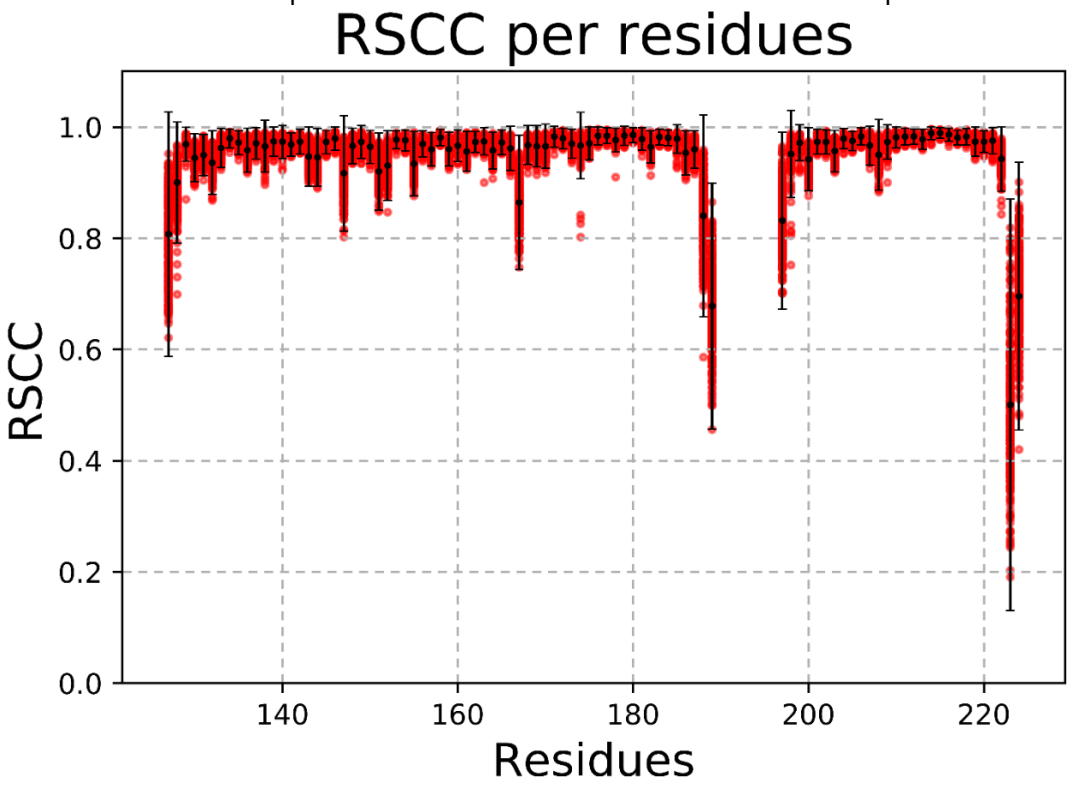

Source: own elaboration.

4.5 In house fragment screening

During this work, we have collected over 100 datasets at Proxima 1 and Proxima 2 beamlines at the Soleil synchrotron in France. The crystals used in the *in-house*

fragment screening were grown in 24-well sitting drop plates, cryo-cooled, and shipped to the beamline.

Our screening was mostly directed to test new potential ligands similar to the fragment Prof Nonato has identified at the Broad Institute (Figure 34_A) and ligands identified by our collaborators using transverse relaxation optimized spectroscopy (TROSY).

Figure 34. ‘B9’ fragment and analogs tested in our in-house screening

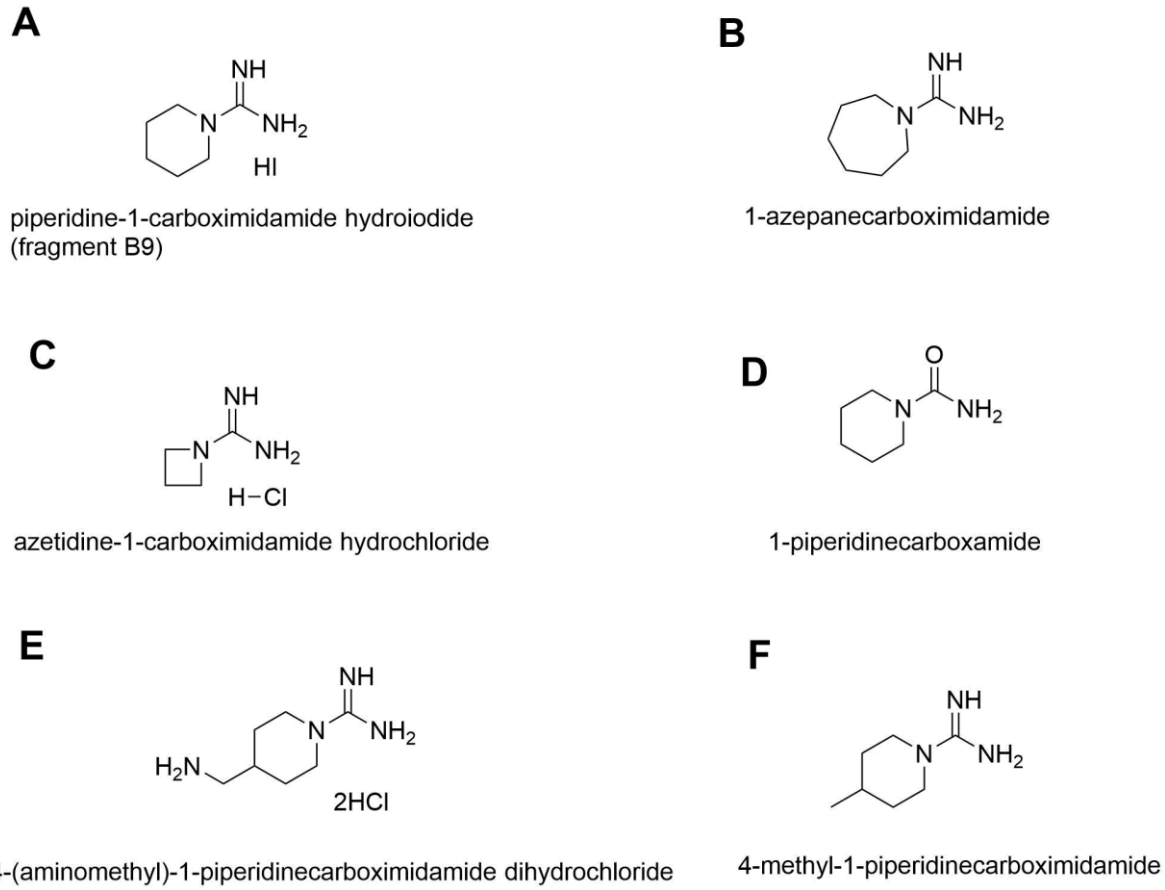

Source: personal file.

Although we could reproduce the electron density for the fragment ‘B9’ (Figure 33), we were unable to correctly model the ligand into it because of the round shape of the density. The B9 fragment binds to a region close to His187, on the opposite side of helix 2, where the ethyl 4-pyrazolecarboxylate binds. We attribute this difficulty to the low occupancy together with some mobility. We were also able to identify some electron density for analogs B, E, and F (Figure 34). However, the same problems arose. These fragments were tested at 10 mM by our collaborators at the Broad

Institute using TROSY, and because no convincing binding was identified, they were no further pursued.

In addition, 19 compounds from Broad institute Fragment Library and 30 benzimidazole derivatives (some depicted in Figure 35) were identified as potential binders to PrP in their screening fragment screening using NMR. These fragments were provided and tested using soaking. The structures were solved with DIMPLE, and after refinement and manual investigation of the datasets, no electron density compatible with compounds was identified. Therefore, we concluded that none of the tested fragments were bound to PrP under the tested conditions.

Figure 35. Some of the promising benzimidazole compounds identified by our collaborators in the Broad Institute and further tested in our in-house fragment screening

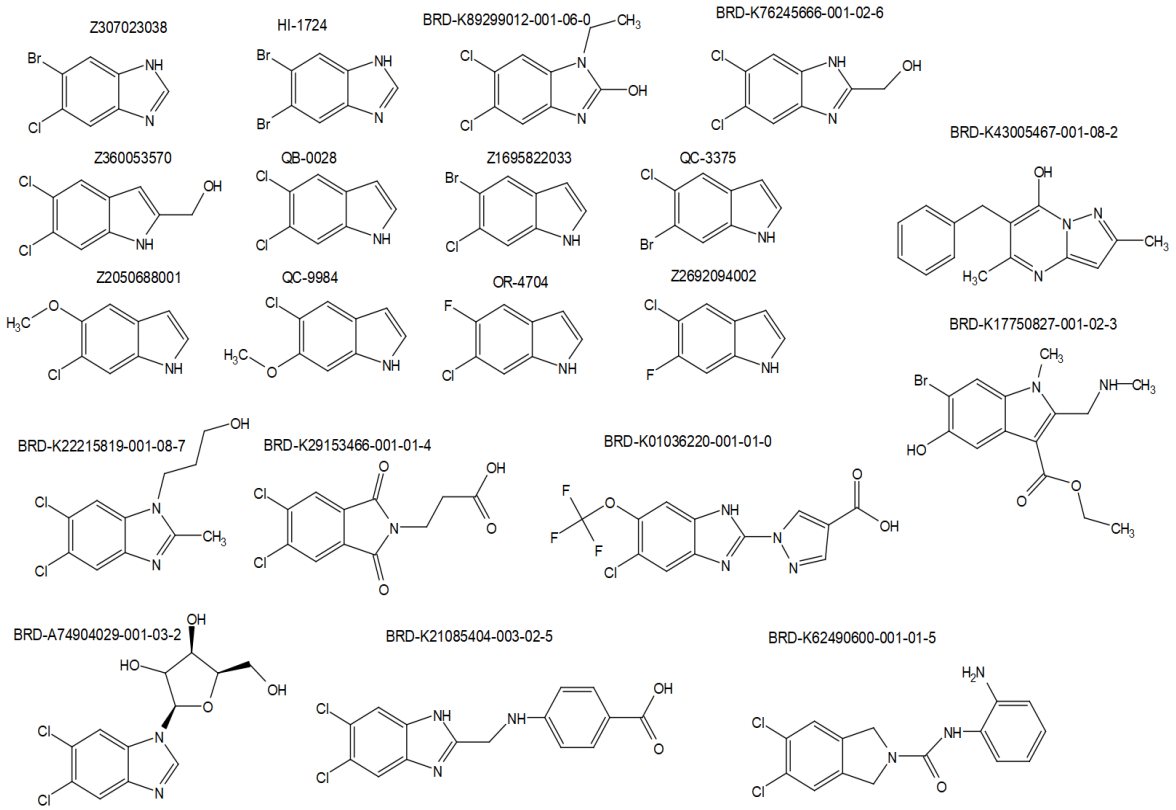

Source: personal file.

4.6 The quest for a new crystal form and new fragment screenings

Until this point of the project, we had successfully established a reproducible protocol for in-house protein production, characterized our crystal system, optimized our crystallization to yield reproducible crystals, and performed an extensive X-ray fragment screening against our protein target. Combined, our XChem campaign and our in-house fragment screening, we have screened more than 600 fragments, and almost 1000 datasets were collected in Diamond and Soleil synchrotrons for this purpose. This considerable effort represents a very collaborative work between our collaborators and us.

We found two small fragments that may bind to a promising region within the prion protein throughout our screening attempts, and these fragments shared a pyrazole ring. Although we had hits, the general feeling was that we could have had more. Moreover, more chemical matter would be required to support pretended efforts in computational and medicinal chemistry.

Our collaborators shared the struggle to find prion protein binders at the Broad Institute. Over the course of our project, we were part of the beautiful work with them, to which we contributed with our in-house fragment screening. They screened over 300,000 fragments combining multiple biophysics techniques, with no obvious hit (REIDENBACH et al., 2020). Their screening showcases how difficult it is to target the prion protein and helps to explain the low hit rate of our X-ray fragment screening. However, we believe that factors not related to the target itself may have contributed to this outcome, such as i) the high salt concentration in our crystallization assays ii) the cadmium iii) our crystal system. With that in mind, we performed a research in the protein data bank to help us understand in further detail our pitfalls.

By querying the pdb for structures related to fragment screening at XChem (QUERY: (Full Text = "pandda" AND (Structure Title NOT CONTAIN SPHRASE "ground" AND Structure Title NOT CONTAINS PHRASE "no ligand modeled")) AND Experimental Method = "X-RAY DIFFRACTION") we observe that 1289 out of 1441 of the structures deposited are PEG-based conditions (Table 6).

To understand why salt-based conditions are deprecated, we need to take into consideration several factors that go from hands-on difficulties to fragment libraries and fragment binding. On the hands-on, one of the difficulties encountered throughout our XChem campaign was the drop drying out fast – and the high salt concentration

contributes to crystal dehydration and heavy precipitation. On the fragment library, fragments usually bind with low affinity to the protein. A turnaround is the use of high concentration fragment libraries (usually between 100-500 mM), solubilized mainly in 100% DMSO. However, the actual amount of the fragments soaked into the crystal drop will be less than the calculated since it will depend on its solubility in the crystallization condition, which is heavily reduced in conditions like ours (2.5 M NaCl). Lastly, salts in high concentration can compete with fragments for binding spots or induce a hydrophobic patch within the protein to become more promiscuous.

Table 6 – Query of the Protein Data Bank reveals that PEG-based conditions are preferred over states based on (in)organic salts (92.80% vs. 5.90%) considering structures with fragments

Crystallization condition	Number of entries
PEG-based	1289 (92.80%)
(In)organic salts	82 (5.90%)
Not specified	18 (1.30%)

Source: own elaboration.

The impact of cadmium is related to the radiation damage, which was previously discussed (Handling cadmium-induced radiation damage) and the fact that they occupy reactive regions of the protein. Because we cannot soak them out of the protein, these potentially interesting regions are unavailable for screening. The only way out is a structure with a different crystal packing.

Finally, by comparing our deposited structure 6DU9 with the structures using the same query, we observe that our system is in a good range of parameters such as pH, Rfactors, and solvent content but is on the lower edge of resolution (Figure 36).

Figure 36. Resolution, Rfactors, pH and solvent content distribution of deposited PDB structures in our query. Our deposited structure 6du9 is in a good range of pH, solvent content and Rfactors, but in the lower edge of resolution

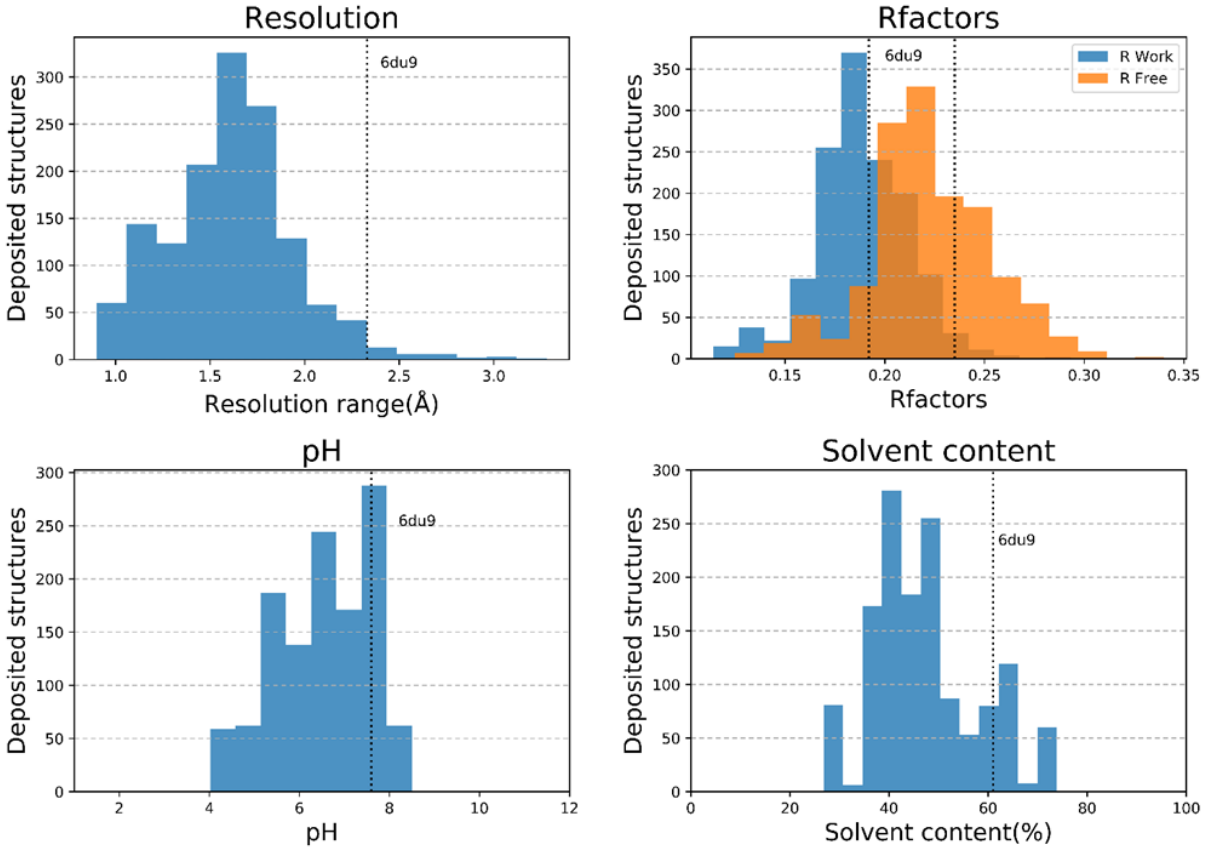

Source: own elaboration.

With this information in hand, we concluded that the low resolution, the cadmium, and the high amount of salt could have played a negative role in our screening. With that in mind, we decided to perform a new screening. Three different approaches were pursued: i) identify a new crystal form for the prion protein, ii) reproduce an existing crystallization condition iii) exchange the salt in our existing crystallization condition for PEG.

The three approaches were pursued simultaneously. The quest for a new crystal form involved screening multiple crystallization conditions and several rounds of optimization of promising conditions.

Our initial screening for a new crystal form made use of the state-of-the-art infrastructure available at the Structural Genomics Consortium at the Oxford University. The screening comprised 30 crystal trays, representing over 8000 unique crystallization conditions tested, followed by eight trays of optimization. These attempts to produce a new crystal form from scratch were unsuccessful. Attempts to reproduce existing PDB 3hak and 1i4m crystallization conditions were also made and were also

unsuccessful. Our most considerable effort attempted to reproduce the reported structure for PDB 4n9o. In this structure, the same HuPrP fragment 90-231 is crystallized in the presence of a nanobody. The nanobody interacts with the prion through a discontinuous epitope, as shown in Figure 37. Regarding our fragment screening intentions, this structure has interesting sites around K185 and H187, where previous hits were identified, solvent-exposed, benefits from being high resolution (1.5 Å), and PEG-based condition (15% PEG 20000). Moreover, the Nb484 stabilizes the N-terminal portion of the HuPrP 90-231, driving the formation of an additional β-strand. The presence of electron density for additional residues (from 118) enabled the fragment screening to target the palindromic region of the prion protein, which was pointed as necessary to the formation of the scrapie prion, and for which pathogenic mutations like G113 and A11V have been reported (BIASINI et al., 2010; COLEMAN et al., 2014; NORSTROM; MASTRIANNI, 2005; SABAREESAN; UDGAONKAR, 2016).

Figure 37. Representation of HPrP bound to a nanobody in the 4n90 structure. Nb484 (orange) interacts with HPrP-90-231 through residues in the N-terminal, α2-α3 loop, and α3

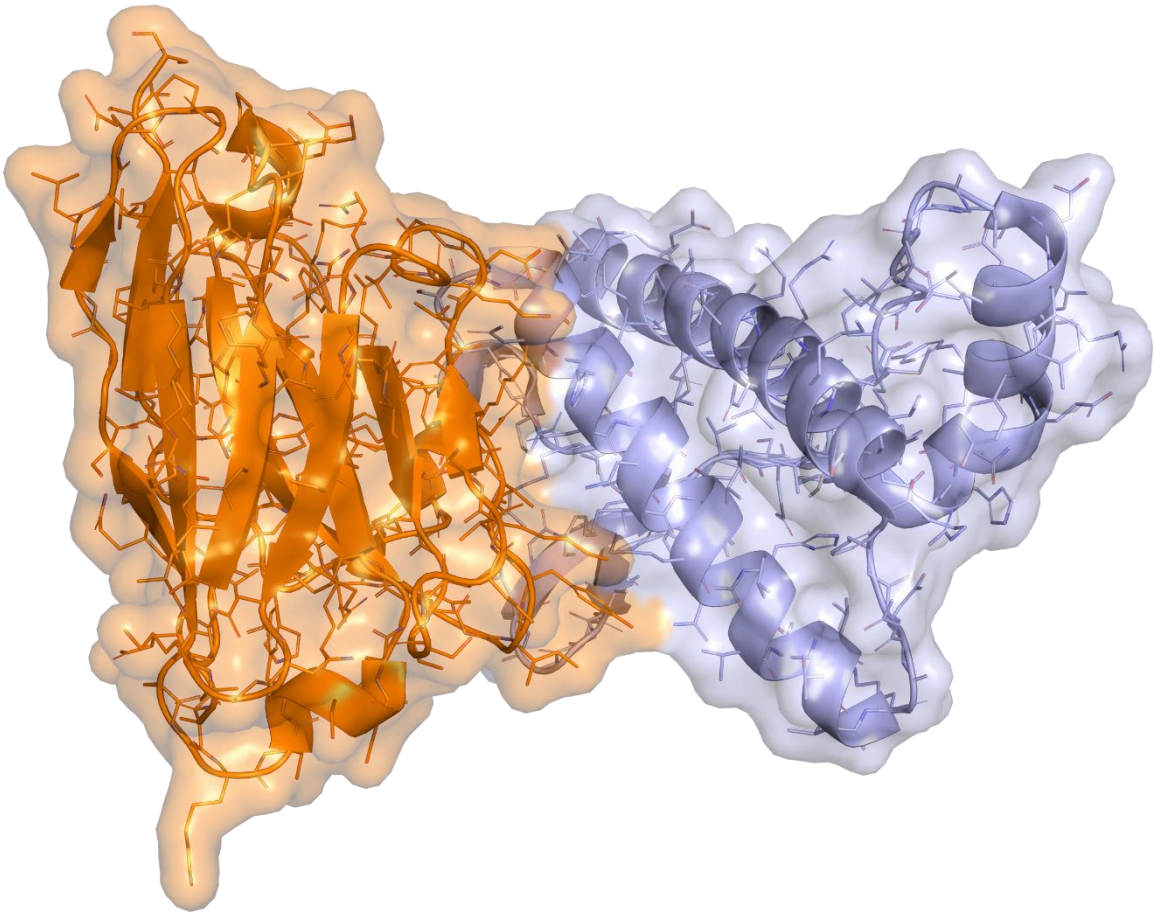

Source: own elaboration.

The nanobody sequence was purchased (Twist Bioscience), and the expression and purification protocols were adapted from the reported in the literature (ABSKHARON et al., 2010, 2014). The main difference between the vector used for our experiments, pNIC-CTHO, and the reported in the literature, pHEN6, is the latter contains the PelB leader sequence preceding the protein sequence. The PelB sequence directs the expressed protein to the periplasm of gram-negative bacteria such as *E. coli*, where protein folding and disulfide bond formation are enhanced by chaperones such as Dbs (disulfide bond formation) family proteins. The construct was designed to include the PelB sequence as an attempt to mimic the reported literature vector (CHOI; LEE, 2004) because Nb484 contains an internal disulfide bond (Cys22-Cys96). The protein was successfully expressed using autoinduction in *E. coli* and purified with affinity column using increasing amounts of imidazole instead of pH variations. Our protein production yielded around 10 mg of soluble protein, with high purity, per liter of cell culture (Figure 38).

Figure 38. SDS-page gel of Nb484 purification steps. Elution from PD10 (well 6) shows a band close to 15 kDa and corresponds to the Nb484

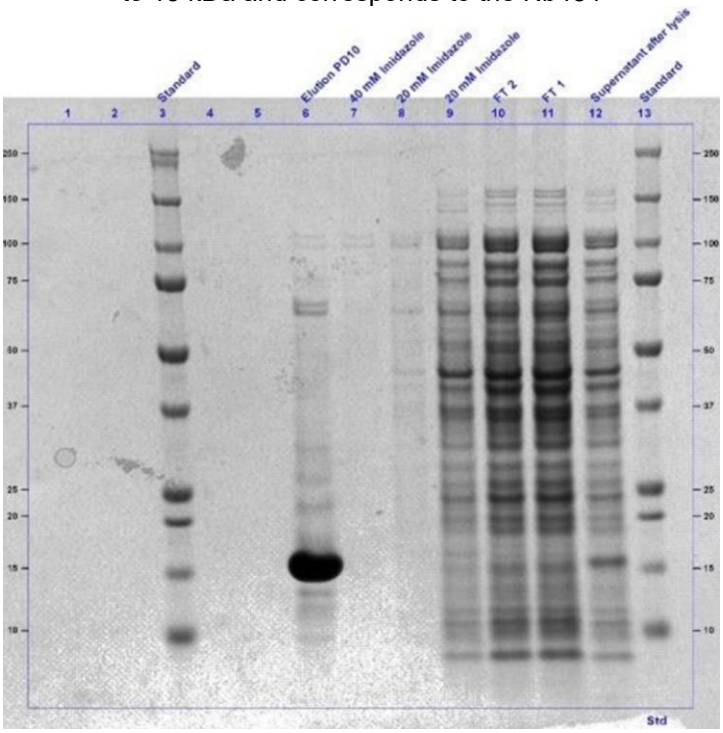

Source: personal file.

We were concerned that the introduction of changes in the expression and purification could affect the protein stability and folding. The correct folding of the nanobody was key for our crystallization experiments since it could affect epitope recognition and binding to the prion protein. After this first step of purification, the sample was analyzed with native and naturing MS. This revealed the Nb484 was folded in solution and had the expected MW (Figure 39). In the next step, the incubation of Nb484 with HuPrP 90-231 allowed the complex formation in solution, which was also verified by native MS, in which the observed mass peaks of 30,500 Da and 30,369 Da match the expected theoretical values for complex intact mass (30,505 Da) and the loss of the methionine initiator (30,374 Da) (Figure 40).

Figure 39. Deconvoluted native(below) and denaturing (top) mass spectrum confirms Nb484 in solution, with compatible MW of 14,226 Da (predicted: 14227,73 Da). Native mass spectrometry suggest native Nb484 binds to HEPES molecule in solution (Δmass of +238 Da)

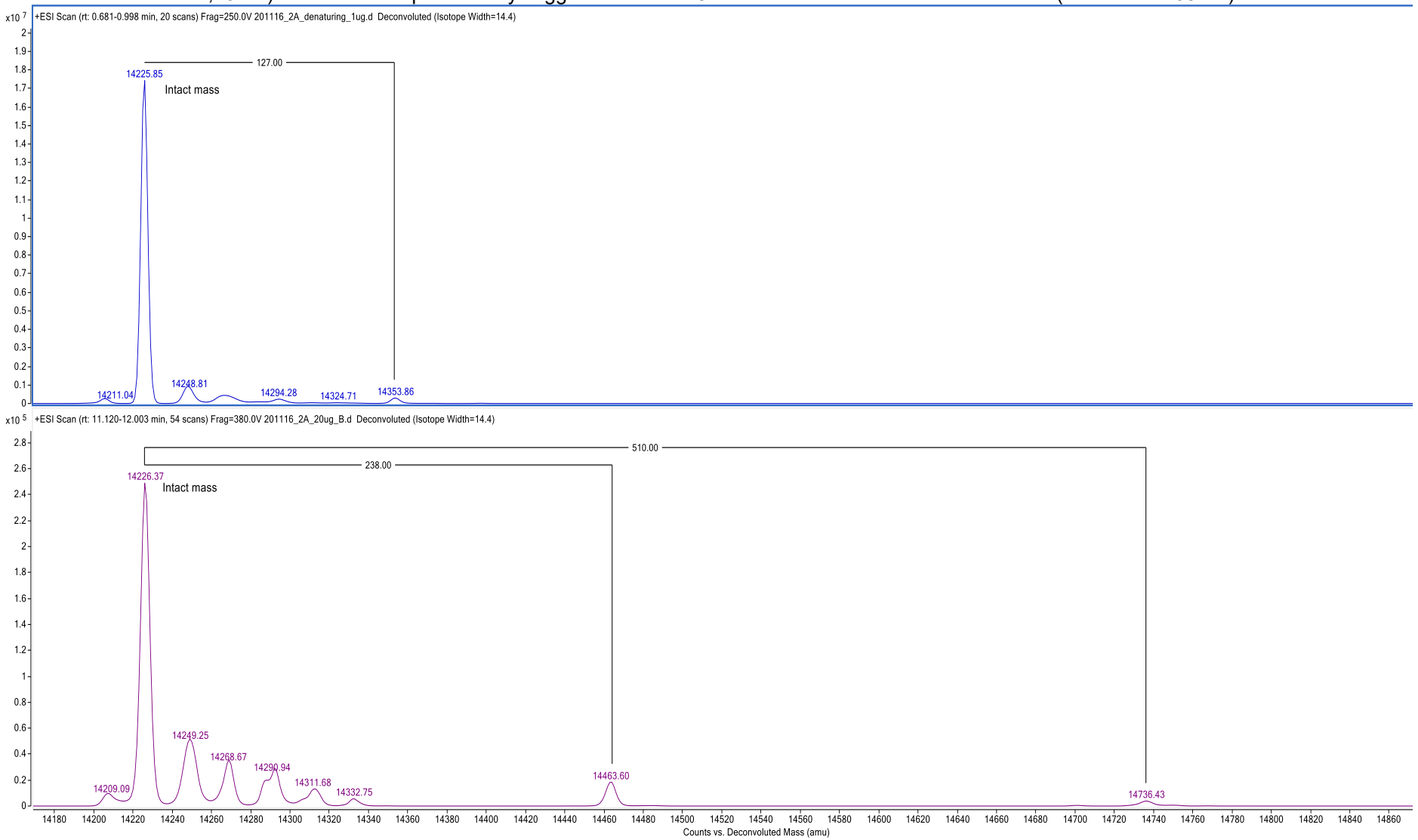

Source: own elaboration.

Figure 40. Confirmation of PrP-Nb484 complex in solution. After incubation of HuPrP 90-231 with Nb484, native mass spectrometry confirmed the native complex was being formed in solution. Observed mass peaks of 30,500 Da and 30,369 Da match the expected theoretical values for complex intact mass (30,505 Da)

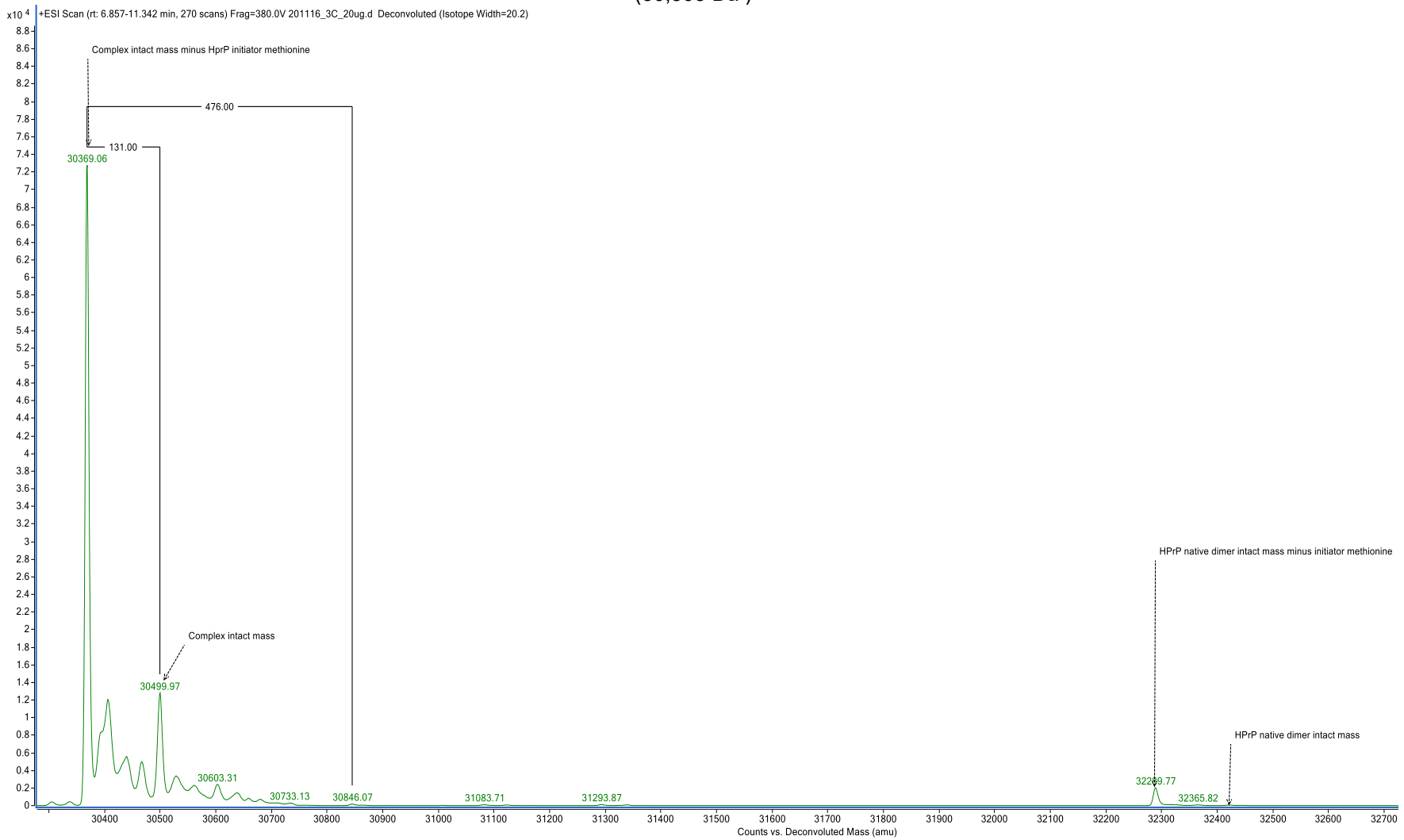

Source: own elaboration.

Before being used in crystallization, the complex was then further purified using size exclusion chromatography, marked by the co-elution of both HuPrP 90-231 and Nb484 (Figure 41). Since in the size exclusion, bigger particles elute first, a shift to the left in the chromatogram indicates a bigger particle was eluting.

Figure 41. Overlay of the size exclusion chromatography elution profile of samples containing only HuPrP 90-231, only Nb484, or both

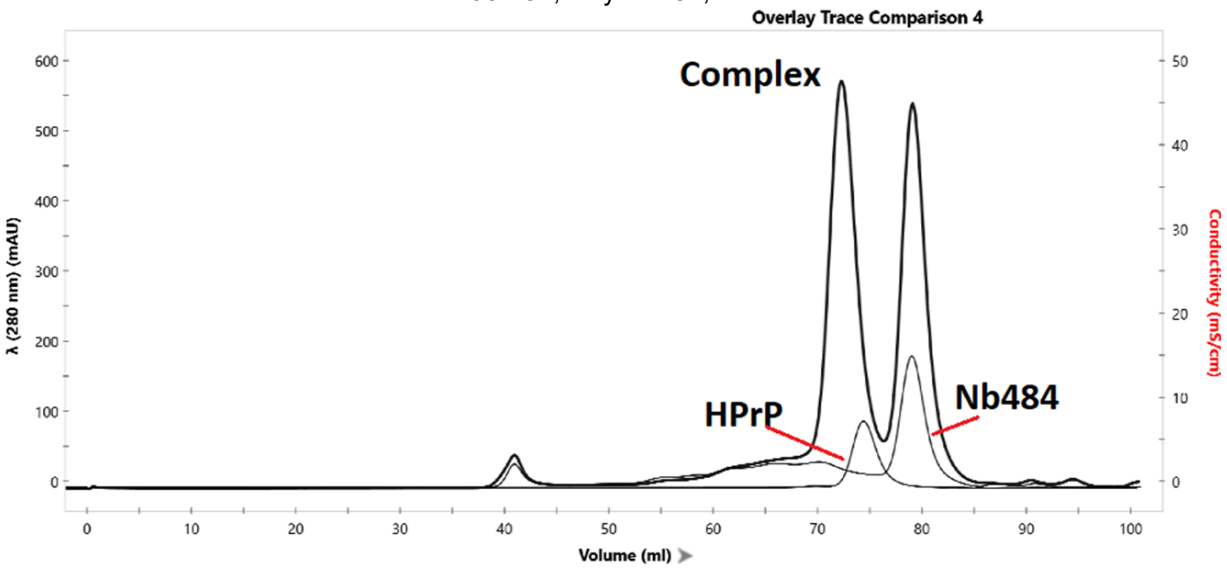

Source: own elaboration.

Our initial efforts screened conditions close to the reported crystallization condition but failed to generate crystals for the complex. The complex was then submitted to multiple crystallization experiments around the reported condition and using crystallization screens. One of our latest screenings yielded some needle-like crystals that would require further optimization before fragment screening (Figure 42).

Figure 42. Initial crystals identified for Nb484-HuPrP 90-231 complex. Left: 0.1 M MES 6.5 25 % v/v PEG Smear Medium; Right: 0.05 M Ammonium acetate 0.15 M Magnesium sulfate heptahydrate 0.1 M HEPES 7.0 12 % v/v PEG Smear Medium

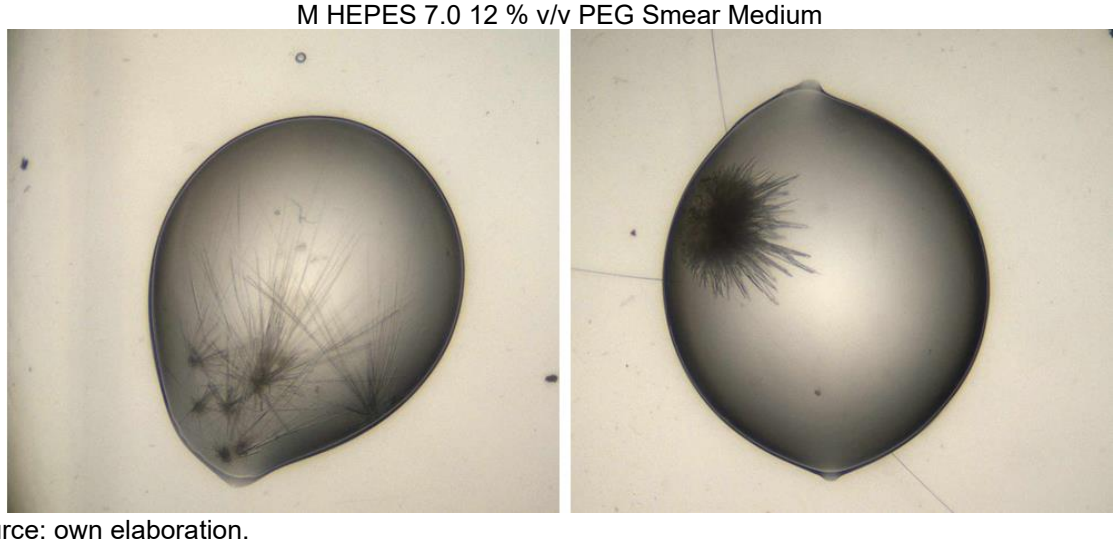

Source: own elaboration.

Another attempt related to exchanging the salt in our existing crystallization condition for PEG proved successful at this stage. Although we have failed to generate crystal from conditions combining multiple PEGs, PEG Smear, and seeding, fully grown crystals could be successfully transferred to a PEG-based condition. In a study reported by Schreuder *et al.*, 1988 it was proposed that “in order to keep the protein crystals intact in different solvents, the solution with the alternative precipitant should neither attract water from the crystal, nor donate water to the crystal.”. To test that, we transferred fully grown crystals (Figure 43_A) to drops containing different PEGs and PEG concentrations. We observed that crystals became fragile and changed their color for less concentrated PEG conditions (Figure 43_B). As the PEG concentration increased, the crystals appeared more rigid (Figure 43_C). The best condition observed in this experiment was 0.1 M Tris pH 7.0, 15 mM $CdCl_2$, 30% PEG Smear medium for which no change in the crystal morphology was observed (Figure 43_D).

Figure 43. PEG-transfer experiment

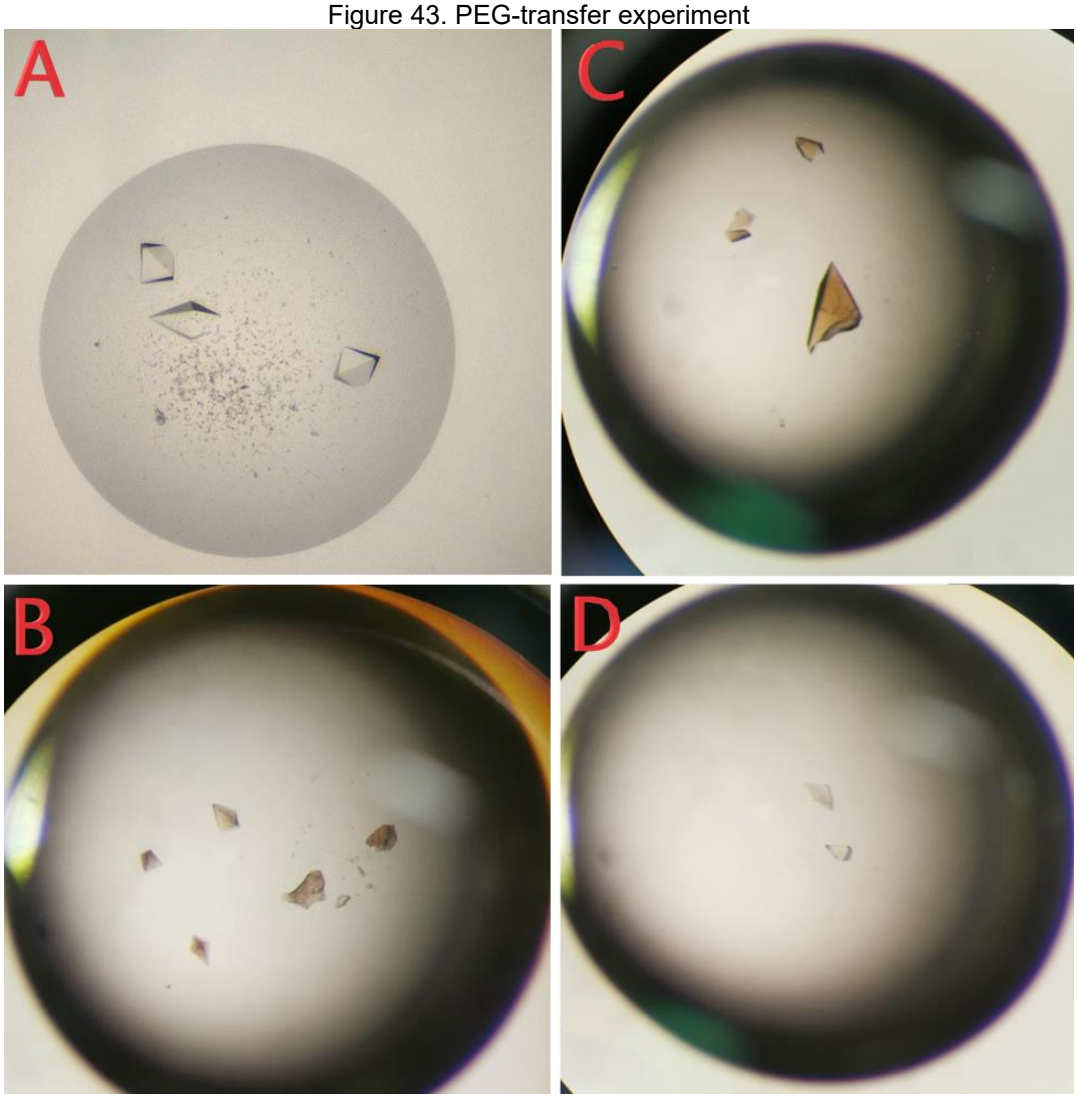

Figure caption
A: Fully grown crystals were transferred to drops containing different PEGs and PEG concentrations.
B: Crystals transferred to drop containing 15% PEG 10k became fragile and brown.
C: Crystals transferred to 30% PEG 10k were still rigid, but still brown.
D: Crystals transferred to 30% PEG Smear medium maintained its morphology.
Source: personal file.

This result was considered very promising for our fragment screening experiments, not only for not containing salt but also because the crystal system was already characterized, which meant that we would be able to use our previous knowledge of solvent screen and our ground state model. Moreover, the screening of some repeated fragments would potentially allow us to identify fragments that did not bind to the protein in our first screening because of the heavy salt content.

The new fragment screening followed the same steps reported in ‘High-throughput fragment screening at XChem’, page 36, the only difference was the addition of a further step: the setup of a source plate, containing crystals of approximately 100 µm which were grown in our previously established condition, and

a destination plate, containing drops with 30% PEG Smear medium replacing the NaCl, and to which the fragments and the crystals were transferred to. It is important to highlight that the soaking time of 4 hours was longer than what we initially intended due to logistical issues.

The screening comprised the testing of 112 fragments from the DSI-poised library, of which 82 were new (Figure 44). We observed that the resolution was slightly lower than our previous run, potentially due to the longer soaking time but also because of the PEG condition. It is interesting to note that our previous solvent screening pointed soaking times longer than two hours as having a significantly negative impact on the crystals. In that sense, the transition to a PEG condition might have increased its resistance to DMSO. This unexpected finding leaves us to wonder which other screening parameters could have been impacted by the transition to a PEG-based condition; it is reasonable to say that the transition to a new system open opportunity to use higher solvent concentrations – leading to higher fragments concentration - and different solvents, such as ethylene glycol.

Figure 44. Top images: picture of a HPrP 90-231 crystal mounted in a loop before data collection and its respective diffraction pattern—bottom images: an overview of the fragments tested in our new screening and resolution distribution of crystals tested

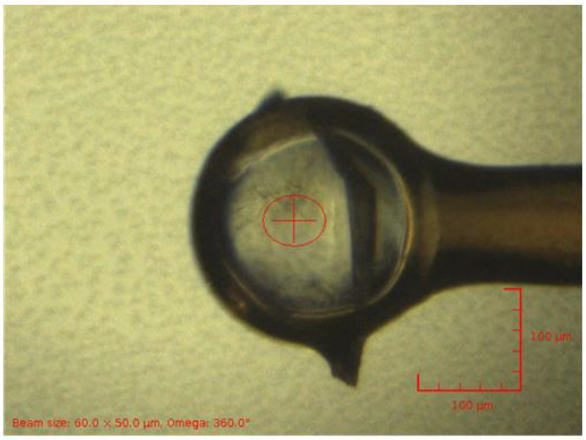

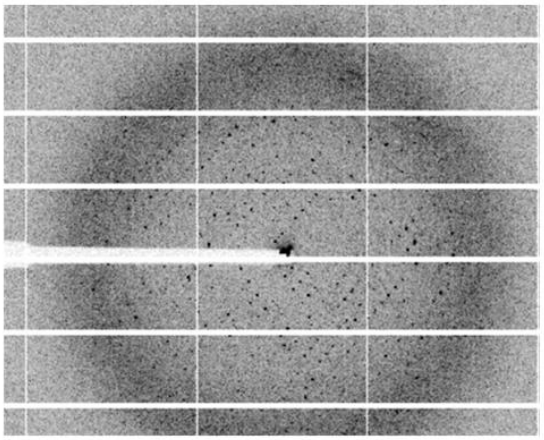

Overview – new screening	
Compounds Screened	112
Re-tested	30
New	82
Concentration	23.8 mM
[DMSO]	5% v/v

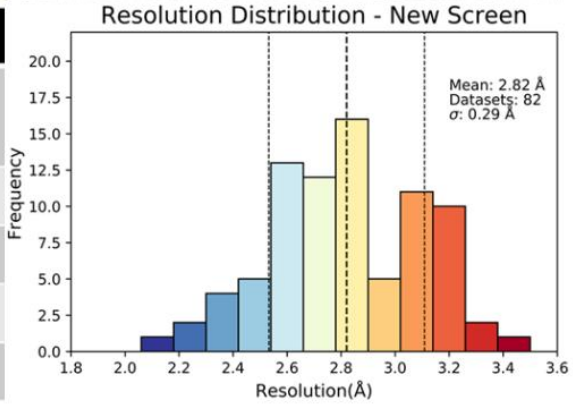

Source: own elaboration.

The incorporation of the datasets into our XChemExplorer session and analysis with our previous PanDDA datasets enabled a faster data analysis. All event maps were investigated manually, but unfortunately, no signal compatible with a hit was observed.

Overall, we believe that the transition to a PEG-based condition improved the crystal system and turned it more fragment-screening friendly. Still, the shorter number of fragments tested, combined with the ‘undruggable’ nature of the target, hindered finding fragment hits.

4.7 Final considerations

Compared to the traditional screening libraries, the fragment-based drug discovery takes advantage of the smaller, less complex nature of fragment molecules (PATEL; BAUMAN; ARNOLD, 2014) to more effectively probe the chemical space of a protein target, providing chemical matter for the development of lead compounds. When paired with X-ray crystallography, the user can obtain direct three-dimensional readouts of the structures of protein-small molecule complexes (DAVIES et al., 2011) that can be used for fragment expansion and identification of additional binding sites. Despite being a powerful tool in structural biology, the low throughput nature and high costs hindered its use as a primary screening tool. As the first Brazilian project to use the XChem platform, we were able to explore the X-ray fragment screening at its best as a high-throughput technique. Taken together, our fragment screening campaign collected over 1000 datasets for solvent testing, pre, and full screening. In total, 808 crystals were soaked with 463 unique fragments for two crystal systems (Table 7). Full details of fragment tested, such as compound structure and library name, and experimental parameters like soaking time, tested concentration, and resolution, can be found in the ‘Appendix’.

Table 7 – Overall number of collected datasets and fragments screened throughout our screening efforts

Fragment screening campaign	Number of entries
Collected datasets	1063
Crystal systems	2
Screened fragments	808
Unique fragments tested	463
Fragments successfully mounted	735
Fragments failed to mount	73
No diffraction	155

Source: own elaboration.

The XChem team improved and streamlined the fragment screening pipeline by tackling low-throughout steps in the sample's preparation, data collection, and analysis. The streamlined process implemented at the XChem enabled the rapid analysis of 620 datasets that diffracted better than 3.5 Å (Figure 45). Moreover, the use of specific equipment's such as the Echo Acoustic Liquid Handler (Labcyte) and the Shifter Device (Oxford Lab Technologies), greatly hastened the sample preparation steps. For example, the Echo can dispense the fragment for an entire 96-well 3-drops plate in 60 seconds, an action that could take a full day if done manually, while the Shifter eases the crystal mounting step. As a result, we obtained an average crystal mounting time of as little as 37 seconds - 10 minutes per puck (Figure 45)!

Figure 45. The XChem platform enabled the performance of high-throughput crystallography by tackling low-throughput steps in sample preparation and analysis. Left graph: Final overall resolution of all fragments tested combined. Right graph: distribution of crystals mounting time with the Shifter Device, with an average of 37 seconds per crystal

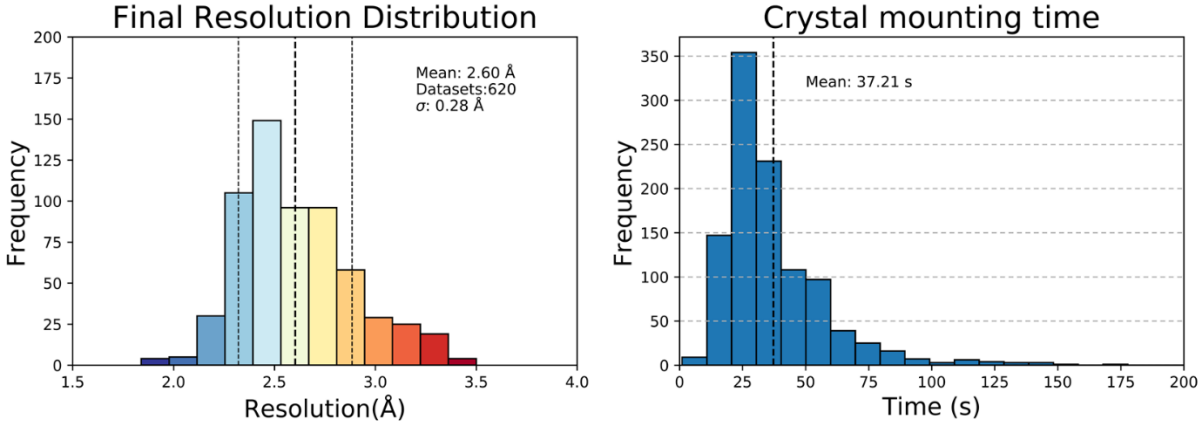

Source: own elaboration.

Finally, it is rewarding to see that our three goals were accomplished, from prion characterization, fragment screening, and in-depth description of the high-throughput method. We hope our journey will provide relevant information for other groups. As a crystallographer, it will be exciting to see crystallography groups in Brazil using the

successful implementations of the XChem and taking full advantage of the new 4th generation synchrotron, Sirius. But also, for another unexpected aspect. Like so many other projects, our work was heavily impacted by the devastating COVID-19. According to John Hopkins University & Medicine Coronavirus Resource Center, there were over 180 million cases and 3.9 million deaths worldwide, over 500 thousand deaths only in Brazil. As an academic visitor in Prof Frank von Delft's laboratory in the Structural Genomics Consortium, the student had the opportunity to contribute, even if slightly, to the Moonshot collaboration and international consortium initiative to develop a COVID antiviral. The student was part of a team effort and helped to analyze the fragment screening outcome against the main protease (Mpro) and Nsp3 macrodomain of SARS-CoV-2, resulting in 106 deposited structures in PDB, two manuscripts (ACHDOUT et al., 2020; SCHULLER et al., 2021) and helped to develop and maintain a SARS-CoV-2 assay tracker (http://sarscov2.assaytracker.net/). This was only possible with the knowledge gained throughout this challenging Ph.D. project.

4.8 Manuscripts published and submitted related to this thesis

Reidenbach AG, Mesleh MF, Casalena D, Vallabh SM, Dahlin JL, Leed AJ, Chan AI, Usanov DL, Yehl JB, Lemke CT, Campbell AJ, Shah RN, Shrestha OK, Sacher JR, **Rangel VL**, Moroco JA, Sathappa M, Nonato MC, Nguyen KT, Wright SK, Liu DR, Wagner FF, Kaushik VK, Auld DS, Schreiber SL, Minikel EV. Multimodal small-molecule screening for human prion protein binders. J Biol Chem. 2020 Sep 25;295(39):13516-13531. DOI: 10.1074/jbc.RA120.014905. Epub 2020 Jul 28. PMID: 32723867; PMCID: PMC7521658.

Leandro Oliveira Bortot*, **Victor Lopes Rangel***, Francesca A. Pavlovici, Kamel El Omari, Armin Wagner, Jose Brandao-Neto, Romain Talon, Frank von Delft, Andrew G Reidenbach, Sonia M Vallabh, Eric Vallabh Minikel, Stuart Schreiber, Maria Cristina Nonato

*both authors contributed equally to this work.

Schuller M, Correy GJ, Gahbauer S, Fearon D, Wu T, Díaz RE, Young ID, Martins LC, Smith DH, Schulze-Gahmen U, Owens TW, Deshpande I, Merz GE, Thwin AC, Biel JT, Peters JK, Moritz M, Herrera N, Kratochvil HT; QCRG Structural Biology Consortium, Aimon A, Bennett JM, Neto JB, Cohen AE, Dias A, Douangamath A, Dunnett L, Fedorov O, Ferla MP, Fuchs M, Gorrie-Stone TJ, Holton JM, Johnson MG, Krojer T, Meigs G, Powell AJ; Johannes Gregor Matthias Rack, **Rangel VL**, Russi S,

Skyner RE, Smith CA, Soares AS, Wierman JL, Zhu K, Jura N, Ashworth A, Irwin J, Thompson MC, Gestwicki JE, von Delft F, Shoichet BK, Fraser JS, Ahel I. Fragment Binding to the Nsp3 Macrodomain of SARS-CoV-2 Identified Through Crystallographic Screening and Computational Docking. bioRxiv [Preprint]. 2020 Nov 24:2020.11.24.393405. DOI: 10.1101/2020.11.24.393405. Update in: Sci Adv. 2021 Apr 14;7(16): PMID: 33269349; PMCID: PMC7709169.

The COVID Moonshot Consortium, Hagit Achdout, Anthony Aimon, Elad Bar-David, Haim Barr, Amir Ben-Shmuel, James Bennett, Melissa L Bobby, Juliane Brun, BVNBS Sarma, Mark Calmiano, Anna Carbery, Emma Cattermole, John D. Chodera, Austin Clyde, Joseph E. Coffland, Galit Cohen, Jason Cole, Alessandro Contini, Lisa Cox, Milan Cvitkovic, Alex Dias, Alice Douangamath, Shirly Duberstein, Tim Dudgeon, Louise Dunnett, Peter K. Eastman, Noam Erez, Michael Fairhead, Daren Fearon, Oleg Fedorov, Matteo Ferla, Holly Foster, Richard Foster, Ronen Gabizon, Paul Gehrtz, Carina Gileadi, Charline Giroud, William G. Glass, Robert Glen, Itai Glinert, Marian Gorichko, Tyler Gorrie-Stone, Edward J Griffen, Jag Heer, Michelle Hill, Sam Horrell, Matthew F.D. Hurley, Tomer Israely, Andrew Jajack, Eric Jnoff, Tobias John, Anastassia L. Kantsadi, Peter W. Kenny, John L. Kiappes, Lizbe Koekemoer, Boris Kovar, Tobias Krojer, Alpha Albert Lee, Bruce A. Lefker, Haim Levy, Nir London, Petra Lukacik, Hannah Bruce Macdonald, Beth MacLean, Tika R. Malla, Tatiana Matviiuk, Willam McCorkindale, Sharon Melamed, Oleg Michurin, Halina Mikolajek, Aaron Morris, Garrett M. Morris, Melody Jane Morwitzer, Demetri Moustakas, Jose Brandao Neto, Vladas Oleinikovas, Gijs J. Overheul, David Owen, Ruby Pai, Jin Pan, Nir Paran, Benjamin Perry, Maneesh Pingle, Jakir Pinjari, Boaz Politi, Ailsa Powell, Vladimir Psenak, Reut Puni, **Victor L. Rangel**, Rambabu N. Reddi, St Patrick Reid, Efrat Resnick, Matthew C. Robinson, Ralph P. Robinson, Dominic Rufa, Christopher Schofield, Aarif Shaikh, Jiye Shi, Khriesto Shurrush, Assa Sittner, Rachael Skyner, Adam Smalley, Mihaela D. Smilova, John Spencer, Claire Strain-Damerell, Vishwanath Swamy, Hadas Tamir, Rachael Tennant, Andrew Thompson, Warren Thompson, Susana Tomasio, Anthony Tumber, Ioannis Vakonakis, Ronald P. van Rij, Finny S. Varghese, Mariana Vaschetto, Einat B. Vitner, Vincent Voelz, Annette von Delft, Frank von Delft, Martin Walsh, Walter Ward, Charlie Weatherall, Shay Weiss, Conor Francis Wild, Matthew Wittmann, Nathan Wright, Yfat Yahalom-Ronen, Daniel Zaidmann, Hadeer Zidane, Nicole Zitzmann (2020) ‘COVID moonshot: Open science discovery of SARS-CoV-2 main protease inhibitors by combining crowdsourcing, high-throughput

experiments, computational simulations, and machine learning', *bioRxiv*. bioRxiv, p. 2020.10.29.339317. Doi: 10.1101/2020.10.29.339317.

5. CONCLUSION

The prion protein, the key role player in the prion disease, has been drawing attention from the scientific community for having a misfolded conformer with the ability to self-replicate and drive the misfolding of other functional prion protein into the misfolded form, resulting in an invariably fatal outcome. Therapeutical approaches proposed for prion disease can explore multiple steps in the disease process, such as protein expression, promotion of protein degradation, relocation of the protein, binding, or stabilizing the prion to block the neurotoxic pathway. Despite being in the spotlight for so long, there are still no ways to cure the disease, and the difficulty to target this protein leads many to classify the prion protein as an undruggable target. The present work describes the journey to shed light upon the prion protein using the X-ray fragment screening approach since fragment hits can provide chemical matter and insights to understand the prion protein and help with drug discovery. This extremely collaborative work took advantage of state-of-the-art infrastructure at the XChem, Diamond Light Source, and the SGC, University of Oxford. Using multiple biochemical and biophysical assays, we prepared the ground to perform one of the most extensive X-ray fragment screenings ever done in a Brazilian project. The in-depth analysis of our crystal system revealed a novel oligomeric arrangement of the prion protein and provided a solid background to perform our fragment screening. The prion protein proved itself a challenging target, and throughout our work, over 800 fragments were tested, and the first structures of prion binders were elucidated. The fragment hits share a pyrazole ring and bind between helix 2 and 3 in a shallow pocket created by the movement of the sidechain of K185. This region has an important role in conformational changes suffered by the prion protein and could potentially be explored in future drug-developments projects.

The fragments were re-tested and bound to the same place with the same pose, a promising indication that it can be further explored. After analyzing other fragment screening campaigns, we concluded that a second screening could be valuable, so a second crystal system was pursued and screened. We believe that the transition to a PEG-based condition improved the crystal system and turned it more fragment-screening friendly, highlighting the importance of a well-structured crystal system for X-ray fragment screening. Moreover, as the first Brazilian project approved to use the XChem pipeline, we thoroughly described our search for prion binders, and we hope

to contribute to the growth and development of fragment screening in Brazil, which is now empowered with one of the first fourth-generation synchrotron light sources in the world.

6. REFERENCES

ABOLA, Enrique; KUHN, Peter; EARNEST, Thomas; STEVENS, Raymond C. Automation of X-ray crystallography. **Nature Structural Biology**, *[S. l.]*, v. 7, n. SUPPL., p. 973–977, 2000. DOI: 10.1038/80754.

ABSKHARON, Romany N. N.; GIACHIN, Gabriele; WOHLKONIG, Alexandre; SOROR, Sameh H.; PARDON, Els; LEGNAME, Giuseppe; STEYAERT, Jan. Probing the N-terminal β-sheet conversion in the crystal structure of the human prion protein bound to a nanobody. **Journal of the American Chemical Society**, *[S. l.]*, v. 136, n. 3, p. 937–944, 2014. DOI: 10.1021/ja407527p.

ABSKHARON, Romany N. N.; SOROR, Sameh H.; PARDON, Els; EL HASSAN, Hassan; LEGNAME, Giuseppe; STEYAERT, Jan; WOHLKONIG, Alexandre. Crystallization and preliminary X-ray diffraction analysis of a specific VHH domain against mouse prion protein. **Acta Crystallographica Section F: Structural Biology and Crystallization Communications**, *[S. l.]*, v. 66, n. 12, p. 1644–1646, 2010. DOI: 10.1107/S1744309110042168.

ACHDOUT, Hagit et al. **COVID moonshot: Open science discovery of SARS-CoV-2 main protease inhibitors by combining crowdsourcing, high-throughput experiments, computational simulations, and machine learningbioRxiv**bioRxiv, , 2020. DOI: 10.1101/2020.10.29.339317. Disponível em: https://doi.org/10.1101/2020.10.29.339317. Acesso em: 1 maio. 2021.

ADAMS, Paul D. et al. PHENIX: A comprehensive Python-based system for macromolecular structure solution. **Acta Crystallographica Section D: Biological Crystallography**, *[S. l.]*, v. 66, n. 2, p. 213–221, 2010. DOI: 10.1107/S0907444909052925. Disponível em: http://scripts.iucr.org/cgi-bin/paper?S0907444909052925. Acesso em: 24 ago. 2018.

AGUILAR-CALVO, Patricia; GARCÍA, Consolación; ESPINOSA, Juan Carlos; ANDREOLETTI, Olivier; TORRES, Juan María. Prion and prion-like diseases in animals. **Virus Research**, *[S. l.]*, v. 207, p. 82–93, 2015. DOI: 10.1016/j.virusres.2014.11.026. Disponível em: http://dx.doi.org/10.1016/j.virusres.2014.11.026.

ALPER, TIKVAH; CRAMP, W. A.; HAIG, D. A.; CLARKE, M. C. Does the Agent of Scrapie Replicate without Nucleic Acid ? **Nature**, *[S. l.]*, v. 214, n. 5090, p. 764–766, 1967. DOI: 10.1038/214764a0. Disponível em: http://www.nature.com/doifinder/10.1038/214764a0. Acesso em: 7 nov. 2018.

ALPER, Tikvah; HAIG, D. A.; CLARKE, M. C. The exceptionally small size of the scrapie agent. **Biochemical and Biophysical Research Communications**, *[S. l.]*, v. 22, n. 3, p. 278–284, 1966. DOI: 10.1016/0006-291X(66)90478-5. Disponível em:

https://www.sciencedirect.com/science/article/pii/0006291X66904785?via%3Dihub. Acesso em: 7 nov. 2018.

ALTIERI, Andrea; SPIRIDONOV, Evgeny A.; SIVTZEV, Semen I.; ISHIBASHI, Daisuke; BIGGI, Silvia; NISHIDA, Noriyuki; BIASINI, Emiliano; KURKIN, Alexander V. Generation, optimization and characterization of novel anti-prion compounds. **Bioorganic & Medicinal Chemistry**, *[S. l.]*, v. 28, n. 21, p. 115717, 2020. DOI: 10.1016/J.BMC.2020.115717.

ANTONYUK, S. V et al. Crystal structure of human prion protein bound to a therapeutic antibody. **Proceedings of the National Academy of Sciences of the United States of America**, *[S. l.]*, v. 106, n. 8, p. 2554–2558, 2009. DOI: 10.1073/pnas.0809170106. Disponível em: https://www.ncbi.nlm.nih.gov/pmc/articles/PMC2637903/pdf/zpq2554.pdf. Acesso em: 18 dez. 2017.

AUGENSTEIN, L. G. Symposium on information theory in biology, Gatlinburg, Tennessee, October 29-31, 1956 : Yockey, Hubert P : Free Download, Borrow, and Streaming : Internet Archive. *In*: 1958, **Anais** [...]. [s.l: s.n.] p. 287–292. Disponível em: https://archive.org/details/symposiumoninfor00yock/page/288. Acesso em: 18 jul. 2019.

B, Caughey; D, Ernst; RE, Race. Congo red inhibition of scrapie agent replication. **Journal of virology**, *[S. l.]*, v. 67, n. 10, p. 6270–6272, 1993. DOI: 10.1128/JVI.67.10.6270-6272.1993. Disponível em: https://pubmed.ncbi.nlm.nih.gov/8103804/. Acesso em: 5 set. 2021.

BAKER, Lisa M. et al. Rapid optimisation of fragments and hits to lead compounds from screening of crude reaction mixtures. **Communications Chemistry**, *[S. l.]*, v. 3, n. 1, 2020. DOI: 10.1038/s42004-020-00367-0.

BARAL, Pravas Kumar; SWAYAMPAKULA, Mridula; ROUT, Manoj Kumar; KAV, Nat N. V.; SPYRACOPOULOS, Leo; AGUZZI, Adriano; JAMES, Michael N. G. Structural Basis of Prion Inhibition by Phenothiazine Compounds. **Structure**, *[S. l.]*, v. 22, n. 2, p. 291–303, 2014. DOI: 10.1016/J.STR.2013.11.009. Disponível em: http://www.cell.com/article/S0969212613004590/fulltext. Acesso em: 5 set. 2021.

BIASINI, Emiliano; TAPELLA, Laura; RESTELLI, Elena; POZZOLI, Manuela; MASSIGNAN, Tania; CHIESA, Roberto. The hydrophobic core region governs mutant prion protein aggregation and intracellular retention. **The Biochemical journal**, *[S. l.]*, v. 430, n. 3, p. 477–86, 2010. DOI: 10.1042/BJ20100615. Disponível em: http://www.ncbi.nlm.nih.gov/pubmed/20626348. Acesso em: 7 dez. 2018.

BIGGI, Silvia et al. Identification of compounds inhibiting prion replication and toxicity

by removing PrPC from the cell surface. **Journal of Neurochemistry**, *[S. l.]*, v. 152, n. 1, p. 136–150, 2020. DOI: 10.1111/JNC.14805.

BLUCHER, Aurora S.; MCWEENEY, Shannon K. Challenges in secondary analysis of high throughput screening data. *In*: PACIFIC SYMPOSIUM ON BIOCOMPUTING 2014, **Anais** [...]. : NIH Public Access, 2014. p. 114–124. DOI: 10.1142/9789814583220_0012. Disponível em: /pmc/articles/PMC3976302/. Acesso em: 26 jun. 2021.

BORTOT, Leandro Oliveira et al. Novel quaternary structures of the human prion protein globular domain. **bioRxiv**, *[S. l.]*, 2020. DOI: 10.1101/2020.11.16.385856. Disponível em: https://doi.org/10.1101/2020.11.16.385856. Acesso em: 25 abr. 2021.

BREMER, Juliane et al. Axonal prion protein is required for peripheral myelin maintenance. **Nature Neuroscience**, *[S. l.]*, v. 13, n. 3, p. 310–318, 2010. DOI: 10.1038/nn.2483. Disponível em: https://www.nature.com/articles/nn.2483. Acesso em: 4 set. 2020.

BÜELER, H.; AGUZZI, A.; SAILER, A.; GREINER, R. A.; AUTENRIED, P.; AGUET, M.; WEISSMANN, C. Mice devoid of PrP are resistant to scrapie. **Cell**, *[S. l.]*, v. 73, n. 7, p. 1339–1347, 1993. DOI: 10.1016/0092-8674(93)90360-3. Disponível em: http://www.ncbi.nlm.nih.gov/pubmed/8100741. Acesso em: 18 dez. 2017.

BÜELER, H.; RAEBER, Alex; SAILER, Andreas; FISCHER, Marek; AGUZZI, Adriano; WEISSMANN, Charles. High prion and PrPSc levels but delayed onset of disease in scrapie-inoculated mice heterozygous for a disrupted PrP gene. **Molecular medicine (Cambridge, Mass.)**, *[S. l.]*, v. 1, n. 1, p. 19–30, 1994. DOI: 10.1007/bf03403528. Disponível em: https://www.ncbi.nlm.nih.gov/pmc/articles/PMC2229922/pdf/molmed00043-0025.pdf. Acesso em: 18 dez. 2017.

CASTLE, Andrew R.; GILL, Andrew C. Physiological Functions of the Cellular Prion Protein. **Frontiers in Molecular Biosciences**, *[S. l.]*, v. 4, p. 19, 2017. DOI: 10.3389/fmolb.2017.00019.

CAUGHEY, Winslow S.; RAYMOND, Lynne D.; HORIUCHI, Motohiro; CAUGHEY, Byron. Inhibition of protease-resistant prion protein formation by porphyrins and phthalocyanines. **Proceedings of the National Academy of Sciences of the United States of America**, *[S. l.]*, v. 95, n. 21, p. 12117–12122, 1998. DOI: 10.1073/pnas.95.21.12117. Disponível em: https://pubmed.ncbi.nlm.nih.gov/9770449/. Acesso em: 5 set. 2021.

CAVALIERE, Paola; TORRENT, Joan; PRIGENT, Stephanie; GRANATA, Vincenzo; PAUWELS, Kris; PASTORE, Annalisa; REZAEI, Human; ZAGARI, Adriana. Binding

of methylene blue to a surface cleft inhibits the oligomerization and fibrillization of prion protein. **Biochimica et Biophysica Acta (BBA) - Molecular Basis of Disease**, *[S. l.]*, v. 1832, n. 1, p. 20–28, 2013. DOI: 10.1016/J.BBADIS.2012.09.005.

CHANDLER, R. L. ENCEPHALOPATHY IN MICE PRODUCED BY INOCULATION WITH SCRAPIE BRAIN MATERIAL. **The Lancet**, *[S. l.]*, v. 277, n. 7191, p. 1378–1379, 1961. DOI: 10.1016/S0140-6736(61)92008-6. Disponível em: http://www.ncbi.nlm.nih.gov/pubmed/13692303. Acesso em: 7 nov. 2017.

CHEN, Cao; DONG, Xiao-Ping. Epidemiological characteristics of human prion diseases. **Infectious Diseases of Poverty**, *[S. l.]*, v. 5, n. 1, p. 47, 2016. DOI: 10.1186/s40249-016-0143-8. Disponível em: http://idpjournal.biomedcentral.com/articles/10.1186/s40249-016-0143-8.

CHEN, Vincent B.; ARENDALL III, W. Bryan; HEADD, Jeffrey J.; KEEDY, Daniel A.; IMMORMINO, Robert M.; KAPRAL, Gary J.; MURRAY, Laura W.; RICHARDSON, Jane S.; RICHARDSON, David C. MolProbity: all-atom structure validation for macromolecular crystallography. **Acta Cryst**, *[S. l.]*, v. 66, p. 12–21, 2010. DOI: 10.1107/S0907444909042073. Disponível em: https://www.ncbi.nlm.nih.gov/pmc/articles/PMC2803126/pdf/d-66-00012.pdf. Acesso em: 6 nov. 2017.

CHOI, J. H.; LEE, S. Y. Secretory and extracellular production of recombinant proteins using Escherichia coli. **Applied Microbiology and Biotechnology**, *[S. l.]*, v. 64, n. 5, p. 625–635, 2004. DOI: 10.1007/s00253-004-1559-9.

COHEN, F. E. et al. Conversion of alpha-helices into beta-sheets features in the formation of the scrapie prion proteins. **Proceedings of the National Academy of Sciences of the United States of America**, *[S. l.]*, v. 90, n. 23, p. 10962–10966, 1993. DOI: VL - 90. Disponível em: http://www.pnas.org/content/90/23/10962.abstract%5Cnhttp://www.pnas.org/content/90/23/10962.full.pdf.

COLEMAN, Bradley M.; HARRISON, Christopher F.; GUO, Belinda; MASTERS, Colin L.; BARNHAM, Kevin J.; LAWSON, Victoria A.; HILL, Andrew F.; CAUGHEY, B. W. Pathogenic Mutations within the Hydrophobic Domain of the Prion Protein Lead to the Formation of Protease-Sensitive Prion Species with Increased Lethality. **Journal of Virology**, *[S. l.]*, v. 88, n. 5, p. 2690–2703, 2014. DOI: 10.1128/jvi.02720-13. Disponível em: http://www.ncbi.nlm.nih.gov/pubmed/24352465. Acesso em: 7 dez. 2018.

COLLINGE, John. PRION DISEASES OF HUMANS AND ANIMALS: Their Causes and Molecular Basis. *[S. l.]*, 2001. Disponível em: http://www.annualreviews.org/doi/pdf/10.1146/annurev.neuro.24.1.519. Acesso em: 8 nov. 2017.

COLLINS, Patrick M. et al. Gentle, fast and effective crystal soaking by acoustic dispensing. **Acta Crystallographica Section D Structural Biology**, *[S. l.]*, v. 73, n. 3, p. 246–255, 2017. DOI: 10.1107/s205979831700331x.

COLLINS, S.; MCLEAN, C. A.; MASTERS, C. L. Gerstmann–Sträussler–Scheinker syndrome,fatal familial insomnia, and kuru: a review ofthese less common human transmissiblespongiform encephalopathies. **Journal of Clinical Neuroscience**, *[S. l.]*, v. 8, n. 5, p. 387–397, 2001. DOI: 10.1054/jocn.2001.0919. Disponível em: http://www.ncbi.nlm.nih.gov/pubmed/11535002. Acesso em: 18 dez. 2017.

CONCEIÇÃO, Raissa A. et al. Synthesis and in silico and in vitro evaluation of trimethoxy-benzamides designed as anti-prion derivatives. **Medicinal Chemistry Research (Print)**, *[S. l.]*, v. 28, n. 12, p. 2128–2141, 2019. DOI: 10.1007/S00044-019-02441-2. Disponível em: http://inis.iaea.org/Search/search.aspx?orig_q=RN:51100213. Acesso em: 5 set. 2021.

DAUTER, Zbigniew. Collection of X-Ray Diffraction Data from Macromolecular Crystals. **Methods in molecular biology (Clifton, N.J.)**, *[S. l.]*, v. 1607, p. 165–184, 2017. DOI: 10.1007/978-1-4939-7000-1_7. Disponível em: http://www.ncbi.nlm.nih.gov/pubmed/28573573. Acesso em: 18 jul. 2019.

DAVIES, Douglas R.; BEGLEY, Darren W.; HARTLEY, Robert C.; STAKER, Bart L.; STEWART, Lance J. Predicting the success of fragment screening by X-ray crystallography. *In*: **Methods in Enzymology**. [s.l.] : Academic Press Inc., 2011. v. 493p. 91–114. DOI: 10.1016/B978-0-12-381274-2.00004-2.

DELEAULT, Nathan R.; HARRIS, Brent T.; REES, Judy R.; SUPATTAPONE, Surachai. Formation of native prions from minimal components in vitro. **Proceedings of the National Academy of Sciences of the United States of America**, *[S. l.]*, v. 104, n. 23, p. 9741–9746, 2007. DOI: 10.1073/pnas.0702662104. Disponível em: https://pubmed.ncbi.nlm.nih.gov/17535913/. Acesso em: 31 maio. 2021.

DIEDERICHS, Kay. Some aspects of quantitative analysis and correction of radiation damage. *In*: ACTA CRYSTALLOGRAPHICA SECTION D: BIOLOGICAL CRYSTALLOGRAPHY 2006, **Anais** [...]. [s.l: s.n.] p. 96–101. DOI: 10.1107/S0907444905031537. Disponível em: https://journals.iucr.org/d/issues/2006/01/00/ba5081/ba5081.pdf. Acesso em: 18 jul. 2019.

DIMASI, Joseph A.; GRABOWSKI, Henry G.; HANSEN, Ronald W. Innovation in the pharmaceutical industry: New estimates of R&D costs. **Journal of Health Economics**, *[S. l.]*, v. 47, p. 20–33, 2016. DOI: 10.1016/j.jhealeco.2016.01.012.

DOH-URA, Katsumi; IWAKI, Toru; CAUGHEY, Byron. Lysosomotropic Agents and Cysteine Protease Inhibitors Inhibit Scrapie-Associated Prion Protein Accumulation. **Journal of Virology**, *[S. l.]*, v. 74, n. 10, p. 4894–4897, 2000. DOI: 10.1128/jvi.74.10.4894-4897.2000. Disponível em: https://pubmed.ncbi.nlm.nih.gov/10775631/. Acesso em: 5 set. 2021.

EMSLEY, P.; LOHKAMP, B.; SCOTT, W. G.; COWTAN, K. Features and development of Coot. **Acta crystallographica. Section D, Biological crystallography**, *[S. l.]*, v. 66, n. Pt 4, p. 486–501, 2010. a. DOI: 10.1107/S0907444910007493. Disponível em: http://www.ncbi.nlm.nih.gov/pubmed/20383002. Acesso em: 6 nov. 2017.

EMSLEY, P.; LOHKAMP, B.; SCOTT, W. G.; COWTAN, K. Features and development of Coot. **Acta Crystallographica Section D: Biological Crystallography**, *[S. l.]*, v. 66, n. 4, p. 486–501, 2010. b. DOI: 10.1107/S0907444910007493. Disponível em: http://www.ncbi.nlm.nih.gov/pubmed/20383002. Acesso em: 24 ago. 2018.

ENGELKE, Anna D. et al. Dimerization of the cellular prion protein inhibits propagation of scrapie prions. **Journal of Biological Chemistry**, *[S. l.]*, v. 293, n. 21, p. 8020–8031, 2018. DOI: 10.1074/jbc.RA117.000990. Disponível em: http://www.ncbi.nlm.nih.gov/pubmed/29636413. Acesso em: 24 ago. 2018.

ERLANSON, Daniel A.; FESIK, Stephen W.; HUBBARD, Roderick E.; JAHNKE, Wolfgang; JHOTI, Harren. Twenty years on: The impact of fragments on drug discovery. **Nature Reviews Drug Discovery**, *[S. l.]*, v. 15, n. 9, p. 605–619, 2016. DOI: 10.1038/nrd.2016.109.

EVANS, Philip R.; MURSHUDOV, Garib N. How good are my data and what is the resolution? **Acta Crystallographica Section D Biological Crystallography**, *[S. l.]*, v. 69, n. 7, p. 1204–1214, 2013. DOI: 10.1107/S0907444913000061. Disponível em: http://www.ncbi.nlm.nih.gov/pubmed/23793146. Acesso em: 24 ago. 2018.

FATTORI, Daniela. **Molecular recognition: The fragment approach in lead generationDrug Discovery Today**, 2004. DOI: 10.1016/S1359-6446(03)03007-1.

FERENCZY, György G.; KESERU, György M. On the enthalpic preference of fragment binding. **MedChemComm**, *[S. l.]*, v. 7, n. 2, p. 332–337, 2016. DOI: 10.1039/c5md00542f. Disponível em: www.rsc.org/medchemcomm. Acesso em: 26 jun. 2021.

FERNÁNDEZ-BORGES, Natalia et al. Unraveling the key to the resistance of canids to prion diseases. **PLOS Pathogens**, *[S. l.]*, v. 13, n. 11, p. e1006716, 2017. DOI: 10.1371/journal.ppat.1006716. Disponível em:

https://dx.plos.org/10.1371/journal.ppat.1006716. Acesso em: 7 dez. 2018.

FISCHER, Marek; RULICKE1, Thomas; RAEBER, Alex; SAILER2, Andreas; MOSER, Markus; OESCH3, Bruno; BRANDNER4, Sebastian; AGUZZI4, Adriano; WEISSMANN5, Charles. Prion protein (PrP) with amino-proximal deletions restoring susceptibility of PrP knockout mice to scrapie. **The EMBO Journal**, *[S. l.]*, v. 15, n. 6, p. 1255–1264, 1996. Disponível em: https://www.ncbi.nlm.nih.gov/pmc/articles/PMC450028/pdf/emboj00006-0055.pdf. Acesso em: 18 dez. 2017.

FOLLET, J. et al. PrP Expression and Replication by Schwann Cells: Implications in Prion Spreading. **Journal of Virology**, *[S. l.]*, v. 76, n. 5, p. 2434–2439, 2002. DOI: 10.1128/jvi.76.5.2434-2439.2002. Disponível em: /pmc/articles/PMC135945/?report=abstract. Acesso em: 4 set. 2020.

FRASER, H.; DICKINSON, A. G. The sequential development of the brain lesions of scrapie in three strains of mice. **Journal of Comparative Pathology**, *[S. l.]*, v. 78, n. 3, p. 301–11, 1968. DOI: 10.1016/0021-9975(68)90006-6. Disponível em: http://www.ncbi.nlm.nih.gov/pubmed/4970192. Acesso em: 13 nov. 2017.

GAJDUSEK, D. C.; GIBBS, C. J.; ALPERS, M.; ALPERS, M. P.; BECK, Elizabeth; DANIEL, P. M.; MATTHEWS, W. B. Transmission and passage of experimenal kuru to chimpanzees. **Science (New York, N.Y.)**, *[S. l.]*, v. 155, n. 3759, p. 212–4, 1967. DOI: 10.1126/science.161.3839.388. Disponível em: http://www.ncbi.nlm.nih.gov/pubmed/6015529. Acesso em: 6 nov. 2017.

GAMBETTI, Pierluigi; KONG, Qingzhong; ZOU, Wenquan; PARCHI, Piero; CHEN, Shu G. Sporadic and familial CJD: classification and characterisation. **British Medical Bulletin**, *[S. l.]*, v. 66, n. 1, p. 213–239, 2003. DOI: 10.1093/BMB/66.1.213. Disponível em: https://academic.oup.com/bmb/article/66/1/213/284818. Acesso em: 5 set. 2021.

GASHAW, Isabella; ELLINGHAUS, Peter; SOMMER, Anette; ASADULLAH, Khusru. **What makes a good drug target?Drug Discovery Today**Elsevier Current Trends, , 2012. DOI: 10.1016/j.drudis.2011.12.008.

GLUSKER, Jenny P. Protein Crystallization. Techniques, Strategies, and Tips Edited by Terese M. Bergfors. International University Line, 1999. ISBN 0963681753. **Crystal Growth & Design**, *[S. l.]*, v. 3, n. 1, p. 109–109, 2003. DOI: 10.1021/cg020059c. Disponível em: https://pubs.acs.org/doi/abs/10.1021/cg020059c. Acesso em: 25 abr. 2021.

GOMES, Mariana P. B.; CORDEIRO, Yraima; SILVA, Jerson L. **The peculiar interaction between mammalian prion protein and RNA.Prion**Taylor & Francis, ,

2008. DOI: 10.4161/pri.2.2.6988. Disponível em: /pmc/articles/PMC2634520/. Acesso em: 31 maio. 2021.

GREIG, J. Russell. Scrapie in sheep. **Journal of Comparative Pathology and Therapeutics**, *[S. l.]*, v. 60, p. 263–266, 1950. DOI: 10.1016/S0368-1742(50)80024-3. Disponível em: https://www.sciencedirect.com/science/article/pii/S0368174250800243. Acesso em: 5 nov. 2018.

GUITART, Kathrin; LOERS, Gabriele; SCHACHNER, Melitta; KLEENE, Ralf. Prion protein regulates glutathione metabolism and neural glutamate and cysteine uptake via excitatory amino acid transporter 3. **Journal of Neurochemistry**, *[S. l.]*, v. 133, n. 4, p. 558–571, 2015. DOI: 10.1111/jnc.13071.

HADLOW, W. J. SCRAPIE AND KURU. **The Lancet**, *[S. l.]*, v. 274, n. 7097, p. 289–290, 1959. DOI: 10.1016/S0140-6736(59)92081-1. Disponível em: http://linkinghub.elsevier.com/retrieve/pii/S0140673659920811. Acesso em: 7 nov. 2017.

HAFNER-BRATKOVIČ, Iva et al. Globular domain of the prion protein needs to be unlocked by domain swapping to support prion protein conversion. **Journal of Biological Chemistry**, *[S. l.]*, v. 286, n. 14, p. 12149–12156, 2011. DOI: 10.1074/jbc.M110.213926. Disponível em: /pmc/articles/PMC3069419/. Acesso em: 25 abr. 2021.

HOLSTI, L. R. Biological effects of ionizing radiation. **Suomen lääkärilehti. Finlands läkartidning**, *[S. l.]*, v. 17, p. 309–319, 1962. Disponível em: https://books.google.com.br/books/about/Biological_Effects_of_Ionizing_Radiation.html?id=IZMTAQAAMAAJ&redir_esc=y. Acesso em: 18 jul. 2019.

HUBBARD, Roderick E. The Role of Fragment-based Discovery in Lead Finding. *In*: [s.l: s.n.]. p. 1–36. DOI: 10.1002/9783527683604.ch01.

HUBER, Sylwia; CASAGRANDE, Fabio; HUG, Melanie N.; WANG, Lisha; HEINE, Philipp; KUMMER, Lutz; PLÜCKTHUN, Andreas; HENNIG, Michael. SPR-based fragment screening with neurotensin receptor 1 generates novel small molecule ligands. **PLoS ONE**, *[S. l.]*, v. 12, n. 5, p. e0175842, 2017. DOI: 10.1371/journal.pone.0175842. Disponível em: https://doi.org/10.1371/journal.pone.0175842. Acesso em: 26 jun. 2021.

HUGHES, J. P.; REES, S. S.; KALINDJIAN, S. B.; PHILPOTT, K. L. **Principles of early drug discoveryBritish Journal of Pharmacology**, 2011. DOI: 10.1111/j.1476-5381.2010.01127.x.

IMBERDIS, Thibaut; HEERES, James T.; YUEH, Han; FANG, Cheng; ZHEN, Jessie; RICH, Celeste B.; GLICKSMAN, Marcie; BEELER, Aaron B.; HARRIS, David A. Identification of Anti-prion Compounds using a Novel Cellular Assay. **The Journal of Biological Chemistry**, *[S. l.]*, v. 291, n. 50, p. 26164, 2016. DOI: 10.1074/JBC.M116.745612. Disponível em: /pmc/articles/PMC5207084/. Acesso em: 5 set. 2021.

JUNG, M. J.; PISTOLESI, D.; PANÀ, A. **Prions, prion diseases and decontamination.Igiene e sanità pubblica**, 2003. Disponível em: https://pubmed.ncbi.nlm.nih.gov/14981553/. Acesso em: 17 maio. 2021.

KABSCH, Wolfgang. Integration, scaling, space-group assignment and post-refinement. **Acta crystallographica. Section D, Biological crystallography**, *[S. l.]*, v. 66, n. Pt 2, p. 133–44, 2010. DOI: 10.1107/S0907444909047374. Disponível em: http://www.ncbi.nlm.nih.gov/pubmed/20124693. Acesso em: 6 nov. 2017.

KEEGAN, Ronan; WOJDYR, Marcin; WINTER, Graeme; ASHTON, Alun. DIMPLE : a difference map pipeline for the rapid screening of crystals on the beamline . **Acta Crystallographica Section A Foundations and Advances**, *[S. l.]*, v. 71, n. a1, p. s18–s18, 2015. DOI: 10.1107/s2053273315099702.

KLATZO, I.; GAJDUSEK, D. C.; ZIGAS, V. Pathology of Kuru. **Laboratory investigation; a journal of technical methods and pathology**, *[S. l.]*, v. 8, n. 4, p. 799–847, 1959. Disponível em: http://www.ncbi.nlm.nih.gov/pubmed/13665963. Acesso em: 7 nov. 2017.

KMETKO, Jan; HUSSEINI, Naji S.; NAIDES, Matthew; KALININ, Yevgeniy; THORNE, Robert E. Quantifying X-ray radiation damage in protein crystals at cryogenic temperatures. **Acta Crystallographica Section D: Biological Crystallography**, *[S. l.]*, v. 62, n. 9, p. 1030–1038, 2006. DOI: 10.1107/S0907444906023869. Disponível em: https://onlinelibrary.wiley.com/doi/pdf/10.1107/S0907444906023869. Acesso em: 18 jul. 2019.

KNAUS, Karen J.; MORILLAS, Manuel; SWIETNICKI, Wieslaw; MALONE, Michael; SUREWICZ, Witold K.; YEE, Vivien C. Crystal structure of the human prion protein reveals a mechanism for oligomerization. **Nature Structural Biology**, *[S. l.]*, v. 8, n. 9, p. 770–774, 2001. DOI: 10.1038/nsb0901-770. Disponível em: http://dx.doi.org/10.1038/nsb0901-770.

KNOWLES, Jonathan; GROMO, Gianni. **Target selection in drug discoveryNature Reviews Drug Discovery**Nat Rev Drug Discov, , 2003. DOI: 10.1038/nrd986. Disponível em: https://pubmed.ncbi.nlm.nih.gov/12509760/. Acesso em: 15 maio. 2021.

KONTEATIS, Zenon. What makes a good fragment in fragment-based drug discovery? **Expert Opinion on Drug Discovery**, *[S. l.]*, 2021. DOI: 10.1080/17460441.2021.1905629. Disponível em: https://www.tandfonline.com/action/journalInformation?journalCode=iedc20. Acesso em: 26 jun. 2021.

KRISSINEL, Evgeny; HENRICK, Kim. Inference of Macromolecular Assemblies from Crystalline State. **Journal of Molecular Biology**, *[S. l.]*, v. 372, n. 3, p. 774–797, 2007. DOI: 10.1016/J.JMB.2007.05.022. Disponível em: https://www.sciencedirect.com/science/article/pii/S0022283607006420?via%3Dihub. Acesso em: 11 jul. 2019.

KROJER, Tobias; TALON, Romain; PEARCE, Nicholas; COLLINS, Patrick; DOUANGAMATH, Alice; BRANDAO-NETO, Jose; DIAS, Alexandre; MARSDEN, Brian; VON DELFT, Frank. The XChemExplorer graphical workflow tool for routine or large-scale protein-ligand structure determination. **Acta Crystallographica Section D: Structural Biology**, *[S. l.]*, v. 73, p. 267–278, 2017. DOI: 10.1107/S2059798316020234. Disponível em: https://doi.org/10.1107/S2059798316020234. Acesso em: 3 maio. 2019.

KÜFFER, Alexander et al. The prion protein is an agonistic ligand of the G protein-coupled receptor Adgrg6. **Nature**, *[S. l.]*, v. 536, n. 7617, p. 464–468, 2016. DOI: 10.1038/nature19312. Disponível em: /pmc/articles/PMC5499706/?report=abstract. Acesso em: 4 set. 2020.

KURT, Timothy D. et al. Prion transmission prevented by modifying the β2-α2 loop structure of host PrPC. **Journal of Neuroscience**, *[S. l.]*, v. 34, n. 3, p. 1022–1027, 2014. DOI: 10.1523/JNEUROSCI.4636-13.2014. Disponível em: /pmc/articles/PMC3891945/. Acesso em: 17 maio. 2021.

KURT, Timothy D.; KONG, Qingzhong; SIGURDSON, Christina J. Human prion protein sequence elements impede cross-species chronic wasting disease transmission The Journal of Clinical Investigation. **J Clin Invest**, *[S. l.]*, v. 125, n. 4, p. 1485–1496, 2015. DOI: 10.1172/JCI79408.

KUWATA, Kazuo et al. Hot spots in prion protein for pathogenic conversion. **Proceedings of the National Academy of Sciences of the United States of America**, *[S. l.]*, v. 104, n. 29, p. 11921, 2007. DOI: 10.1073/PNAS.0702671104. Disponível em: /pmc/articles/PMC1924567/. Acesso em: 5 set. 2021.

LAMOREE, Bas; HUBBARD, Roderick E. **Current perspectives in fragment-based lead discovery (FBLD)Essays in Biochemistry**Portland Press Ltd, , 2017. DOI: 10.1042/EBC20170028. Disponível em: https://pubmed.ncbi.nlm.nih.gov/29118093/. Acesso em: 26 jun. 2021.

LEE, Jeongmin; KIM, Su Yeon; HWANG, Kyu Jam; JU, Young Ran; WOO, Hee Jong. Prion Diseases as Transmissible Zoonotic Diseases. **Osong Public Health and Research Perspectives**, *[S. l.]*, v. 4, n. 1, p. 57–66, 2013. DOI: 10.1016/j.phrp.2012.12.008. Disponível em: http://dx.doi.org/10.1016/j.phrp.2012.12.008.

LEE, Seungjoo; ANTONY, Lizamma; HARTMANN, Rune; KNAUS, Karen J.; SUREWICZ, Krystyna; SUREWICZ, Witold K.; YEE, Vivien C. Conformational diversity in prion protein variants influences intermolecular β-sheet formation. **The EMBO Journal**, *[S. l.]*, v. 29, n. 1, p. 251–262, Disponível em: http://www.ncbi.nlm.nih.gov/pubmed/19927125. Acesso em: 18 dez. 2017.

LI, Qingxin. **Application of Fragment-Based Drug Discovery to Versatile TargetsFrontiers in Molecular Biosciences**Frontiers Media S.A., , 2020. DOI: 10.3389/fmolb.2020.00180. Disponível em: www.frontiersin.org. Acesso em: 26 jun. 2021.

LIBERSKI, Pawel P.; SIKORSKA, Beata; LINDENBAUM, Shirley; GOLDFARB, Lev G.; MCLEAN, Catriona; HAINFELLNER, Johannes A.; BROWN, Paul. Kuru: Genes, cannibals and neuropathology. **Journal of Neuropathology and Experimental Neurology**, *[S. l.]*, v. 71, n. 2, p. 92–103, 2012. DOI: 10.1097/NEN.0b013e3182444efd. Disponível em: http://www.ncbi.nlm.nih.gov/pubmed/22249461. Acesso em: 18 dez. 2017.

LIMA, Gustavo M. A.; TALIBOV, Vladimir O.; JAGUDIN, Elmir; SELE, Celeste; NYBLOM, Maria; KNECHT, Wolfgang; LOGAN, Derek T.; SJOGREN, Tove; MUELLER, Uwe. FragMAX: The fragment-screening platform at the MAX IV Laboratory. **Acta Crystallographica Section D: Structural Biology**, *[S. l.]*, v. 76, p. 771–777, 2020. DOI: 10.1107/S205979832000889X.

LIN, Yibin. **What's happened over the last five years with high-throughput protein crystallization screening?Expert Opinion on Drug Discovery**Taylor and Francis Ltd, , 2018. DOI: 10.1080/17460441.2018.1465924. Disponível em: https://www.tandfonline.com/action/journalInformation?journalCode=iedc20. Acesso em: 26 jun. 2021.

LINDEN, Rafael; MARTINS, Vilma R.; PRADO, Marco A. M.; CAMMAROTA, Martín; IZQUIERDO, Iván; BRENTANI, Ricardo R. **Physiology of the prion proteinPhysiological Reviews**Physiol Rev, , 2008. DOI: 10.1152/physrev.00007.2007. Disponível em: https://pubmed.ncbi.nlm.nih.gov/18391177/. Acesso em: 5 set. 2021.

LONG, Fei; NICHOLLS, Robert A.; EMSLEY, Paul; GRAŽULIS, Saulius; MERKYS, Andrius; VAITKUS, Antanas; MURSHUDOV, Garib N. AceDRG: A stereochemical description generator for ligands. **Acta Crystallographica Section D: Structural**

Biology, *[S. l.]*, v. 73, n. 2, p. 112–122, 2017. DOI: 10.1107/S2059798317000067. Disponível em: http://www.ncbi.nlm.nih.gov/pubmed/28177307. Acesso em: 15 out. 2019.

LUFT, Joseph R.; SNELL, Edward H.; DETITTA, George T. **Lessons from high-throughput protein crystallization screening: 10 years of practical experienceExpert Opinion on Drug Discovery**, 2011. DOI: 10.1517/17460441.2011.566857.

LÜHRS, Thorsten; ZAHN, Ralph; WÜTHRICH, Kurt. Amyloid formation by recombinant full-length prion proteins in phospholipid bicelle solutions. **Journal of Molecular Biology**, *[S. l.]*, v. 357, n. 3, p. 833–841, 2006. DOI: 10.1016/j.jmb.2006.01.016. Disponível em: http://www.ncbi.nlm.nih.gov/pubmed/16466741. Acesso em: 24 ago. 2018.

M, Vogtherr; S, Grimme; B, Elshorst; DM, Jacobs; K, Fiebig; C, Griesinger; R, Zahn. Antimalarial drug quinacrine binds to C-terminal helix of cellular prion protein. **Journal of medicinal chemistry**, *[S. l.]*, v. 46, n. 17, p. 3563–3564, 2003. DOI: 10.1021/JM034093H. Disponível em: https://pubmed.ncbi.nlm.nih.gov/12904059/. Acesso em: 5 set. 2021.

MALLUCCI, G.; DICKINSON, Andrew; LINEHAN, Jacqueline; KLÖHN, Peter-Christian; BRANDNER, Sebastian; COLLINGE, John. Depleting Neuronal PrP in Prion Infection Prevents Disease and Reverses Spongiosis. **Science**, *[S. l.]*, v. 302, n. 5646, p. 871–874, 2003. DOI: 10.1126/science.1090187. Disponível em: http://www.ncbi.nlm.nih.gov/pubmed/14593181. Acesso em: 18 dez. 2017.

MASHIMA, Tsukasa et al. Development and structural determination of an anti-PrPC aptamer that blocks pathological conformational conversion of prion protein. **Scientific Reports**, *[S. l.]*, v. 10, n. 1, p. 1–11, 2020. DOI: 10.1038/s41598-020-61966-4. Disponível em: http://dx.doi.org/10.1038/s41598-020-61966-4.

MASTRIANNI, James A. The genetics of prion diseases. **Genetics in Medicine**, *[S. l.]*, v. 12, n. 4, p. 187–195, 2010. DOI: 10.1097/GIM.0b013e3181cd7374. Disponível em: http://www.ncbi.nlm.nih.gov/pubmed/20216075. Acesso em: 8 nov. 2017.

MCCOY, Airlie J.; GROSSE-KUNSTLEVE, Ralf W.; ADAMS, Paul D.; WINN, Martyn D.; STORONI, Laurent C.; READ, Randy J.; IUCR. *Phaser* crystallographic software. **Journal of Applied Crystallography**, *[S. l.]*, v. 40, n. 4, p. 658–674, 2007. DOI: 10.1107/S0021889807021206. Disponível em: http://www.ncbi.nlm.nih.gov/pubmed/19461840. Acesso em: 6 nov. 2017.

MCPHERSON, Alexander; GAVIRA, Jose A. **Introduction to protein crystallizationActa Crystallographica Section F:Structural Biology**

CommunicationsInternational Union of Crystallography, , 2014. DOI: 10.1107/S2053230X13033141. Disponível em: /pmc/articles/PMC3943105/. Acesso em: 25 abr. 2021.

MEYER, Rudolf K.; MCKINLEY, M. P.; BOWMAN, Karen A.; BRAUNFELD, Michael B.; BARRY, Ronald A.; PRUSINER, Stanley B. Separation and properties of cellular and scrapie prion proteins. **Proceedings of the National Academy of Sciences of the United States of America**, *[S. l.]*, v. 83, n. 8, p. 2310–2314, 1986. DOI: 10.1073/pnas.83.8.2310.

MINIKEL, Eric Vallabh et al. Quantifying prion disease penetrance using large population control cohorts. **Science Translational Medicine**, *[S. l.]*, v. 8, n. 322, 2016. DOI: 10.1126/scitranslmed.aad5169. Disponível em: www.ScienceTranslationalMedicine.org. Acesso em: 17 maio. 2021.

MURRAY, Christopher W.; REES, David C. The rise of fragment-based drug discovery. **Nature Chemistry**, *[S. l.]*, v. 1, n. 3, p. 187–192, 2009. DOI: 10.1038/nchem.217. Disponível em: www.nature.com/naturechemistry. Acesso em: 26 jun. 2021.

MURSHUDOV, Garib N.; SKUBÁK, Pavol; LEBEDEV, Andrey A.; PANNU, Navraj S.; STEINER, Roberto A.; NICHOLLS, Robert A.; WINN, Martyn D.; LONG, Fei; VAGIN, Alexei A. REFMAC5 for the refinement of macromolecular crystal structures. **Acta crystallographica. Section D, Biological crystallography**, *[S. l.]*, v. 67, n. Pt 4, p. 355–67, 2011. DOI: 10.1107/S0907444911001314. Disponível em: http://www.ncbi.nlm.nih.gov/pubmed/21460454. Acesso em: 24 ago. 2018.

NG, Jia Tsing; DEKKER, Carien; KROEMER, Markus; OSBORNE, Michael; VON DELFT, Frank. Using textons to rank crystallization droplets by the likely presence of crystals. **Acta Crystallographica Section D: Biological Crystallography**, *[S. l.]*, v. 70, n. 10, p. 2702–2718, 2014. DOI: 10.1107/S1399004714017581.

NORSTROM, Eric M.; MASTRIANNI, James A. The AGAAAAGA palindrome in PrP is required to generate a productive PrPSc-PrPC complex that leads to prion propagation. **The Journal of biological chemistry**, *[S. l.]*, v. 280, n. 29, p. 27236–43, 2005. DOI: 10.1074/jbc.M413441200. Disponível em: http://www.ncbi.nlm.nih.gov/pubmed/15917252. Acesso em: 7 dez. 2018.

O'REILLY, Marc; CLEASBY, Anne; DAVIES, Thomas G.; HALL, Richard J.; LUDLOW, R. Frederick; MURRAY, Christopher W.; TISI, Dominic; JHOTI, Harren. **Crystallographic screening using ultra-low-molecular-weight ligands to guide drug designDrug Discovery Today**Elsevier Ltd, , 2019. DOI: 10.1016/j.drudis.2019.03.009.

OESCH, B. et al. A cellular gene encodes scrapie PrP 27-30 protein. **Cell**, *[S. l.]*, v. 40, n. 4, p. 735–46, 1985. Disponível em: http://www.ncbi.nlm.nih.gov/pubmed/2859120. Acesso em: 8 nov. 2017.

OREM, Nicholas R.; GEOGHEGAN, James C.; DELEAULT, Nathan R.; KASCSAK, Richard; SUPATTAPONE, Surachai. Copper (II) ions potently inhibit purified PrPres amplification. **Journal of Neurochemistry**, *[S. l.]*, v. 96, n. 5, p. 1409–1415, 2006. DOI: 10.1111/j.1471-4159.2006.03650.x. Disponível em: http://doi.wiley.com/10.1111/j.1471-4159.2006.03650.x. Acesso em: 10 nov. 2017.

OSBORNE, James; PANOVA, Stanislava; RAPTI, Magdalini; URUSHIMA, Tatsuya; JHOTI, Harren. **Fragments: Where are we now?Biochemical Society Transactions**Portland Press Ltd, , 2020. DOI: 10.1042/BST20190694. Disponível em: /biochemsoctrans/article/48/1/271/221949/Fragments-where-are-we-now. Acesso em: 27 jun. 2021.

PALMER, Ira; WINGFIELD, Paul T. Preparation and extraction of insoluble (Inclusion-body) proteins from Escherichia coli. **Current Protocols in Protein Science**, *[S. l.]*, v. 1, n. SUPPL.70, 2012. DOI: 10.1002/0471140864.ps0603s70. Disponível em: http://www.kinematica-inc.com. Acesso em: 29 jun. 2019.

PANEGYRES, Peter K.; ARMARI, Elizabeth. Therapies for human prion diseases. **American journal of neurodegenerative disease**, *[S. l.]*, v. 2, n. 3, p. 176–86, 2013. Disponível em: http://www.ncbi.nlm.nih.gov/pubmed/24093082. Acesso em: 18 dez. 2017.

PATEL, Disha; BAUMAN, Joseph D.; ARNOLD, Eddy. Advantages of crystallographic fragment screening: Functional and mechanistic insights from a powerful platform for efficient drug discovery. **Progress in Biophysics and Molecular Biology**, *[S. l.]*, v. 116, n. 2–3, p. 92–100, 2014. DOI: 10.1016/J.PBIOMOLBIO.2014.08.004. Disponível em: https://www.sciencedirect.com/science/article/pii/S0079610714000790?via%3Dihub. Acesso em: 7 maio. 2019.

PEARCE, Nicholas M. et al. A multi-crystal method for extracting obscured crystallographic states from conventionally uninterpretable electron density. **Nature Communications**, *[S. l.]*, v. 8, 2017. DOI: 10.1038/ncomms15123. Disponível em: www.nature.com/naturecommunications. Acesso em: 28 jun. 2019.

PFEIFFER, C. C.; BRAVERMAN, E. R. Zinc, the brain and behavior. **Biological Psychiatry**, *[S. l.]*, v. 17, n. 4, p. 513–532, 1982. Disponível em: http://www.ncbi.nlm.nih.gov/pubmed/7082716. Acesso em: 10 nov. 2017.

POTTERTON, Liz et al. CCP 4 i 2: The new graphical user interface to the CCP 4

program suite. **Acta Crystallographica Section D: Structural Biology**, *[S. l.]*, v. 74, p. 68–84, 2018. DOI: 10.1107/S2059798317016035. Disponível em: https://doi.org/10.1107/S2059798317016035. Acesso em: 26 jun. 2019.

PRIOLA, Suzette A.; RAINES, Anne; CAUGHEY, Winslow S. Porphyrin and phthalocyanine antiscrapie compounds. **Science**, *[S. l.]*, v. 287, n. 5457, p. 1503–1506, 2000. DOI: 10.1126/science.287.5457.1503. Disponível em: https://pubmed.ncbi.nlm.nih.gov/10688802/. Acesso em: 5 set. 2021.

PRUSINER, S. B. Novel proteinaceous infectious particles cause scrapie. **Science (New York, N.Y.)**, *[S. l.]*, v. 216, n. 4542, p. 136–44, 1982. Disponível em: http://www.ncbi.nlm.nih.gov/pubmed/6801762. Acesso em: 7 nov. 2017.

PRUSINER, Stanley B. et al. Transgenetic studies implicate interactions between homologous PrP isoforms in scrapie prion replication. **Cell**, *[S. l.]*, v. 63, n. 4, p. 673–686, 1990. DOI: 10.1016/0092-8674(90)90134-Z. Disponível em: http://www.cell.com/article/009286749090134Z/fulltext. Acesso em: 17 maio. 2021.

PRUSINER, Stanley B. Prions. **Proceedings of the National Academy of Sciences**, *[S. l.]*, v. 95, n. 23, p. 13363–13383, 1998. DOI: 10.1073/pnas.95.23.13363. Disponível em: http://www.pnas.org/content/95/23/13363.abstract.

RAINARD, Julie M.; PANDARAKALAM, George C.; MCELROY, Stuart P. **Using Microscale Thermophoresis to Characterize Hits from High-Throughput Screening: A European Lead Factory PerspectiveSLAS Discovery**SAGE Publications Inc., , 2018. DOI: 10.1177/2472555217744728. Disponível em: /pmc/articles/PMC5824829/. Acesso em: 26 jun. 2021.

RAMBOLD, Angelika S.; MÜLLER, Veronika; RON, Uri; BEN-TAL, Nir; WINKLHOFER, Konstanze F.; TATZELT, Jörg. Stress-protective signalling of prion protein is corrupted by scrapie prions. **EMBO Journal**, *[S. l.]*, v. 27, n. 14, p. 1974–1984, 2008. DOI: 10.1038/emboj.2008.122. Disponível em: /pmc/articles/PMC2486277/. Acesso em: 25 abr. 2021.

RATHI, Prakash Chandra; LUDLOW, R. Frederick; HALL, Richard J.; MURRAY, Christopher W.; MORTENSON, Paul N.; VERDONK, Marcel L. Predicting “Hot” and “Warm” Spots for Fragment Binding. **Journal of Medicinal Chemistry**, *[S. l.]*, v. 60, n. 9, p. 4036–4046, 2017. DOI: 10.1021/acs.jmedchem.7b00366.

RAYMOND, G. J. et al. Evidence of a molecular barrier limiting susceptibility of humans, cattle and sheep to chronic wasting disease. **EMBO Journal**, *[S. l.]*, v. 19, n. 17, p. 4425–4430, 2000. DOI: 10.1093/emboj/19.17.4425. Disponível em: /pmc/articles/PMC302048/. Acesso em: 17 maio. 2021.

REIDENBACH, Andrew G. et al. Multimodal small-molecule screening for human prion protein binders. **Journal of Biological Chemistry**, *[S. l.]*, v. 295, n. 39, p. 13516–13531, 2020. DOI: 10.1074/jbc.ra120.014905. Disponível em: http://dx.doi.org/10.1074/jbc.RA120.014905.

RESNICK, Efrat et al. Rapid Covalent-Probe Discovery by Electrophile-Fragment Screening. **Journal of the American Chemical Society**, *[S. l.]*, v. 141, n. 22, p. 8951–8968, 2019. DOI: 10.1021/jacs.9b02822.

ROBERT, Xavier; GOUET, Patrice. Deciphering key features in protein structures with the new ENDscript server. **Nucleic Acids Research**, *[S. l.]*, v. 42, n. W1, p. W320–W324, 2014. DOI: 10.1093/nar/gku316. Disponível em: http://espript.ibcp.fr. Acesso em: 4 set. 2020.

ROBSON-TULL, Jacob. Biophysical screening in fragment-based drug design: A brief overview. **Bioscience Horizons**, *[S. l.]*, v. 11, 2018. DOI: 10.1093/biohorizons/hzy015.

ROHMAN, Mattias; WINGFIELD, Jonathan. High-throughput screening using mass spectrometry within drug discovery. *In*: **Methods in Molecular Biology**. [s.l.] : Humana Press Inc., 2016. v. 1439p. 47–63. DOI: 10.1007/978-1-4939-3673-1_3. Disponível em: https://pubmed.ncbi.nlm.nih.gov/27316987/. Acesso em: 26 jun. 2021.

ROUCOU, Xavier. Regulation of PrPC signaling and processing by dimerization. **Frontiers in Cell and Developmental Biology**, *[S. l.]*, v. 2, p. 57, 2014. DOI: 10.3389/fcell.2014.00057.

SABAREESAN, A. T.; UDGAONKAR, Jayant B. Pathogenic Mutations within the Disordered Palindromic Region of the Prion Protein Induce Structure Therein and Accelerate the Formation of Misfolded Oligomers. **Journal of Molecular Biology**, *[S. l.]*, v. 428, n. 20, p. 3935–3947, 2016. DOI: 10.1016/j.jmb.2016.08.015. Disponível em: https://pubmed.ncbi.nlm.nih.gov/27545411/. Acesso em: 23 maio. 2021.

SABORIO, G. P.; PERMANNE, B.; SOTO, C. Sensitive detection of pathological prion protein by cyclic amplification of protein misfolding. **Nature**, *[S. l.]*, v. 411, n. 6839, p. 810–813, 2001. DOI: 10.1038/35081095. Disponível em: www.nature.com. Acesso em: 31 maio. 2021.

SAFAR, Jiri G.; DEARMOND, Stephen J.; KOCIUBA, Katarzyna; DEERING, Camille; DIDORENKO, Svetlana; BOUZAMONDO-BERNSTEIN, Essia; PRUSINER, Stanley B.; TREMBLAY, Patrick. Prion clearance in bigenic mice. **Journal of General Virology**, *[S. l.]*, v. 86, n. 10, p. 2913–2923, 2005. DOI: 10.1099/vir.0.80947-0. Disponível em: http://www.ncbi.nlm.nih.gov/pubmed/16186247. Acesso em: 18 dez.

2017.

SANCHEZ-GARCIA, Jonatan; FERNANDEZ-FUNEZ, Pedro. D159 and S167 are protective residues in the prion protein from dog and horse, two prion-resistant animals. **Neurobiology of Disease**, *[S. l.]*, v. 119, p. 1–12, 2018. DOI: 10.1016/J.NBD.2018.07.011. Disponível em: https://www.sciencedirect.com/science/article/pii/S0969996118302481?dgcid=rss_sd_all. Acesso em: 7 dez. 2018.

SCHÄTZL, Hermann M.; COSTA, Maria Da; TAYLOR, Leslie; COHEN, Fred E.; PRUSINER, Stanley B. Prion Protein Gene Variation Among Primates. **Journal of Molecular Biology**, *[S. l.]*, v. 245, n. 4, p. 362–374, 1995. DOI: 10.1006/jmbi.1994.0030. Disponível em: https://ac.els-cdn.com/S0022283684700301/1-s2.0-S0022283684700301-main.pdf?_tid=c5b74bcc-c3ea-11e7-856c-00000aab0f01&acdnat=1510080058_5344b0d4e9a97a012b5c33b2aeb17675. Acesso em: 7 nov. 2017.

SCHIEBEL, Johannes et al. High-Throughput Crystallography: Reliable and Efficient Identification of Fragment Hits. **Structure**, *[S. l.]*, v. 24, n. 8, p. 1398–1409, 2016. DOI: 10.1016/j.str.2016.06.010.

SCHMITT-ULMS, Gerold; MEHRABIAN, Mohadeseh; WILLIAMS, Declan; EHSANI, Sepehr. The IDIP framework for assessing protein function and its application to the prion protein. **Biological Reviews**, *[S. l.]*, 2021. DOI: 10.1111/BRV.12731. Disponível em: https://onlinelibrary.wiley.com/doi/full/10.1111/brv.12731. Acesso em: 5 set. 2021.

SCHNEIDER, Thomas R.; SHELDRICK, George M. Substructure solution with *SHELXD*. **Acta Crystallographica Section D Biological Crystallography**, *[S. l.]*, v. 58, n. 10, p. 1772–1779, 2002. DOI: 10.1107/S0907444902011678. Disponível em: http://scripts.iucr.org/cgi-bin/paper?S0907444902011678. Acesso em: 23 maio. 2019.

SCHREUDER, H. A.; GROENDIJK, H.; VAN DER LAAN, J. M.; WIERENGA, R. K. The transfer of protein crystals from their original mother liquor to a solution with a completely different precipitant. **Journal of Applied Crystallography**, *[S. l.]*, v. 21, n. 5, p. 426–429, 1988. DOI: 10.1107/S0021889888004108.

SCHULLER, Marion et al. Fragment binding to the Nsp3 macrodomain of SARS-CoV-2 identified through crystallographic screening and computational docking. **Science Advances**, *[S. l.]*, v. 7, n. 16, p. eabf8711, 2021. DOI: 10.1126/sciadv.abf8711. Disponível em: https://advances.sciencemag.org/lookup/doi/10.1126/sciadv.abf8711. Acesso em: 1 maio. 2021.

SHUN, Tong Yinh; LAZO, John S.; SHARLOW, Elizabeth R.; JOHNSTON, Paul A. **Identifying actives from HTS data sets: Practical approaches for the selection of an appropriate HTS data-processing method and quality control reviewJournal of Biomolecular Screening**SAGE PublicationsSage CA: Los Angeles, CA, , 2011. DOI: 10.1177/1087057110389039. Disponível em: www.slas.org. Acesso em: 26 jun. 2021.

SIGURDSSON, Bjorn. Rida, A chronic encephalitis of Sheep With General Remarks on Infections Which Develop Slowly and Some of Their Special Characteristics. **British Veterinary Journal**, *[S. l.]*, p. 341–354, 1954. DOI: 10.1016/S0007-1935(17)50172-4. Disponível em: https://ac.els-cdn.com/S0007193517501724/1-s2.0-S0007193517501724-main.pdf?_tid=68e75886-c31f-11e7-9f00-00000aacb35e&acdnat=1509992713_2cb8bb74ef4d1d172c6c8e0087a3bf9e. Acesso em: 6 nov. 2017.

SORENSON, Alanna E.; SCHAEFFER, Patrick M. High-throughput differential scanning fluorimetry of GFP-tagged proteins. *In*: **Methods in Molecular Biology**. [s.l.] : Humana Press Inc., 2020. v. 2089p. 69–85. DOI: 10.1007/978-1-0716-0163-1_5. Disponível em: https://pubmed.ncbi.nlm.nih.gov/31773648/. Acesso em: 26 jun. 2021.

SPAGNOLLI, Giovanni; RIGOLI, Marta; ORIOLI, Simone; SEVILLANO, Alejandro M.; FACCIOLI, Pietro; WILLE, Holger; BIASINI, Emiliano; REQUENA, Jesús R. Full atomistic model of prion structure and conversion. **PLOS Pathogens**, *[S. l.]*, v. 15, n. 7, p. e1007864, 2019. DOI: 10.1371/JOURNAL.PPAT.1007864. Disponível em: https://journals.plos.org/plospathogens/article?id=10.1371/journal.ppat.1007864. Acesso em: 5 set. 2021.

SPEVACEK, Ann R.; EVANS, Eric G. B.; MILLER, Jillian L.; MEYER, Heidi C.; PELTON, Jeffrey G.; MILLHAUSER, Glenn L. Zinc Drives a Tertiary Fold in the Prion Protein with Familial Disease Mutation Sites at the Interface. **Structure/Folding and Design**, *[S. l.]*, v. 21, p. 236–246, 2013. DOI: 10.1016/j.str.2012.12.002. Disponível em: http://dx.doi.org/10.1016/j.str.2012.12.002. Acesso em: 10 nov. 2017.

TEN EYCK, Lynn F. Fast Fourier transform calculation of electron density maps. **Methods in Enzymology**, *[S. l.]*, v. 115, n. C, p. 324–337, 1985. DOI: 10.1016/0076-6879(85)15024-X.

TICKLE, Ian J. Statistical quality indicators for electron-density maps. **Acta Crystallographica Section D: Biological Crystallography**, *[S. l.]*, v. 68, n. 4, p. 454–467, 2012. DOI: 10.1107/S0907444911035918. Disponível em: /pmc/articles/PMC3322605/?report=abstract. Acesso em: 14 set. 2020.

TOMPA, Peter; TUSNÁDY, Gábor E.; FRIEDRICH, Peter; SIMON, István. The role of dimerization in prion replication. **Biophysical journal**, *[S. l.]*, v. 82, n. 4, p. 1711–8,

2002. DOI: 10.1016/S0006-3495(02)75523-9. Disponível em: http://www.ncbi.nlm.nih.gov/pubmed/11916832. Acesso em: 24 ago. 2018.

TRAKHANOV, Sergei; KREIMER, David I.; PARKIN, Sean; AMES, Giovanna Ferro Luzzi; RUPP, Bernhard. Cadmium-induced crystallization of proteins: II. Crystallization of the Salmonella typhimurium histidine-binding protein in complex with L-histidine, L-arginine, or L-lysine. **Protein Science**, *[S. l.]*, v. 7, n. 3, p. 600–604, 1998. DOI: 10.1002/pro.5560070308. Disponível em: /pmc/articles/PMC2143943/?report=abstract. Acesso em: 25 abr. 2021.

VANIK, David L.; SUREWICZ, Krystyna A.; SUREWICZ, Witold K. Molecular basis of barriers for interspecies transmissibility of mammalian prions. **Molecular Cell**, *[S. l.]*, v. 14, n. 1, p. 139–145, 2004. DOI: 10.1016/S1097-2765(04)00155-8.

VIDAL, Enric et al. Dogs are resistant to prion infection, due to the presence of aspartic or glutamic acid at position 163 of their prion protein. **FASEB Journal**, *[S. l.]*, v. 34, n. 3, p. 3969–3982, 2020. DOI: 10.1096/fj.201902646R. Disponível em: https://pubmed.ncbi.nlm.nih.gov/31944411/. Acesso em: 17 maio. 2021.

VONRHEIN, Clemens; FLENSBURG, Claus; KELLER, Peter; SHARFF, Andrew; SMART, Oliver; PACIOREK, Wlodek; WOMACK, Thomas; BRICOGNE, Gérard. Data processing and analysis with the autoPROC toolbox. **Acta crystallographica. Section D, Biological crystallography**, *[S. l.]*, v. 67, n. Pt 4, p. 293–302, 2011. DOI: 10.1107/S0907444911007773. Disponível em: http://www.ncbi.nlm.nih.gov/pubmed/21460447. Acesso em: 24 ago. 2018.

WATSON, Neil et al. The importance of ongoing international surveillance for Creutzfeldt–Jakob disease. **Nature Reviews Neurology 2021 17:6**, *[S. l.]*, v. 17, n. 6, p. 362–379, 2021. DOI: 10.1038/s41582-021-00488-7. Disponível em: https://www.nature.com/articles/s41582-021-00488-7. Acesso em: 5 set. 2021.

WATT, Nicole T.; GRIFFITHS, Heledd H.; HOOPER, Nigel M. Neuronal zinc regulation and the prion protein. **Prion**, *[S. l.]*, v. 7, n. 3, p. 203–8, 2013. DOI: 10.4161/pri.24503. Disponível em: http://www.landesbioscience.com/journals/prion/article/24503/.

WINN, Martyn D. et al. Overview of the CCP4 suite and current developments. **Acta Crystallographica Section D: Biological Crystallography**, *[S. l.]*, v. 67, n. 4, p. 235–242, 2011. DOI: 10.1107/S0907444910045749. Disponível em: http://www.ncbi.nlm.nih.gov/pubmed/21460441. Acesso em: 24 ago. 2018.

WINTER, Graeme et al. DIALS: Implementation and evaluation of a new integration package. **Acta Crystallographica Section D: Structural Biology**, *[S. l.]*, v. 74, p. 85–97, 2018. DOI: 10.1107/S2059798317017235. Disponível em:

https://doi.org/10.1107/S2059798317017235. Acesso em: 19 fev. 2019.

WOOD, Daniel J. et al. FragLites - Minimal, Halogenated Fragments Displaying Pharmacophore Doublets. An Efficient Approach to Druggability Assessment and Hit Generation. **Journal of Medicinal Chemistry**, *[S. l.]*, v. 62, n. 7, p. 3741–3752, 2019. DOI: 10.1021/acs.jmedchem.9b00304.

WOOK HYEON, Jae et al. Discovery of Novel Anti-prion Compounds Using In Silico and In Vitro Approaches. **Nature Publishing Group**, *[S. l.]*, v. 5, p. 14944, 2015. DOI: 10.1038/srep14944. Disponível em: www.nature.com/scientificreports. Acesso em: 5 set. 2021.

WU, Bainan; BARILE, Elisa; DE, Surya; WEI, Jun; PURVES, Angela; PELLECCHIA, Maurizio. High-Throughput Screening by Nuclear Magnetic Resonance (HTS by NMR) for the Identification of PPIs Antagonists. **Current Topics in Medicinal Chemistry**, *[S. l.]*, v. 15, n. 20, p. 2032–2042, 2015. DOI: 10.2174/1568026615666150519102459. Disponível em: https://pubmed.ncbi.nlm.nih.gov/25986689/. Acesso em: 26 jun. 2021.

YAMAGUCHI, Keiichi et al. A designer molecular chaperone against transmissible spongiform encephalopathy slows disease progression in mice and macaques. **Nature Biomedical Engineering 2019 3:3**, *[S. l.]*, v. 3, n. 3, p. 206–219, 2019. DOI: 10.1038/s41551-019-0349-8. Disponível em: https://www.nature.com/articles/s41551-019-0349-8. Acesso em: 5 set. 2021.

ZABEL, Mark D.; AVERY, Anne C. **Prions—Not Your Immunologist's PathogenPLoS Pathogens**Public Library of Science, , 2015. DOI: 10.1371/journal.ppat.1004624. Disponível em: /pmc/articles/PMC4335031/. Acesso em: 17 maio. 2021.

ZAHN, Ralph et al. NMR solution structure of the human prion protein. **Proceedings of the National Academy of Sciences of the United States of America**, *[S. l.]*, v. 97, n. 1, p. 145–150, 2000. DOI: 10.1073/pnas.97.1.145.

ZHANG, Jiapu. The structural stability of wild-type horse prion protein. **Journal of Biomolecular Structure and Dynamics**, *[S. l.]*, v. 29, n. 2, p. 369–377, 2011. DOI: 10.1080/07391102.2011.10507391. Disponível em: https://pubmed.ncbi.nlm.nih.gov/21875155/. Acesso em: 17 maio. 2021.

Table shows all tested compounds in our fragment screening: 2d structure of each compound, their respective library, code and details of the experiment such as compound concentration in the drop, solvent fraction, soaking time, if crystal harvesting was successful or not, mounting time and resolution of the collected dataset.

Entry ID	Structure	Mol Weight (g/mol)	Library Name	Compound Code	Compound Concentration (mM)	Solvent Fraction (%, v/v)	Soaking Time	Harvest Status	Crystal Name	Mounting Time	Resolution Overall (Å)
1	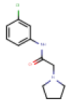	238.72	DSIpoised	Z2735692823	23.80	5	01:04:08	done	HPrP-x0207	00:00:25	43.025 - 2.318
2	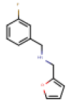	205.23	DSIpoised	Z2737076969	23.80	5	01:04:30	done	HPrP-x0208	00:00:20	42.999 - 3.011
3	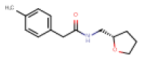	233.31	DSIpoised	Z2064898339	23.80	5	01:04:44	done	HPrP-x0209	00:00:13	51.668 - 3.376
4	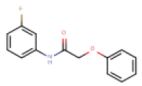	245.25	DSIpoised	Z19735192	23.80	5	01:05:05	done	HPrP-x0210	00:00:18	42.678 - 2.611
5	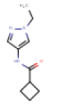	193.25	DSIpoised	Z373768900	23.80	5	01:05:27	done	HPrP-x0211	00:00:21	43.178 - 2.498
6	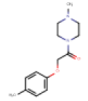	248.33	DSIpoised	Z2856434836	23.80	5	01:06:03	done	HPrP-x0212	00:00:35	42.887 - 2.710
7	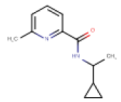	204.27	DSIpoised	Z287256168	23.80	5	01:06:22	done	HPrP-x0213	00:00:16	None
8	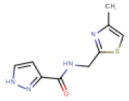	222.27	DSIpoised	Z466628048	23.80	5	01:06:41	done	HPrP-x0214	00:00:16	None

Entry ID	Structure	Mol Weight (g/mol)	Library Name	Compound Code	Compound Concentration (mM)	Solvent Fraction (%, v/v)	Soaking Time	Harvest Status	Crystal Name	Mounting Time	Resolution Overall (Å)
9	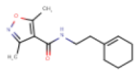	248.33	DSIpoised	Z69092635	23.80	5	01:06:59	done	HPrP-x0215	00:00:16	None
10	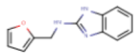	213.24	DSIpoised	Z57299526	23.80	5	01:07:22	fail		00:00:22	
11	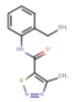	247.32	DSIpoised	Z89385775	23.80	5	01:08:00	done	HPrP-x0216	00:00:36	None
12	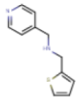	204.29	DSIpoised	Z2856434816	23.80	5	01:08:26	done	HPrP-x0217	00:00:25	None
13	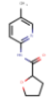	206.25	DSIpoised	Z71580604	23.80	5	01:08:47	done	HPrP-x0218	00:00:19	42.799 - 2.507
14	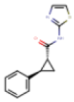	244.31	DSIpoised	Z2064107709	23.80	5	01:09:20	done	HPrP-x0219	00:00:30	None
15	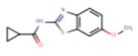	248.30	DSIpoised	Z27678561	23.80	5	01:10:17	done	HPrP-x0220	00:00:47	65.701 - 2.173
16	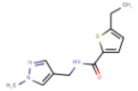	249.33	DSIpoised	Z804566442	23.80	5	01:10:59	done	HPrP-x0221	00:00:31	42.693 - 2.520
17	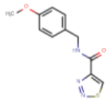	249.29	DSIpoised	Z741218268	23.80	5	01:11:30	done	HPrP-x0222	00:00:26	66.045 - 2.590

Entry ID	Structure	Mol Weight (g/mol)	Library Name	Compound Code	Compound Concentration (mM)	Solvent Fraction (%, v/v)	Soaking Time	Harvest Status	Crystal Name	Mounting Time	Resolution Overall (Å)
18	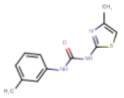	247.32	DSIpoised	Z44602971	23.80	5	01:13:18	done	HPrP-x0223	00:01:45	42.180 - 2.265
19		222.63	DSIpoised	Z86622311	23.80	5	01:13:50	done	HPrP-x0224	00:00:30	42.699 - 2.571
20	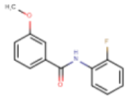	245.25	DSIpoised	Z28290384	23.80	5	01:14:16	done	HPrP-x0225	00:00:23	65.394 - 2.673
21	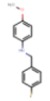	231.27	DSIpoised	Z57328997	23.80	5	01:14:46	done	HPrP-x0226	00:00:29	50.61 - 4.13
22	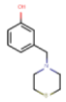	209.31	DSIpoised	Z2856434857	23.80	5	01:15:22	done	HPrP-x0227	00:00:35	42.724 - 2.961
23	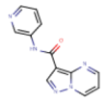	239.24	DSIpoised	Z296054478	23.80	5	01:16:19	done	HPrP-x0228	00:00:55	42.723 - 2.538
24	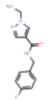	247.27	DSIpoised	Z1203107138	23.80	5	01:17:02	done	HPrP-x0229	00:00:42	65.215 - 2.470
25	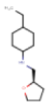	211.35	DSIpoised	Z2856434866	23.80	5	01:17:25	done	HPrP-x0230	00:00:22	50.704 - 2.274
26	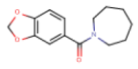	247.29	DSIpoised	Z31432226	23.80	5	01:17:40	done	HPrP-x0231	00:00:13	42.861 - 2.501

Entry ID	Structure	Mol Weight (g/mol)	Library Name	Compound Code	Compound Concentration (mM)	Solvent Fraction (%, v/v)	Soaking Time	Harvest Status	Crystal Name	Mounting Time	Resolution Overall (Å)
27	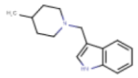	228.34	DSIpoised	Z2856434912	23.80	5	01:18:14	done	HPrP-x0232	00:00:32	50.728 - 2.668
28	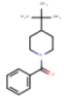	245.37	DSIpoised	Z1217741507	23.80	5	01:18:43	done	HPrP-x0233	00:00:28	42.497 - 3.020
29	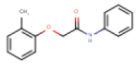	241.29	DSIpoised	Z19733979	23.80	5	01:19:02	done	HPrP-x0234	00:00:17	50.950 - 2.474
30	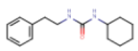	246.35	DSIpoised	Z44585920	23.80	5	01:19:28	done	HPrP-x0235	00:00:25	42.580 - 2.574
31	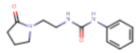	247.30	DSIpoised	Z2472938267	23.80	5	01:19:57	done	HPrP-x0236	00:00:27	42.860 - 2.296
32	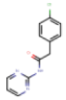	247.68	DSIpoised	Z203581214	23.80	5	01:20:22	done	HPrP-x0237	00:00:23	65.263 - 2.265
33	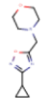	209.25	DSIpoised	Z295848548	23.80	5	01:21:27	done	HPrP-x0238	00:01:02	65.262 - 2.454
34	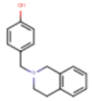	239.32	DSIpoised	Z2856434812	23.80	5	01:21:52	done	HPrP-x0239	00:00:24	50.84 - 3.30
35	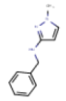	187.25	DSIpoised	Z1401333862	23.80	5	01:22:13	done	HPrP-x0240	00:00:19	42.814 - 2.493

Entry ID	Structure	Mol Weight (g/mol)	Library Name	Compound Code	Compound Concentration (mM)	Solvent Fraction (%, v/v)	Soaking Time	Harvest Status	Crystal Name	Mounting Time	Resolution Overall (Å)
36	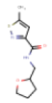	226.29	DSIpoised	Z1881545321	23.80	5	01:22:45	done	HPrP-x0241	00:00:31	39.818 - 2.400
37		239.33	DSIpoised	Z2856434929	23.80	5	01:23:18	done	HPrP-x0242	00:00:31	50.659 - 2.604
38	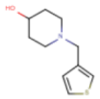	197.30	DSIpoised	Z2856434899	23.80	5	01:23:29	fail		00:00:08	
39		206.21	DSIpoised	Z240297434	23.80	5	01:23:55	done	HPrP-x0243	00:00:23	50.654 - 2.836
40	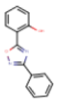	238.25	DSIpoised	Z276351322	23.80	5	01:24:20	done	HPrP-x0244	00:00:23	65.079 - 2.486
41	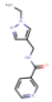	230.27	DSIpoised	Z275181224	23.80	5	01:25:25	done	HPrP-x0245	00:01:03	50.727 - 2.198
42	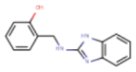	239.28	DSIpoised	Z1587220559	23.80	5	01:25:49	done	HPrP-x0246	00:00:21	42.934 - 2.392
43	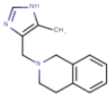	227.31	DSIpoised	Z2856434879	23.80	5	01:41:42	done	HPrP-x0247	00:02:26	42.842 - 2.673
44	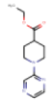	235.29	DSIpoised	Z31217395	23.80	5	01:27:26	done	HPrP-x0248	00:00:42	42.726 - 2.874

Entry ID	Structure	Mol Weight (g/mol)	Library Name	Compound Code	Compound Concentration (mM)	Solvent Fraction (%, v/v)	Soaking Time	Harvest Status	Crystal Name	Mounting Time	Resolution Overall (Å)
45	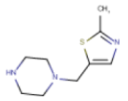	197.30	DSIpoised	Z1171217421	23.80	5	01:27:49	done	HPrP-x0249	00:00:21	50.679 - 2.787
46	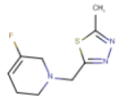	213.27	DSIpoised	Z1619978933	23.80	5	01:28:06	done	HPrP-x0250	00:00:16	42.994 - 2.381
47		207.28	DSIpoised	Z1675346324	23.80	5	01:28:23	done	HPrP-x0251	00:00:16	42.71 - 2.83
48	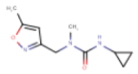	209.25	DSIpoised	Z369936976	23.80	5	01:29:27	done	HPrP-x0252	00:01:03	65.437 - 2.346
49	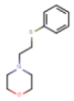	223.33	DSIpoised	Z2856434865	23.80	5	01:29:49	done	HPrP-x0253	00:00:20	65.452 - 2.567
50	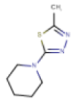	183.27	DSIpoised	Z1251207602	23.80	5	01:30:39	done	HPrP-x0254	00:00:47	None
51		208.31	DSIpoised	Z1694504496	23.80	5	01:32:33	done	HPrP-x0255	00:01:53	None
52	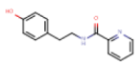	242.28	DSIpoised	Z730649594	23.80	5	01:33:29	done	HPrP-x0256	00:00:54	65.370 - 2.435
53	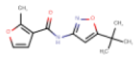	248.28	DSIpoised	Z1086293874	23.80	5	01:33:57	done	HPrP-x0257	00:00:26	65.613 - 2.659

Entry ID	Structure	Mol Weight (g/mol)	Library Name	Compound Code	Compound Concentration (mM)	Solvent Fraction (%, v/v)	Soaking Time	Harvest Status	Crystal Name	Mounting Time	Resolution Overall (Å)
54	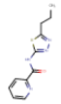	248.30	DSIpoised	Z52425517	23.80	5	01:34:18	done	HPrP-x0258	00:00:18	42.733 - 2.437
55		223.27	DSIpoised	Z1983897532	23.80	5	01:34:32	done	HPrP-x0259	00:00:13	65.512 - 2.487
56		249.31	DSIpoised	Z17497990	23.80	5	01:35:11	done	HPrP-x0260	00:00:36	42.701 - 2.723
57	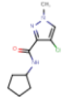	227.69	DSIpoised	Z275151340	23.80	5	01:35:30	done	HPrP-x0261	00:00:16	42.777 - 2.721
58	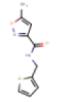	222.26	DSIpoised	Z29692148	23.80	5	01:35:48	done	HPrP-x0262	00:00:16	42.810 - 2.404
59	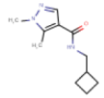	207.28	DSIpoised	Z396380540	23.80	5	01:36:22	done	HPrP-x0263	00:00:32	42.823 - 2.510
60	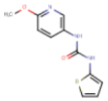	249.29	DSIpoised	Z1152242726	23.80	5	01:36:38	done	HPrP-x0264	00:00:15	51.180 - 3.099
61	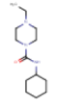	239.36	DSIpoised	Z2856434830	23.80	5	01:37:07	done	HPrP-x0265	00:00:27	65.766 - 2.859
62	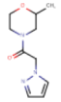	209.25	DSIpoised	Z217038356	23.80	5	01:37:32	done	HPrP-x0266	00:00:24	42.641 - 2.301

Entry ID	Structure	Mol Weight (g/mol)	Library Name	Compound Code	Compound Concentration (mM)	Solvent Fraction (%, v/v)	Soaking Time	Harvest Status	Crystal Name	Mounting Time	Resolution Overall (Å)
63	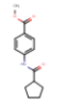	247.29	DSIpoised	Z28226359	23.80	5	01:38:00	done	HPrP-x0267	00:00:26	50.681 - 2.734
64	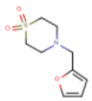	215.27	DSIpoised	Z2856434926	23.80	5	01:38:13	done	HPrP-x0268	00:00:10	42.879 - 2.554
65	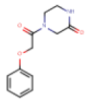	234.26	DSIpoised	Z31602870	23.80	5	01:38:27	done	HPrP-x0269	00:00:13	42.718 - 2.402
66	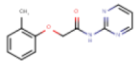	243.27	DSIpoised	Z53834613	23.80	5	01:38:58	done	HPrP-x0270	00:00:28	42.656 - 2.327
67	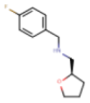	209.26	DSIpoised	Z2856434824	23.80	5	01:39:13	done	HPrP-x0271	00:00:12	42.920 - 2.557
68		226.29	DSIpoised	Z73240835	23.80	5	01:44:02	done	HPrP-x0272	00:02:17	42.332 - 2.819
69		146.98	FragLite	NCL-00023819	10.10	10	00:41:47	done	HPrP-x0305	00:00:51	43.038 - 2.337
70		193.98	FragLite	NCL-00023818	10.10	10	00:42:44	done	HPrP-x0306	00:00:55	None
71		147.96	FragLite	NCL-00023820	10.10	10	00:43:28	done	HPrP-x0307	00:00:40	51.192 - 2.470

Entry ID	Structure	Mol Weight (g/mol)	Library Name	Compound Code	Compound Concentration (mM)	Solvent Fraction (%, v/v)	Soaking Time	Harvest Status	Crystal Name	Mounting Time	Resolution Overall (Å)
72		173.01	FragLite	NCL-00023823	10.10	10	00:44:30	done	HPrP-x0308	00:01:00	None
73		220.01	FragLite	NCL-00023822	10.10	10	00:45:32	done	HPrP-x0309	00:00:59	51.336 - 2.723
74		174.00	FragLite	NCL-00023825	10.10	10	00:46:01	done	HPrP-x0310	00:00:27	None
75		221.00	FragLite	NCL-00023824	10.10	10	00:46:53	done	HPrP-x0311	00:00:50	None
76		236.08	FragLite	NCL-00023830	10.10	10	00:48:09	done	HPrP-x0312	00:00:45	None
77		283.08	FragLite	NCL-00023829	10.10	10	00:48:30	fail		00:00:05	
78	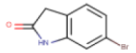	212.05	FragLite	NCL-00023827	10.10	10	00:49:25	done	HPrP-x0313	00:00:52	42.678 - 2.378
79		214.06	FragLite	NCL-00023828	10.10	10	00:50:48	done	HPrP-x0314	00:01:20	None
80		247.04	FragLite	NCL-00023826	10.10	10	00:51:34	done	HPrP-x0315	00:00:43	51.142 - 2.740

Entry ID	Structure	Mol Weight (g/mol)	Library Name	Compound Code	Compound Concentration (mM)	Solvent Fraction (%, v/v)	Soaking Time	Harvest Status	Crystal Name	Mounting Time	Resolution Overall (Å)
81		158.99	FragLite	NCL-00023832	10.10	10	00:52:12	done	HPrP-x0316	00:00:36	43.097 - 2.268
82		205.99	FragLite	NCL-00023831	10.10	10	00:53:17	done	HPrP-x0317	00:01:04	43.192 - 2.509
83		188.02	FragLite	NCL-00023836	10.10	10	00:53:51	done	HPrP-x0318	00:00:32	None
84	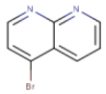	209.05	FragLite	NCL-00023833	10.10	10	00:54:51	done	HPrP-x0319	00:00:56	None
85		235.10	FragLite	NCL-00023835	10.10	10	00:56:22	done	HPrP-x0320	00:01:29	None
86		188.02	FragLite	NCL-00024670	10.10	10	00:57:09	done	HPrP-x0321	00:00:44	51.402 - 2.766
87	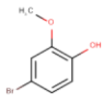	203.04	FragLite	NCL-00024774	10.10	10	00:57:42	done	HPrP-x0322	00:00:32	51.434 - 3.340
88		202.05	FragLite	NCL-00024674	10.10	10	00:58:45	done	HPrP-x0323	00:00:59	43.004 - 2.658
89		198.02	FragLite	NCL-00024661	10.10	10	00:59:45	done	HPrP-x0324	00:00:58	None

Entry ID	Structure	Mol Weight (g/mol)	Library Name	Compound Code	Compound Concentration (mM)	Solvent Fraction (%, v/v)	Soaking Time	Harvest Status	Crystal Name	Mounting Time	Resolution Overall (Å)
90	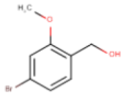	217.06	FragLite	NCL-00024662	10.10	10	01:00:25	done	HPrP-x0325	00:00:27	50.944 - 2.675
91		191.03	FragLite	NCL-00024671	10.10	10	01:01:06	done	HPrP-x0326	00:00:38	None
92		217.02	FragLite	NCL-00024667	10.10	10	01:01:42	done	HPrP-x0327	00:00:33	None
93		212.05	FragLite	NCL-00024663	10.10	10	01:02:41	done	HPrP-x0328	00:00:57	66.20 - 3.57
94		205.06	FragLite	NCL-00024673	10.10	10	01:03:26	done	HPrP-x0329	00:00:43	None
95		205.01	FragLite	NCL-00024890	10.10	10	01:04:24	done	HPrP-x0330	00:00:55	None
96		218.05	FragLite	NCL-00024672	10.10	10	01:05:20	done	HPrP-x0331	00:00:54	None
97		232.08	FragLite	NCL-00024387	10.10	10	01:06:02	done	HPrP-x0332	00:00:39	43.064 - 2.692
98		232.03	FragLite	NCL-00024773	10.10	10	01:06:41	done	HPrP-x0333	00:00:37	None

Entry ID	Structure	Mol Weight (g/mol)	Library Name	Compound Code	Compound Concentration (mM)	Solvent Fraction (%, v/v)	Soaking Time	Harvest Status	Crystal Name	Mounting Time	Resolution Overall (Å)
99	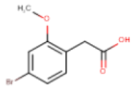	245.07	FragLite	NCL-00024665	10.10	10	01:07:17	done	HPrP-x0334	00:00:34	None
100		146.98	FragLite	NCL-00023819	4.80	5	01:08:34	done	HPrP-x0335	00:01:14	51.342 - 2.775
101		193.98	FragLite	NCL-00023818	4.80	5	01:09:33	done	HPrP-x0336	00:00:57	43.270 - 2.809
102		147.96	FragLite	NCL-00023820	4.80	5	01:10:49	done	HPrP-x0337	00:01:13	43.169 - 2.709
103		173.01	FragLite	NCL-00023823	4.80	5	01:11:34	done	HPrP-x0338	00:00:43	51.500 - 2.959
104		220.01	FragLite	NCL-00023822	4.80	5	01:12:03	done	HPrP-x0339	00:00:25	65.926 - 2.619
105		174.00	FragLite	NCL-00023825	4.80	5	01:12:31	done	HPrP-x0340	00:00:26	43.312 - 2.445
106		221.00	FragLite	NCL-00023824	4.80	5	01:13:14	done	HPrP-x0341	00:00:40	None
107		236.08	FragLite	NCL-00023830	4.80	5	01:13:52	done	HPrP-x0342	00:00:35	None

Entry ID	Structure	Mol Weight (g/mol)	Library Name	Compound Code	Compound Concentration (mM)	Solvent Fraction (%, v/v)	Soaking Time	Harvest Status	Crystal Name	Mounting Time	Resolution Overall (Å)
108		283.08	FragLite	NCL-00023829	4.80	5	01:15:33	done	HPrP-x0343	00:01:38	51.355 - 2.592
109	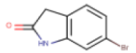	212.05	FragLite	NCL-00023827	4.80	5	01:16:29	done	HPrP-x0344	00:00:52	32.99 - 1.89
110		214.06	FragLite	NCL-00023828	4.80	5	01:17:11	done	HPrP-x0345	00:00:40	51.291 - 2.543
111		247.04	FragLite	NCL-00023826	4.80	5	01:17:49	done	HPrP-x0346	00:00:35	43.084 - 2.461
112		158.99	FragLite	NCL-00023832	4.80	5	01:18:35	done	HPrP-x0347	00:00:43	51.81 - 4.33
113		205.99	FragLite	NCL-00023831	4.80	5	01:19:29	done	HPrP-x0348	00:00:53	42.695 - 2.296
114		188.02	FragLite	NCL-00023836	4.80	5	01:20:11	done	HPrP-x0349	00:00:38	43.284 - 2.559
115	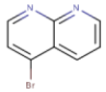	209.05	FragLite	NCL-00023833	4.80	5	01:21:21	done	HPrP-x0350	00:01:07	43.118 - 2.447
116		235.10	FragLite	NCL-00023835	4.80	5	01:22:04	done	HPrP-x0351	00:00:41	66.502 - 2.710

Entry ID	Structure	Mol Weight (g/mol)	Library Name	Compound Code	Compound Concentration (mM)	Solvent Fraction (%, v/v)	Soaking Time	Harvest Status	Crystal Name	Mounting Time	Resolution Overall (Å)
117	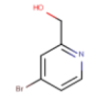	188.02	FragLite	NCL-00024670	4.80	5	01:23:27	done	HPrP-x0352	00:01:21	43.390 - 3.285
118	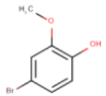	203.04	FragLite	NCL-00024774	4.80	5	01:25:33	done	HPrP-x0353	00:02:02	51.336 - 2.475
119		202.05	FragLite	NCL-00024674	4.80	5	01:26:10	done	HPrP-x0354	00:00:34	66.089 - 2.479
120		198.02	FragLite	NCL-00024661	4.80	5	01:26:44	done	HPrP-x0355	00:00:32	None
121	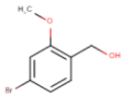	217.06	FragLite	NCL-00024662	4.80	5	01:28:00	done	HPrP-x0356	00:01:13	51.712 - 3.736
122		191.03	FragLite	NCL-00024671	4.80	5	01:28:33	done	HPrP-x0357	00:00:31	42.988 - 2.950
123		217.02	FragLite	NCL-00024667	4.80	5	01:29:10	done	HPrP-x0358	00:00:34	None
124		212.05	FragLite	NCL-00024663	4.80	5	01:29:52	done	HPrP-x0359	00:00:39	43.072 - 2.426
125		205.06	FragLite	NCL-00024673	4.80	5	01:30:53	done	HPrP-x0360	00:00:59	66.11 - 2.97

Entry ID	Structure	Mol Weight (g/mol)	Library Name	Compound Code	Compound Concentration (mM)	Solvent Fraction (%, v/v)	Soaking Time	Harvest Status	Crystal Name	Mounting Time	Resolution Overall (Å)
126		205.01	FragLite	NCL-00024890	4.80	5	01:31:23	done	HPrP-x0361	00:00:28	None
127		218.05	FragLite	NCL-00024672	4.80	5	01:31:32	fail		00:00:06	
128		232.08	FragLite	NCL-00024387	4.80	5	01:32:09	done	HPrP-x0362	00:00:35	43.078 - 2.728
129		232.03	FragLite	NCL-00024773	4.80	5	01:32:49	done	HPrP-x0363	00:00:38	None
130	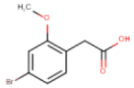	245.07	FragLite	NCL-00024665	4.80	5	01:35:30	done	HPrP-x0364	00:00:42	None
131		146.98	FragLite	NCL-00023819	4.80	5	01:36:04	done	HPrP-x0365	00:00:31	42.744 - 2.465
132		193.98	FragLite	NCL-00023818	4.80	5	01:36:51	done	HPrP-x0366	00:00:42	51.136 - 2.688
133		147.96	FragLite	NCL-00023820	4.80	5	01:37:18	done	HPrP-x0367	00:00:22	51.343 - 2.355
134		173.01	FragLite	NCL-00023823	4.80	5	01:38:18	done	HPrP-x0368	00:00:56	43.072 - 2.164

Entry ID	Structure	Mol Weight (g/mol)	Library Name	Compound Code	Compound Concentration (mM)	Solvent Fraction (%, v/v)	Soaking Time	Harvest Status	Crystal Name	Mounting Time	Resolution Overall (Å)
135		220.01	FragLite	NCL-00023822	4.80	5	01:38:57	done	HPrP-x0369	00:00:37	65.818 - 2.408
136		174.00	FragLite	NCL-00023825	4.80	5	01:40:06	done	HPrP-x0370	00:01:04	43.207 - 2.729
137		221.00	FragLite	NCL-00023824	4.80	5	01:40:58	done	HPrP-x0371	00:00:50	None
138		236.08	FragLite	NCL-00023830	4.80	5	01:41:30	done	HPrP-x0372	00:00:27	42.77 - 5.06
139		283.08	FragLite	NCL-00023829	4.80	5	01:42:07	done	HPrP-x0373	00:00:33	42.63 - 3.34
140	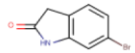	212.05	FragLite	NCL-00023827	4.80	5	01:42:45	done	HPrP-x0374	00:00:36	43.047 - 2.588
141		214.06	FragLite	NCL-00023828	4.80	5	01:43:17	done	HPrP-x0375	00:00:29	42.723 - 2.283
142		247.04	FragLite	NCL-00023826	4.80	5	01:43:44	done	HPrP-x0376	00:00:25	51.163 - 2.397
143		158.99	FragLite	NCL-00023832	4.80	5	01:44:26	done	HPrP-x0377	00:00:40	43.025 - 2.961

Entry ID	Structure	Mol Weight (g/mol)	Library Name	Compound Code	Compound Concentration (mM)	Solvent Fraction (%, v/v)	Soaking Time	Harvest Status	Crystal Name	Mounting Time	Resolution Overall (Å)
144		205.99	FragLite	NCL-00023831	4.80	5	01:45:31	done	HPrP-x0378	00:01:03	51.764 - 2.961
145		188.02	FragLite	NCL-00023836	4.80	5	01:46:04	done	HPrP-x0379	00:00:31	65.810 - 3.119
146	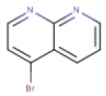	209.05	FragLite	NCL-00023833	4.80	5	01:47:01	done	HPrP-x0380	00:00:53	51.434 - 2.338
147		235.10	FragLite	NCL-00023835	4.80	5	01:48:11	done	HPrP-x0381	00:01:05	43.206 - 2.722
148		188.02	FragLite	NCL-00024670	4.80	5	01:48:49	done	HPrP-x0382	00:00:35	43.059 - 2.128
149	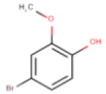	203.04	FragLite	NCL-00024774	4.80	5	01:50:06	done	HPrP-x0383	00:01:16	66.049 - 2.408
150		202.05	FragLite	NCL-00024674	4.80	5	01:50:36	done	HPrP-x0384	00:00:28	51.269 - 2.546
151		198.02	FragLite	NCL-00024661	4.80	5	01:51:19	done	HPrP-x0385	00:00:41	None
152	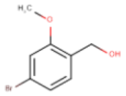	217.06	FragLite	NCL-00024662	4.80	5	01:52:21	done	HPrP-x0386	00:00:58	137.62 - 7.70

Entry ID	Structure	Mol Weight (g/mol)	Library Name	Compound Code	Compound Concentration (mM)	Solvent Fraction (%, v/v)	Soaking Time	Harvest Status	Crystal Name	Mounting Time	Resolution Overall (Å)
153		191.03	FragLite	NCL-00024671	4.80	5	01:53:39	done	HPrP-x0387	00:01:14	43.059 - 2.358
154		217.02	FragLite	NCL-00024667	4.80	5	01:53:47	fail		00:00:06	
155		212.05	FragLite	NCL-00024663	4.80	5	01:54:39	done	HPrP-x0388	00:00:48	43.335 - 2.711
156		205.06	FragLite	NCL-00024673	4.80	5	01:56:13	done	HPrP-x0389	00:01:32	43.141 - 2.353
157		205.01	FragLite	NCL-00024890	4.80	5	01:56:46	done	HPrP-x0390	00:00:30	None
158		218.05	FragLite	NCL-00024672	4.80	5	01:59:46	fail		00:00:23	
159		232.08	FragLite	NCL-00024387	4.80	5	02:00:30	fail		00:00:41	
160		232.03	FragLite	NCL-00024773	4.80	5	02:01:39	fail		00:01:06	
161	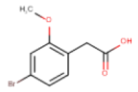	245.07	FragLite	NCL-00024665	4.80	5	02:02:03	fail		00:00:21	

Entry ID	Structure	Mol Weight (g/mol)	Library Name	Compound Code	Compound Concentration (mM)	Solvent Fraction (%, v/v)	Soaking Time	Harvest Status	Crystal Name	Mounting Time	Resolution Overall (Å)
162	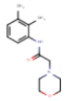	248.33	DSIpoised	Z2856434834	23.80	5	01:36:31	done	HPrP-x0559	00:00:29	43.151 - 2.448
163	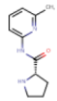	205.26	DSIpoised	Z1267881672	23.80	5	01:36:54	done	HPrP-x0560	00:00:21	51.614 - 2.671
164		203.25	DSIpoised	Z1348371854	23.80	5	01:37:32	done	HPrP-x0561	00:00:35	None
165	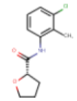	239.70	DSIpoised	Z1545312521	23.80	5	01:38:06	done	HPrP-x0562	00:00:32	51.081 - 2.225
166	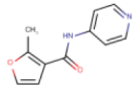	202.21	DSIpoised	Z136583524	23.80	5	01:38:11	fail		00:00:04	
167	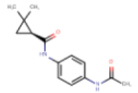	246.31	DSIpoised	Z1505719304	23.80	5	01:38:55	done	HPrP-x0563	00:00:43	42.906 - 2.231
168	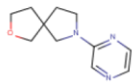	205.26	DSIpoised	Z1401276297	23.80	5	01:39:30	done	HPrP-x0564	00:00:33	None
169	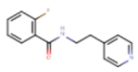	244.27	DSIpoised	Z1310876699	23.80	5	01:39:39	fail		00:00:04	
170		227.26	DSIpoised	Z30802768	23.80	5	01:40:39	done	HPrP-x0565	00:00:58	42.948 - 3.237

Entry ID	Structure	Mol Weight (g/mol)	Library Name	Compound Code	Compound Concentration (mM)	Solvent Fraction (%, v/v)	Soaking Time	Harvest Status	Crystal Name	Mounting Time	Resolution Overall (Å)
171	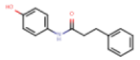	241.29	DSIpoised	Z69118333	23.80	5	01:41:21	done	HPrP-x0566	00:00:38	42.761 - 2.268
172	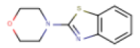	220.29	DSIpoised	Z56767623	23.80	5	01:42:13	done	HPrP-x0567	00:00:50	65.664 - 2.764
173	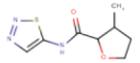	213.26	DSIpoised	Z1827602749	23.80	5	01:42:35	done	HPrP-x0568	00:00:21	43.03 - 3.83
174	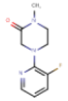	209.22	DSIpoised	Z1373445602	23.80	5	01:43:14	done	HPrP-x0569	00:00:26	42.916 - 2.687
175	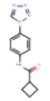	243.27	DSIpoised	Z26552420	23.80	5	01:43:42	done	HPrP-x0570	00:00:19	42.957 - 2.146
176	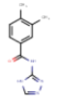	216.24	DSIpoised	Z2856434827	23.80	5	01:45:02	done	HPrP-x0571	00:01:17	49.81 - 1.36
177	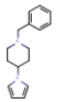	240.35	DSIpoised	Z2856434898	23.80	5	01:45:38	done	HPrP-x0572	00:00:33	43.112 - 2.693
178	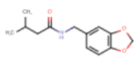	235.28	DSIpoised	Z27695365	23.80	5	01:46:15	done	HPrP-x0573	00:00:34	42.644 - 2.300
179	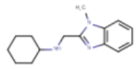	243.35	DSIpoised	Z2856434855	23.80	5	01:46:40	done	HPrP-x0574	00:00:22	43.000 - 2.271

Entry ID	Structure	Mol Weight (g/mol)	Library Name	Compound Code	Compound Concentration (mM)	Solvent Fraction (%, v/v)	Soaking Time	Harvest Status	Crystal Name	Mounting Time	Resolution Overall (Å)
180	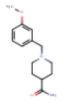	248.33	DSIpoised	Z2856434854	23.80	5	01:07:21	done	HPrP-x0391	00:01:24	51.37 - 4.14
181	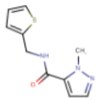	221.28	DSIpoised	Z915492990	23.80	5	01:08:15	done	HPrP-x0392	00:00:51	43.077 - 2.389
182	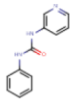	213.24	DSIpoised	Z44592329	23.80	5	01:10:32	fail		00:02:16	
183		235.31	DSIpoised	Z1623890017	23.80	5	01:11:57	done	HPrP-x0393	00:01:20	43.119 - 2.911
184	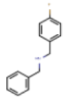	215.27	DSIpoised	Z2856434783	23.80	5	01:12:37	done	HPrP-x0394	00:00:35	51.28 - 3.77
185	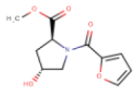	239.23	DSIpoised	Z1614545742	23.80	5	01:12:51	fail		00:00:07	
186	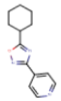	229.28	DSIpoised	Z57715447	23.80	5	01:13:06	fail		00:00:07	
187		231.17	DSIpoised	Z57111868	23.80	5	01:14:09	done	HPrP-x0395	00:00:56	43.120 - 3.318
188	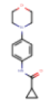	246.31	DSIpoised	Z30485868	23.80	5	01:15:15	done	HPrP-x0396	00:00:49	65.531 - 2.516

Entry ID	Structure	Mol Weight (g/mol)	Library Name	Compound Code	Compound Concentration (mM)	Solvent Fraction (%, v/v)	Soaking Time	Harvest Status	Crystal Name	Mounting Time	Resolution Overall (Å)
189	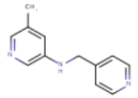	199.26	DSIpoised	Z1478435544	23.80	5	01:16:10	done	HPrP-x0397	00:00:46	None
190	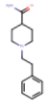	232.33	DSIpoised	Z2856434897	23.80	5	01:17:10	done	HPrP-x0398	00:00:49	None
191		222.26	DSIpoised	Z2856434942	23.80	5	01:18:06	done	HPrP-x0399	00:00:48	None
192	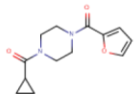	248.28	DSIpoised	Z32327641	23.80	5	01:20:54	done	HPrP-x0400	00:02:38	43.193 - 2.909
193	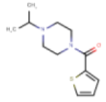	238.35	DSIpoised	Z2856434826	23.80	5	01:21:40	done	HPrP-x0401	00:00:36	None
194	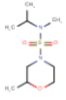	236.33	DSIpoised	Z416341642	23.80	5	01:22:24	done	HPrP-x0402	00:00:37	None
195	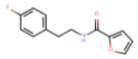	233.24	DSIpoised	Z26769872	23.80	5	01:23:14	done	HPrP-x0403	00:00:47	51.397 - 2.735
196	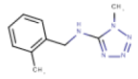	203.25	DSIpoised	Z57778470	23.80	5	01:24:04	done	HPrP-x0404	00:00:44	42.667 - 2.546
197	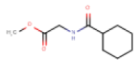	199.25	DSIpoised	Z18618496	23.80	5	01:24:54	done	HPrP-x0405	00:00:42	51.263 - 2.688

Entry ID	Structure	Mol Weight (g/mol)	Library Name	Compound Code	Compound Concentration (mM)	Solvent Fraction (%, v/v)	Soaking Time	Harvest Status	Crystal Name	Mounting Time	Resolution Overall (Å)
198	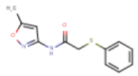	248.30	DSIpoised	Z19750454	23.80	5	01:25:40	done	HPrP-x0406	00:00:39	51.012 - 2.703
199	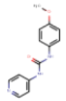	243.27	DSIpoised	Z321318226	23.80	5	01:25:59	fail		00:00:07	
200	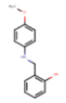	229.28	DSIpoised	Z56943440	23.80	5	01:26:39	done	HPrP-x0407	00:00:33	51.313 - 2.758
201	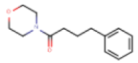	233.31	DSIpoised	Z419995480	23.80	5	01:27:23	done	HPrP-x0408	00:00:32	51.241 - 2.726
202	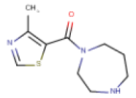	225.31	DSIpoised	Z803153598	23.80	5	01:27:59	done	HPrP-x0409	00:00:26	None
203		173.26	DSIpoised	Z1103351268	23.80	5	01:28:37	done	HPrP-x0410	00:00:26	None
204	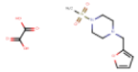	334.34	DSIpoised	Z2241115980	23.80	5	01:29:07	done	HPrP-x0411	00:00:24	66.095 - 2.819
205	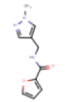	205.22	DSIpoised	Z275179758	23.80	5	01:29:52	done	HPrP-x0412	00:00:43	None
206	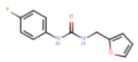	234.23	DSIpoised	Z44584202	23.80	5	01:30:31	done	HPrP-x0413	00:00:29	43.108 - 2.490

Entry ID	Structure	Mol Weight (g/mol)	Library Name	Compound Code	Compound Concentration (mM)	Solvent Fraction (%, v/v)	Soaking Time	Harvest Status	Crystal Name	Mounting Time	Resolution Overall (Å)
207	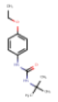	236.32	DSIpoised	Z44586802	23.80	5	01:31:05	done	HPrP-x0414	00:00:27	None
208		213.34	DSIpoised	Z1461982627	23.80	5	01:32:20	done	HPrP-x0415	00:01:05	51.191 - 2.688
209	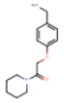	247.34	DSIpoised	Z18839017	23.80	5	01:33:02	done	HPrP-x0416	00:00:34	43.101 - 2.598
210	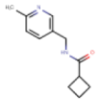	204.27	DSIpoised	Z437516460	23.80	5	01:33:49	done	HPrP-x0417	00:00:37	42.965 - 2.564
211	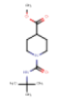	242.32	DSIpoised	Z44567722	23.80	5	01:35:52	done	HPrP-x0418	00:01:05	None
212	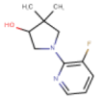	210.25	DSIpoised	Z1929757385	23.80	5	01:36:28	done	HPrP-x0419	00:00:30	66.14 - 4.82
213	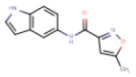	241.25	DSIpoised	Z1190787729	23.80	5	01:37:22	done	HPrP-x0420	00:00:50	51.426 - 2.631
214	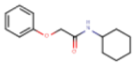	233.31	DSIpoised	Z19735904	23.80	5	01:38:05	done	HPrP-x0421	00:00:33	None
215		225.35	DSIpoised	Z1259335913	23.80	5	01:39:00	done	HPrP-x0422	00:00:46	None

Entry ID	Structure	Mol Weight (g/mol)	Library Name	Compound Code	Compound Concentration (mM)	Solvent Fraction (%, v/v)	Soaking Time	Harvest Status	Crystal Name	Mounting Time	Resolution Overall (Å)
216	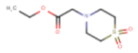	221.27	DSIpoised	Z2856434920	23.80	5	01:39:34	done	HPrP-x0423	00:00:28	None
217	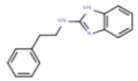	237.31	DSIpoised	Z57299529	23.80	5	01:40:17	done	HPrP-x0424	00:00:31	None
218		205.30	DSIpoised	Z2217052426	23.80	5	01:40:52	done	HPrP-x0425	00:00:26	42.810 - 2.514
219		247.68	DSIpoised	Z56346825	23.80	5	01:41:53	done	HPrP-x0426	00:00:32	43.026 - 2.560
220	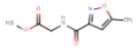	198.18	DSIpoised	Z375990520	23.80	5	01:42:29	done	HPrP-x0427	00:00:22	None
221	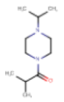	198.31	DSIpoised	Z106307058	23.80	5	01:42:36	fail		00:00:04	
222	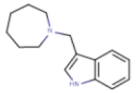	228.34	DSIpoised	Z2856434848	23.80	5	01:43:15	done	HPrP-x0428	00:00:31	65.958 - 2.823
223	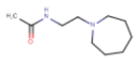	184.28	DSIpoised	Z169226638	23.80	5	01:43:42	done	HPrP-x0429	00:00:17	None
224	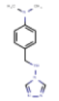	217.28	DSIpoised	Z57258487	23.80	5	01:46:00	done	HPrP-x0430	00:02:12	43.001 - 2.623

Entry ID	Structure	Mol Weight (g/mol)	Library Name	Compound Code	Compound Concentration (mM)	Solvent Fraction (%, v/v)	Soaking Time	Harvest Status	Crystal Name	Mounting Time	Resolution Overall (Å)
225	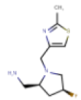	229.32	DSIpoised	Z2444997446	23.80	5	01:46:34	done	HPrP-x0431	00:00:25	None
226		208.28	DSIpoised	Z2466069494	23.80	5	01:47:25	done	HPrP-x0432	00:00:41	None
227	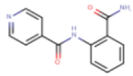	241.25	DSIpoised	Z91797745	23.80	5	01:48:35	done	HPrP-x0433	00:00:51	None
228	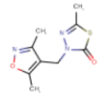	225.27	DSIpoised	Z1899842917	23.80	5	01:48:48	fail		00:00:05	
229	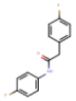	247.25	DSIpoised	Z27805986	23.80	5	01:49:31	done	HPrP-x0434	00:00:32	None
230		235.30	DSIpoised	Z431807512	23.80	5	01:49:46	fail		00:00:04	
231	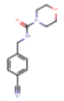	245.28	DSIpoised	Z509756472	23.80	5	01:50:24	done	HPrP-x0435	00:00:27	43.03 - 2.72
232	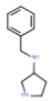	176.26	DSIpoised	Z1827898537	23.80	5	01:50:51	done	HPrP-x0436	00:00:23	None
233	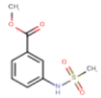	229.25	DSIpoised	Z24758179	23.80	5	01:51:29	done	HPrP-x0437	00:00:26	42.968 - 2.833

Entry ID	Structure	Mol Weight (g/mol)	Library Name	Compound Code	Compound Concentration (mM)	Solvent Fraction (%, v/v)	Soaking Time	Harvest Status	Crystal Name	Mounting Time	Resolution Overall (Å)
234	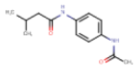	234.30	DSIpoised	Z27653940	23.80	5	01:52:02	done	HPrP-x0438	00:00:28	42.897 - 2.690
235	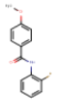	245.25	DSIpoised	Z28290321	23.80	5	01:52:35	done	HPrP-x0439	00:00:27	65.700 - 2.428
236		242.29	DSIpoised	Z57614330	23.80	5	01:53:20	done	HPrP-x0440	00:00:42	51.279 - 2.482
237	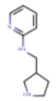	177.25	DSIpoised	Z1262327505	23.80	5	01:53:49	done	HPrP-x0441	00:00:22	None
238	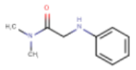	178.24	DSIpoised	Z104584152	23.80	5	01:54:38	done	HPrP-x0442	00:00:44	None
239	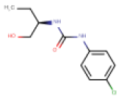	242.70	DSIpoised	Z1593306637	23.80	5	01:55:47	done	HPrP-x0443	00:00:58	43.18 - 4.09
240		191.28	DSIpoised	Z31244728	23.80	5	01:56:20	done	HPrP-x0444	00:00:25	65.798 - 2.957
241	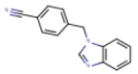	233.27	DSIpoised	Z26333434	23.80	5	01:56:27	fail		00:00:04	
242	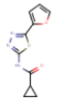	235.26	DSIpoised	Z165141116	23.80	5	01:57:04	done	HPrP-x0445	00:00:31	None

Entry ID	Structure	Mol Weight (g/mol)	Library Name	Compound Code	Compound Concentration (mM)	Solvent Fraction (%, v/v)	Soaking Time	Harvest Status	Crystal Name	Mounting Time	Resolution Overall (Å)
243	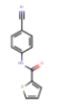	228.27	DSIpoised	Z30612387	23.80	5	01:58:02	done	HPrP-x0446	00:00:50	65.845 - 2.467
244	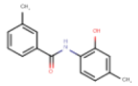	241.29	DSIpoised	Z33452549	23.80	5	01:58:28	done	HPrP-x0447	00:00:21	None
245	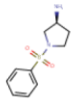	226.29	DSIpoised	Z2443429438	23.80	5	01:58:57	done	HPrP-x0448	00:00:18	65.689 - 2.651
246	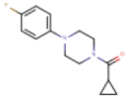	248.30	DSIpoised	Z30620520	23.80	5	01:59:23	done	HPrP-x0449	00:00:19	42.959 - 2.542
247	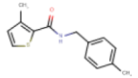	245.34	DSIpoised	Z28429425	23.80	5	02:00:05	done	HPrP-x0450	00:00:35	50.90 - 3.76
248	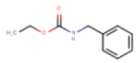	179.22	DSIpoised	Z31478129	23.80	5	02:00:54	done	HPrP-x0451	00:00:30	65.904 - 2.535
249	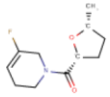	189.00	DSIpoised	Z2272040604	23.80	5	02:01:23	done	HPrP-x0452	00:00:27	43.103 - 2.509
250	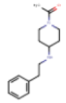	246.35	DSIpoised	Z2856434883	23.80	5	02:01:55	done	HPrP-x0453	00:00:26	None
251	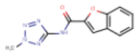	243.23	DSIpoised	Z57292378	23.80	5	02:02:35	done	HPrP-x0454	00:00:35	None

Entry ID	Structure	Mol Weight (g/mol)	Library Name	Compound Code	Compound Concentration (mM)	Solvent Fraction (%, v/v)	Soaking Time	Harvest Status	Crystal Name	Mounting Time	Resolution Overall (Å)
252		211.21	DSIpoised	Z54226006	23.80	5	02:03:43	done	HPrP-x0455	00:01:02	51.061 - 3.150
253	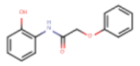	243.26	DSIpoised	Z68195082	23.80	5	02:04:16	done	HPrP-x0456	00:00:23	42.726 - 2.721
254	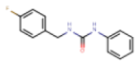	244.27	DSIpoised	Z44609285	23.80	5	02:05:14	done	HPrP-x0457	00:00:55	42.85 - 3.02
255	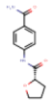	234.26	DSIpoised	Z1545313172	23.80	5	02:07:06	done	HPrP-x0458	00:01:51	None
256	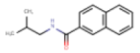	227.31	DSIpoised	Z32385991	23.80	5	02:07:39	done	HPrP-x0459	00:00:27	None
257	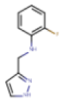	191.21	DSIpoised	Z1545196403	23.80	5	02:08:30	done	HPrP-x0460	00:00:44	51.07 - 5.70
258	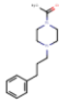	246.35	DSIpoised	Z2856434884	23.80	5	02:09:38	done	HPrP-x0461	00:01:04	None
259	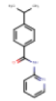	240.31	DSIpoised	Z85525355	23.80	5	02:11:04	done	HPrP-x0462	00:01:24	51.154 - 3.494
260	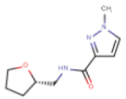	209.25	DSIpoised	Z2643472210	23.80	5	02:11:59	done	HPrP-x0463	00:00:53	None

Entry ID	Structure	Mol Weight (g/mol)	Library Name	Compound Code	Compound Concentration (mM)	Solvent Fraction (%, v/v)	Soaking Time	Harvest Status	Crystal Name	Mounting Time	Resolution Overall (Å)
261	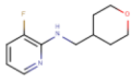	210.25	DSIpoised	Z1373430305	23.80	5	02:12:47	done	HPrP-x0464	00:00:41	43.05 - 3.77
262	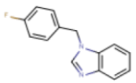	226.25	DSIpoised	Z26333448	23.80	5	02:13:27	done	HPrP-x0465	00:00:34	51.068 - 2.671
263		239.27	DSIpoised	Z54226095	23.80	5	02:14:14	done	HPrP-x0466	00:00:45	None
264		240.25	DSIpoised	Z2856434829	23.80	5	02:14:51	done	HPrP-x0467	00:00:30	66.000 - 2.625
265	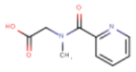	194.19	DSIpoised	Z1171978788	23.80	5	02:15:25	done	HPrP-x0468	00:00:31	65.743 - 2.736
266	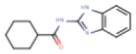	243.31	DSIpoised	Z27666218	23.80	5	02:16:09	done	HPrP-x0469	00:00:40	65.727 - 2.539
267	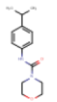	248.33	DSIpoised	Z208334100	23.80	5	02:17:02	done	HPrP-x0470	00:00:44	65.721 - 3.235
268	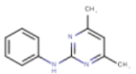	199.26	DSIpoised	Z285675722	23.80	5	00:43:35	done	HPrP-x0471	00:00:51	42.756 - 2.283
269		246.24	DSIpoised	Z55290386	23.80	5	00:44:28	done	HPrP-x0472	00:00:49	51.247 - 2.329

Entry ID	Structure	Mol Weight (g/mol)	Library Name	Compound Code	Compound Concentration (mM)	Solvent Fraction (%, v/v)	Soaking Time	Harvest Status	Crystal Name	Mounting Time	Resolution Overall (Å)
270	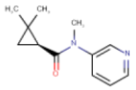	204.27	DSIpoised	Z1506050651	23.80	5	00:44:58	done	HPrP-x0473	00:00:23	51.262 - 2.533
271	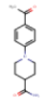	246.31	DSIpoised	Z126933926	23.80	5	00:46:01	done	HPrP-x0474	00:00:52	42.998 - 2.328
272	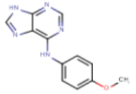	241.25	DSIpoised	Z276545932	23.80	5	00:46:33	done	HPrP-x0475	00:00:29	65.797 - 2.628
273		227.32	DSIpoised	Z45516134	23.80	5	00:47:36	done	HPrP-x0476	00:00:57	None
274	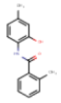	241.29	DSIpoised	Z33452282	23.80	5	00:48:10	done	HPrP-x0477	00:00:28	None
275		144.22	DSIpoised	Z818732104	23.80	5	00:48:47	done	HPrP-x0478	00:00:29	43.088 - 2.288
276	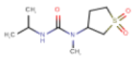	234.31	DSIpoised	Z445856640	23.80	5	00:49:09	done	HPrP-x0479	00:00:16	42.76 - 4.47
277	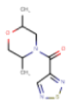	227.28	DSIpoised	Z768399682	23.80	5	00:50:10	done	HPrP-x0480	00:00:56	66.002 - 2.604
278	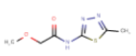	187.22	DSIpoised	Z263785508	23.80	5	00:50:40	done	HPrP-x0481	00:00:23	50.982 - 2.709

Entry ID	Structure	Mol Weight (g/mol)	Library Name	Compound Code	Compound Concentration (mM)	Solvent Fraction (%, v/v)	Soaking Time	Harvest Status	Crystal Name	Mounting Time	Resolution Overall (Å)
279		195.24	DSIpoised	Z2856434791	23.80	5	00:51:25	done	HPrP-x0482	00:00:43	None
280		175.20	DSIpoised	Z373221060	23.80	5	00:51:48	done	HPrP-x0483	00:00:17	51.187 - 2.824
281		210.32	DSIpoised	Z1328078283	23.80	5	00:52:32	done	HPrP-x0484	00:00:34	
282		247.68	DSIpoised	Z57515803	23.80	5	00:52:38	fail		00:00:03	
283	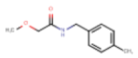	193.25	DSIpoised	Z33297786	23.80	5	00:53:22	done	HPrP-x0485	00:00:21	51.047 - 2.765
284	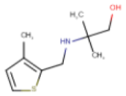	199.31	DSIpoised	Z2856434821	23.80	5	00:53:29	fail		00:00:04	
285	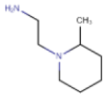	142.25	DSIpoised	Z1245580425	23.80	5	00:54:34	done	HPrP-x0486	00:00:57	51.384 - 2.641
286		168.20	DSIpoised	Z135394292	23.80	5	00:54:56	fail		00:00:21	
287	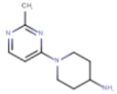	192.27	DSIpoised	Z1333043417	23.80	5	00:55:45	done	HPrP-x0487	00:00:45	43.058 - 2.462

Entry ID	Structure	Mol Weight (g/mol)	Library Name	Compound Code	Compound Concentration (mM)	Solvent Fraction (%, v/v)	Soaking Time	Harvest Status	Crystal Name	Mounting Time	Resolution Overall (Å)
288	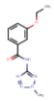	247.26	DSIpoised	Z57292400	23.80	5	00:56:42	done	HPrP-x0488	00:00:55	42.679 - 2.355
289	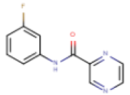	217.20	DSIpoised	Z28143241	23.80	5	00:57:09	done	HPrP-x0489	00:00:25	42.975 - 2.205
290		247.26	DSIpoised	Z2234920345	23.80	5	00:57:44	done	HPrP-x0490	00:00:28	42.673 - 2.284
291		158.25	DSIpoised	Z2429435052	23.80	5	00:58:12	done	HPrP-x0491	00:00:26	51.307 - 2.464
292		191.27	DSIpoised	Z2856434862	23.80	5	00:58:49	done	HPrP-x0492	00:00:31	43.036 - 2.269
293	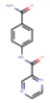	242.24	DSIpoised	Z30242120	23.80	5	00:59:21	done	HPrP-x0493	00:00:24	43.147 - 2.537
294	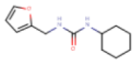	222.29	DSIpoised	Z44584192	23.80	5	01:00:07	done	HPrP-x0494	00:00:40	42.950 - 2.613
295	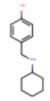	205.30	DSIpoised	Z2241127906	23.80	5	01:00:50	done	HPrP-x0495	00:00:38	51.253 - 2.304
296	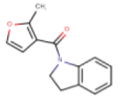	227.26	DSIpoised	Z89307993	23.80	5	01:01:29	done	HPrP-x0496	00:00:36	65.876 - 2.315

Entry ID	Structure	Mol Weight (g/mol)	Library Name	Compound Code	Compound Concentration (mM)	Solvent Fraction (%, v/v)	Soaking Time	Harvest Status	Crystal Name	Mounting Time	Resolution Overall (Å)
297	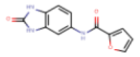	243.22	DSIpoised	Z26794338	23.80	5	01:02:09	done	HPrP-x0497	00:00:37	42.742 - 2.220
298	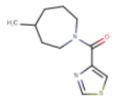	224.32	DSIpoised	Z1101755952	23.80	5	01:02:47	done	HPrP-x0498	00:00:36	None
299		199.30	DSIpoised	Z57257264	23.80	5	01:03:37	done	HPrP-x0499	00:00:48	42.683 - 2.256
300	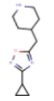	207.28	DSIpoised	Z2442270563	23.80	5	01:03:42	fail		00:00:03	
301	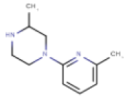	191.28	DSIpoised	Z1267885772	23.80	5	01:03:48	fail		00:00:03	
302	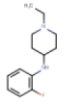	222.31	DSIpoised	Z2856434868	23.80	5	01:03:54	fail		00:00:04	
303	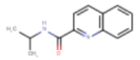	214.27	DSIpoised	Z31385861	23.80	5	01:04:43	done	HPrP-x0500	00:00:44	66.089 - 2.520
304	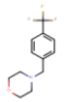	245.25	DSIpoised	Z2856434871	23.80	5	01:05:32	done	HPrP-x0501	00:00:45	65.845 - 2.838
305	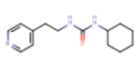	247.34	DSIpoised	Z111507846	23.80	5	01:05:39	fail		00:00:05	

Entry ID	Structure	Mol Weight (g/mol)	Library Name	Compound Code	Compound Concentration (mM)	Solvent Fraction (%, v/v)	Soaking Time	Harvest Status	Crystal Name	Mounting Time	Resolution Overall (Å)
306		223.58	DSIpoised	Z111810692	23.80	5	01:07:02	done	HPrP-x0502	00:01:21	65.677 - 2.847
307	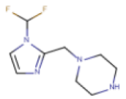	216.24	DSIpoised	Z2444672448	23.80	5	01:07:33	done	HPrP-x0503	00:00:29	None
308	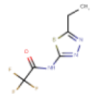	225.19	DSIpoised	Z275156196	23.80	5	01:08:10	done	HPrP-x0504	00:00:31	None
309	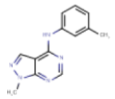	239.28	DSIpoised	Z56983806	23.80	5	01:08:44	done	HPrP-x0505	00:00:27	43.066 - 2.540
310	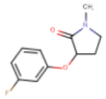	209.22	DSIpoised	Z1217960891	23.80	5	01:09:27	done	HPrP-x0506	00:00:40	51.167 - 2.516
311		241.73	DSIpoised	Z437584380	23.80	5	01:09:33	fail		00:00:05	
312	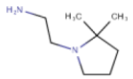	142.25	DSIpoised	Z1741815708	23.80	5	01:10:21	done	HPrP-x0507	00:00:34	43.028 - 2.395
313	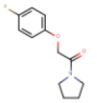	223.25	DSIpoised	Z19735067	23.80	5	01:10:26	fail		00:00:03	
314	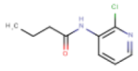	198.65	DSIpoised	Z240654968	23.80	5	01:10:51	done	HPrP-x0508	00:00:22	42.971 - 2.283

Entry ID	Structure	Mol Weight (g/mol)	Library Name	Compound Code	Compound Concentration (mM)	Solvent Fraction (%, v/v)	Soaking Time	Harvest Status	Crystal Name	Mounting Time	Resolution Overall (Å)
315	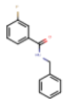	229.25	DSIpoised	Z27749656	23.80	5	01:11:20	done	HPrP-x0509	00:00:27	43.106 - 2.711
316	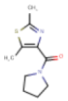	210.30	DSIpoised	Z1497321453	23.80	5	01:11:25	fail		00:00:03	
317	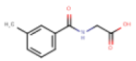	193.20	DSIpoised	Z56827661	23.80	5	01:13:19	done	HPrP-x0510	00:01:52	None
318	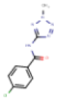	237.65	DSIpoised	Z57292434	23.80	5	01:13:42	done	HPrP-x0511	00:00:18	65.24 - 4.33
319	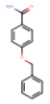	227.26	DSIpoised	Z26312102	23.80	5	01:14:22	done	HPrP-x0512	00:00:34	42.97 - 2.47
320	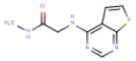	222.27	DSIpoised	Z52584368	23.80	5	01:14:49	done	HPrP-x0513	00:00:20	42.950 - 2.302
321	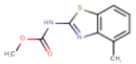	222.26	DSIpoised	Z192981502	23.80	5	01:15:27	done	HPrP-x0514	00:00:35	65.864 - 2.535
322	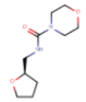	214.27	DSIpoised	Z2064898127	23.80	5	01:15:33	fail		00:00:03	
323	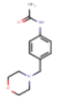	234.30	DSIpoised	Z2856434875	23.80	5	01:15:38	fail		00:00:03	

Entry ID	Structure	Mol Weight (g/mol)	Library Name	Compound Code	Compound Concentration (mM)	Solvent Fraction (%, v/v)	Soaking Time	Harvest Status	Crystal Name	Mounting Time	Resolution Overall (Å)
324	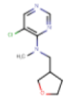	227.69	DSIpoised	Z1787627869	23.80	5	01:16:06	done	HPrP-x0515	00:00:26	None
325		140.15	DSIpoised	Z755044716	23.80	5	01:16:12	fail		00:00:04	
326	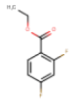	186.16	DSIpoised	Z53836105	23.80	5	01:16:41	done	HPrP-x0516	00:00:23	43.148 - 2.374
327	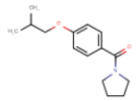	247.34	DSIpoised	Z31480458	23.80	5	01:17:25	done	HPrP-x0517	00:00:35	43.072 - 2.709
328	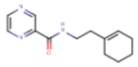	231.30	DSIpoised	Z69091635	23.80	5	01:17:59	done	HPrP-x0518	00:00:31	42.924 - 2.371
329	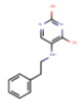	231.26	DSIpoised	Z57744604	23.80	5	01:18:28	done	HPrP-x0519	00:00:27	42.674 - 2.383
330	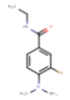	210.25	DSIpoised	Z907784200	23.80	5	01:18:55	done	HPrP-x0520	00:00:25	43.099 - 2.571
331	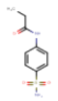	228.27	DSIpoised	Z27682767	23.80	5	01:19:18	done	HPrP-x0521	00:00:19	42.887 - 2.682
332	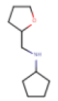	169.27	DSIpoised	Z90504169	23.80	5	01:19:52	done	HPrP-x0522	00:00:32	42.963 - 2.468

Entry ID	Structure	Mol Weight (g/mol)	Library Name	Compound Code	Compound Concentration (mM)	Solvent Fraction (%, v/v)	Soaking Time	Harvest Status	Crystal Name	Mounting Time	Resolution Overall (Å)
333	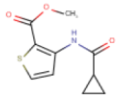	225.26	DSIpoised	Z109092588	23.80	5	01:20:20	done	HPrP-x0523	00:00:27	42.669 - 2.264
334		137.19	DSIpoised	Z1267773786	23.80	5	01:20:43	done	HPrP-x0524	00:00:21	43.035 - 2.335
335	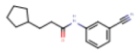	242.32	DSIpoised	Z26548228	23.80	5	01:21:07	done	HPrP-x0525	00:00:21	43.16 - 4.72
336		225.33	DSIpoised	Z31721798	23.80	5	01:21:51	done	HPrP-x0526	00:00:43	39.855 - 2.485
337	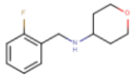	209.26	DSIpoised	Z823455846	23.80	5	01:22:18	done	HPrP-x0527	00:00:25	51.07 - 3.66
338		157.26	DSIpoised	Z103740620	23.80	5	01:22:43	done	HPrP-x0528	00:00:18	51.371 - 2.519
339	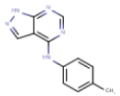	225.26	DSIpoised	Z57101343	23.80	5	01:22:48	fail		00:00:04	
340	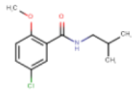	241.72	DSIpoised	Z32386228	23.80	5	01:23:11	done	HPrP-x0529	00:00:21	51.231 - 2.385
341	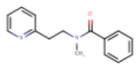	240.31	DSIpoised	Z68277692	23.80	5	01:23:37	done	HPrP-x0530	00:00:23	50.987 - 2.937

Entry ID	Structure	Mol Weight (g/mol)	Library Name	Compound Code	Compound Concentration (mM)	Solvent Fraction (%, v/v)	Soaking Time	Harvest Status	Crystal Name	Mounting Time	Resolution Overall (Å)
342	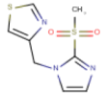	243.30	DSIpoised	Z1328968520	23.80	5	01:24:54	done	HPrP-x0531	00:01:15	51.098 - 2.607
343		238.26	DSIpoised	Z192955056	23.80	5	01:25:15	done	HPrP-x0532	00:00:18	65.819 - 3.103
344		231.30	DSIpoised	Z2856434849	23.80	5	01:25:49	done	HPrP-x0533	00:00:32	51.162 - 2.393
345	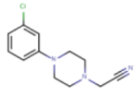	235.72	DSIpoised	Z2856434806	23.80	5	01:26:25	done	HPrP-x0534	00:00:34	43.112 - 3.278
346		136.20	DSIpoised	Z1259341037	23.80	5	01:26:31	fail		00:00:04	
347		205.27	DSIpoised	Z328695024	23.80	5	01:26:54	done	HPrP-x0535	00:00:22	66.094 - 2.711
348	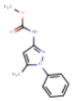	231.26	DSIpoised	Z1581680287	23.80	5	01:27:46	done	HPrP-x0536	00:00:48	65.799 - 2.275
349	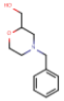	207.27	DSIpoised	Z1259086950	23.80	5	01:27:52	fail		00:00:04	
350	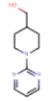	193.25	DSIpoised	Z645232558	23.80	5	01:27:57	fail		00:00:03	

Entry ID	Structure	Mol Weight (g/mol)	Library Name	Compound Code	Compound Concentration (mM)	Solvent Fraction (%, v/v)	Soaking Time	Harvest Status	Crystal Name	Mounting Time	Resolution Overall (Å)
351	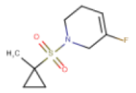	219.27	DSIpoised	Z2277255954	23.80	5	01:28:24	done	HPrP-x0537	00:00:26	None
352	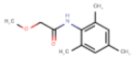	207.27	DSIpoised	Z57260516	23.80	5	01:28:49	done	HPrP-x0538	00:00:23	51.073 - 2.764
353	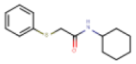	249.37	DSIpoised	Z19751622	23.80	5	01:29:18	done	HPrP-x0539	00:00:27	42.989 - 2.380
354	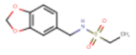	243.28	DSIpoised	Z53860899	23.80	5	01:29:40	done	HPrP-x0540	00:00:20	42.796 - 2.399
355	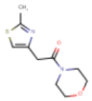	226.29	DSIpoised	Z31720228	23.80	5	01:30:03	done	HPrP-x0541	00:00:21	None
356	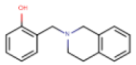	239.32	DSIpoised	Z2856434881	23.80	5	01:31:02	done	HPrP-x0542	00:00:56	None
357	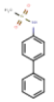	247.31	DSIpoised	Z45641455	23.80	5	01:31:49	done	HPrP-x0543	00:00:44	51.22 - 2.79
358		137.19	DSIpoised	Z31190928	23.80	5	01:32:15	done	HPrP-x0544	00:00:25	43.03 - 2.51
359	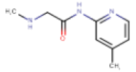	179.22	DSIpoised	Z927746322	23.80	5	01:32:20	fail		00:00:03	

Entry ID	Structure	Mol Weight (g/mol)	Library Name	Compound Code	Compound Concentration (mM)	Solvent Fraction (%, v/v)	Soaking Time	Harvest Status	Crystal Name	Mounting Time	Resolution Overall (Å)
360	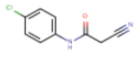	194.62	DSIpoised	Z56837087	23.80	5	01:32:53	done	HPrP-x0545	00:00:30	66.06 - 2.62
361	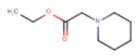	171.24	DSIpoised	Z2856434773	23.80	5	01:33:34	done	HPrP-x0546	00:00:39	42.82 - 2.61
362		247.74	DSIpoised	Z354992234	23.80	5	01:33:40	fail		00:00:04	
363	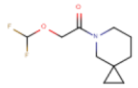	219.23	DSIpoised	Z2074076908	23.80	5	01:34:04	done	HPrP-x0547	00:00:22	None
364	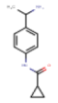	204.27	DSIpoised	Z1891773393	23.80	5	01:34:57	done	HPrP-x0548	00:00:51	None
365	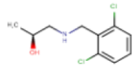	234.12	DSIpoised	Z2856434909	23.80	5	01:35:21	done	HPrP-x0549	00:00:22	None
366	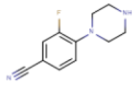	205.24	DSIpoised	Z939944666	23.80	5	01:37:47	done	HPrP-x0550	00:02:23	65.723 - 2.529
367		217.26	DSIpoised	Z2142244288	23.80	5	01:39:59	done	HPrP-x0551	00:02:08	65.754 - 2.499
368	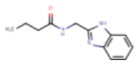	217.27	DSIpoised	Z26781952	23.80	5	01:40:48	done	HPrP-x0552	00:00:47	43.009 - 2.317

Entry ID	Structure	Mol Weight (g/mol)	Library Name	Compound Code	Compound Concentration (mM)	Solvent Fraction (%, v/v)	Soaking Time	Harvest Status	Crystal Name	Mounting Time	Resolution Overall (Å)
369		213.30	DSIpoised	Z1439422127	23.80	5	01:40:52	fail		00:00:03	
370		169.19	DSIpoised	Z57292369	23.80	5	01:41:14	done	HPrP-x0553	00:00:20	65.679 - 2.782
371	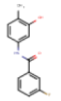	245.25	DSIpoised	Z1430613393	23.80	5	01:42:06	done	HPrP-x0554	00:00:51	None
372		240.28	DSIpoised	Z2856434851	23.80	5	01:42:30	done	HPrP-x0555	00:00:21	65.843 - 2.764
373	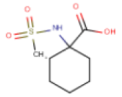	221.27	DSIpoised	Z133622412	23.80	5	01:42:52	done	HPrP-x0556	00:00:21	None
374	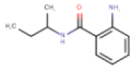	192.26	DSIpoised	Z56040660	23.80	5	01:43:22	done	HPrP-x0557	00:00:27	42.961 - 2.597
375	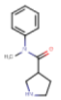	204.27	DSIpoised	Z2447286438	23.80	5	01:43:26	fail		00:00:03	
376		208.27	DSIpoised	Z57261895	23.80	5	01:44:06	done	HPrP-x0558	00:00:39	50.925 - 2.506
377	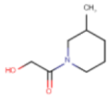	157.21	DSIpoised	Z228585534	23.80	5	00:45:52	done	HPrP-x0575	00:00:32	

Entry ID	Structure	Mol Weight (g/mol)	Library Name	Compound Code	Compound Concentration (mM)	Solvent Fraction (%, v/v)	Soaking Time	Harvest Status	Crystal Name	Mounting Time	Resolution Overall (Å)
378	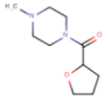	198.27	DSIpoised	Z31432964	23.80	5	00:46:33	done	HPrP-x0576	00:00:30	
379	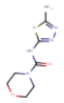	228.27	DSIpoised	Z410633222	23.80	5	00:49:03	done	HPrP-x0577	00:00:03	
380	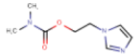	183.21	DSIpoised	Z1722836661	23.80	5	00:49:44	done	HPrP-x0578	00:00:36	
381	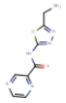	235.27	DSIpoised	Z26824727	23.80	5	00:52:09	done	HPrP-x0579	00:02:23	
382	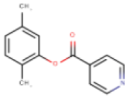	227.26	DSIpoised	Z30891796	23.80	5	00:53:53	done	HPrP-x0580	00:01:42	
383	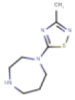	198.29	DSIpoised	Z1578665941	23.80	5	00:54:54	done	HPrP-x0581	00:00:56	
384		201.27	DSIpoised	Z2856434840	23.80	5	00:55:52	done	HPrP-x0582	00:00:55	
385	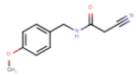	204.23	DSIpoised	Z190662888	23.80	5	00:56:51	done	HPrP-x0583	00:00:57	
386	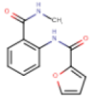	244.25	DSIpoised	Z30272547	23.80	5	00:57:38	done	HPrP-x0584	00:00:44	

Entry ID	Structure	Mol Weight (g/mol)	Library Name	Compound Code	Compound Concentration (mM)	Solvent Fraction (%, v/v)	Soaking Time	Harvest Status	Crystal Name	Mounting Time	Resolution Overall (Å)
387	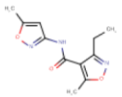	235.24	DSIpoised	Z117233350	23.80	5	00:58:08	done	HPrP-x0585	00:00:28	
388		200.24	DSIpoised	Z2856434804	23.80	5	00:58:51	done	HPrP-x0586	00:00:41	
389		230.28	DSIpoised	Z1673618163	23.80	5	00:59:21	done	HPrP-x0587	00:00:28	
390		225.21	DSIpoised	Z394039592	23.80	5	00:59:58	done	HPrP-x0588	00:00:34	
391		247.17	DSIpoised	Z56767614	23.80	5	01:02:00	done	HPrP-x0589	00:02:00	
392		205.27	DSIpoised	Z56791867	23.80	5	01:03:19	done	HPrP-x0590	00:01:17	
393	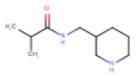	184.28	DSIpoised	Z1262327459	23.80	5	01:03:53	done	HPrP-x0591	00:00:31	51.90 - 3.87
394	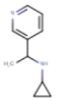	162.24	DSIpoised	Z1263529721	23.80	5	01:04:33	done	HPrP-x0592	00:00:38	43.246 - 2.575
395	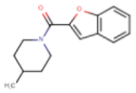	243.31	DSIpoised	Z32665176	23.80	5	01:05:05	done	HPrP-x0593	00:00:29	None

Entry ID	Structure	Mol Weight (g/mol)	Library Name	Compound Code	Compound Concentration (mM)	Solvent Fraction (%, v/v)	Soaking Time	Harvest Status	Crystal Name	Mounting Time	Resolution Overall (Å)
396	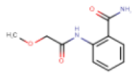	208.22	DSIpoised	Z57260539	23.80	5	01:05:41	done	HPrP-x0594	00:00:33	42.866 - 2.441
397	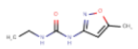	169.18	DSIpoised	Z56880342	23.80	5	01:07:00	done	HPrP-x0595	00:01:17	51.330 - 2.709
398	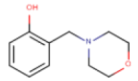	193.25	DSIpoised	Z2856434887	23.80	5	01:07:21	done	HPrP-x0596	00:00:20	51.394 - 2.326
399		180.21	DSIpoised	Z1449748885	23.80	5	01:07:43	done	HPrP-x0597	00:00:19	43.297 - 2.673
400	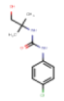	242.70	DSIpoised	Z123970702	23.80	5	01:08:24	done	HPrP-x0598	00:00:40	43.202 - 2.538
401	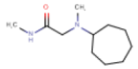	198.31	DSIpoised	Z204776284	23.80	5	01:09:09	done	HPrP-x0599	00:00:43	42.853 - 2.743
402	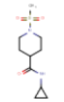	246.33	DSIpoised	Z227998000	23.80	5	01:09:45	done	HPrP-x0600	00:00:33	43.175 - 2.719
403		210.28	DSIpoised	Z1259339735	23.80	5	01:10:28	done	HPrP-x0601	00:00:40	43.172 - 2.320
404		192.31	DSIpoised	Z2856434894	23.80	5	01:10:59	done	HPrP-x0602	00:00:28	43.070 - 2.520

Entry ID	Structure	Mol Weight (g/mol)	Library Name	Compound Code	Compound Concentration (mM)	Solvent Fraction (%, v/v)	Soaking Time	Harvest Status	Crystal Name	Mounting Time	Resolution Overall (Å)
405	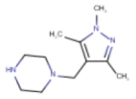	208.31	DSIpoised	Z1263820300	23.80	5	01:11:25	done	HPrP-x0603	00:00:23	43.030 - 2.300
406		227.69	DSIpoised	Z68299550	23.80	5	01:11:55	done	HPrP-x0604	00:00:28	None
407	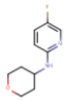	196.23	DSIpoised	Z1172243962	23.80	5	01:12:33	done	HPrP-x0605	00:00:34	42.986 - 2.451
408		248.23	DSIpoised	Z44586758	23.80	5	01:12:58	done	HPrP-x0606	00:00:23	66.114 - 3.406
409		237.28	DSIpoised	Z2856434944	23.80	5	01:14:37	done	HPrP-x0607	00:01:37	43.017 - 2.402
410	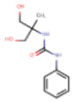	224.26	DSIpoised	Z57472297	23.80	5	01:15:10	done	HPrP-x0608	00:00:31	50.788 - 2.568
411	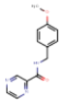	243.27	DSIpoised	Z30871350	23.80	5	01:15:48	done	HPrP-x0609	00:00:36	51.236 - 2.365
412	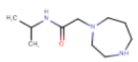	199.30	DSIpoised	Z1262254278	23.80	5	01:16:18	done	HPrP-x0610	00:00:27	43.182 - 2.386
413		140.14	DSIpoised	Z1124201124	23.80	5	01:17:30	done	HPrP-x0611	00:01:10	42.669 - 2.153

Entry ID	Structure	Mol Weight (g/mol)	Library Name	Compound Code	Compound Concentration (mM)	Solvent Fraction (%, v/v)	Soaking Time	Harvest Status	Crystal Name	Mounting Time	Resolution Overall (Å)
414	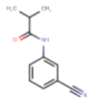	188.23	DSIpoised	Z26548083	23.80	5	01:18:35	done	HPrP-x0612	00:01:03	51.568 - 2.560
415		235.30	DSIpoised	Z134785326	23.80	5	01:19:23	done	HPrP-x0613	00:00:45	42.638 - 2.383
416	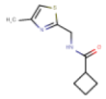	210.30	DSIpoised	Z212122838	23.80	5	01:19:43	done	HPrP-x0614	00:00:18	43.026 - 2.472
417	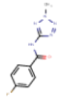	221.20	DSIpoised	Z57292433	23.80	5	01:20:03	done	HPrP-x0615	00:00:15	None
418		243.28	DSIpoised	Z123856654	23.80	5	01:20:59	done	HPrP-x0616	00:00:54	65.371 - 3.289
419	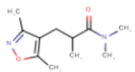	210.28	DSIpoised	Z1246465616	23.80	5	01:21:54	done	HPrP-x0617	00:00:33	51.441 - 2.555
420		142.25	DSIpoised	Z1245580461	23.80	5	01:22:16	done	HPrP-x0618	00:00:20	42.731 - 2.431
421	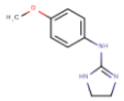	191.23	DSIpoised	Z57186564	23.80	5	01:22:39	done	HPrP-x0619	00:00:21	51.472 - 2.256
422		150.18	DSIpoised	Z1148747945	23.80	5	01:22:46	fail		00:00:04	

Entry ID	Structure	Mol Weight (g/mol)	Library Name	Compound Code	Compound Concentration (mM)	Solvent Fraction (%, v/v)	Soaking Time	Harvest Status	Crystal Name	Mounting Time	Resolution Overall (Å)
423		224.23	DSIpoised	Z1818332938	23.80	5	01:23:07	done	HPrP-x0620	00:00:19	51.226 - 2.572
424		167.21	DSIpoised	Z1263714198	23.80	5	01:23:32	done	HPrP-x0621	00:00:23	42.635 - 2.963
425	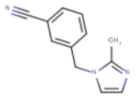	197.24	DSIpoised	Z319545618	23.80	5	01:24:16	done	HPrP-x0622	00:00:42	66.109 - 2.855
426	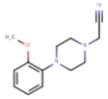	231.30	DSIpoised	Z2856434807	23.80	5	01:24:38	done	HPrP-x0623	00:00:18	51.170 - 2.698
427	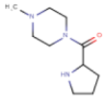	197.28	DSIpoised	Z241832786	23.80	5	01:25:01	done	HPrP-x0624	00:00:21	51.165 - 2.503
428	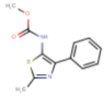	248.30	DSIpoised	Z979145504	23.80	5	01:25:27	done	HPrP-x0625	00:00:22	79.56 - 3.67
429		142.20	DSIpoised	Z1650040241	23.80	5	01:25:49	done	HPrP-x0626	00:00:19	11.33 - 1.60
430		174.20	DSIpoised	Z1273312153	23.80	5	01:26:36	done	HPrP-x0627	00:00:43	None
431		223.62	DSIpoised	Z275154304	23.80	5	01:26:57	done	HPrP-x0628	00:00:19	None

Entry ID	Structure	Mol Weight (g/mol)	Library Name	Compound Code	Compound Concentration (mM)	Solvent Fraction (%, v/v)	Soaking Time	Harvest Status	Crystal Name	Mounting Time	Resolution Overall (Å)
432	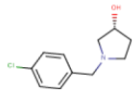	211.69	DSIpoised	Z2856434858	23.80	5	01:27:37	done	HPrP-x0629	00:00:37	51.57 - 2.52
433	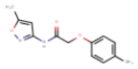	246.27	DSIpoised	Z19731563	23.80	5	01:28:04	done	HPrP-x0630	00:00:25	65.918 - 2.468
434	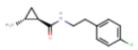	237.73	DSIpoised	Z1802166390	23.80	5	01:28:28	done	HPrP-x0631	00:00:22	None
435		170.26	DSIpoised	Z927412236	23.80	5	01:29:08	done	HPrP-x0632	00:00:38	43.207 - 2.277
436	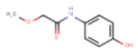	181.19	DSIpoised	Z943693514	23.80	5	01:29:46	done	HPrP-x0633	00:00:36	42.745 - 2.281
437	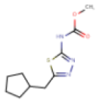	241.31	DSIpoised	Z1119505742	23.80	5	01:30:31	done	HPrP-x0634	00:00:42	43.077 - 3.592
438		166.23	DSIpoised	Z1891776952	23.80	5	01:31:12	done	HPrP-x0635	00:00:38	42.848 - 2.464
439		156.20	DSIpoised	Z969560582	23.80	5	01:32:13	done	HPrP-x0636	00:00:56	51.583 - 2.200
440		174.25	DSIpoised	Z1137725943	23.80	5	01:32:37	done	HPrP-x0637	00:00:22	51.455 - 2.424

Entry ID	Structure	Mol Weight (g/mol)	Library Name	Compound Code	Compound Concentration (mM)	Solvent Fraction (%, v/v)	Soaking Time	Harvest Status	Crystal Name	Mounting Time	Resolution Overall (Å)
441	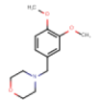	237.30	DSIpoised	Z2856434878	23.80	5	01:33:06	done	HPrP-x0638	00:00:27	51.205 - 2.635
442		205.66	DSIpoised	Z45527714	23.80	5	01:34:24	done	HPrP-x0639	00:01:15	65.187 - 3.078
443	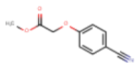	191.19	DSIpoised	Z19234337	23.80	5	01:35:04	done	HPrP-x0640	00:00:37	43.402 - 2.399
444	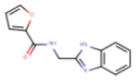	241.25	DSIpoised	Z26781964	23.80	5	01:35:51	done	HPrP-x0641	00:00:44	51.438 - 2.714
445	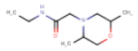	200.28	DSIpoised	Z355728146	23.80	5	01:36:38	done	HPrP-x0642	00:00:45	43.254 - 2.318
446	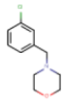	211.69	DSIpoised	Z2856434856	23.80	5	01:36:58	done	HPrP-x0643	00:00:17	36.469 - 2.553
447	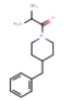	245.37	DSIpoised	Z30162334	23.80	5	01:37:27	done	HPrP-x0644	00:00:26	51.535 - 2.499
448	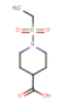	221.27	DSIpoised	Z53825020	23.80	5	01:37:49	done	HPrP-x0645	00:00:20	None
449	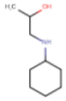	157.26	DSIpoised	Z2856434893	23.80	5	01:38:23	done	HPrP-x0646	00:00:33	51.471 - 2.214

Entry ID	Structure	Mol Weight (g/mol)	Library Name	Compound Code	Compound Concentration (mM)	Solvent Fraction (%, v/v)	Soaking Time	Harvest Status	Crystal Name	Mounting Time	Resolution Overall (Å)
450	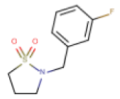	229.27	DSIpoised	Z729352906	23.80	5	01:38:45	done	HPrP-x0647	00:00:18	51.558 - 2.571
451	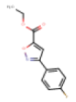	235.21	DSIpoised	Z2106600670	23.80	5	01:39:29	done	HPrP-x0648	00:00:43	51.439 - 2.698
452	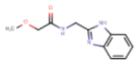	219.24	DSIpoised	Z111529496	23.80	5	01:40:11	done	HPrP-x0649	00:00:38	65.956 - 2.417
453	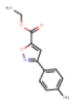	231.25	DSIpoised	Z793500562	23.80	5	01:40:36	done	HPrP-x0650	00:00:23	None
454	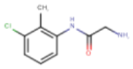	198.65	DSIpoised	Z85956652	23.80	5	01:41:00	done	HPrP-x0651	00:00:22	42.576 - 2.407
455	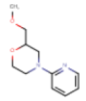	208.26	DSIpoised	Z1272480091	23.80	5	01:41:29	fail		00:00:27	
456		218.30	DSIpoised	Z31792168	23.80	5	01:41:54	done	HPrP-x0652	00:00:23	51.309 - 2.525
457	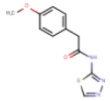	249.29	DSIpoised	Z86416929	23.80	5	01:42:27	done	HPrP-x0653	00:00:29	43.326 - 2.566
458	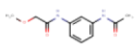	222.24	DSIpoised	Z31735562	23.80	5	01:50:54	done	HPrP-x0654	00:00:01	43.374 - 2.073

Entry ID	Structure	Mol Weight (g/mol)	Library Name	Compound Code	Compound Concentration (mM)	Solvent Fraction (%, v/v)	Soaking Time	Harvest Status	Crystal Name	Mounting Time	Resolution Overall (Å)
459	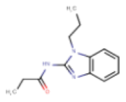	231.30	DSIpoised	Z29077827	23.80	5	01:51:27	done	HPrP-x0655	00:00:30	51.306 - 2.211
460	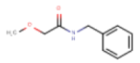	179.22	DSIpoised	Z31478538	23.80	5	01:51:56	done	HPrP-x0656	00:00:27	43.077 - 2.521
461	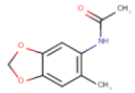	193.20	DSIpoised	Z1635496816	23.80	5	01:52:42	done	HPrP-x0657	00:00:43	43.67 - 4.49
462	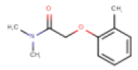	193.25	DSIpoised	Z19733482	23.80	5	01:53:32	done	HPrP-x0658	00:00:47	51.423 - 2.742
463	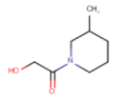	157.21	DSIpoised	Z228585534	23.80	5	00:45:36	done	HPrP-x0702	00:00:44	None
464	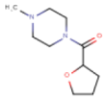	198.27	DSIpoised	Z31432964	23.80	5	00:47:01	done	HPrP-x0703	00:01:20	66.122 - 2.736
465	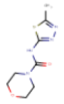	228.27	DSIpoised	Z410633222	23.80	5	00:47:23	done	HPrP-x0704	00:00:20	42.994 - 2.685
466	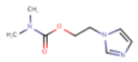	183.21	DSIpoised	Z1722836661	23.80	5	00:47:30	fail		00:00:06	
467	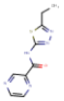	235.27	DSIpoised	Z26824727	23.80	5	00:47:56	done	HPrP-x0705	00:00:24	50.946 - 2.485

Entry ID	Structure	Mol Weight (g/mol)	Library Name	Compound Code	Compound Concentration (mM)	Solvent Fraction (%, v/v)	Soaking Time	Harvest Status	Crystal Name	Mounting Time	Resolution Overall (Å)
468	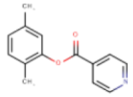	227.26	DSIpoised	Z30891796	23.80	5	00:48:05	fail		00:00:08	
469	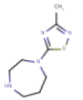	198.29	DSIpoised	Z1578665941	23.80	5	00:48:11	fail		00:00:04	
470	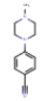	201.27	DSIpoised	Z2856434840	23.80	5	00:48:40	done	HPrP-x0706	00:00:28	42.948 - 2.348
471	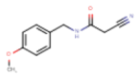	204.23	DSIpoised	Z190662888	23.80	5	00:49:12	done	HPrP-x0707	00:00:30	42.850 - 2.873
472		244.25	DSIpoised	Z30272547	23.80	5	00:49:41	done	HPrP-x0708	00:00:28	51.058 - 2.595
473	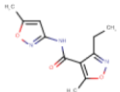	235.24	DSIpoised	Z117233350	23.80	5	00:50:08	done	HPrP-x0709	00:00:25	51.340 - 2.289
474		200.24	DSIpoised	Z2856434804	23.80	5	00:50:50	fail		00:00:41	
475		230.28	DSIpoised	Z1673618163	23.80	5	00:51:12	done	HPrP-x0710	00:00:21	51.162 - 2.628
476		225.21	DSIpoised	Z394039592	23.80	5	00:51:39	done	HPrP-x0711	00:00:25	51.035 - 2.721

Entry ID	Structure	Mol Weight (g/mol)	Library Name	Compound Code	Compound Concentration (mM)	Solvent Fraction (%, v/v)	Soaking Time	Harvest Status	Crystal Name	Mounting Time	Resolution Overall (Å)
477		247.17	DSIpoised	Z56767614	23.80	5	00:51:57	done	HPrP-x0712	00:00:16	43.051 - 2.621
478		205.27	DSIpoised	Z56791867	23.80	5	00:52:24	done	HPrP-x0713	00:00:25	43.05 - 4.01
479	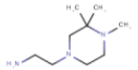	171.29	DSIpoised	Z1992316315	23.80	5	00:52:56	done	HPrP-x0714	00:00:30	65.865 - 2.728
480		156.23	DSIpoised	Z1787158625	23.80	5	00:53:15	done	HPrP-x0715	00:00:18	51.175 - 2.432
481	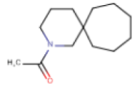	209.33	DSIpoised	Z1275599911	23.80	5	00:53:44	done	HPrP-x0716	00:00:28	51.106 - 2.438
482	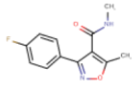	234.23	DSIpoised	Z363104204	23.80	5	00:54:05	done	HPrP-x0717	00:00:20	43.163 - 2.269
483		177.25	DSIpoised	Z32014663	23.80	5	00:54:29	done	HPrP-x0718	00:00:22	65.643 - 2.603
484		141.21	DSIpoised	Z818727262	23.80	5	00:54:49	done	HPrP-x0719	00:00:19	65.958 - 2.618
485		159.19	DSIpoised	Z1454840342	23.80	5	00:55:31	done	HPrP-x0720	00:00:41	51.008 - 2.592

Entry ID	Structure	Mol Weight (g/mol)	Library Name	Compound Code	Compound Concentration (mM)	Solvent Fraction (%, v/v)	Soaking Time	Harvest Status	Crystal Name	Mounting Time	Resolution Overall (Å)
486	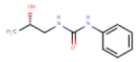	194.23	DSIpoised	Z1563512128	23.80	5	00:55:53	done	HPrP-x0721	00:00:20	None
487		186.16	DSIpoised	Z55671900	23.80	5	00:57:12	done	HPrP-x0722	00:01:18	51.022 - 2.481
488		194.23	DSIpoised	Z235341991	23.80	5	00:57:49	done	HPrP-x0723	00:00:35	43.071 - 1.937
489		142.20	DSIpoised	Z1741785925	23.80	5	00:57:57	fail		00:00:06	
490	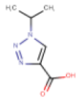	155.16	DSIpoised	Z2510259379	23.80	5	00:58:32	done	HPrP-x0724	00:00:33	None
491	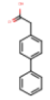	212.25	DSIpoised	Z2856434779	23.80	5	00:58:51	done	HPrP-x0725	00:00:18	50.688 - 2.899
492	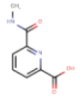	180.16	DSIpoised	Z1816233707	23.80	5	00:59:00	fail		00:00:08	
493	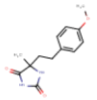	248.28	DSIpoised	Z56772132	23.80	5	00:59:20	done	HPrP-x0726	00:00:18	51.015 - 2.586
494	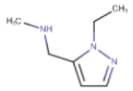	139.20	DSIpoised	Z2856434839	23.80	5	01:00:09	done	HPrP-x0727	00:00:48	None

Entry ID	Structure	Mol Weight (g/mol)	Library Name	Compound Code	Compound Concentration (mM)	Solvent Fraction (%, v/v)	Soaking Time	Harvest Status	Crystal Name	Mounting Time	Resolution Overall (Å)
495	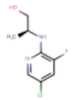	204.63	DSIpoised	Z1432018343	23.80	5	01:00:32	done	HPrP-x0728	00:00:21	51.035 - 2.192
496	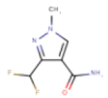	175.14	DSIpoised	Z1515654336	23.80	5	01:01:36	done	HPrP-x0729	00:01:03	51.017 - 2.425
497		233.29	DSIpoised	Z48847594	23.80	5	01:02:06	done	HPrP-x0730	00:00:27	42.937 - 3.102
498	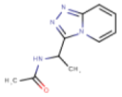	204.23	DSIpoised	Z131516158	23.80	5	01:02:40	done	HPrP-x0731	00:00:32	50.974 - 2.438
499		163.24	DSIpoised	Z53825479	23.80	5	01:02:45	fail		00:00:04	
500	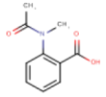	193.20	DSIpoised	Z223688272	23.80	5	01:03:07	done	HPrP-x0732	00:00:20	None
501	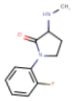	208.24	DSIpoised	Z1186029914	23.80	5	01:03:30	done	HPrP-x0733	00:00:22	42.631 - 1.904
502	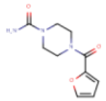	223.23	DSIpoised	Z198194396	23.80	5	01:03:35	fail		00:00:03	
503	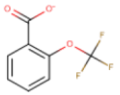	205.11	DSIpoised	Z2856434778	23.80	5	01:03:39	fail		00:00:03	

Entry ID	Structure	Mol Weight (g/mol)	Library Name	Compound Code	Compound Concentration (mM)	Solvent Fraction (%, v/v)	Soaking Time	Harvest Status	Crystal Name	Mounting Time	Resolution Overall (Å)
504	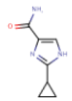	151.17	DSIpoised	Z1407672867	23.80	5	01:04:10	done	HPrP-x0734	00:00:29	None
505	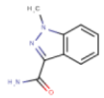	175.19	DSIpoised	Z2697514548	23.80	5	01:04:49	done	HPrP-x0735	00:00:38	65.821 - 1.981
506		192.27	DSIpoised	Z1139246057	23.80	5	01:04:54	fail		00:00:03	
507		178.24	DSIpoised	Z1267882044	23.80	5	01:05:00	fail		00:00:04	
508		207.29	DSIpoised	Z2735592898	23.80	5	01:05:31	done	HPrP-x0736	00:00:30	42.953 - 2.562
509	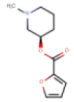	209.25	DSIpoised	Z2940170964	23.80	5	01:06:14	done	HPrP-x0737	00:00:41	None
510		199.27	DSIpoised	Z45617795	23.80	5	01:06:35	done	HPrP-x0738	00:00:20	79.53 - 4.25
511		244.08	DSIpoised	Z1891776064	23.80	5	01:07:12	done	HPrP-x0739	00:00:35	65.70 - 2.95
512		140.19	DSIpoised	Z1674937530	23.80	5	01:07:52	fail		00:00:38	

Entry ID	Structure	Mol Weight (g/mol)	Library Name	Compound Code	Compound Concentration (mM)	Solvent Fraction (%, v/v)	Soaking Time	Harvest Status	Crystal Name	Mounting Time	Resolution Overall (Å)
513		139.20	DSIpoised	Z2856434888	23.80	5	01:08:08	done	HPrP-x0740	00:00:14	None
514	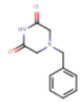	204.23	DSIpoised	Z2856434910	23.80	5	01:08:32	done	HPrP-x0741	00:00:22	None
515		179.23	DSIpoised	Z1247413608	23.80	5	01:08:56	done	HPrP-x0742	00:00:23	42.856 - 2.368
516		122.17	DSIpoised	Z2856434762	23.80	5	01:09:01	fail		00:00:03	
517	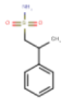	199.27	DSIpoised	Z1407673036	23.80	5	01:09:40	done	HPrP-x0743	00:00:38	43.024 - 2.545
518		171.20	DSIpoised	Z90122368	23.80	5	01:09:45	fail		00:00:03	
519		171.20	DSIpoised	Z1259162160	23.80	5	01:09:50	fail		00:00:03	
520		199.63	DSIpoised	Z19727416	23.80	5	01:10:22	done	HPrP-x0744	00:00:30	None
521	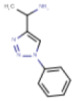	188.23	DSIpoised	Z2527301677	23.80	5	01:10:42	done	HPrP-x0745	00:00:19	None

Entry ID	Structure	Mol Weight (g/mol)	Library Name	Compound Code	Compound Concentration (mM)	Solvent Fraction (%, v/v)	Soaking Time	Harvest Status	Crystal Name	Mounting Time	Resolution Overall (Å)
522	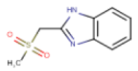	210.25	DSIpoised	Z126932614	23.80	5	01:10:46	fail		00:00:02	
523		196.17	DSIpoised	Z1262246195	23.80	5	01:11:19	done	HPrP-x0746	00:00:31	65.790 - 2.918
524		189.23	DSIpoised	Z1509882419	23.80	5	01:11:42	done	HPrP-x0747	00:00:21	65.509 - 2.426
525		192.22	DSIpoised	Z87615031	23.80	5	01:12:19	done	HPrP-x0748	00:00:35	42.863 - 2.516
526	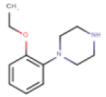	206.29	DSIpoised	Z425387594	23.80	5	01:12:48	done	HPrP-x0749	00:00:28	65.768 - 3.048
527		204.27	DSIpoised	Z1650168321	23.80	5	01:13:14	fail		00:00:24	
528	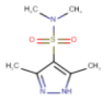	203.26	DSIpoised	Z94597856	23.80	5	01:13:50	done	HPrP-x0750	00:00:34	50.904 - 2.854
529	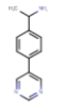	199.26	DSIpoised	Z1696822287	23.80	5	01:13:54	fail		00:00:03	
530	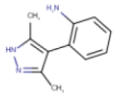	187.25	DSIpoised	Z1270312110	23.80	5	00:48:23	done	HPrP-x0659	00:00:53	None

Entry ID	Structure	Mol Weight (g/mol)	Library Name	Compound Code	Compound Concentration (mM)	Solvent Fraction (%, v/v)	Soaking Time	Harvest Status	Crystal Name	Mounting Time	Resolution Overall (Å)
531		159.19	DSIpoised	Z1312590981	23.80	5	00:49:19	done	HPrP-x0660	00:00:50	65.793 - 2.954
532	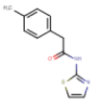	232.30	DSIpoised	Z90713255	23.80	5	00:50:09	done	HPrP-x0661	00:00:48	51.295 - 2.325
533	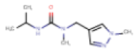	210.28	DSIpoised	Z183344018	23.80	5	00:50:47	done	HPrP-x0662	00:00:31	66.170 - 2.851
534		129.20	DSIpoised	Z2856434900	23.80	5	00:51:32	done	HPrP-x0663	00:00:44	65.940 - 3.260
535	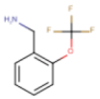	191.15	DSIpoised	Z2856434776	23.80	5	00:52:12	done	HPrP-x0664	00:00:29	66.070 - 2.580
536		233.36	DSIpoised	Z2856434874	23.80	5	00:54:14	done	HPrP-x0665	00:01:53	None
537		177.16	DSIpoised	Z2027158783	23.80	5	00:55:08	done	HPrP-x0666	00:00:53	51.187 - 2.545
538	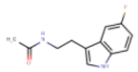	220.25	DSIpoised	Z1220452176	23.80	5	00:56:05	done	HPrP-x0667	00:00:55	42.957 - 2.530
539		142.25	DSIpoised	Z1741966630	23.80	5	00:56:49	done	HPrP-x0668	00:00:35	42.776 - 2.334

Entry ID	Structure	Mol Weight (g/mol)	Library Name	Compound Code	Compound Concentration (mM)	Solvent Fraction (%, v/v)	Soaking Time	Harvest Status	Crystal Name	Mounting Time	Resolution Overall (Å)
540		197.17	DSIpoised	Z364328788	23.80	5	00:57:39	done	HPrP-x0669	00:00:49	65.538 - 2.885
541	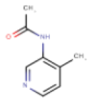	150.18	DSIpoised	Z1129283193	23.80	5	00:58:02	done	HPrP-x0670	00:00:22	43.005 - 2.399
542		249.29	DSIpoised	Z271004858	23.80	5	00:58:31	done	HPrP-x0671	00:00:26	43.160 - 2.637
543		139.16	DSIpoised	Z383325512	23.80	5	00:59:07	done	HPrP-x0672	00:00:35	65.954 - 2.236
544		191.21	DSIpoised	Z1454310449	23.80	5	00:59:31	done	HPrP-x0673	00:00:23	42.725 - 2.400
545		218.25	DSIpoised	Z300245038	23.80	5	01:00:12	done	HPrP-x0674	00:00:40	42.926 - 2.578
546	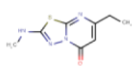	210.26	DSIpoised	Z1896598013	23.80	5	01:01:05	done	HPrP-x0675	00:00:50	42.837 - 2.399
547	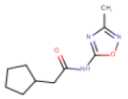	209.25	DSIpoised	Z729726784	23.80	5	01:01:16	fail		00:00:09	
548	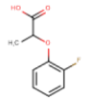	184.17	DSIpoised	Z65532537	23.80	5	01:01:23	fail		00:00:05	

Entry ID	Structure	Mol Weight (g/mol)	Library Name	Compound Code	Compound Concentration (mM)	Solvent Fraction (%, v/v)	Soaking Time	Harvest Status	Crystal Name	Mounting Time	Resolution Overall (Å)
549	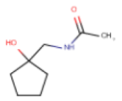	157.21	DSIpoised	Z1203329531	23.80	5	01:01:53	done	HPrP-x0676	00:00:29	65.350 - 2.832
550		142.20	DSIpoised	Z90664455	23.80	5	01:02:01	fail		00:00:06	
551	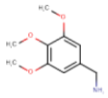	197.23	DSIpoised	Z1741959530	23.80	5	01:02:30	done	HPrP-x0677	00:00:27	65.561 - 2.536
552		156.14	DSIpoised	Z1273141646	23.80	5	01:02:58	done	HPrP-x0678	00:00:27	50.383 - 3.223
553	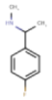	153.20	DSIpoised	Z166605480	23.80	5	01:03:03	fail		00:00:04	
554	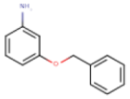	199.25	DSIpoised	Z933326822	23.80	5	01:03:27	done	HPrP-x0679	00:00:22	43.244 - 2.484
555	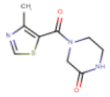	225.27	DSIpoised	Z422344882	23.80	5	01:03:48	done	HPrP-x0680	00:00:19	51.228 - 2.667
556		207.24	DSIpoised	Z133632670	23.80	5	01:04:11	done	HPrP-x0681	00:00:21	None
557		223.25	DSIpoised	Z198194394	23.80	5	01:04:55	done	HPrP-x0682	00:00:43	None

Entry ID	Structure	Mol Weight (g/mol)	Library Name	Compound Code	Compound Concentration (mM)	Solvent Fraction (%, v/v)	Soaking Time	Harvest Status	Crystal Name	Mounting Time	Resolution Overall (Å)
558	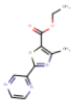	249.29	DSIpoised	Z735557654	23.80	5	01:05:24	done	HPrP-x0683	00:00:20	43.018 - 2.581
559	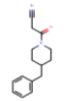	242.32	DSIpoised	Z1688493887	23.80	5	01:05:55	done	HPrP-x0684	00:00:30	51.116 - 3.057
560		232.20	DSIpoised	Z2856434931	23.80	5	01:06:15	done	HPrP-x0685	00:00:19	None
561		145.18	DSIpoised	Z57478994	23.80	5	01:06:43	done	HPrP-x0686	00:00:26	65.955 - 2.454
562		180.13	DSIpoised	Z1268152398	23.80	5	01:07:07	fail		00:00:22	
563	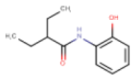	207.27	DSIpoised	Z1331830630	23.80	5	01:07:46	done	HPrP-x0687	00:00:38	51.195 - 2.458
564		122.17	DSIpoised	Z2856434786	23.80	5	01:08:20	done	HPrP-x0688	00:00:32	42.959 - 2.317
565	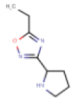	167.21	DSIpoised	Z1350579414	23.80	5	01:08:40	done	HPrP-x0689	00:00:18	None
566		227.69	DSIpoised	Z275179946	23.80	5	01:09:57	done	HPrP-x0690	00:01:15	51.172 - 2.462

Entry ID	Structure	Mol Weight (g/mol)	Library Name	Compound Code	Compound Concentration (mM)	Solvent Fraction (%, v/v)	Soaking Time	Harvest Status	Crystal Name	Mounting Time	Resolution Overall (Å)
567	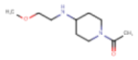	200.28	DSIpoised	Z2856434813	23.80	5	01:10:27	done	HPrP-x0691	00:00:29	43.132 - 2.924
568	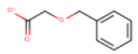	165.17	DSIpoised	Z2856434906	23.80	5	01:10:47	done	HPrP-x0692	00:00:18	65.417 - 2.723
569		137.14	DSIpoised	Z19684186	23.80	5	01:11:06	done	HPrP-x0693	00:00:18	51.404 - 2.874
570		189.18	DSIpoised	Z2856434809	23.80	5	01:12:14	done	HPrP-x0694	00:01:06	65.671 - 2.719
571		184.28	DSIpoised	Z1267773591	23.80	5	01:12:40	fail		00:00:24	
572		152.20	DSIpoised	Z952656810	23.80	5	01:13:04	done	HPrP-x0695	00:00:22	65.841 - 3.114
573	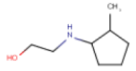	143.23	DSIpoised	Z1396419547	23.80	5	01:13:24	done	HPrP-x0696	00:00:18	51.17 - 4.29
574	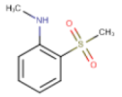	185.24	DSIpoised	Z285782452	23.80	5	01:13:46	done	HPrP-x0697	00:00:19	None
575		151.17	DSIpoised	Z57040482	23.80	5	01:14:17	done	HPrP-x0698	00:00:29	43.032 - 2.436

Entry ID	Structure	Mol Weight (g/mol)	Library Name	Compound Code	Compound Concentration (mM)	Solvent Fraction (%, v/v)	Soaking Time	Harvest Status	Crystal Name	Mounting Time	Resolution Overall (Å)
576		199.64	DSIpoised	Z906021418	23.80	5	01:14:48	done	HPrP-x0699	00:00:28	50.950 - 2.447
577	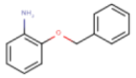	199.25	DSIpoised	Z336089202	23.80	5	01:15:44	done	HPrP-x0700	00:00:55	42.939 - 2.532
578		209.63	DSIpoised	Z1374778753	23.80	5	01:16:17	done	HPrP-x0701	00:00:32	41.08 - 6.18
579		99.09	MiniFrag	Z1245635875	937.50	37	00:30:19	done	HPrP-x0780	00:00:29	65.883 - 2.404
580		68.08	MiniFrag	Z1741966780	937.50	37	00:31:23	done	HPrP-x0781	00:00:21	51.170 - 2.421
581		158.00	MiniFrag	Z1250132521	937.50	37	00:32:18	done	HPrP-x0782	00:00:35	65.701 - 2.415
582	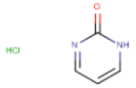	132.55	MiniFrag	Z1201023052	937.50	37	00:33:35	done	HPrP-x0783	00:00:32	43.009 - 2.359
583		101.15	MiniFrag	Z1506115273	937.50	37	00:34:23	fail			
584		69.07	MiniFrag	Z1198386795	937.50	37	00:35:26	done	HPrP-x0784	00:00:29	43.06 - 2.81

Entry ID	Structure	Mol Weight (g/mol)	Library Name	Compound Code	Compound Concentration (mM)	Solvent Fraction (%, v/v)	Soaking Time	Harvest Status	Crystal Name	Mounting Time	Resolution Overall (Å)
585		95.11	MiniFrag	Z1741970824	937.50	37	00:36:29	done	HPrP-x0785	00:00:21	51.014 - 2.380
586	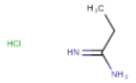	108.57	MiniFrag	Z1741969146	937.50	37	00:38:41	done	HPrP-x0786	00:00:35	42.858 - 2.501
587		100.08	MiniFrag	Z57131035	937.50	37	00:40:23	done	HPrP-x0787	00:00:32	65.893 - 2.547
588	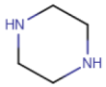	86.14	MiniFrag	Z1245537944	937.50	37	00:41:18	done	HPrP-x0788	00:00:29	51.272 - 2.590
589		75.07	MiniFrag	Z955123660	937.50	37	00:42:23	done	HPrP-x0789	00:00:21	65.738 - 2.436
590		101.11	MiniFrag	Z1318268680	937.50	37	00:43:13	done	HPrP-x0790	00:00:35	50.891 - 2.364
591		128.15	MiniFrag	Z166605460	937.50	37	00:44:40	done	HPrP-x0791	00:00:32	42.955 - 2.234
592		99.09	MiniFrag	Z57127349	937.50	37	00:45:38	done	HPrP-x0792	00:00:29	65.832 - 2.674
593		94.12	MiniFrag	Z275118248	937.50	37	00:47:34	done	HPrP-x0793	00:00:21	50.943 - 2.335

Entry ID	Structure	Mol Weight (g/mol)	Library Name	Compound Code	Compound Concentration (mM)	Solvent Fraction (%, v/v)	Soaking Time	Harvest Status	Crystal Name	Mounting Time	Resolution Overall (Å)
594		107.13	MiniFrag	Z425449766	937.50	37	00:49:46	done	HPrP-x0794	00:00:35	50.787 - 2.168
595		100.16	MiniFrag	Z1954801734	937.50	37	00:51:24	done	HPrP-x0795	00:00:32	42.983 - 2.360
596		85.11	MiniFrag	Z940713508	937.50	37	00:54:26	done	HPrP-x0796	00:00:29	50.970 - 2.209
597		95.10	MiniFrag	Z1741982125	937.50	37	00:55:29	done	HPrP-x0797	00:00:21	42.964 - 2.341
598		89.09	MiniFrag	Z33546369	937.50	37	00:56:04	done	HPrP-x0798	00:00:35	50.978 - 2.563
599		264.26	MiniFrag	Z1741961236	937.50	37	00:58:23	done	HPrP-x0799	00:00:32	51.143 - 2.487
600		72.11	MiniFrag	Z1259087003	937.50	37	00:59:22	done	HPrP-x0800	00:00:29	43.060 - 2.448
601	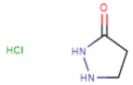	122.55	MiniFrag	Z2935001239	937.50	37	01:00:04	done	HPrP-x0801	00:00:21	65.835 - 2.819
602		94.11	MiniFrag	Z966690946	937.50	37	01:01:06	done	HPrP-x0802	00:00:35	

Entry ID	Structure	Mol Weight (g/mol)	Library Name	Compound Code	Compound Concentration (mM)	Solvent Fraction (%, v/v)	Soaking Time	Harvest Status	Crystal Name	Mounting Time	Resolution Overall (Å)
603	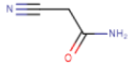	84.08	MiniFrag	Z56896153	937.50	37	01:01:49	done	HPrP-x0803	00:00:32	51.206 - 2.376
604		99.13	MiniFrag	Z33546656	937.50	37	01:02:38	done	HPrP-x0804	00:00:29	51.185 - 2.545
605		102.09	MiniFrag	Z1262398400	937.50	37	01:03:29	done	HPrP-x0805	00:00:21	51.267 - 2.267
606		84.08	MiniFrag	Z56866006	937.50	37	01:04:41	done	HPrP-x0806	00:00:35	65.470 - 2.355
607		100.12	MiniFrag	Z1270212509	937.50	37	01:05:29	done	HPrP-x0807	00:00:32	50.779 - 2.316
608	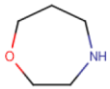	101.15	MiniFrag	Z1198107508	937.50	37	01:06:29	done	HPrP-x0808	00:00:29	50.814 - 2.448
609		85.15	MiniFrag	Z1741971800	937.50	37	01:07:17	done	HPrP-x0809	00:00:21	42.869 - 2.433
610		122.14	MiniFrag	Z3241250482	937.50	37	01:08:05	done	HPrP-x0810	00:00:35	42.684 - 2.402
611		100.12	MiniFrag	Z56968535	937.50	37	01:10:03	done	HPrP-x0811	00:00:29	50.999 - 2.194

Entry ID	Structure	Mol Weight (g/mol)	Library Name	Compound Code	Compound Concentration (mM)	Solvent Fraction (%, v/v)	Soaking Time	Harvest Status	Crystal Name	Mounting Time	Resolution Overall (Å)
612		94.12	MiniFrag	Z955123498	937.50	37	01:11:53	done	HPrP-x0812	00:00:21	50.987 - 2.399
613		95.11	MiniFrag	Z1741968196	937.50	37	01:12:52	done	HPrP-x0813	00:00:35	51.088 - 2.859
614		87.08	MiniFrag	Z3235036808	937.50	37	01:13:53	done	HPrP-x0814	00:00:32	42.914 - 2.478
615		94.07	MiniFrag	Z1436620465	937.50	37	01:15:05	fail			
616		101.15	MiniFrag	Z57127565	937.50	37	01:16:12	done	HPrP-x0815	00:00:29	65.830 - 2.886
617	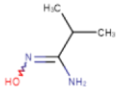	102.14	MiniFrag	Z1741972444	937.50	37	01:17:55	done	HPrP-x0816	00:00:29	42.957 - 2.376
618		96.09	MiniFrag	Z3219959731	937.50	37	01:19:02	done	HPrP-x0817	00:00:21	65.466 - 2.374
619	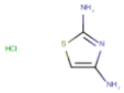	151.61	MiniFrag	Z234893769	937.50	37	01:19:57	done	HPrP-x0818	00:00:35	42.922 - 2.296
620		95.11	MiniFrag	Z1480642703	937.50	37	01:20:54	done	HPrP-x0819	00:00:32	42.714 - 2.360

Entry ID	Structure	Mol Weight (g/mol)	Library Name	Compound Code	Compound Concentration (mM)	Solvent Fraction (%, v/v)	Soaking Time	Harvest Status	Crystal Name	Mounting Time	Resolution Overall (Å)
621	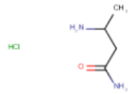	138.60	MiniFrag	Z1459435569	937.50	37	01:21:38	fail			
622	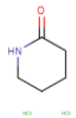	99.13	MiniFrag	Z1201023039	937.50	37	01:22:15	done	HPrP-x0820	00:00:29	42.684 - 2.384
623		170.04	MiniFrag	Z2692604705	937.50	37	01:22:54	done	HPrP-x0821	00:00:21	42.878 - 2.386
624	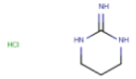	135.60	MiniFrag	Z1954800348	937.50	37	01:23:32	done	HPrP-x0822	00:00:35	50.762 - 2.366
625		72.11	MiniFrag	Z955123562	937.50	37	01:24:21	done	HPrP-x0823	00:00:32	42.771 - 2.459
626	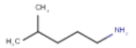	101.19	MiniFrag	Z3219863192	937.50	37	01:25:13	done	HPrP-x0824	00:00:29	42.751 - 2.232
627	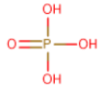	97.99	MiniFrag	Z1954805639	937.50	37	01:26:20	done	HPrP-x0825	00:00:21	43.014 - 2.248
628		79.10	MiniFrag	Z940713324	937.50	37	01:27:10	done	HPrP-x0826	00:00:35	51.253 - 2.203
629		102.14	MiniFrag	Z56887677	937.50	37	01:27:54	done	HPrP-x0827	00:00:32	42.931 - 2.143

Entry ID	Structure	Mol Weight (g/mol)	Library Name	Compound Code	Compound Concentration (mM)	Solvent Fraction (%, v/v)	Soaking Time	Harvest Status	Crystal Name	Mounting Time	Resolution Overall (Å)
630		146.98	MiniFrag	Z275169750	937.50	37	01:28:38	done	HPrP-x0828	00:00:29	42.614 - 2.211
631		68.08	MiniFrag	Z1245636370	937.50	37	01:29:35	done	HPrP-x0829	00:00:21	65.586 - 2.412
632		74.08	MiniFrag	Z955123616	937.50	37	01:30:18	done	HPrP-x0830	00:00:35	50.903 - 2.547
633		83.09	MiniFrag	Z241119328	937.50	37	01:31:02	done	HPrP-x0831	00:00:32	42.899 - 2.405
634		84.08	MiniFrag	Z56761437	937.50	37	01:32:23	done	HPrP-x0832	00:00:29	50.84 - 2.48
635	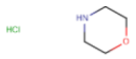	123.58	MiniFrag	Z3234810942	937.50	37	01:33:03	done	HPrP-x0833	00:00:21	42.780 - 2.452
636	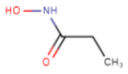	89.09	MiniFrag	Z59181971	937.50	37	01:33:50	done	HPrP-x0834	00:00:35	42.872 - 2.299
637		86.09	MiniFrag	Z1741976468	937.50	37	01:34:29	done	HPrP-x0835	00:00:32	51.796 - 1.917
638	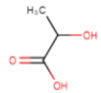	90.08	MiniFrag	Z1741982441	937.50	37	01:36:14	done	HPrP-x0836	00:00:29	42.755 - 2.667

Entry ID	Structure	Mol Weight (g/mol)	Library Name	Compound Code	Compound Concentration (mM)	Solvent Fraction (%, v/v)	Soaking Time	Harvest Status	Crystal Name	Mounting Time	Resolution Overall (Å)
639		99.92	MiniFrag	Z1741980935	937.50	37	01:36:53	done	HPrP-x0837	00:00:21	42.878 - 2.511
640		98.11	MiniFrag	Z1962142017	937.50	37	01:38:18	done	HPrP-x0838	00:00:35	42.899 - 2.438
641		101.15	MiniFrag	Z1333717631	937.50	37	01:38:53	done	HPrP-x0839	00:00:32	42.969 - 2.399
642		71.12	MiniFrag	Z1198394159	937.50	37	01:40:06	done	HPrP-x0840	00:00:29	42.940 - 2.442
643		67.09	MiniFrag	Z1245735215	937.50	37	01:41:35	done	HPrP-x0841	00:00:21	66.057 - 2.810
644		84.08	MiniFrag	Z1741972704	937.50	37	01:42:14	done	HPrP-x0842	00:00:35	43.044 - 2.329
645	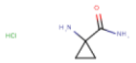	136.58	MiniFrag	Z1415893881	937.50	37	01:43:03	done	HPrP-x0843	00:00:32	42.770 - 2.269
646		88.06	MiniFrag	Z1741977082	937.50	37	01:43:50	done	HPrP-x0844	00:00:29	65.569 - 2.302
647	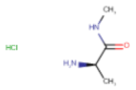	138.60	MiniFrag	Z1346385420	937.50	37	01:44:26	done	HPrP-x0845	00:00:21	51.137 - 2.213

Entry ID	Structure	Mol Weight (g/mol)	Library Name	Compound Code	Compound Concentration (mM)	Solvent Fraction (%, v/v)	Soaking Time	Harvest Status	Crystal Name	Mounting Time	Resolution Overall (Å)
648	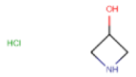	109.55	MiniFrag	Z1262327449	937.50	37	01:45:44	done	HPrP-x0846	00:00:35	36.087 - 2.333
649	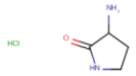	136.58	MiniFrag	Z3234814534	937.50	37	01:46:33	done	HPrP-x0847	00:00:32	51.078 - 2.357
650	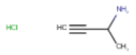	105.57	MiniFrag	Z1954800314	937.50	37	01:47:54	done	HPrP-x0848	00:00:29	42.962 - 2.610
651	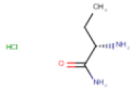	138.60	MiniFrag	Z1450533799	937.50	37	01:48:45	done	HPrP-x0849	00:00:21	
652	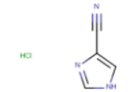	129.55	MiniFrag	Z2301685688	937.50	37	01:49:42	done	HPrP-x0850	00:00:35	43.143 - 2.677
653	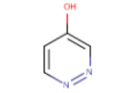	96.09	MiniFrag	Z1741975221	937.50	37	01:50:33	done	HPrP-x0851	00:00:29	42.798 - 2.479
654	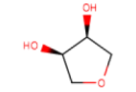	104.11	MiniFrag	Z3235034972	937.50	37	01:51:24	done	HPrP-x0852	00:00:21	42.988 - 2.462
655	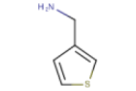	113.18	MiniFrag	Z1262255347	937.50	37	01:52:31	done	HPrP-x0853	00:00:35	42.749 - 2.493
656	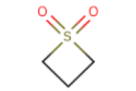	106.14	MiniFrag	Z3234823734	937.50	37	01:53:18	done	HPrP-x0854	00:00:32	42.929 - 2.252

Entry ID	Structure	Mol Weight (g/mol)	Library Name	Compound Code	Compound Concentration (mM)	Solvent Fraction (%, v/v)	Soaking Time	Harvest Status	Crystal Name	Mounting Time	Resolution Overall (Å)
657		146.98	FragLite	NCL-00023819	4.80	5		done	HPrP-x0855	00:00:29	
658		146.98	FragLite	NCL-00023819	10.10	10		done	HPrP-x0856	00:00:25	
659		146.98	FragLite	NCL-00023819	14.90	15		done	HPrP-x0857	00:00:22	
660		220.01	FragLite	NCL-00023822	4.80	5		done	HPrP-x0858	00:00:27	42.760 - 2.453
661		220.01	FragLite	NCL-00023822	10.10	10		done	HPrP-x0859	00:00:28	
662		220.01	FragLite	NCL-00023822	14.90	15		done	HPrP-x0860	00:00:22	
663		188.02	FragLite	NCL-00024670	4.80	5		done	HPrP-x0861	00:00:18	43.194 - 2.072
664		188.02	FragLite	NCL-00024670	10.10	10		done	HPrP-x0862	00:00:25	
665		188.02	FragLite	NCL-00024670	14.90	15		done	HPrP-x0863	00:00:46	

Entry ID	Structure	Mol Weight (g/mol)	Library Name	Compound Code	Compound Concentration (mM)	Solvent Fraction (%, v/v)	Soaking Time	Harvest Status	Crystal Name	Mounting Time	Resolution Overall (Å)
666		140.14	DSIpoised	Z1124201124	23.80	5		done	HPrP-x0864	00:00:22	42.965 - 2.216
667		140.14	DSIpoised	Z1124201124	50.60	10		done	HPrP-x0865	00:00:27	
668		140.14	DSIpoised	Z1124201124	74.50	15		done	HPrP-x0866	00:00:33	
669	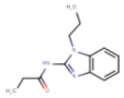	231.30	DSIpoised	Z29077827	23.80	5		done	HPrP-x0867	00:00:18	
670	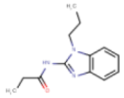	231.30	DSIpoised	Z29077827	50.60	10		done	HPrP-x0868	00:00:26	
671	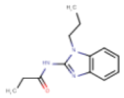	231.30	DSIpoised	Z29077827	74.50	15		done	HPrP-x0869	00:00:53	
672		194.23	DSIpoised	Z235341991	23.80	5		done	HPrP-x0870	00:00:32	
673		194.23	DSIpoised	Z235341991	50.60	10		done	HPrP-x0871	00:00:21	42.722 - 2.440
674		194.23	DSIpoised	Z235341991	74.50	15		done	HPrP-x0872	00:00:21	

Entry ID	Structure	Mol Weight (g/mol)	Library Name	Compound Code	Compound Concentration (mM)	Solvent Fraction (%, v/v)	Soaking Time	Harvest Status	Crystal Name	Mounting Time	Resolution Overall (Å)
675	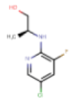	204.63	DSIpoised	Z1432018343	23.80	5		done	HPrP-x0873	00:00:30	43.087 - 2.445
676	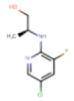	204.63	DSIpoised	Z1432018343	50.60	10		done	HPrP-x0874	00:00:22	43.009 - 2.293
677	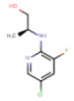	204.63	DSIpoised	Z1432018343	74.50	15		done	HPrP-x0875	00:00:22	
678		208.24	DSIpoised	Z1186029914	23.80	5		done	HPrP-x0876	00:00:18	42.776 - 1.841
679	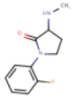	208.24	DSIpoised	Z1186029914	50.60	10		done	HPrP-x0877	00:00:19	43.173 - 2.072
680	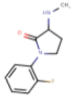	208.24	DSIpoised	Z1186029914	74.50	15		done	HPrP-x0878	00:00:29	
681	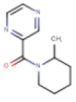	205.26	DSIpoised	Z32968340	23.80	5		done	HPrP-x0879	00:01:38	42.731 - 2.379
682	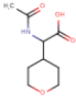	201.22	DSIpoised	Z1891772663	23.80	5		done	HPrP-x0880	00:00:18	
683	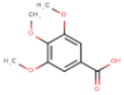	212.20	DSIpoised	Z2734782702	23.80	5		fail		00:00:06	

Entry ID	Structure	Mol Weight (g/mol)	Library Name	Compound Code	Compound Concentration (mM)	Solvent Fraction (%, v/v)	Soaking Time	Harvest Status	Crystal Name	Mounting Time	Resolution Overall (Å)
684	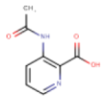	180.16	DSIpoised	Z1815155460	23.80	5		done	HPrP-x0881	00:00:34	42.959 - 2.526
685		214.24	DSIpoised	Z45656995	23.80	5		done	HPrP-x0882	00:00:21	36.163 - 2.268
686	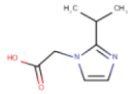	168.20	DSIpoised	Z2446040567	23.80	5		done	HPrP-x0883	00:00:18	36.139 - 2.308
687		179.24	DSIpoised	Z1530301542	23.80	5		done	HPrP-x0884	00:00:20	
688	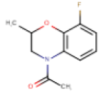	209.22	DSIpoised	Z1730522163	23.80	5		done	HPrP-x0885	00:00:43	65.795 - 2.519
689		228.27	DSIpoised	Z30932204	23.80	5		done	HPrP-x0886	00:00:19	43.118 - 2.533
690	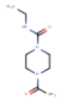	199.25	DSIpoised	Z44590919	23.80	5		done	HPrP-x0887	00:00:40	42.685 - 2.320
691		180.20	DSIpoised	Z2856434918	23.80	5		done	HPrP-x0888	00:00:20	
692	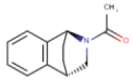	201.27	DSIpoised	Z2017861827	23.80	5		done	HPrP-x0889	00:00:24	43.021 - 2.498

Entry ID	Structure	Mol Weight (g/mol)	Library Name	Compound Code	Compound Concentration (mM)	Solvent Fraction (%, v/v)	Soaking Time	Harvest Status	Crystal Name	Mounting Time	Resolution Overall (Å)
693	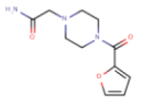	237.26	DSIpoised	Z2856434793	23.80	5		done	HPrP-x0890	00:00:26	43.094 - 2.519
694	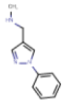	187.25	DSIpoised	Z102768020	23.80	5		done	HPrP-x0891	00:00:18	66.192 - 3.345
695		147.18	DSIpoised	Z1429867185	23.80	5		done	HPrP-x0892	00:00:29	65.782 - 2.459
696	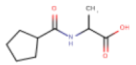	185.22	DSIpoised	Z1238477790	23.80	5		done	HPrP-x0893	00:00:19	
697		140.14	DSIpoised	Z1124201124	23.80	5	04:12:00	done	HPrP-x0954	00:00:47	
698	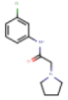	238.72	DSIpoised	Z2735692823	23.80	5	04:12:37	done	HPrP-x0955	00:00:33	64.902 - 2.543
699	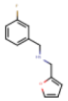	205.23	DSIpoised	Z2737076969	23.80	5	04:13:18	done	HPrP-x0956	00:00:38	42.373 - 2.616
700	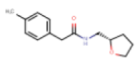	233.31	DSIpoised	Z2064898339	23.80	5	04:14:05	done	HPrP-x0957	00:00:25	35.846 - 2.724
701	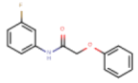	245.25	DSIpoised	Z19735192	23.80	5	04:15:19	done	HPrP-x0958	00:01:13	50.685 - 2.624

Entry ID	Structure	Mol Weight (g/mol)	Library Name	Compound Code	Compound Concentration (mM)	Solvent Fraction (%, v/v)	Soaking Time	Harvest Status	Crystal Name	Mounting Time	Resolution Overall (Å)
702	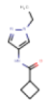	193.25	DSIpoised	Z373768900	23.80	5	04:16:45	done	HPrP-x0959	00:00:42	64.890 - 2.885
703		248.33	DSIpoised	Z2856434836	23.80	5	04:17:48	done	HPrP-x0960	00:00:43	42.497 - 2.756
704	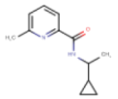	204.27	DSIpoised	Z287256168	23.80	5	04:18:23	done	HPrP-x0961	00:00:29	50.543 - 2.623
705	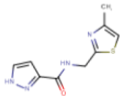	222.27	DSIpoised	Z466628048	23.80	5	04:18:58	done	HPrP-x0962	00:00:34	50.692 - 2.723
706	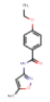	246.27	DSIpoised	Z86948938	23.80	5	04:19:40	done	HPrP-x0963	00:00:33	42.473 - 3.065
707	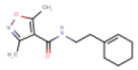	248.33	DSIpoised	Z69092635	23.80	5	04:20:50	done	HPrP-x0964	00:01:06	42.120 - 2.958
708	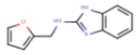	213.24	DSIpoised	Z57299526	23.80	5	04:21:31	done	HPrP-x0965	00:00:30	
709	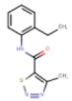	247.32	DSIpoised	Z89385775	23.80	5	04:22:32	done	HPrP-x0966	00:00:50	35.557 - 2.813
710	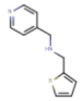	204.29	DSIpoised	Z2856434816	23.80	5	04:23:09	done	HPrP-x0967	00:00:29	50.711 - 3.209

Entry ID	Structure	Mol Weight (g/mol)	Library Name	Compound Code	Compound Concentration (mM)	Solvent Fraction (%, v/v)	Soaking Time	Harvest Status	Crystal Name	Mounting Time	Resolution Overall (Å)
711	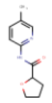	206.25	DSIpoised	Z71580604	23.80	5	04:23:53	done	HPrP-x0968	00:00:31	50.376 - 2.557
712	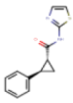	244.31	DSIpoised	Z2064107709	23.80	5	04:24:27	done	HPrP-x0969	00:00:32	64.950 - 2.935
713	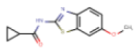	248.30	DSIpoised	Z27678561	23.80	5	04:25:04	done	HPrP-x0970	00:00:25	64.938 - 3.103
714	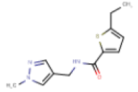	249.33	DSIpoised	Z804566442	23.80	5	04:31:43	done	HPrP-x0971	00:00:28	65.437 - 2.876
715	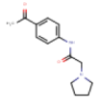	246.31	DSIpoised	Z2856434916	23.80	5	04:33:02	fail		00:00:54	
716	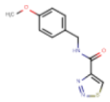	249.29	DSIpoised	Z741218268	23.80	5	04:33:37	done	HPrP-x0972	00:00:28	42.583 - 3.177
717	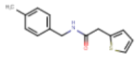	245.34	DSIpoised	Z28429411	23.80	5	04:34:27	done	HPrP-x0973	00:00:46	42.608 - 2.357
718	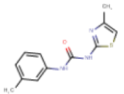	247.32	DSIpoised	Z44602971	23.80	5	04:34:55	done	HPrP-x0974	00:00:27	42.481 - 2.729
719		222.63	DSIpoised	Z86622311	23.80	5	04:35:38	done	HPrP-x0975	00:00:32	64.918 - 2.564

Entry ID	Structure	Mol Weight (g/mol)	Library Name	Compound Code	Compound Concentration (mM)	Solvent Fraction (%, v/v)	Soaking Time	Harvest Status	Crystal Name	Mounting Time	Resolution Overall (Å)
720	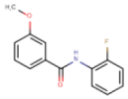	245.25	DSIpoised	Z28290384	23.80	5	04:37:17	done	HPrP-x0976	00:01:16	50.610 - 3.134
721	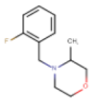	209.26	DSIpoised	Z369042042	23.80	5	04:37:45	done	HPrP-x0977	00:00:25	50.743 - 3.128
722	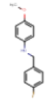	231.27	DSIpoised	Z57328997	23.80	5	04:38:36	done	HPrP-x0978	00:00:43	64.526 - 2.886
723		209.31	DSIpoised	Z2856434857	23.80	5	04:39:09	done	HPrP-x0979	00:00:27	42.151 - 2.739
724	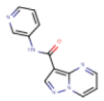	239.24	DSIpoised	Z296054478	23.80	5	04:39:38	done	HPrP-x0980	00:00:22	42.345 - 2.883
725	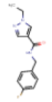	247.27	DSIpoised	Z1203107138	23.80	5	04:40:11	done	HPrP-x0981	00:00:27	35.730 - 2.774
726	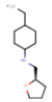	211.35	DSIpoised	Z2856434866	23.80	5	04:41:35	done	HPrP-x0982	00:01:15	42.547 - 3.172
727	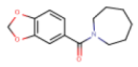	247.29	DSIpoised	Z31432226	23.80	5	04:42:33	done	HPrP-x0983	00:00:50	50.630 - 3.019
728	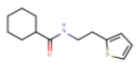	237.36	DSIpoised	Z29191465	23.80	5	04:43:13	done	HPrP-x0984	00:00:39	65.233 - 2.952

Entry ID	Structure	Mol Weight (g/mol)	Library Name	Compound Code	Compound Concentration (mM)	Solvent Fraction (%, v/v)	Soaking Time	Harvest Status	Crystal Name	Mounting Time	Resolution Overall (Å)
729	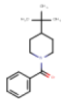	245.37	DSIpoised	Z1217741507	23.80	5	04:43:52	done	HPrP-x0985	00:00:37	50.770 - 3.726
730	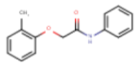	241.29	DSIpoised	Z19733979	23.80	5	04:44:26	done	HPrP-x0986	00:00:32	50.511 - 2.890
731	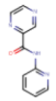	200.20	DSIpoised	Z85525386	23.80	5	04:44:56	done	HPrP-x0987	00:00:28	64.958 - 2.728
732	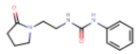	247.30	DSIpoised	Z2472938267	23.80	5	04:45:21	done	HPrP-x0988	00:00:24	42.472 - 2.989
733	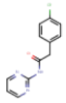	247.68	DSIpoised	Z203581214	23.80	5	04:46:03	done	HPrP-x0989	00:00:41	42.236 - 2.703
734		235.30	DSIpoised	Z31484539	23.80	5	04:46:44	done	HPrP-x0990	00:00:37	65.712 - 3.428
735	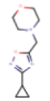	209.25	DSIpoised	Z295848548	23.80	5	04:47:31	done	HPrP-x0991	00:00:32	42.564 - 3.475
736	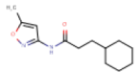	236.32	DSIpoised	Z86949053	23.80	5	04:48:06	done	HPrP-x0992	00:00:32	64.834 - 2.873
737	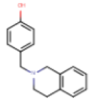	239.32	DSIpoised	Z2856434812	23.80	5	04:48:42	done	HPrP-x0993	00:00:33	50.616 - 2.854

Entry ID	Structure	Mol Weight (g/mol)	Library Name	Compound Code	Compound Concentration (mM)	Solvent Fraction (%, v/v)	Soaking Time	Harvest Status	Crystal Name	Mounting Time	Resolution Overall (Å)
738	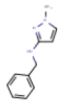	187.25	DSIpoised	Z1401333862	23.80	5	04:49:26	done	HPrP-x0994	00:00:41	50.581 - 3.207
739	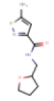	226.29	DSIpoised	Z1881545321	23.80	5	04:50:02	done	HPrP-x0995	00:00:33	65.833 - 3.081
740		239.33	DSIpoised	Z2856434929	23.80	5	04:50:25	done	HPrP-x0996	00:00:22	50.630 - 3.068
741	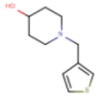	197.30	DSIpoised	Z2856434899	23.80	5	04:50:53	done	HPrP-x0997	00:00:27	42.317 - 3.415
742	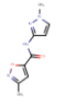	206.21	DSIpoised	Z240297434	23.80	5	04:51:33	done	HPrP-x0998	00:00:38	50.779 - 3.898
743	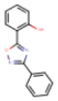	238.25	DSIpoised	Z276351322	23.80	5	04:52:23	done	HPrP-x0999	00:00:48	42.100 - 2.803
744	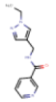	230.27	DSIpoised	Z275181224	23.80	5	04:52:56	done	HPrP-x1000	00:00:30	50.679 - 3.172
745	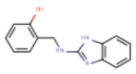	239.28	DSIpoised	Z1587220559	23.80	5	04:55:11	done	HPrP-x1001	00:00:02	50.789 - 3.514
746	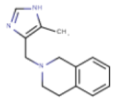	227.31	DSIpoised	Z2856434879	23.80	5	04:55:40	done	HPrP-x1002	00:00:26	67.651 - 4.555

Entry ID	Structure	Mol Weight (g/mol)	Library Name	Compound Code	Compound Concentration (mM)	Solvent Fraction (%, v/v)	Soaking Time	Harvest Status	Crystal Name	Mounting Time	Resolution Overall (Å)
747	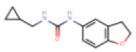	232.28	DSIpoised	Z413792090	23.80	5	04:56:15	done	HPrP-x1003	00:00:34	41.959 - 3.782
748	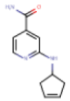	203.25	DSIpoised	Z1416571195	23.80	5	04:56:45	done	HPrP-x1004	00:00:28	50.521 - 3.326
749	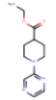	235.29	DSIpoised	Z31217395	23.80	5	04:57:14	done	HPrP-x1005	00:00:26	41.186 - 4.168
750	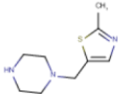	197.30	DSIpoised	Z1171217421	23.80	5	04:57:37	done	HPrP-x1006	00:00:21	50.607 - 3.570
751	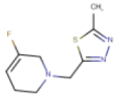	213.27	DSIpoised	Z1619978933	23.80	5	04:58:09	done	HPrP-x1007	00:00:23	65.070 - 3.144
752		207.28	DSIpoised	Z1675346324	23.80	5	04:58:42	done	HPrP-x1008	00:00:29	50.390 - 3.347
753	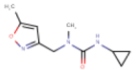	209.25	DSIpoised	Z369936976	23.80	5	04:59:11	done	HPrP-x1009	00:00:26	65.29 - 4.35
754		223.33	DSIpoised	Z2856434865	23.80	5	04:59:40	done	HPrP-x1010	00:00:27	50.371 - 2.806
755		183.27	DSIpoised	Z1251207602	23.80	5	05:00:08	done	HPrP-x1011	00:00:25	41.168 - 3.082

Entry ID	Structure	Mol Weight (g/mol)	Library Name	Compound Code	Compound Concentration (mM)	Solvent Fraction (%, v/v)	Soaking Time	Harvest Status	Crystal Name	Mounting Time	Resolution Overall (Å)
756	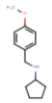	205.30	DSIpoised	Z2856434940	23.80	5	05:00:52	done	HPrP-x1012	00:00:43	42.352 - 3.730
757	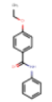	241.29	DSIpoised	Z27782760	23.80	5	05:01:27	done	HPrP-x1013	00:00:33	42.242 - 2.414
758	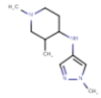	208.31	DSIpoised	Z1694504496	23.80	5	05:01:53	done	HPrP-x1014	00:00:24	65.080 - 2.287
759	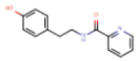	242.28	DSIpoised	Z730649594	23.80	5	05:03:14	done	HPrP-x1015	00:01:17	64.753 - 2.327
760	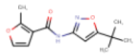	248.28	DSIpoised	Z1086293874	23.80	5	05:04:14	done	HPrP-x1016	00:00:59	65.351 - 2.886
761	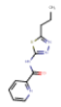	248.30	DSIpoised	Z52425517	23.80	5	05:04:45	done	HPrP-x1017	00:00:28	
762	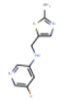	223.27	DSIpoised	Z1983897532	23.80	5	05:05:26	done	HPrP-x1018	00:00:40	50.437 - 2.860
763	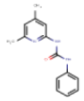	241.29	DSIpoised	Z1693429442	23.80	5	05:05:50	done	HPrP-x1019	00:00:22	42.232 - 2.882
764		249.31	DSIpoised	Z17497990	23.80	5	05:06:15	done	HPrP-x1020	00:00:22	42.523 - 2.599

Entry ID	Structure	Mol Weight (g/mol)	Library Name	Compound Code	Compound Concentration (mM)	Solvent Fraction (%, v/v)	Soaking Time	Harvest Status	Crystal Name	Mounting Time	Resolution Overall (Å)
765	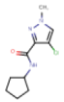	227.69	DSIpoised	Z275151340	23.80	5	05:06:42	done	HPrP-x1021	00:00:26	49.817 - 3.418
766	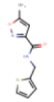	222.26	DSIpoised	Z29692148	23.80	5	05:07:18	done	HPrP-x1022	00:00:33	49.840 - 4.360
767	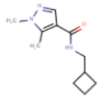	207.28	DSIpoised	Z396380540	23.80	5	05:08:13	done	HPrP-x1023	00:00:52	64.834 - 3.077
768	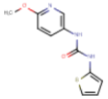	249.29	DSIpoised	Z1152242726	23.80	5	05:08:38	done	HPrP-x1024	00:00:18	50.651 - 3.110
769	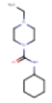	239.36	DSIpoised	Z2856434830	23.80	5	05:09:17	done	HPrP-x1025	00:00:20	50.396 - 3.176
770	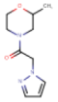	209.25	DSIpoised	Z217038356	23.80	5	05:09:42	done	HPrP-x1026	00:00:21	50.659 - 2.949
771	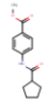	247.29	DSIpoised	Z28226359	23.80	5	05:10:05	done	HPrP-x1027	00:00:20	64.86 - 3.43
772	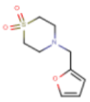	215.27	DSIpoised	Z2856434926	23.80	5	05:10:30	done	HPrP-x1028	00:00:23	35.819 - 2.760
773	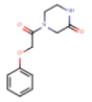	234.26	DSIpoised	Z31602870	23.80	5	05:11:30	done	HPrP-x1029	00:00:56	42.325 - 2.642

Entry ID	Structure	Mol Weight (g/mol)	Library Name	Compound Code	Compound Concentration (mM)	Solvent Fraction (%, v/v)	Soaking Time	Harvest Status	Crystal Name	Mounting Time	Resolution Overall (Å)
774	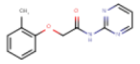	243.27	DSIpoised	Z53834613	23.80	5	05:11:51	done	HPrP-x1030	00:00:18	50.340 - 2.852
775		223.23	DSIpoised	Z86417414	23.80	5	05:12:19	done	HPrP-x1031	00:00:25	35.697 - 3.273
776	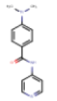	241.29	DSIpoised	Z85517292	23.80	5	05:12:47	done	HPrP-x1032	00:00:26	50.464 - 3.240
777	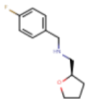	209.26	DSIpoised	Z2856434824	23.80	5	05:14:03	done	HPrP-x1033	00:01:13	35.771 - 2.251
778	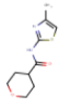	226.29	DSIpoised	Z73240835	23.80	5	05:14:30	done	HPrP-x1034	00:00:26	42.199 - 3.274
779		248.33	DSIpoised	Z2856434834	23.80	5	05:15:02	done	HPrP-x1035	00:00:25	50.253 - 3.030
780	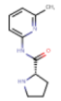	205.26	DSIpoised	Z1267881672	23.80	5	05:15:26	done	HPrP-x1036	00:00:22	42.645 - 2.674
781		203.25	DSIpoised	Z1348371854	23.80	5	05:16:01	done	HPrP-x1037	00:00:25	42.274 - 2.684
782	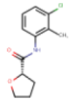	239.70	DSIpoised	Z1545312521	23.80	5	05:16:25	done	HPrP-x1038	00:00:23	42.493 - 3.014

Entry ID	Structure	Mol Weight (g/mol)	Library Name	Compound Code	Compound Concentration (mM)	Solvent Fraction (%, v/v)	Soaking Time	Harvest Status	Crystal Name	Mounting Time	Resolution Overall (Å)
783	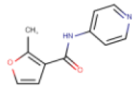	202.21	DSIpoised	Z136583524	23.80	5	05:17:44	done	HPrP-x1039	00:01:10	50.857 - 2.824
784	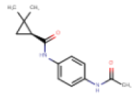	246.31	DSIpoised	Z1505719304	23.80	5	05:18:06	done	HPrP-x1040	00:00:19	51.368 - 3.395
785	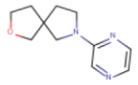	205.26	DSIpoised	Z1401276297	23.80	5	05:18:30	done	HPrP-x1041	00:00:22	50.637 - 3.380
786	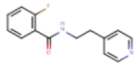	244.27	DSIpoised	Z1310876699	23.80	5	05:20:04	done	HPrP-x1042	00:01:32	42.235 - 2.733
787	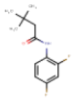	227.26	DSIpoised	Z30802768	23.80	5	05:21:16	done	HPrP-x1043	00:01:10	42.409 - 2.459
788	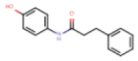	241.29	DSIpoised	Z69118333	23.80	5	05:21:39	done	HPrP-x1044	00:00:22	42.484 - 3.066
789	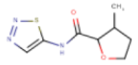	213.26	DSIpoised	Z1827602749	23.80	5	05:22:11	done	HPrP-x1045	00:00:28	
790	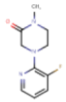	209.22	DSIpoised	Z1373445602	23.80	5	05:22:40	done	HPrP-x1046	00:00:27	42.557 - 2.635
791	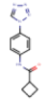	243.27	DSIpoised	Z26552420	23.80	5	05:23:51	fail		00:01:09	

Entry ID	Structure	Mol Weight (g/mol)	Library Name	Compound Code	Compound Concentration (mM)	Solvent Fraction (%, v/v)	Soaking Time	Harvest Status	Crystal Name	Mounting Time	Resolution Overall (Å)
792	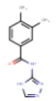	216.24	DSIpoised	Z2856434827	23.80	5	05:24:15	done	HPrP-x1047	00:00:22	
793	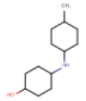	211.35	DSIpoised	Z2241963319	23.80	5	05:24:47	done	HPrP-x1048	00:00:22	42.670 - 3.989
794	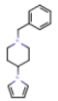	240.35	DSIpoised	Z2856434898	23.80	5	05:26:04	done	HPrP-x1049	00:01:15	42.517 - 2.583
795	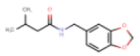	235.28	DSIpoised	Z27695365	23.80	5	05:26:32	done	HPrP-x1050	00:00:24	42.603 - 3.803
796	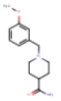	248.33	DSIpoised	Z2856434854	23.80	5	05:27:11	done	HPrP-x1051	00:00:37	42.005 - 2.961
797	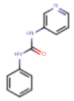	213.24	DSIpoised	Z44592329	23.80	5	05:28:39	done	HPrP-x1052	00:01:25	42.440 - 2.312
798	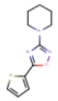	235.31	DSIpoised	Z1623890017	23.80	5	05:29:02	done	HPrP-x1053	00:00:21	50.286 - 2.880
799	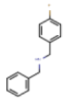	215.27	DSIpoised	Z2856434783	23.80	5	05:29:34	done	HPrP-x1054	00:00:30	35.772 - 2.423
800	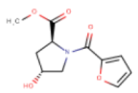	239.23	DSIpoised	Z1614545742	23.80	5	05:29:57	done	HPrP-x1055	00:00:21	50.491 - 2.883

Entry ID	Structure	Mol Weight (g/mol)	Library Name	Compound Code	Compound Concentration (mM)	Solvent Fraction (%, v/v)	Soaking Time	Harvest Status	Crystal Name	Mounting Time	Resolution Overall (Å)
801	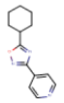	229.28	DSIpoised	Z57715447	23.80	5	05:30:37	done	HPrP-x1056	00:00:39	42.735 - 2.575
802		231.17	DSIpoised	Z57111868	23.80	5	05:31:01	done	HPrP-x1057	00:00:21	42.370 - 2.517
803	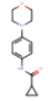	246.31	DSIpoised	Z30485868	23.80	5	05:31:28	done	HPrP-x1058	00:00:26	36.711 - 5.204
804	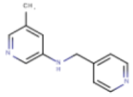	199.26	DSIpoised	Z1478435544	23.80	5	05:31:52	done	HPrP-x1059	00:00:21	
805	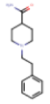	232.33	DSIpoised	Z2856434897	23.80	5	05:32:20	done	HPrP-x1060	00:00:25	50.657 - 3.427
806	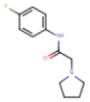	222.26	DSIpoised	Z2856434942	23.80	5	05:33:07	done	HPrP-x1061	00:00:45	50.818 - 2.996
807	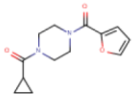	248.28	DSIpoised	Z32327641	23.80	5	05:33:30	done	HPrP-x1062	00:00:20	50.655 - 2.801
808		236.33	DSIpoised	Z416341642	23.80	5	05:34:10	done	HPrP-x1063	00:00:39	42.220 - 3.296